METAL-FREE ROOM-TEMPERATURE PHOSPHORESCENCE

EDITED BY: Shuzo Hirata, Sebastian Reineke, Abhijit Patra and
Wang Zhang Yuan

PUBLISHED IN: Frontiers in Chemistry and Frontiers in Physics

frontiers Research Topics

Frontiers eBook Copyright Statement

ISSN 1664-8714
ISBN 978-2-83250-422-2
DOI 10.3389/978-2-83250-422-2

About Frontiers

Frontiers is more than just an open-access publisher of scholarly articles: it is a pioneering approach to the world of academia, radically improving the way scholarly research is managed. The grand vision of Frontiers is a world where all people have an equal opportunity to seek, share and generate knowledge. Frontiers provides immediate and permanent online open access to all its publications, but this alone is not enough to realize our grand goals.

Frontiers Journal Series

The Frontiers Journal Series is a multi-tier and interdisciplinary set of open-access, online journals, promising a paradigm shift from the current review, selection and dissemination processes in academic publishing. All Frontiers journals are driven by researchers for researchers; therefore, they constitute a service to the scholarly community. At the same time, the Frontiers Journal Series operates on a revolutionary invention, the tiered publishing system, initially addressing specific communities of scholars, and gradually climbing up to broader public understanding, thus serving the interests of the lay society, too.

Dedication to Quality

Each Frontiers article is a landmark of the highest quality, thanks to genuinely collaborative interactions between authors and review editors, who include some of the world's best academicians. Research must be certified by peers before entering a stream of knowledge that may eventually reach the public - and shape society; therefore, Frontiers only applies the most rigorous and unbiased reviews.
Frontiers revolutionizes research publishing by freely delivering the most outstanding research, evaluated with no bias from both the academic and social point of view. By applying the most advanced information technologies, Frontiers is catapulting scholarly publishing into a new generation.

What are Frontiers Research Topics?

Frontiers Research Topics are very popular trademarks of the Frontiers Journals Series: they are collections of at least ten articles, all centered on a particular subject. With their unique mix of varied contributions from Original Research to Review Articles, Frontiers Research Topics unify the most influential researchers, the latest key findings and historical advances in a hot research area! Find out more on how to host your own Frontiers Research Topic or contribute to one as an author by contacting the Frontiers Editorial Office: frontiersin.org/about/contact

METAL-FREE ROOM-TEMPERATURE PHOSPHORESCENCE

Topic Editors:
Shuzo Hirata, The University of Electro-Communications, Japan
Sebastian Reineke, Technical University Dresden, Germany
Abhijit Patra, Indian Institute of Science Education and Research, Bhopal, India
Wang Zhang Yuan, Shanghai Jiao Tong University, China

Citation: Hirata, S., Reineke, S., Patra, A., Yuan, W. Z., eds. (2022). Metal-Free Room-Temperature Phosphorescence. Lausanne: Frontiers Media SA. doi: 10.3389/978-2-83250-422-2

Table of Contents

frontiers | Frontiers in Chemistry

TYPE Editorial
PUBLISHED 23 September 2022
DOI 10.3389/fchem.2022.1025674

OPEN ACCESS

EDITED AND REVIEWED BY
Francesco Zinna,
University of Pisa, Italy

*CORRESPONDENCE
Shuzo Hirata,
shuzohirata@uec.ac.jp
Sebastian Reineke,
sebastian.reineke@tu-dresden.de
Abhijit Patra,
abhijit@iiserb.ac.in
Wang Zhang Yuan,
wzhyuan@sjtu.edu.cn

SPECIALTY SECTION
This article was submitted to Physical Chemistry and Chemical Physics, a section of the journal Frontiers in Chemistry

RECEIVED 23 August 2022
ACCEPTED 30 August 2022
PUBLISHED 23 September 2022

CITATION
Hirata S, Reineke S, Patra A and Yuan WZ (2022), Editorial: Metal-free room-temperature phosphorescence.
Front. Chem. 10:1025674.
doi: 10.3389/fchem.2022.1025674

Editorial: Metal-free room-temperature phosphorescence

Shuzo Hirata[1]*, Sebastian Reineke[2]*, Abhijit Patra[3]* and Wang Zhang Yuan[4]*

[1]The University of Electro-Communications, Tokyo, Japan, [2]Dresden Integrated Center for Applied Physics and Photonic Materials (IAPP), Technische Universität Dresden, Dresden, Germany, [3]Indian Institute of Science Education and Research Bhopal, Bhopal, India, [4]Shanghai Jiao Tong University, Shanghai, China

KEYWORDS

room-temperature phosphorescence, metal-free RTP, persistent RTP, delayed emission, triplet state, nonradiative deactivation, oxygen quenching, intersystem crossing

Editorial on the Research Topic
Metal-Free Room-Temperature Phosphorescence

Room-temperature phosphorescence (RTP) from metal-free materials has recently attracted the interest of the scientific community in a variety of imaging fields owing to the fact that it provides high-resolution information independent of the autofluorescence and dual-colored emitting characteristics, which are advantages that fluorescent materials and phosphorescent heavy-metal complexes do not possess. State-of-the-art advances in security, sensors, and bioimaging have been proposed using the aforementioned advantages. This Research Topic includes ten articles on the latest advances in this research area.

Suppression of triplet deactivation, including oxygen quenching, is an important factor to enhance the RTP properties. An article by (Yang et al.) reports oxygen sensing using thianthrene derivatives doped into amorphous polymer matrices. The thianthrene chromophores show dual emission of fluorescence and RTP in the polymers because folding-induced spin–orbit coupling of the chromophores greatly enhances the RTP characteristics. Ratiometric imaging owing to the dual fluorescence and the enhanced RTP allows easy quantitative detection of oxygen under a variety of conditions. Furthermore, the relationship between the RTP intensity and oxygen concentration provides quantitative information about the oxygen permeability in solid materials.

As different triplet-quenching characteristics independent of oxygen, a study by (Thomas et al.) investigates the change of the triplet nonradiative processes of RTP chromophores doped in a polymer host under inert conditions depending on different preparation techniques of the films. Residual solvents and the role of guest chromophores in enhancing the intermolecular interactions of the polymer matrices are proposed as reasons for the different nonradiative deactivation from the triplet state. For the interaction between the guest chromophore and polymer host, the tendency of smaller triplet deactivation using polymers with lower molecular weights is also introduced.

A study by (Kusama and Hirata) investigates the nonradiative process from the triplet state of guest chromophores under the oxygen-free condition from the viewpoint of the intramolecular nonradiative transition of the guest and the endothermic intermolecular triplet quenching between the guest and molecular host. Experiments using large different persistent RTP yield depending on thermo-reversible amorphous/crystal changes of the host–guest solid reveal that the different diffusion constants of the molecular host are largely related to the magnitude of the endothermic intermolecular triplet quenching.

As another article introducing suppressed triplet deactivation, Zhou et al. explains the details of the RTP characteristics of cotton fibers. The clustering of the non-aromatic units in the cotton fibers is explained as the generation source of the RTP, and the RTP characteristics are observed in the central part of the fibers. An increase of the concentration of sodium ions is explained to increase the rigidity, which reduces nonradiative deactivation from the triplet state.

The topic of triplet deactivation is also related to RTP from carbon nanodots. Patir and Gogoi show the matrix-free RTP characteristics of chlorine-doped carbon nitride dots (CNDs) in air. The authors explain that the C–Cl or C–NH_2 groups on the surface of the CNDs provide rigidity via hydrogen bonding, reducing the nonradiative transition from the triplet state. This allows persistent RTP even when the CNDs are not surrounded by a solid matrix.

Research regarding the triplet generation yield is also crucial for enhancing the RTP characteristics. Vasilev et al. explains efficient triplet generation by photoexcitation of synthesized porphyrin derivatives using the photon up-conversion properties. Although the triplet-generation capability is often small for heavy-atom-free chromophores with a small energy gap, an adequate triplet generation yield is obtained for the synthesized heavy-atom-free porphyrins.

As other report focusing on the contribution of triplet generation to the RTP characteristics, Cao et al. introduces benzophenone (BPO) doped with thianthrene (TTR). Analysis using different concentrations of TTR indicates that the triplet–triplet energy transfer from the BPO host to the TTR guest after excitation of BPO contributes to enhance the RTP yield. A TTR/BPO material with an optimized TTR concentration shows RTP with 46% quantum efficiency and a lifetime of 9.17 ms from isolated TTR under ambient conditions.

Research regarding the relationship between the RTP characteristics and the conjugated backbone may be crucial for providing additional insight into enhancing the RTP characteristics, Takewaki et al. reports mechano/thermoresponsive RTP chromism from solids of thienyl diketone derivatives. Although thienyl diketone derivatives form the skew conformer generate green RTP in the crystalline state of the solid, an amorphous state containing some of the thienyl diketone derivatives shows yellow RTP characteristics after grinding. After heating of the amorphous state, the crystalline state with green RTP characteristics is recovered.

9,10-Diphenylfluorescence derivatives substituted with bromine as guest chromophores showing delayed emission characteristics are reported by (Zhang et al.). The derivatives show different delayed emission spectra in the crystalline state, doped state in the amorphous polymer, and dissolving state in degassed organic solvents. The delayed emission has multi-exponential decay characteristics, and the magnitude of the average time of decay is from 1 μs to 100 ms.

In addition to the RTP characteristics, utilization of stabilized triplet excitons is also crucial for expanding applications. Yang et al. prepared a co-crystal composed of 9,10-di (4-carboxyphenyl)anthracene (DCPA) and acridine (AD) [(DCPA) $(AD)_2$]. [(DCPA) $(AD)_2$] shows long-lived triplet excitons as the RTP characteristics with a lifetime of 325 μs. The authors propose that the long-lived triplet state, as well as separation of the molecule orbitals, between DCPA and AD of the crystals contributes to a greater change of the long-distance exciton transfer and good electron–hole separation ability, resulting in excellent photoelectric response performance.

Although metal-free RTP materials and their applications have been reported recently, the articles in this themed issue provide proposals and novel insight for previously unclear points regarding the photophysical processes related to the triplet state from the viewpoint of RTP. The editors believe that this Research Topic of articles will inspire readers to consider the idea of improvement of a variety of opto-electronics and photonics applications, as well as enhancement of the RTP characteristics.

Author contributions

All authors listed have made a substantial, direct, and intellectual contribution to the work and approved it for publication.

Conflict of interest

The authors declare that the research was conducted in the absence of any commercial or financial relationships that could be construed as a potential conflict of interest.

Publisher's note

frontiers in Chemistry

ORIGINAL RESEARCH
published: 04 November 2021
doi: 10.3389/fchem.2021.765374

Room-Temperature Phosphorescent Co-Crystal Showing Direct White Light and Photo-Electric Conversion

*Xiao-Gang Yang[1], Wen-Jing Qin[1], Ji-Rui Zhang[1], Xu-Ke Tian[1], Xin Fan[1], Lu-Fang Ma[1] and Dongpeng Yan[2]**

[1]College of Chemistry and Chemical Engineering, Luoyang Normal University, Henan Province Function-oriented Porous Materials Key Laboratory, Luoyang, China, [2]College of Chemistry, Beijing Key Laboratory of Energy Conversion and Storage Materials, Beijing Normal University, Beijing, China

The development of molecular crystalline materials with efficient room-temperature phosphorescence has been obtained much attention due to their fascinating photophysical properties and potential applications in the fields of data storage, bioimaging and photodynamic therapy. Herein, a new co-crystal complex [(DCPA)(AD)$_2$] (DCPA = 9,10-di (4-carboxyphenyl)anthracene; AD = acridine) has been synthesized by a facile solvothermal process. Crystal structure analysis reveals that the co-crystal possesses orderly and alternant arrangement of DCPA donors and AD acceptors at molecular level. Fixed by strong hydrogen bonds, the DCPA molecule displays seriously twisty spatial conformation. Density functional theory (DFT) calculations show well separation of HOMO and LUMO for this co-crystal system, suggesting the efficient triplet excitons generation. Photoluminescence measurements show intensive cyan fluorescence (58.20 ns) and direct white phosphorescence (325 μs) emission at room-temperature. The transient current density–time curve reveals a typical switching electric response under the irradiation of simulated light, reveal that the [(DCPA)(AD)$_2$] co-crystal has a high photoelectric response performance.

Keywords: room temperature phosphorescence, co-crystal, white light, triplet excitons, photoelectric response

Edited by:
Wang Zhang Yuan,
Shanghai Jiao Tong University, China

Reviewed by:
Xiaobo Huang,
Wenzhou University, China
Zhaosheng Qian,
Zhejiang Normal University, China
Manman Fang,
Tianjin University, China

***Correspondence:**
Dongpeng Yan
yandp@bnu.edu.cn

Received: *27 August 2021*
Accepted: *23 September 2021*
Published: *04 November 2021*

Citation:
Yang X-G, Qin W-J, Zhang J-R, Tian X-K, Fan X, Ma L-F and Yan D (2021) Room-Temperature Phosphorescent Co-Crystal Showing Direct White Light and Photo-Electric Conversion. Front. Chem. 9:765374. doi: 10.3389/fchem.2021.765374

INTRODUCTION

The rational design of molecular crystalline materials with long-lived room-temperature phosphorescence (RTP) has atracted tremendous attentions owing to their extended potential to create new opportunities in the development of photocatalytic reactions, photodynamic therapy, optical storage, organic light emitting diodes, and bioimaging (Bhattacharjee and Hirata, 2020; Jiang et al., 2018; Gao and Ma, 2021; Hirata, 2019; Gu et al., 2019; Lei et al., 2019; Wang et al., 2020; Wang et al., 2021; Li and Li, 2020; Yang et al., 2019; Yang et al., 2020; Gao et al., 2021; Chen et al., 2021). Besides the traditional noble-metal (ruthenium, platinum, iridium) based complexes (Xiang et al., 2013), breakthroughs have been achieved during the past decade on pure organics, polymers, metal–organic frameworks (MOFs), organic–inorganic hybrid perovskite and host–guest doping (Mu et al., 2017; Lu et al., 2019; Zhou and Yan, 2019; Lei et al., 2020; Liu et al., 2020; Lei et al., 2021; Wu et al., 2021; Zhou et al., 2021). Promising strategies (such as crystallization, H-aggregation, halogen bonding) have also been vastly accepted to obtain efficient RTP (Bolton et al., 2011; Gong et al., 2015; Kenry and Liu, 2019; Wang et al., 2020), and the inherent principle is absolutely focused on promoting triplet excitons generation.

TABLE 1 | Crystallographic data for [(DCPA) $(AD)_2$].

Compound	**[(DCPA) $(AD)_2$]**
Empirical formula	$C_{27}H_{18}NO_2$
Formula weight	388.42
Crystal system	Triclinic
Space group	$P\bar{1}$
a (Å)	7.6078 (15)
b (Å)	9.2412 (15)
c (Å)	15.023 (2)
α (°)	94.670 (13)
β (°)	100.910 (15)
γ (°)	107.507 (16)
V ($Å^3$)	978.2 (3)
Z	2
D (g cm^{-3})	1.319
μ (mm^{-1})	0.083
R_{int}	0.0963
Goof	0.913
R_1 ($I > 2\sigma$ (I))	0.0907
wR_2 ($I > 2\sigma(I)$)	0.0913

Considering the spin-forbidden intersystem crossing (ISC) from excited singlet state to excited triplet state, the rate of ISC can be enhanced by reducing the energy gap (ΔE_{ST}) between the lowest singlet excited state and a nearby triplet state. Small ΔE_{ST} can be achieved by designing the charge transfer of donor-acceptor system with large spatial separation between the HOMO and LUMO (Parke and Rivard, 2018). To date, many single component organic molecules with twisted donor-acceptor spatial conformation have been demonstrated as efficient RTP materials (Xiao et al., 2020; Xu et al., 2021). However, triplet state excitons of multi-component co-crystal donor-acceptor systems are still relatively limited (Zhou and Yan, 2019; Zhou et al., 2020), and the systematical investigation is needed for well understanding the relationship between their structures and photophysical behaviors.

In this paper, one new type of co-crystal [(DCPA) $(AD)_2$] has been obtained under solvothermal conditions by the selection of 9,10-di (4-carboxyphenyl)anthracene (DCPA) electron donor and acridine (AD) electron acceptor. The obtained donor-acceptor co-crystal system shows alternant arrangement of DCPA and AD components at the molecular level. The crystal structure and density functional theory (DFT) calculations reveal that the DCPA molecule fixed by strong hydrogen bonds displays seriously twisty spatial conformation. This structure feature affords well separation of HOMO-LUMO, promoting for the generation of triplet excitons. As a result, the formation of [(DCPA) $(AD)_2$] co-crystal exhibits cyan fluorescence and direct white long-lived RTP under ambient condition.

EXPERIMENTAL

Materials and General Methods

9,10-di (4-carboxyphenyl)anthracene (DCPA), acridine (AD) and anhydrous ethanol were purchased commercially. Single-crystal X-ray diffraction data were collected by Oxford Diffraction SuperNova area-detector diffractometer with the program of CrysAlisPro. The crystal structure was solved by SHELXS-2014 and SHELXL-2014 software (Sheldrick 2008). The crystallographic data for [(DCPA) $(AD)_2$] were listed in **Table 1**. The CIF file (CCDC No. 2104581) presented in this study can be downloaded free of charge *via* http://www.ccdc.cam.ac.uk/conts/retrieving.html.

Phase purity of co-crystal powders were tested by Bruker D8-ADVANCE X-ray diffractometer with Cu $K\alpha$ radiation. Elemental analysis was performed by Perkin–Elmer Elementarvario elemental analysis instrument. Fourier transform infrared (FT-IR) spectra were measured by SHIMADZU IR Spirit-T spectrometer from 4,000 to 400 cm^{-1} with KBr pellet. UV-vis absorption spectra were detected by Shimadzu UV-3600 plus UV-vis-NIR spectrophotometer. Thermo gravimetric analysis (TGA) experiments were measured by SII EXSTAR6000 TG/DTA6300 thermal analyzer from room temperature to 800°C. The fluorescent and phosphorescent spectra were conducted on Edinburgh FLS1000 fluorescence spectrometer excited by xenon arc lamp (Xe900) and microsecond flash lamp, respectively. The time-resolved phosphorescent decay curves were measured by a microsecond flash lamp with a frequency of 100 Hz. Optoelectronic properties were tested on CHI 660 E electrochemical analyzer in a standard three-electrode system. The working electrode, counter electrode, reference electrode, and electrolyte is [(DCPA) $(AD)_2$] powders modified indium tin oxide (ITO) glass, platinum wire, Ag/AgCl, and 0.5 M sodium sulfate aqueous solution, respectively. The linear sweep voltammetry (LSV) was recorded by the voltage rang of 0.2 to −1 V with a scan rate of 50 mV/s. The transient photocurrent were measured by on–off cycle's illumination of Xe lamp (300 W) with bias potential (vs Ag/AgCl) of 0 and −0.5 V.

Synthesis of [(DCPA) $(AD)_2$].

A mixture of 9,10-di (4-carboxyphenyl)anthracene (0.1 mmol, 41.8 mg), acridine (0.2 mmol, 35.8 mg) and 8 ml EtOH was sealed into a Teflon reactor (23 ml), and heated at 120°C for 12 h. Then, the light yellow block crystals can be obtained after naturally cooled to room temperature. Anal. Calc (%) for $C_{27}H_{18}NO_2$: C 83.48, H 4.67, N 3.61; found (%): C 83.12, H 4.33, N 3.46. IR (KBr pellet, cm^{-1}): 3,415(w), 3,054(w), 1,947(w), 1,692(s), 1,607(m), 1,572(m), 1,524(m), 1,440(m), 1,401(m), 1,281(s), 1,100(m), 920(m), 853(w), 774(s), 735(s), 673(m), 505(m).

RESULTS AND DISCUSSION

Crystal Structure Description

High-grade light yellow block single crystals of the two-component [(DCPA) $(AD)_2$] co-crystal were synthesized under the solvothermal condition from the mixture of DCPA and AD (**Figure 1A**) with a 1:2 stoichiometry in ethanol solution. Single-crystal X-ray diffraction analysis reveals that [(DCPA) $(AD)_2$] crystallizes in triclinic $P\bar{1}$ space group, and the asymmetric unit consists of two AD and one DCPA molecules. In the co-crystal system, the DCPA molecules are linked together by C–H···O

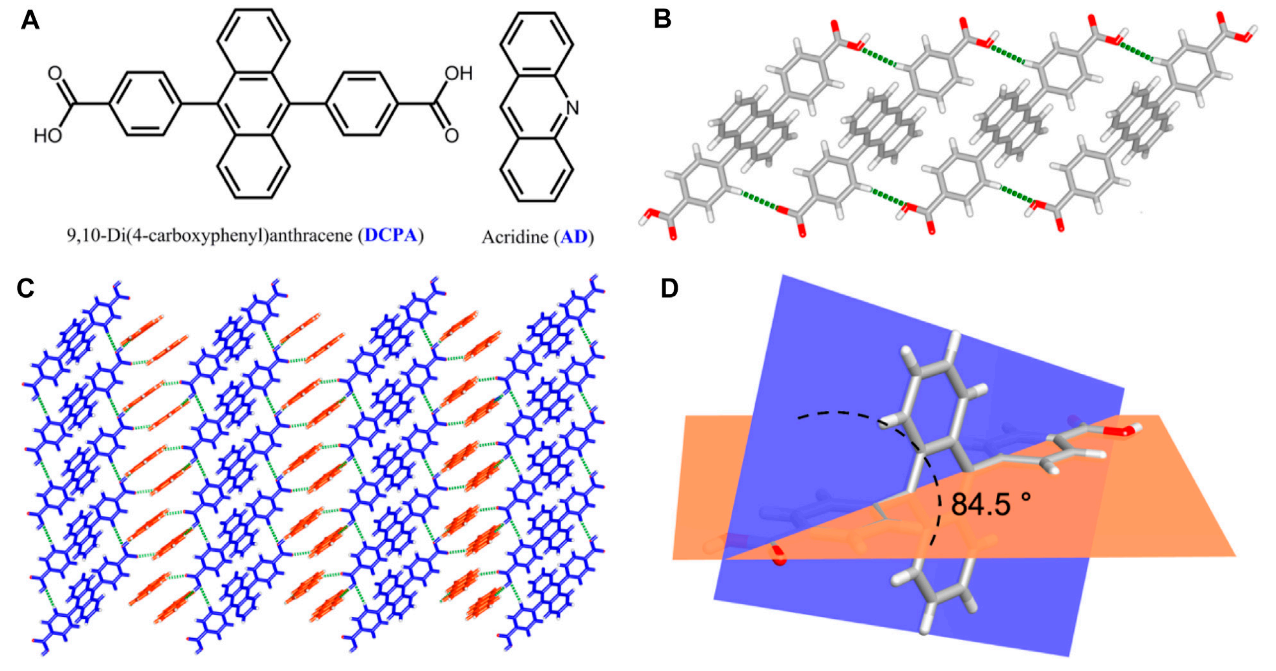

FIGURE 1 | (A) Chemical structures of DCPA and AD molecules in this work. **(B)** 1D chain-like structure of DCPA extended by C–H···O hydrogen bonds. **(C)** View of the 2D sheet constructed by the alternant arrangement of DCPA and AD molecules through C–H···O and O–H···N hydrogen bonds. **(D)** Torsion angles between benzene acid arm and the anthracene core.

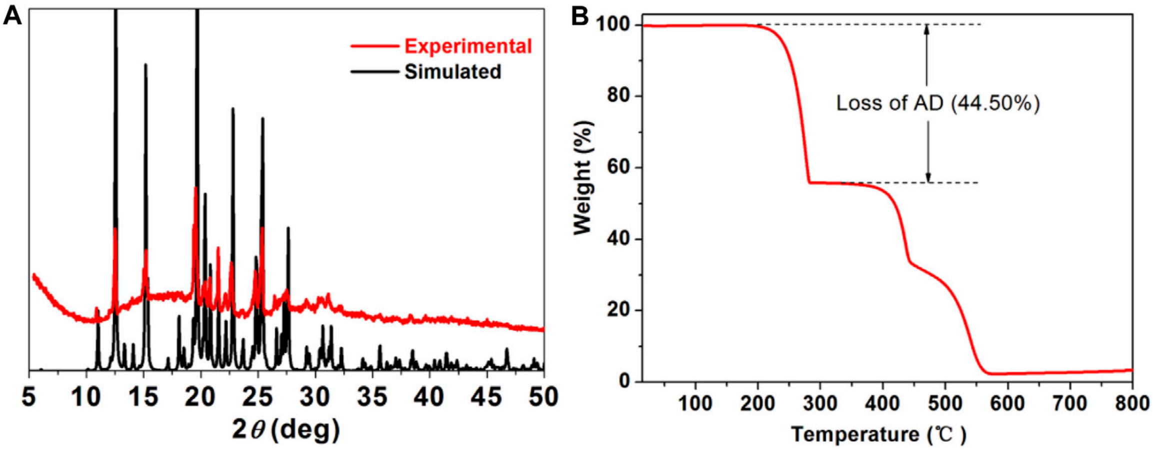

FIGURE 2 | (A) PXRD patterns of simulated (black) and as synthesized **DCPA-AD** (red). **(B)** Thermo gravimetric analysis curve of **DCPA-AD**.

hydrogen bonds (C6–H6···O2: H6···O2 = 2.69 Å, ∠C6–H6···O2 = 141.30°) to form a 1D chain (**Figure 1B**). Pairs of AD molecules arrange in a head-to-tail π-stacking mode with short interplanar distance of 3.66 Å, which extends the DCPA 1D chain into a 2D sheet with the alternant arrangement of DCPA and AD molecules (**Figure 1C**).

Owing to above mentioned hydrogen bond interactions, the DCPA chromophores are highly fixed in an ordered arrangement at the molecular level, which exhibits a seriously twist conformation with torsion angles between benzene acid arm and the anthracene core up to 84.5° (**Figure 1D**). These supramolecular interactions also provide rigid environment to restrict the molecular motions/vibrations, minimizing the nonradiative loss of single/triplet excitons and facilitate for efficient emission (Yang et al., 2020).

Powder X-ray Diffraction and Thermal Gravimetric Analysis

Powder X-ray diffraction (PXRD) experiment was conducted to detect the phase purity of [(DCPA) $(AD)_2$] co-crystal

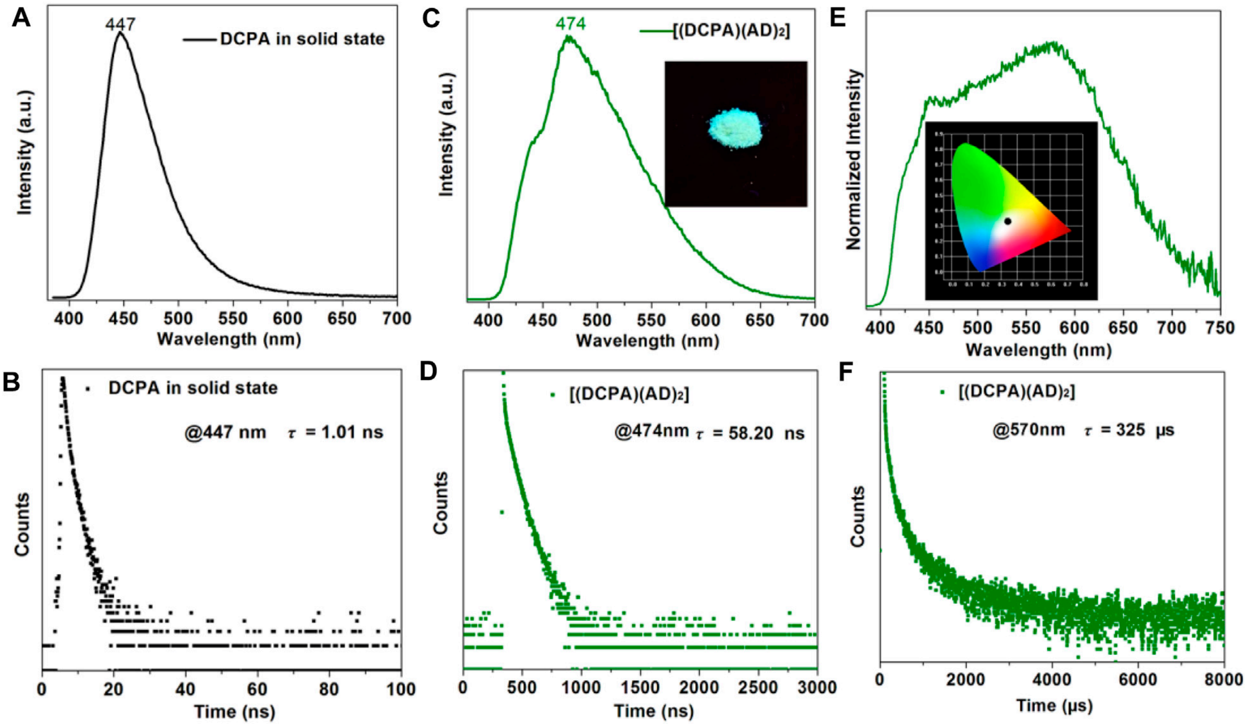

FIGURE 3 | Fluorescence spectra **(A)** decay curve **(B)** of DCPA in solid state (λ_{ex} = 329 nm). Fluorescence spectra **(C)** decay curve **(D)** of [(DCPA) $(AD)_2$] co-crystal in solid state (λ_{ex} = 365 nm). Insert shows solid state samples under UV (365 nm) light radiation. Phosphorescence spectra **(E)** decay curve **(F)** of [(DCPA) $(AD)_2$] co-crystal in solid state (λ_{ex} = 365 nm). Insert shows CIE-1931 chromaticity diagram (0.33,0.34) of [(DCPA) $(AD)_2$] co-crystal with white phosphorescence emission. All of these measurements were recorded under ambient condition.

(**Figure 2A**). The experiment diffraction peaks match well with the simulated one, providing the high purity and good crystalline degree of the as-synthesized samples. Thermo gravimetric (**Figure 2B**) curve shows the first weight loss of about 44.50% in the range of 200–283°C, assigning to the loss of AD molecules (calculated: 46.14%). Additional heating results in the gradual decomposition of framework of co-crystal.

PHOTOLUMINESCENCE PROPERTIES

The steady-state, transient-state photoluminescence (PL) spectra and time-resolved PL decay curves of both [(DCPA) $(AD)_2$] co-crystal, pure DCPA and AD in solid state were recorded at room temperture. **Figure 3A** illustrates the fluorescence spectra of DCPA in solid state, which shows strong dark-blue emission owing to the presence of the anthracene chromophore (λ_{ex} = 329 nm). The fluorescence decay curve estimated at the maximal emission peak at 447 nm gives rise to a short lifetime of 1.01 ns(**Figure 3B**), whereas the single component AD has an emission peak at 396 nm and lifetime of 2.88 ns(Yang et al., 2020). By contrast, the formation of co-crystal presents a red-shift of the emission peak to long wavelength at 474 nm, attaching with a weak shoulder at about 443 nm when excited at 365 nm (**Figure 3C**), suggesting the charge transfer interaction between the DCPA donor and AD acceptor. Apart from the emission peak, the [(DCPA) $(AD)_2$] co-crystal also shows much longer fluorescence lifetime up to 58.20 ns(**Figure 3D**), which is more than 50 times as long as that of free DCPA molecules in solid state.

The delayed PL spectrum shows a broad emission region spanning nearly the whole visible spectra with a maximum peak at 570 nm (**Figure 3E**). The time-resolved PL decay curve affords a long lifetime of 325 μs, indicating long-lived RTP emission of [(DCPA) $(AD)_2$] co-crystal (**Figure 3F**). The inserts show the cyan emission of [(DCPA) $(AD)_2$] crystalline powders irradiated under UV (365 nm) and the CIE-1931 chromaticity coordinate obtained from the phosphorescence spectra. The chromaticity coordinate of (0.33,0.34) is close to the optimum white-light with value of (0.33,0.33). The above results indicate that the fromation of co-crystal can largely tune the fluorescence emission of DCPA from dark-blue to cyan, and prolong the lifetime more than 50 times. In our opinion, the strong supramolecular interactions efficiently reduce the nonradiative loss of single/triplet excitons, and further enable prolonged PL lifetime.

Density Functional Theory Calculations

Density functional theory (DFT) calculations were conducted by Dmol^3 module in Material Studio software package (Delley 2000) based on the X-ray single crystal diffraction data of [(DCPA) $(AD)_2$]. The results show the highest occupied molecular orbital

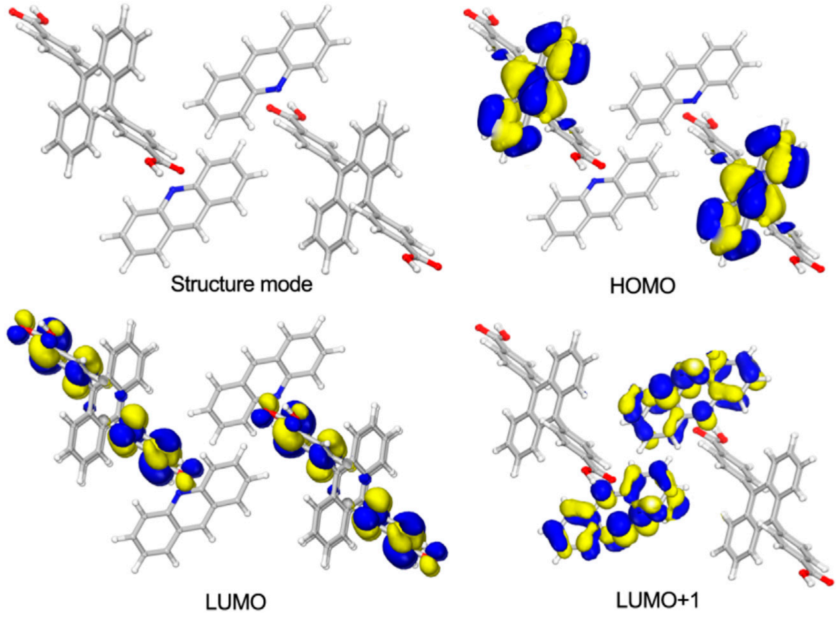

FIGURE 4 | The structure mode and selected molecular orbitals of [(DCPA) (AD)$_2$].

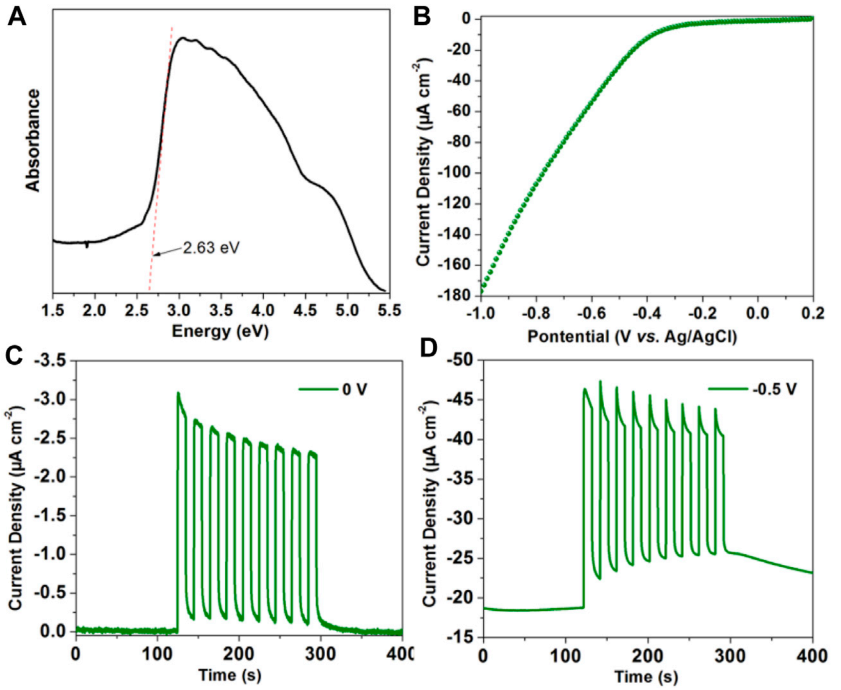

FIGURE 5 | (A) UV-VIS-NIR absorption of as synthesized [(DCPA) (AD)$_2$]. **(B)** The linear sweep voltammetry curve of as synthesized [(DCPA) (AD)$_2$] modified ITO electrode measured in 0.5 M Na_2SO_4 aqueous solution. Transient current density–time curve of [(DCPA) (AD)$_2$] at bias potential of 0 V **(C)** and −0.5 V **(D)** with the periodic on-off cycles of light radiation.

(HOMO) is occupied by the anthracene core of DCPA molecules, whereas the lowest unoccupied molecular orbital (LUMO) is exclusively located on the benzene acid groups. The LUMO+1 mainly appears on AD molecules (**Figure 4**). Herein, the seriously twist conformation of DCPA molecule leads to large spatial separation of the HOMO and LUMO. The alternant arrangement of DCPA electron donor and AD electron acceptor further promotes the separation of molecular orbitals, boosting the spin-orbit coupling and intersystem crossing for efficient triplet state exciton generation.

Photo-Electronic Performance

It has been found that the long-lived triplet state excitons have more chance for the electron migration (Yang et al., 2019). Encouraged by the long-lived RTP of [(DCPA) $(AD)_2$] co-crystal in this work, its photo-electronic properties have been further conducted by a three-electrode system in Na_2SO_4 aqueous solution. The UV-Vis absorption spectrum shows an optical band gap of 2.63 eV (471 nm), consisting with the fluorescence emission peak (**Figure 5A**). The linear sweep voltammetry (LSV) curve reveals that the [(DCPA) $(AD)_2$] co-crystal material can generate large current with the addition of negative potential (**Figure 5B**). The absence of redox peak suggests that the [(DCPA) $(AD)_2$] co-crystal is stable within the applied bias potential from 0.2 to −1 V.

The transient current density–time curve reveals a typical on/off switching response under the irradiation of simulated light. Without only bias potential, it generates high photocurrent up to $-3.1\ \mu A\ cm^{-2}$ with the momentary light radiation. Under the initiatory dark condition, extremely small dark current of about $0.002\ \mu A\ cm^{-2}$ can be detected (**Figure 5C**). The rate of current between light radiation and dark conditions was calculated up to 1,550. By the addition of −0.5 V bias potential, it generates more large current of about $-46.5\ \mu A\ cm^{-2}$ under light radiation (**Figure 5D**). All these results reveal that the [(DCPA) $(AD)_2$] co-crystal has superior photoelectric response performance, which can be applied in the future photoelectric detector device.

CONCLUSION

In summary, we report a rare example of direct white-light RTP co-crystal material [(DCPA) $(AD)_2$], which can be synthesized under a facile solvothermal condition. The framework of [(DCPA) $(AD)_2$] shows an orderly distribution of heterojuction at the molecular level: alternant arrangement of DCPA electronic donors and AD electron acceptors bonded together through strong C–H···O and O–H···N hydrogen bonds. Fixed by these supramolecular interactions, the molecular motions/vibrations can be restricted, which affords long-lasting singlet and triplet excitons through minimize the nonradiative loss. In addition, the seriously twist conformation of DCPA molecule is beneficial to the separation of molecule orbitals. Combined with the introduction of AD acceptor, it provides efficient platform for long distance exciton transfer and good electron-hole separation ability, possessing superior photoelectric response performance. Therefore, this work not only develops a new type of white-light RTP co-crystal, but also provides a perspective to deeply understand the relationship among molecular structure, stacking mode and photoelectric performance.

DATA AVAILABILITY STATEMENT

The data presented in the study are deposited in the (Cambridge Crystallographic Data Centre) repository, accession number (2104581).

AUTHOR CONTRIBUTIONS

XY, LF, and D conceived the idea and designed research. WJ, JR, XK, and X synthesized and characterized materials; all authors analyzed data and wrote the paper.

FUNDING

This work was supported by the National Natural Science Foundation of China (No. 21971100, 21771021, 21822501, and 22061130206), Project of Central Plains Science and Technology Innovation Leading Talents of Henan Province (No. 204200510001), Project for Science and Technology Innovation Talents in Universities of Henan Province (No. 21HASTIT006), and Key Scientific Research Projects of Higher Education of Henan Province (No. 20A150005).

REFERENCES

Bhattacharjee, I., and Hirata, S. (2020). Highly Efficient Persistent Room-Temperature Phosphorescence from Heavy Atom-Free Molecules Triggered by Hidden Long Phosphorescent Antenna. *Adv. Mater.* 32, 2001348. doi:10.1002/adma.202001348

Bolton, O., Lee, K., Kim, H.-J., Lin, K. Y., and Kim, J. (2011). Activating Efficient Phosphorescence from Purely Organic Materials by Crystal Design. *Nat. Chem* 3, 205–210. doi:10.1038/nchem.984

Chen, C., Chi, Z., Chong, K. C., Batsanov, A. S., Yang, Z., Mao, Z., et al. (2021). Carbazole Isomers Induce Ultralong Organic Phosphorescence. *Nat. Mater.* 20, 175–180. doi:10.1038/s41563-020-0797-2

Delley, B. (2000). From Molecules to Solids with the DMol3 Approach. *J. Chem. Phys.* 113 (18), 7756–7764. doi:10.1063/1.1316015

Gao, H., and Ma, X. (2021). Recent Progress on Pure Organic Room Temperature Phosphorescent Polymers. *Aggregate* 2. doi:10.1002/agt2.38

Gao, R., Kodaimati, M. S., and Yan, D. (2021). Recent Advances in Persistent Luminescence Based on Molecular Hybrid Materials. *Chem. Soc. Rev.* 50, 5564–5589. doi:10.1039/d0cs01463j

Gong, Y., Zhao, L., Peng, Q., Fan, D., Yuan, W. Z., Zhang, Y., et al. (2015). Crystallization-induced Dual Emission from Metal- and Heavy Atom-free Aromatic Acids and Esters. *Chem. Sci.* 6, 4438–4444. doi:10.1039/c5sc00253b

Gu, L., Shi, H., Bian, L., Gu, M., Ling, K., Wang, X., et al. (2019). Colour-tunable Ultra-long Organic Phosphorescence of a Single-Component Molecular crystal. *Nat. Photon.* 13 (6), 406–411. doi:10.1038/s41566-019-0408-4

Hirata, S. (2017). Recent Advances in Materials with Room-Temperature Phosphorescence: Photophysics for Triplet Exciton Stabilization. *Adv. Opt. Mater.* 5 (17), 1700116. doi:10.1002/adom.201700116

Jiang, K., Wang, Y., Cai, C., and Lin, H. (2018). Conversion of Carbon Dots from Fluorescence to Ultralong Room-Temperature Phosphorescence by Heating for Security Applications. *Adv. Mater.* 30, 1800783. doi:10.1002/adma.201800783

Kenry, Chen. C., Chen, C., and Liu, B. (2019). Enhancing the Performance of Pure Organic Room-Temperature Phosphorescent Luminophores. *Nat. Commun.* 10, 2111. doi:10.1038/s41467-019-10033-2

Lei, Y., Dai, W., Guan, J., Guo, S., Ren, F., Zhou, Y., et al. (2020). Wide-Range Color-Tunable Organic Phosphorescence Materials for Printable and Writable Security Inks. *Angew. Chem. Int. Ed.* 59, 16054–16060. doi:10.1002/anie.202003585

Lei, Y., Dai, W., Tian, Y., Yang, J., Li, P., Shi, J., et al. (2019). Revealing Insight into Long-Lived Room-Temperature Phosphorescence of Host-Guest Systems. *J. Phys. Chem. Lett.* 10, 6019–6025. doi:10.1021/acs.jpclett.9b02411

Lei, Y., Yang, J., Dai, W., Lan, Y., Yang, J., Zheng, X., et al. (2021). Efficient and Organic Host-Guest Room-Temperature Phosphorescence: Tunable Triplet-Singlet Crossing and Theoretical Calculations for Molecular Packing. *Chem. Sci.* 12, 6518–6525. doi:10.1039/d1sc01175h

Li, Q., and Li, Z. (2020). Molecular Packing: Another Key point for the Performance of Organic and Polymeric Optoelectronic Materials. *Acc. Chem. Res.* 53, 962–973. doi:10.1021/acs.accounts.0c00060

Liu, S., Fang, X., Lu, B., and Yan, D. (2020). Wide Range zero-thermal-quenching Ultralong Phosphorescence from Zero-Dimensional Metal Halide Hybrids. *Nat. Commun.* 11, 4649. doi:10.1038/s41467-020-18482-w

Lu, X.-M., Zhai, Z.-M., Liu, X.-Y., Li, F.-F., Yang, X.-G., Li, J.-Y., et al. (2019). Near-infrared Phosphorescence Emission of Zn(II) Coordination Polymer Based on 3,5-Bis(1-Imidazoly)pyridine: Syntheses, Structure and Photoelectron Performance. *J. Solid State. Chem.* 279, 120958. doi:10.1016/j.jssc.2019.120958

Mu, Y., Shi, H., Wang, Y., Ding, H., and Li, J. (2017). CNDs@zeolite: New Room-Temperature Phosphorescent Materials Derived by Pyrolysis of Organo-Templated Zeolites. *J. Mater. Chem. C* 5, 10894–10899. doi:10.1039/C7TC03487C

Parke, S. M., and Rivard, E. (2018). Aggregation Induced Phosphorescence in the Main Group. *Isr. J. Chem.* 58, 915–926. doi:10.1002/ijch.201800039

Sheldrick, G. M. (2008). A Short History ofSHELX. *Acta Cryst. Sect A.* 64, 112–122. doi:10.1107/S0108767307043930

Wang, D., Xie, Y., Wu, X., Lei, Y., Zhou, Y., Cai, Z., et al. (2021). Excitation-dependent Triplet-Singlet Intensity from Organic Host-Guest Materials: Tunable Color, white-light Emission, and Room-Temperature Phosphorescence. *J. Phys. Chem. Lett.* 12 (12), 1814–1821. doi:10.1021/acs.jpclett.1c00188

Wang, H.-R., Yang, X.-G., Qin, J.-H., and Ma, L.-F. (2020). Long-lived Room Temperature Phosphorescence of Organic-Inorganic Hybrid Systems. *Inorg. Chem. Front.* 8, 1942–1950. doi:10.1039/d0qi01508c

Wang, W., Zhang, Y., and Jin, W. J. (2020). Halogen Bonding in Room-Temperature Phosphorescent Materials. *Coord. Chem. Rev.* 404, 213107. doi:10.1016/j.ccr.2019.213107

Wu, H.-X., Lu, X.-M., Chen, J.-Y., Yang, X.-G., Qin, W.-J., and Ma, L.-F. (2021). Long Afterglow of a Nonporous Coordination Polymer with Tunable Room-Temperature Phosphorescence by the Doping of Dye Molecules. *Inorg. Chem.* 60 (2), 846–851. doi:10.1021/acs.inorgchem.0c02888

Xiang, H., Cheng, J., Ma, X., Zhou, X., and Chruma, J. J. (2013). Near-infrared Phosphorescence: Materials and Applications. *Chem. Soc. Rev.* 42, 6128–6185. doi:10.1039/c3cs60029g

Xiao, F., Wang, M., Lei, Y., Dai, W., Zhou, Y., Liu, M., et al. (2020). Achieving crystal-induced Room Temperature Phosphorescence and Reversible Photochromic Properties by strong Intermolecular Interactions. *J. Mater. Chem. C* 8, 17410–17416. doi:10.1039/d0tc03980b

Xu, Z., Climent, C., Brown, C. M., Hean, D., Bardeen, C. J., Casanova, D., et al. (2021). Controlling Ultralong Room Temperature Phosphorescence in Organic Compounds with Sulfur Oxidation State. *Chem. Sci.* 12, 188–195. doi:10.1039/d0sc04715e

Yang, X.-G., Lu, X.-M., Zhai, Z.-M., Zhao, Y., Liu, X.-Y., Ma, L.-F., et al. (2019). Facile Synthesis of a Micro-scale MOF Host-Guest with Long-Lasting Phosphorescence and Enhanced Optoelectronic Performance. *Chem. Commun.* 55, 11099–11102. doi:10.1039/c9cc05708k

Yang, X.-G., Zhai, Z.-M., Lu, X.-M., Ma, L.-F., and Yan, D. (2020). Fast Crystallization-Deposition of Orderly Molecule Level Heterojunction Thin Films Showing Tunable Up-Conversion and Ultrahigh Photoelectric Response. *ACS Cent. Sci.* 6, 1169–1178. doi:10.1021/acscentsci.0c00447

Yang, X.-G., Zhai, Z.-M., Lu, X.-M., Qin, J.-H., Li, F.-F., and Ma, L.-F. (2020). Hexanuclear Zn(II)-Induced Dense π-Stacking in a Metal-Organic Framework Featuring Long-Lasting Room Temperature Phosphorescence. *Inorg. Chem.* 59, 10395–10399. doi:10.1021/acs.inorgchem.0c01415

Zhou, B., Xiao, G., and Yan, D. (2021). Boosting Wide-Range Tunable Long-Afterglow in 1D Metal-Organic Halide Micro/Nanocrystals for Space/Time-Resolved Information Photonics. *Adv. Mater.* 33, 2007571. doi:10.1002/adma.202007571

Zhou, B., and Yan, D. (2019). Hydrogen-Bonded Two-Component Ionic Crystals Showing Enhanced Long-Lived Room-Temperature Phosphorescence via TADF-Assisted Förster Resonance Energy Transfer. *Adv. Funct. Mater.* 29, 1807599. doi:10.1002/adfm.201807599

Zhou, B., and Yan, D. (2019). Simultaneous Long-Persistent Blue Luminescence and High Quantum Yield within 2D Organic-Metal Halide Perovskite Micro/Nanosheets. *Angew. Chem. Int. Ed.* 58, 15128–15135. doi:10.1002/ange.20190976010.1002/anie.201909760

Zhou, B., Zhao, Q., Tang, L., and Yan, D. (2020). Tunable Room Temperature Phosphorescence and Energy Transfer in Ratiometric Co-crystals. *Chem. Commun.* 56, 7698–7701. doi:10.1039/D0CC02730H

Conflict of Interest: The authors declare that the research was conducted in the absence of any commercial or financial relationships that could be construed as a potential conflict of interest.

frontiers in Chemistry

ORIGINAL RESEARCH
published: 16 November 2021
doi: 10.3389/fchem.2021.788577

Thermo-Reversible Persistent Phosphorescence Modulation Reveals the Large Contribution Made by Rigidity to the Suppression of Endothermic Intermolecular Triplet Quenching

*Tomoya Kusama and Shuzo Hirata**

Department of Engineering Science, University of Electro-Communications, Tokyo, Japan

OPEN ACCESS

Edited by:
Rene A. Nome,
State University of Campinas, Brazil

Reviewed by:
Debdas Ray,
Shiv Nadar University, India
Yan Dongpeng,
Beijing Normal University, China

***Correspondence:**
Shuzo Hirata
shuzohirata@uec.ac.jp

Specialty section:
This article was submitted to Physical Chemistry and Chemical Physics,
a section of the journal Frontiers in Chemistry

Received: *02 October 2021*
Accepted: *26 October 2021*
Published: *16 November 2021*

Citation:
Kusama T and Hirata S (2021) Thermo-Reversible Persistent Phosphorescence Modulation Reveals the Large Contribution Made by Rigidity to the Suppression of Endothermic Intermolecular Triplet Quenching.
Front. Chem. 9:788577.
doi: 10.3389/fchem.2021.788577

The suppression of thermally driven triplet deactivation is crucial for efficient persistent room-temperature phosphorescence (*p*RTP). However, the mechanism by which triplet deactivation occurs in metal-free molecular solids at room temperature (RT) remains unclear. Herein, we report a large *p*RTP intensity change in a molecular guest that depended on the reversible amorphous–crystal phase change in the molecular host, and we confirm the large contribution made by the rigidity of the host in suppressing intermolecular triplet quenching in the guest. (*S*)-(–)-2,2′-Bis(diphenylphosphino)-1,1′-binaphthyl ((*S*)-BINAP) was doped as a guest into a highly purified (*S*)-bis(diphenylphosphino)-5,5′,6,6′,7,7′,8,8′-octahydro-1,1′-binaphthyl ((*S*)-H_8-BINAP) host. It was possible to reversibly form the amorphous and crystalline states of the solid by cooling to RT from various temperatures. The RTP yield (Φ_p) originating from the (*S*)-BINAP was 6.7% in the crystalline state of the (*S*)-H_8-BINAP host, whereas it decreased to 0.31% in the amorphous state. Arrhenius plots showing the rate of nonradiative deactivation from the lowest triplet excited state (T_1) of the amorphous and crystalline solids indicated that the large difference in Φ_p between the crystalline and amorphous states was mostly due to the discrepancy in the magnitude of quenching of intermolecular triplet energy transfer from the (*S*)-BINAP guest to the (*S*)-H_8-BINAP host. Controlled analyses of the T_1 energy of the guest and host, and of the reorganization energy of the intermolecular triplet energy transfer from the guest to the host, confirmed that the large difference in intermolecular triplet quenching was due to the discrepancy in the magnitude of the diffusion constant of the (*S*)-H_8-BINAP host between its amorphous and crystalline states. Quantification of both the T_1 energy and the diffusion constant of molecules used in solid materials is crucial for a meaningful discussion of the intermolecular triplet deactivation of various metal-free solid materials.

Keywords: persistent room-temperature phosphorescence, triplet quenching, nonradiative deactivation, phase change, diffusion constant, reorganization energy

INTRODUCTION

Room-temperature phosphorescence (RTP) with an emission lifetime of more than 100 ms—i.e., persistent RTP (*p*RTP)—from metal-free molecular solids occurs after ceasing exposure to fluorescence-independent excitation light (Clapp. 1939; Zhang et al., 2007; Hirata et al., 2013). Because autofluorescence-independent *p*RTP can be detected using small-scale and low-cost photo detectors, chemicals and materials with *p*RTP characteristics are crucial for state-of-the-art security, sensing, and bioimaging applications (Deng et al., 2013; Zhang et al., 2014; Fateminia et al., 2017; Zhen et al., 2017; Louis et al., 2019; Zhou and Yan, 2019). Efficient *p*RTP produces much brighter persistent emission compared with the general long persistent luminescence from materials that has been reported previously (Bhattacharjee and Hirata, 2020). Therefore, photophysical insight into chemicals and/or materials to access the efficiency and brightness of *p*RTP is crucial. Because *p*RTP from metal-free chromophores is a slow process (Hirata, 2017), the suppression of thermo-driven triplet deactivation is necessary for efficient *p*RTP. However, the mechanism by which the triplet deactivation of metal-free molecular solids occurs at RT remains unclear.

Triplet deactivation includes both intramolecular radiationless transition from the lowest triplet excited state (T_1) to the ground state (S_0) and the T_1 quenching caused by intermolecular interactions. The rate of the intermolecular radiation-less transition at RT (k_{nr}(RT)) is related to spin–orbit coupling including vibrations and the energy gap between T_1 and the S_0 of the target chromophores (Schlag et al., 1971; Metz et al., 1972; Metz, 1973). However, the rate of the T_1 quenching caused by intermolecular interactions (k_q(RT)) is based on charge transfer theory (Köhler and Bässler, 2011). In the 1980s, k_{nr}(RT) and k_q(RT) were considered separately using benzophenone as a guest in polymer matrices, and the k_{nr}(RT) of benzophenone was found to be almost independent of temperature from 77 K to RT (Horie and Mita, 1982; Horie et al., 1984). Recently, cooperative analysis of optical measurements and quantum chemical calculations have confirmed that the k_{nr}(RT) values of a variety of heavy atom-free chromophores are less than $10^0\ s^{-1}$ (Bhattacharjee et al., 2021; Hirata and Bhattacharjee et al., 2021). This indicates that most triplet deactivation of materials is caused by the k_q(RT) (Hirata et al., 2020; Hirata and ; Bhattacharjee et al., 2021). With regard to the k_q(RT) of host–guest molecular solids, it is generally necessary for the host molecules to have a larger T_1 energy than the metal-based phosphorescence guests to suppress the k_q(RT) (Adachi et al., 2001). However, for heavy atom-free and/or metal-free guests, a long-lived T_1 at RT generally requires the host molecules to have a considerably greater T_1 than the guests to significantly suppress the k_q(RT) (Hirata et al., 2013; Totani et al., 2013). Contrary to general discussions about the contribution made by the T_1 energy difference between the host molecules and the guest chromophores to the k_q(RT), triplet deactivation due to the rigidity of the materials has often been reported, although it is still regarded as phenomenological (Zhao et al., 2020). Although recent analyses suggest that rigidity—including intermolecular interactions—might not be related to k_{nr}(RT) but to k_q(RT), investigations into the physical factors governing rigidity and the T_1 energy difference between the host and the guest have not been reported.

Herein, we report the dependency of the thermo-reversible intensity change of green *p*RTP of a guest on the amorphous–crystalline phase change of a host molecule, and determine the contribution made by the rigidity of the host in the suppression of endothermic intermolecular triplet quenching. (*S*)-(−)-2,2′-Bis(diphenylphosphino)-1,1′-binaphthyl ((*S*)-BINAP) was doped into a highly purified (*S*)-bis(diphenylphosphino)-5,5′,6,6′,7,7′,8,8′-octahydro-1,1′-binaphthyl ((*S*)-H_8-BINAP) host. The host–guest material in the crystalline state produced green *p*RTP under ambient conditions, and the RTP yield (Φ_p(RT)) was 6.7%. However, the Φ_p(RT) of the host–guest material in the amorphous state decreased to 0.31%, even when the materials were stored in a high vacuum. Detailed optical measurements indicated that the large Φ_p(RT) in the crystalline state was caused by both the increase in the triplet generation yield of the (*S*)-BINAP guest and the large decrease of k_q(RT) in the crystalline state compared with in the amorphous state. The comparable T_1 energy values of the (*S*)-H_8-BINAP host in both the amorphous and crystalline states suggests that the decrease in k_q(RT) was caused by the suppressed molecular diffusion of the (*S*)-H_8-BINAP host molecules in the crystalline state. The suppressed molecular diffusion in the crystalline (*S*)-H_8-BINAP host was observed using molecular dynamic simulation. Thus, suppressed molecular diffusion is a crucial factor for minimizing the endothermic intermolecular triplet energy transfer that induces triplet quenching.

RESULTS AND DISCUSSION

Thermo-Reversible Intensity Change of Persistent Room-temperature Phosphorescence

Commercially available (*S*)-H_8-BINAP crystals often generate green *p*RTP after ultraviolet (UV) excitation has ceased (**Supplementary Figure S1A**) because of the presence of (*S*)-BINAP as an impurity (**Supplementary Figure S2**). After careful repeated purification of the (*S*)-H_8-BINAP using silica column chromatography, however, we noted that the purified crystals of (*S*)-H_8-BINAP did not produce *p*RTP (**Supplementary Figure S1B**) (Hirata et al., 2020). First (*S*)-BINAP powder was dissolved in molten pure (*S*)-H_8-BINAP at 220°C. Next, the molten materials were placed on a quartz substrate on a hotplate at 250°C which is higher temperature than a melting point of 208°C of (*S*)-H_8-BINAP host (**Supplementary Figure S3**), and the substrate was quenched to room temperature (RT) to prepare an amorphous 5 wt% (*S*)-BINAP-doped (*S*)-H_8-BINAP film. The resulting amorphous film of 5 wt% (*S*)-BINAP-doped (*S*)-H_8-BINAP produced markedly weak *p*RTP after ceasing UV excitation (**Figure 1B**; top). The weak *p*RTP of the amorphous 5 wt% (*S*)-BINAP-doped (*S*)-H_8-BINAP film did not increase under vacuum. The amorphous form of 5 wt% (*S*)-BINAP-doped (*S*)-H_8-BINAP has a glass transition temperature of 104°C and crystallizes at 165°C (**Figure 1A**; top). After crystallization at

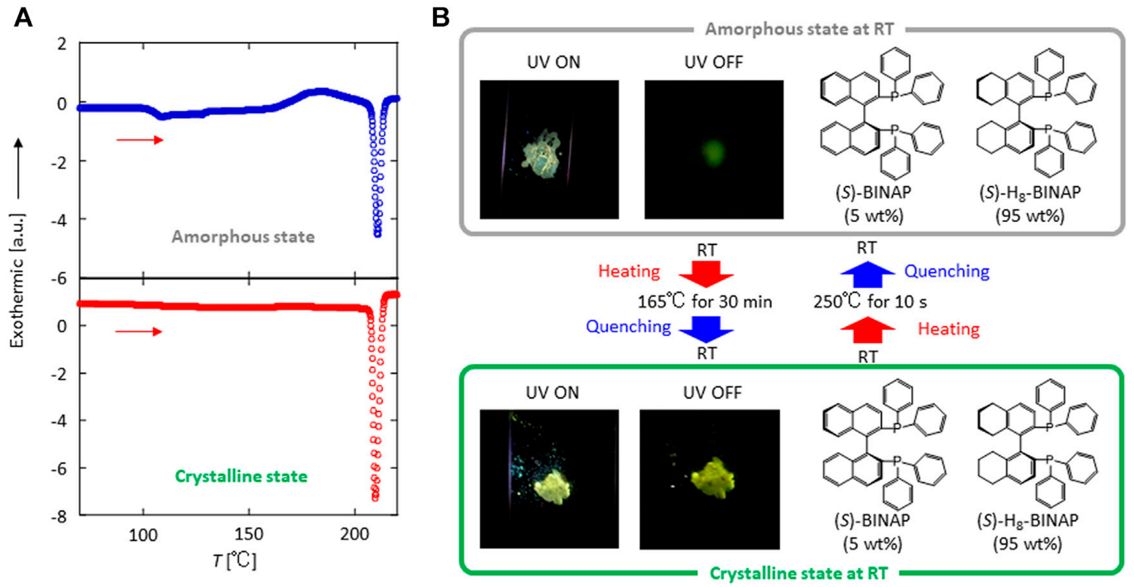

FIGURE 1 | Reversible crystal–amorphous phase change at RT and *p*RTP characteristics of the (*S*)-BINAP doped (*S*)-H_8-BINAP solid. **(A)** Differential scanning calorimetry characteristics of amorphous state **(upper)** and crystalline state **(lower)** when heated at 5°C/min. **(B)** Emission behavior during and immediately after excitation by exposure to radiation (330 nm) of amorphous **(upper)** and crystalline **(lower)** solids. ((*S*)-BINAP = (*S*)-(–)-2,2′-bis(diphenylphosphino)-1,1′-binaphthyl (*S*)-H_8-BINAP = (*S*)-bis(diphenylphosphino)-5,5′,6,6′,7,7′,8,8′-octahydro-1,1′-binaphthyl; *p*RTP = persistent room-temperature phosphorescence).

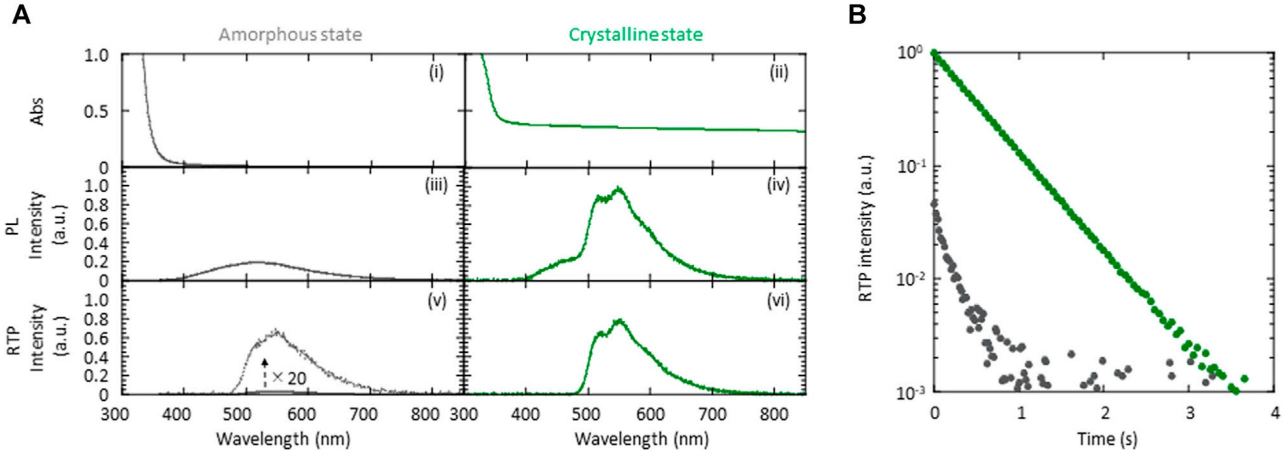

FIGURE 2 | Absorption and emission characteristics of 5 wt% (*S*)-BINAP-doped (*S*)-H_8-BINAP films. **(A)** Absorption (i, ii), steady-state RT emission (iii, iv), and RTP (v, vi) spectra of amorphous (gray) and crystalline (green) films. **(B)** RTP decay characteristics of amorphous (gray) and crystalline (green) films. The RTP intensity immediately after ceasing excitation in the crystalline state was normalized to one and the initial intensity of RTP immediately after ceasing excitation in the amorphous state was set by considering the difference in Φ_p(RT) between the crystalline and amorphous states. In **(A)** and **(B)**, the excitation wavelength used for emission measurements was 330 nm. (RT = room-temperature; RTP = room-temperature phosphorescence; (*S*)-BINAP = (*S*)-(–)-2,2′-bis(diphenylphosphino)-1,1′-binaphthyl (*S*)-H_8-BINAP = (*S*)-bis(diphenylphosphino)-5,5′,6,6′,7,7′,8,8′-octahydro-1,1′-binaphthyl).

165°C for 30 min, the produced 5 wt% (*S*)-BINAP-doped (*S*)-H_8-BINAP crystalline films (**Figure 1A**; lower) produced much brighter green *p*RTP compared with the amorphous form after exposure to excitation light of 330 nm had ceased (**Figure 1B**; lower).

More detailed optical measurements were performed to investigate the differences in the *p*RTP characteristics between the crystalline and amorphous states of 5 wt% (*S*)-BINAP-doped (*S*)-H_8-BINAP solid. Both the crystalline and amorphous 5 wt% (*S*)-BINAP-doped (*S*)-H_8-BINAP films absorbed radiation at 330 nm ((i) and (ii) in **Figure 2A**). The amorphous 5 wt% (*S*)-BINAP-doped (*S*)-H_8-BINAP film produced a fluorescence spectrum beginning at approximately 400 nm ((iii) in **Figure 2A**), and the steady-state RT

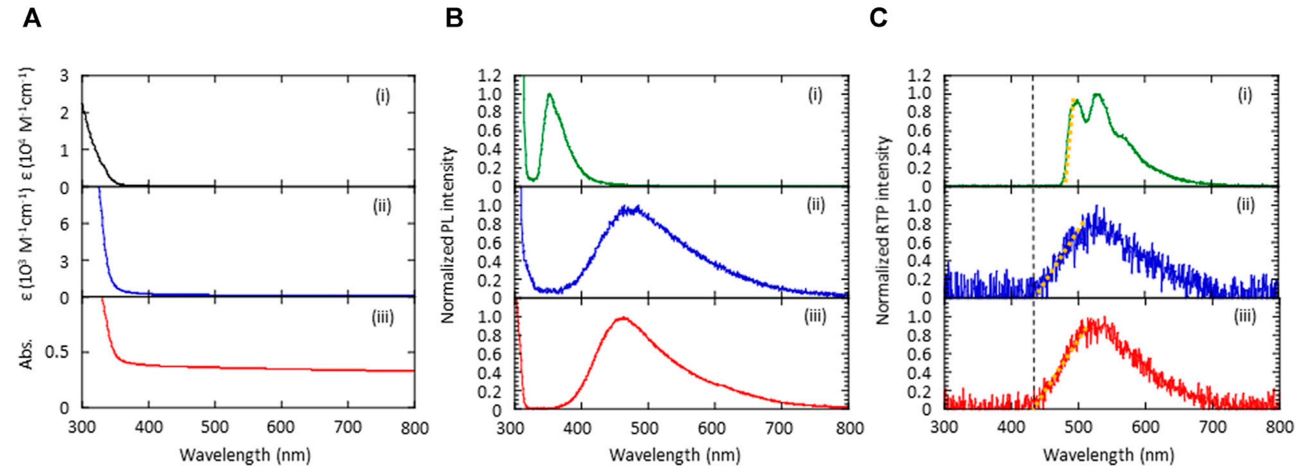

FIGURE 3 | Absorption and emission spectra of (*S*)-BINAP molecularly dispersed in 2Me-THF (i), an amorphous (*S*)-H_8-BINAP film (ii), and a crystalline (*S*)-H_8-BINAP film (iii). **(A)** Absorption spectra. **(B)** Fluorescence spectra obtained by excitation at 300 nm at RT. **(C)** Phosphorescence spectra obtained after ceasing excitation at 300 nm at 77 K. The orange dotted lines in the graph were used to determine the onset energy of T_1. (2Me-THF = 2-methyltetrahydrofuran; RT = room-temperature; (*S*)-BINAP = (*S*)-(–)-2,2′-bis(diphenylphosphino)-1,1′-binaphthyl (*S*)-H_8-BINAP = (*S*)-bis(diphenylphosphino)-5,5′,6,6′,7,7′,8,8′-octahydro-1,1′-binaphthyl).

emission yield was 2.5%. Immediately after excitation by exposure to UV radiation ceased, a weak green *p*RTP remained ((v) in **Figure 2A**). The quantum yield of phosphorescence at RT (Φ_p(RT)) was estimated to be 0.31% by comparing the intensity of the steady-state RT emission spectrum ((iii) in **Figure 2A**) with the RTP spectral intensity immediately after ceasing excitation ((v) in **Figure 2A**). The RTP decay had multi-exponential characteristics (gray in **Figure 2B**). For the crystalline 5 wt % (*S*)-BINAP-doped (*S*)-H_8-BINAP films, the larger increase of absorbance at wavelengths less than 350 nm resulted from the absorption of (*S*)-BINAP and (*S*)-H_8-BINAP ((ii) in **Figure 2A**). An increase of the baseline at wavelengths longer than 400 nm was caused by light scattering arising from the polycrystalline films. In contrast to the amorphous state, the crystalline 5 wt% (*S*)-BINAP-doped (*S*)-H_8-BINAP film had two large peaks at 510 and 545 nm under steady-state UV excitation at 330 nm in addition to fluorescence spectra commencing at approximately 400 nm ((iv) in **Figure 2A**). The steady-state RT emission yield was 9.8%. After ceasing excitation, a large RTP spectra with peaks at 510 and 545 nm remained ((vi) in **Figure 2A**). Φ_p(RT) was determined to be 6.7% by comparing the spectral intensity of steady-state RT emission ((iv) in **Figure 2A**) with the RTP spectral intensity immediately after ceasing excitation ((vi) in **Figure 2A**). The RTP had single exponential decay characteristics (green in **Figure 2B**). Thus, the intensity of the *p*RTP produced by the 5 wt% (*S*)-BINAP-doped (*S*)-H_8-BINAP solid differed by approximately 20 times when comparing the crystal and amorphous states of the materials. The large Φ_p(RT) of (*S*)-BINAP-doped (*S*)-H_8-BINAP crystalline films does not change at concentrations of (*S*)-BINAP from 5 wt% to 15 wt%, but substantially decreased at higher concentrations of (*S*)-BINAP (**Supplementary Figure S4** and **Supplementary Table S1**).

FUNDAMENTAL PHOTOPHYSICAL PROPERTIES

The absorption and emission characteristics of the (*S*)-BINAP guest and the (*S*)-H_8-BINAP host were measured to determine the mechanism by which green *p*RTP was generated by the 5 wt% (*S*)-BINAP-doped (*S*)-H_8-BINAP films. When dissolved in 2-methyltetrahydrofuran (2Me-THF), the (*S*)-BINAP guest produced an absorption spectrum at wavelengths of less than 350 nm, and the molar absorption coefficient (ε) at 330 nm was 6.1×10^3 M^{-1} cm^{-1} (**Figure 3A**; (i)). The neat amorphous film of (*S*)-H_8-BINAP had a long small tail of absorption in the 350–400 nm range, and an ε at 330 nm of 6.4×10^2 M^{-1} cm^{-1} when the density of the amorphous (*S*)-H_8-BINAP solid was considered to be approximately 1 (**Figure 3A**; (ii)). The comparison of ε between the (*S*)-BINAP guest and the (*S*)-H_8-BINAP host indicated that the (*S*)-BINAP guest absorbed 33% of the excitation light at 330 nm when the amorphous 5 wt% (*S*)-BINAP-doped (*S*)-H_8-BINAP films were irradiated with excitation light. In the neat crystalline film of (*S*)-H_8-BINAP, light scattering increased from the baseline at wavelengths longer than 350 nm, whereas (*S*)-H_8-BINAP exhibited marked absorption at wavelengths less than 350 nm (**Figure 3A**; (iii)).

The (*S*)-BINAP guest dissolved in 2Me-THF produced a fluorescence spectrum with a peak at 353 nm (**Figure 3B**; (i)). The amorphous and crystalline (*S*)-H_8-BINAP hosts produced broad fluorescence spectra with onset energies at approximately 400 nm (**Figure 3B**; 2) and (iii)). Thus, the energy of the lowest singlet excited state (S_1) of the amorphous and crystalline (*S*)-H_8-BINAP hosts was slightly smaller than that of the molecularly dispersed (*S*)-BINAP. However, the T_1 energy of the molecularly dispersed (*S*)-BINAP was much smaller than that of the amorphous and crystalline (*S*)-H_8-BINAP hosts. The (*S*)-BINAP molecularly dispersed in 2Me-THF produced green persistent phosphorescence at 77 K immediately after ceasing

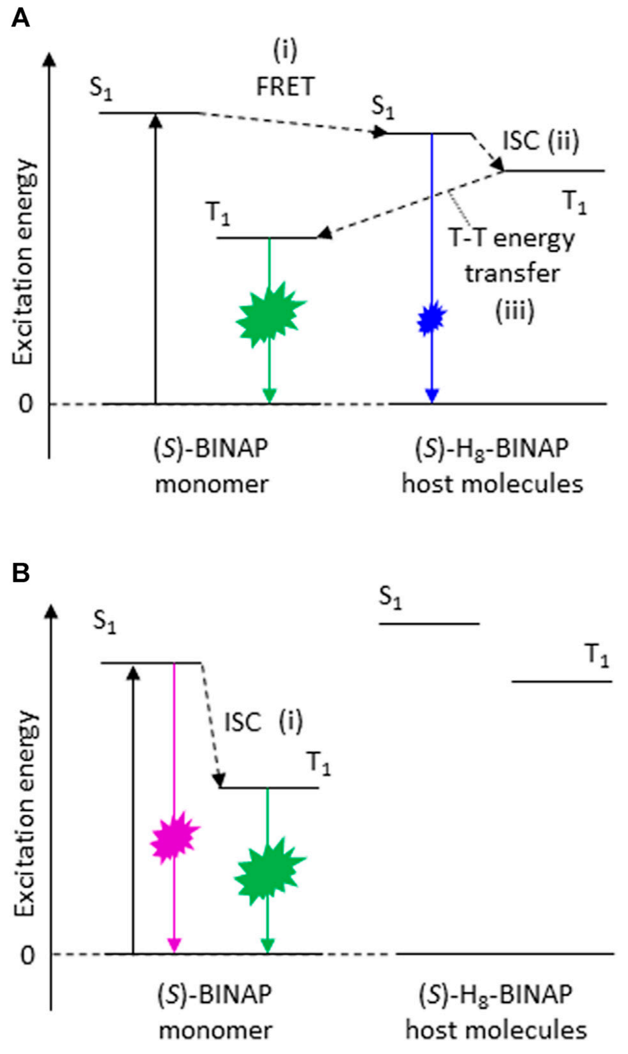

FIGURE 4 | Scheme showing T_1 generation in (*S*)-BINAP. **(A)** In (*S*)-H$_8$-BINAP hosts. **(B)** In amorphous *β*-estradiol host. ((*S*)-BINAP = (*S*)-(–)-2,2′-bis(diphenylphosphino)-1,1′-binaphthyl (*S*)-H$_8$-BINAP = (*S*)-bis(diphenylphosphino)-5,5′,6,6′,7,7′,8,8′-octahydro-1,1′-binaphthyl).

excitation at 330 nm (**Figure 3C**; (i)). The spectral shape produced by the phosphorescence and the energy of the molecularly dispersed (*S*)-BINAP was comparable to those of the amorphous and crystalline 5 wt% (*S*)-BINAP-doped (*S*)-H$_8$-BINAP films. Because neat solid (*S*)-BINAP does not produce RTP at all, even when it is in a vacuum, the green *p*RTP of the amorphous and crystalline 5 wt% (*S*)-BINAP-doped (*S*)-H$_8$-BINAP films was caused by the molecularly dispersed (*S*)-BINAP. Although high-concentration doping is not generally appropriate when different chromophores are doped into different crystalline molecules, the similar sizes and structures of (*S*)-BINAP and (*S*)-H$_8$-BINAP may allow the efficient replacement of (*S*)-H$_8$-BINAP by (*S*)-BINAP in a (*S*)-H$_8$-BINAP crystalline lattice. At 77K, both the amorphous and crystalline neat films of (*S*)-H$_8$-BINAP produced broad phosphorescence spectra with onset energies of approximately 425 nm (**Figure 3C**; 2) and (iii)). The comparable S_1 and T_1 energies between the amorphous and crystalline (*S*)-H$_8$-BINAP hosts do not satisfactorily explain the large difference in the Φ_p(RT) between the (*S*)-BINAP in the amorphous (*S*)-H$_8$-BINAP host and that in the crystalline (*S*)-H$_8$-BINAP host. Appropriate discussions about Φ_p(RT) generally require investigation of both the generation yield of T_1 and the T_1-S_0 processes (Hirata, 2017). Therefore, the following two sections comprise a discussion of these two points.

TRIPLET GENERATION SCHEME

The T_1 generation mechanism and the yield of the (*S*)-BINAP doped into the (*S*)-H$_8$-BINAP host were investigated. Again, we note that the (*S*)-BINAP dissolved in 2Me-THF produced fluorescence with a peak wavelength at 353 nm (**Figure 3B**, (i)). However, the peak disappeared, and a broad-fluorescence spectra with an onset energy at approximately 400 nm appeared when the (*S*)-BINAP was doped into the amorphous and crystalline (*S*)-H$_8$-BINAP hosts ((iii) and (iv) of **Figure 2A**, respectively). Those fluorescence spectra are comparable to the fluorescence spectra of the amorphous and crystalline (*S*)-H$_8$-BINAP hosts ((ii) and (iii) of **Figure 3B**, respectively). The S_1 energy of (*S*)-BINAP was transferred to the amorphous and crystalline (*S*)-H$_8$-BINAP hosts via fluorescence resonance energy transfer (FRET) ((i) in **Figure 4A**). The generated S_1 energy of the (*S*)-H$_8$-BINAP hosts allowed intersystem crossing (ISC) from S_1 to generate T_1 in the (*S*)-H$_8$-BINAP hosts ((ii) in **Figure 4A**). Finally, the generated T_1 in the (*S*)-H$_8$-BINAP hosts was effectively trapped by the T_1 of the (*S*)-BINAP, because the T_1 of the (*S*)-BINAP was much less than that of the (*S*)-H$_8$-BINAP hosts ((iii) in **Figure 4A**).

The T_1 generation yield of the (*S*)-BINAP in the (*S*)-H$_8$-BINAP host (Φ_t) via the processes from (i) to (iii) in **Figure 4A** has the following relationship with Φ_p(77 K):

$$\boldsymbol{\Phi_p(77K) = \Phi_t k_p \tau_p(77K)} \tag{1}$$

where k_p is the rate constant of phosphorescence of the (*S*)-BINAP guest. (*S*)-BINAP doped into an amorphous *β*-estradiol host produced a fluorescence spectrum at 355 nm (blue in **Supplementary Figure S2A**), and generated green *p*RTP (green in **Supplementary Figure S5A,B**). In addition, the fluorescence energy of the (*S*)-BINAP doped into the amorphous *β*-estradiol was comparable to that of the (*S*)-BINAP dissolved in 2Me-THF. Therefore, the T_1 of the (*S*)-BINAP doped into the amorphous *β*-estradiol was formed via the ISC from S_1 to the triplet states ((i) in **Figure 4B**). The Φ_p(RT) of the (*S*)-BINAP doped into the amorphous *β*-estradiol can be expressed as (Hirata, 2017):

$$\boldsymbol{\Phi_p(RT) = \Phi_{isc} k_p \tau_p(RT)} \tag{2}$$

where Φ_{isc} is the ISC yield from S_1 to the triplet states. The Φ_{isc} of the molecularly dispersed (*S*)-BINAP was quantified as 0.29 using a transient absorption technique (**Supplementary Figure S6**; **Supplementary Table S2**) (Bhattacharjee and Hirata, 2020).

TABLE 1 | Photophysical values relating to phosphorescence of 5 wt% (S)-BINAP-doped (S)-H_8-BINAP solids in crystalline and amorphous states.

Phase of host	Φ_t[a] (%)	Φ_p(RT) (%)	Φ_p(77 K) (%)	τ_p(77 K) (s)	k_{nr}(RT) + k_q(RT)[b] (s^{-1})	k_{nr}(RT)[c] (s^{-1})	k_q(RT)[d] (s^{-1})
Crystal	68	6.7	12.5	0.75	2.24	1.65	0.59
Amorphous	15	0.31	2.3	0.63	11.5	2.15	9.36

[a] *Values determined using* ***Eq. 1****.*

[b] *Values calculated by substituting* Φ_t*,* Φ_p*(RT), and* τ_p*(77 K) into* ***Eq. 4****.*

[c] *Values determined using fitting lines in* ***Figure 5B****.*

[d] *Values determined by subtracting* k_{nr}*(RT) determined using fitting lines in* ***Figure 5B*** *from* k_{nr}*(RT) +* k_q*(RT).*

(S)-BINAP = (S)-(–)-2,2′-bis(diphenylphosphino)-1,1′-binaphthyl (S)-H_8*-BINAP = (S)-bis(diphenylphosphino)-5,5′,6,6′,7,7′,8,8′-octahydro-1,1′-binaphthyl; RT = room temperature.*

Because 0.3 wt% (*S*)-BINAP doped into *β*-estradiol had an Φ_p(RT) of 0.052 and a τ_p(RT) of 0.72 s (**Supplementary Figure S5C**), the k_p of (*S*)-BINAP was quantified as 0.25 s^{-1} according to the values of Φ_{isc}, Φ_p(RT), and τ_p(RT) in **Eq. (2)**. The optically determined k_p was comparable to 0.22 s^{-1}, which was the k_p value calculated using the optimized T_1 geometry of (*S*)-BINAP. In addition, the locally excited transition characteristics between T_1 and S_0, which can be used to explain the optically observed vibrational shape of the *p*RTP spectra of (*S*)-BINAP, were calculated for the optimized T_1 geometry of (*S*)-BINAP (**Supplementary Figure S7A**). The calculated T_1-S_0 transition energy based on the optimized T_1 geometry of (*S*)-BINAP provides a simple statistical explanation for the green color of the *p*RTP of the (*S*)-BINAP (**Supplementary Figure S7B**). The Φ_p(77K) and τ_p(77K) values of the amorphous 5 wt% (*S*)-BINAP-doped (*S*)-H_8-BINAP film were 0.023 and 0.63 s, respectively. The optically determined k_p, the Φ_p(77K), and the τ_p(77K) were substituted into **Eq. 1** to determine the Φ_t = 0.15 of the amorphous 5 wt% (*S*)-BINAP-doped (*S*)-H_8-BINAP film (**Table 1**). Similarly, the Φ_p(77K) and τ_p(77K) values of the crystalline 5 wt% (*S*)-BINAP-doped (*S*)-H_8-BINAP film were 0.125 and 0.75 s, respectively. The k_p, the Φ_p(RT), and the τ_p(RT) were substituted into **Eq. 1** to determine the Φ_t = 0.68 of the crystalline 5 wt% (*S*)-BINAP-doped (*S*)-H_8-BINAP film (**Table 1**). Hence the approximate 4.5 times difference in Φ_t between the crystalline and amorphous 5 wt% (*S*)-BINAP-doped (*S*)-H_8-BINAP films. However, the difference in Φ_t was still small compared with the approximate 20 times difference in Φ_p(RT) between the crystalline and amorphous 5 wt% (*S*)-BINAP-doped (*S*)-H_8-BINAP films. Therefore, further investigation about the mechanism of transition from T_1 to S_0 in the films is required.

LARGE DIFFERENT TRIPLET DEACTIVATION DEPENDING ON THE PHASE CHANGE OF THE HOST

To investigate the large difference in Φ_p(RT) between the amorphous and crystalline states of the 5 wt% (*S*)-BINAP-doped (*S*)-H_8-BINAP, the temperature dependence of the emission characteristics of the two materials was determined. The fluorescence characteristics were almost independent of temperature in both the amorphous and crystalline states (**Supplementary Figure S8**), whereas there was a large difference between the temperature dependence of the phosphorescence characteristics of the amorphous and crystalline states (**Figure 5A** and **Supplementary Figure S9**) of the 5 wt% (*S*)-BINAP-doped (*S*)-H_8-BINAP solid. The Φ_p of the crystalline 5 wt% (*S*)-BINAP-doped (*S*)-H_8-BINAP decreased from 12.5 to 6.7% as the temperature increased from 77 K to RT (red in **Figure 5A**). In contrast, the Φ_p of the amorphous 5 wt% (*S*)-BINAP-doped (*S*)-H_8-BINAP decreased markedly from 2.3 to 0.31% as the temperature increased from 77 K to RT (blue in **Figure 5A**). The phosphorescence lifetime at *T* ($\tau_p(T)$) is generally expressed as (Hirata, 2017):

$$\boldsymbol{\tau_p(T) = 1/\left[k_p + k_{nr}(T) + k_q(T)\right]} \tag{3}$$

The following equation can be produced from **Eq. 1** and **Eq. 3**:

$$\boldsymbol{k_{nr}(T) + k_q(T) = \Phi_t k_p/\Phi_p(T) - k_p} \tag{4}$$

For the amorphous 5 wt% (*S*)-BINAP-doped (*S*)-H_8-BINAP film, Φ_t = 0.15, k_p = 0.25 s^{-1}, and $\Phi_p(T)$ (blue plots in **Figure 5A**) were substituted into **Eq. 4** to determine the $k_{nr}(T) + k_q(T)$ of the molecularly dispersed (*S*)-BINAP in the amorphous (*S*)-H_8-BINAP host (blue plots in **Figure 5B**). For the 5 wt% (*S*)-BINAP doped into the crystalline (*S*)-H_8-BINAP film, Φ_t = 0.68, k_p = 0.25 s^{-1}, and $\Phi_p(T)$ (red plots in **Figure 5A**) were substituted into **Eq. 4** to determine the $k_{nr}(T) + k_q(T)$ of the molecularly dispersed (*S*)-BINAP in the crystalline (*S*)-H_8-BINAP host (red plots in **Figure 5B**).

The $k_{nr}(T) + k_q(T)$ of (*S*)-BINAP did not increase significantly when (*S*)-BINAP was doped into the crystalline (*S*)-H_8-BINAP host (red in **Figure 5B**). However, the $k_{nr}(T) + k_q(T)$ of (*S*)-BINAP increased markedly in the amorphous (*S*)-H_8-BINAP host (blue in **Figure 5B**). We note that $k_{nr}(T) + k_q(T)$ was comparable in the low-temperature range, whereas it was markedly different in the high-temperature range. In previous research, the very small increase in $k_{nr}(T) + k_q(T)$ in the low-temperature range was often caused by $k_{nr}(T)$ (Hirata et al., 2013; Kwon et al., 2015). The lack of a marked increase in $k_{nr}(T)$ as the temperature increases has been confirmed from experimental and theoretical viewpoints using a variety of heavy atom-free chemical backbones (Bhattacharjee et al., 2021; Hirata and Bhattacharjee, 2021). Therefore, the lack of a marked increase in $k_{nr}(T)$ in (*S*)-BINAP is plausible. Indeed, the theoretical calculations that depend on spin–orbit coupling with consideration for vibrations support the idea that the $k_{nr}(T)$ in

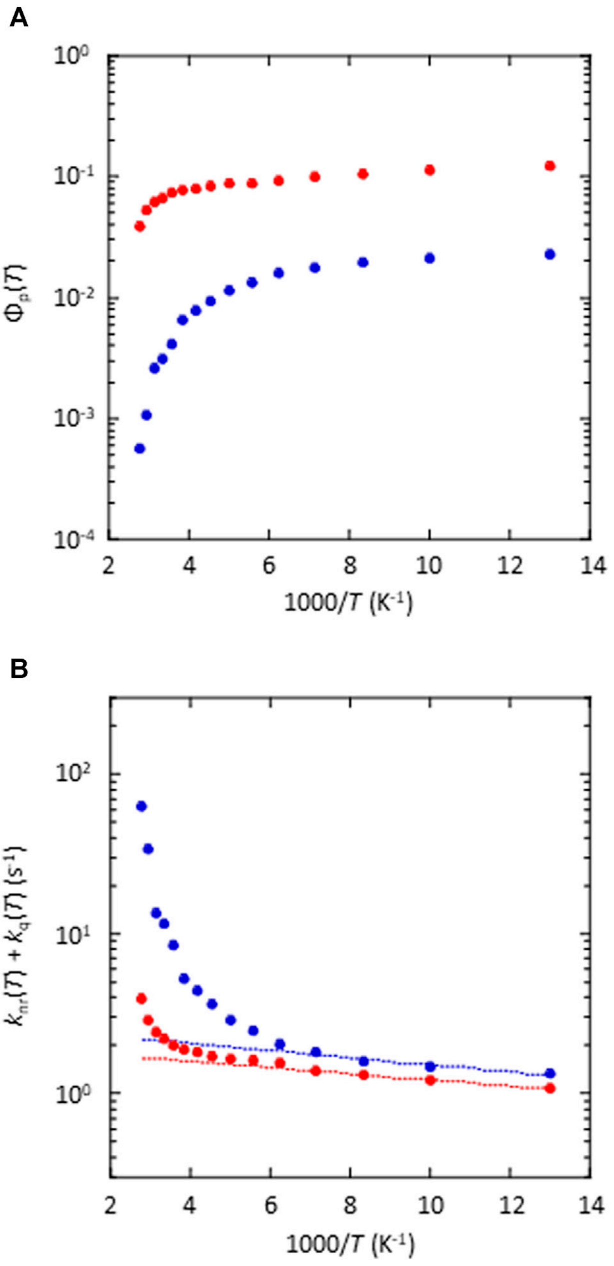

FIGURE 5 | Temperature dependence of phosphorescence and nonradiative deactivation of amorphous (blue) and crystalline (red) 5 wt% (*S*)-BINAP-doped (*S*)-H$_8$-BINAP. **(A)** Temperature dependence of $\Phi_p(T)$. The excitation wavelength was 330 nm. **(B)** Temperature dependence of $k_{nr}(T) + k_q(T)$. The dashed lines are fitting lines for $k_{nr}(T)$, which was determined according to the exponential function for data from 77K to 140 K. ((*S*)-BINAP = (*S*)-(–)-2,2′-bis(diphenylphosphino)-1,1′-binaphthyl (*S*)-H$_8$-BINAP = (*S*)-bis(diphenylphosphino)-5,5′,6,6′,7,7′,8,8′-octahydro-1,1′-binaphthyl).

(*S*)-BINAP hardly increased from 77 K to RT (**Supplementary Figure S10**). Therefore, $k_{nr}(T)$ is almost independent of intermolecular interactions between (*S*)-BINAP and (*S*)-H$_8$-BINAP. Because the comparable $k_{nr}(T)$ values of (*S*)-BINAP in different phase conditions were estimated (**Figure 5B**), the large difference in $k_{nr}(T) + k_q(T)$ at high temperatures was caused by intermolecular processes, i.e., $k_q(T)$.

DISCUSSION OF THE DRIVING FORCE BEHIND INTERMOLECULAR TRIPLET QUENCHING

Triplet quenching caused by endothermic triplet–triplet energy transfer has been reported for metal-free and/or heavy atom-free chromophores with small k_p and k_{nr}(RT) values, even when the T_1 energy of the host is much larger than that of the guest, and the solid materials are under high vacuum (Hirata et al., 2013; Totani et al., 2013). In research on organic light emitting diodes, k_q(RT) values of varying magnitudes are often discussed in terms of the difference in the T_1 energy between the guest and host (ΔE) (Adachi et al., 2001). However, the absence of a significant difference between the onset energy values of the phosphorescence spectra of the amorphous and crystalline states of (*S*)-H$_8$-BINAP (**Figure 3C**; (ii) and (iii)) indicates that the T_1 energy of the neat (*S*)-H$_8$-BINAP solid hardly changed between those states. Because the onset energy of phosphorescence of the (*S*)-BINAP guest also hardly changed between the amorphous and crystalline states of (*S*)-H$_8$-BINAP host, the ΔE of the 5 wt% (*S*)-BINAP-doped (*S*)-H$_8$-BINAP was comparable between those states. Therefore, other physical viewpoints are crucial for explaining the difference in k_q(RT) values between the amorphous and crystalline states of 5 wt% (*S*)-BINAP-doped (*S*)-H$_8$-BINAP solid.

It may be necessary to consider other diffusion-limited processes to determine potential factors that contribute to k_q(RT). Although endothermic processes are not generally rapid, the diffusion process in a solid state is potentially slower than a slow endothermic process. Because this condition satisfies the definition of a diffusion-limited process, the observable rate constant k_q(RT) can be expressed using the formula for a general diffusion-limited process (Fukuzumi et al., 2003; Chakraborty et al., 2006):

$$k_q(T) = \frac{k_{diff}(T)k_{et}(T)}{\left[k_{diff}(T) + k_{et}(T)\right]} \tag{5}$$

where $k_{diff}(T)$ is the diffusion rate constant at T and $k_{et}(T)$ is the rate constant of triplet deactivation via triplet–triplet energy transfer from guest to host. $k_{diff}(T)$ is generally expressed as: (Horie et al., 1984)

$$k_{diff}(T) = 4\pi RD(T)N[C] \tag{6}$$

where R is the reaction radius between guest and host, $D(T)$ is the diffusion coefficient at T K, N is the Avogadro number, and $[C]$ is the concentration of host. Because Dexter energy transfer is often discussed using the double electron transfer model according to Marcus-based theory (Dexter, 1953; Marcus, 1956; Closs et al., 1989; Köhler and Bässler, 2011), $k_{et}(T)$ may be expressed based on the following Marcus formula:

$$k_{et}(T) = \nu\left(\frac{1}{\sqrt{4k\lambda T}}\right) exp\left[-\frac{(\lambda + \Delta E)^2}{4\lambda kT}\right] \tag{7}$$

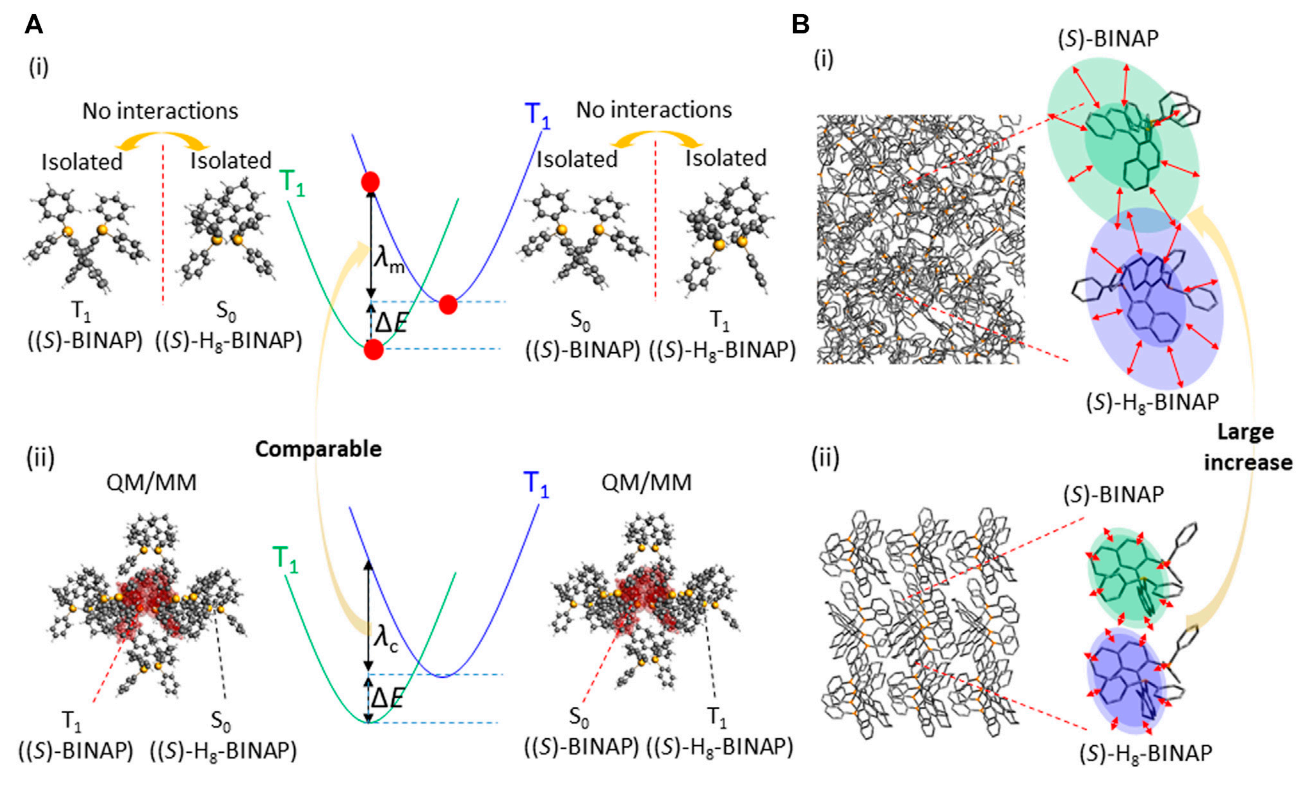

FIGURE 6 | Physical behavior relating to k_q(RT) except for ΔE from the perspective of intermolecular interactions between an (*S*)-BINAP guest and the (*S*)-H_8-BINAP host molecules. **(A)** Reorganization energy for endothermic triplet–triplet energy transfer. (i) represents a case in which (*S*)-BINAP and (*S*)-H_8-BINAP have no intermolecular interactions. (ii) represents a case in which a molecule in a crystalline lattice of (*S*)-H_8-BINAP is replaced by (*S*)-BINAP. **(B)** The diffusion constant; (i) and (ii) represent the amorphous and crystalline states, respectively. The red arrows indicate different magnitudes of the diffusion constant at RT between the amorphous and crystalline states. (RT = room temperature; (*S*)-BINAP = (*S*)-(–)-2,2′-bis(diphenylphosphino)-1,1′-binaphthyl (*S*)-H_8-BINAP = (*S*)-bis(diphenylphosphino)-5,5′,6,6′,7,7′,8,8′-octahydro-1,1′-binaphthyl).

where ν is the frequency of the motion in the reactant potential well between guest and host, λ is the reorganization energy for triplet–triplet energy transfer, and k is the Boltzman constant. **Eq. 5** and **Eq. 6** indicate that D(RT) is almost proportional to k_q(RT) when k_{diff}(RT) is much less than k_{et}(RT). Although the relationship between k_q(RT) and ΔE is mostly considered with regard to solid molecular materials in the field of organic light emitting diodes (Adachi et al., 2001; Hirata et al., 2013; Notsuka et al., 2017), **Eqs. 5–7** indicate that an increase in λ and a decrease in D(RT) also contribute to the suppression of k_q(RT). Therefore, consideration of ΔE, λ, and D(RT) is necessary for a discussion of the difference in k_q(RT) values between amorphous and crystalline states.

If λ in the crystalline state is much larger than it is in the amorphous state due to more potential intermolecular interactions, the difference in the number of intermolecular interactions causes a large difference in k_q(RT), even when ΔE is comparable. Under the condition that (*S*)-BINAP had intermolecular interactions with the (*S*)-H_8-BINAP molecules in the crystalline (*S*)-H_8-BINAP lattice (λ_c), the reorganization energy with regard to the energy transfer from T_1 of (*S*)-BINAP to T_1 of (*S*)-H_8-BINAP was calculated to enable further discussion of the contribution made by λ to k_q(RT) (**Figure 6A**; (ii)). Initially, a molecule of (*S*)-H_8-BINAP in the crystalline lattice of (*S*)-H_8-BINAP was replaced by (*S*)-BINAP (**Supplementary Figure S11A**; (I)). The S_0 and T_1 geometries of the replaced (*S*)-BINAP were optimized without changing any of the coordinates of the (*S*)-H_8-BINAP molecules around the (*S*)-BINAP (**Supplementary Figure S11A**, (II)). Subsequently, the S_0 and T_1 geometries of the (*S*)-H_8-BINAP molecule in the crystalline lattice of (*S*)-H_8-BINAP were optimized without changing any of the coordinates of the (*S*)-H_8-BINAP molecules around the target (*S*)-H_8-BINAP (**Supplementary Figure S11B**; (III)). The four geometries were used to determine λ_c, and λ_c = 1.59 eV was calculated using the Amsterdam Modeling Suite (AMS) 2020 software package with the B3LYP functional and the TZP basis set (**Supplementary Material**, **Section 4**). The reorganization energy relating to the energy transfer from T_1 of (*S*)-BINAP to T_1 of (*S*)-H_8-BINAP under the condition that (*S*)-BINAP and (*S*)-H_8-BINAP had no intermolecular interactions (λ_m) was also calculated (**Figure 6A**; (i) and **Supplementary Figure S12**). The S_0 and T_1 geometries were calculated for isolated molecules of (*S*)-BINAP and (*S*)-H_8-BINAP. The four geometries were used to determine λ_m, and λ_m = 1.84 eV was calculated using the AMS 2020 software package with the B3LYP functional and the TZP basis set (**Supplementary Material**, **Section 4**). Although a larger λ in the crystalline state had been logically considered because intermolecular interactions may cause more energy to coordinate change for reorganization, λ_c was slightly smaller than λ_m. For example, the reorganization energy for charge transfer between molecules in a crystalline semiconductor is 0.1 eV (Liu et al., 2017). However, this is often less than that calculated for isolated molecules without any intermolecular interactions (Narushima et al., 2019). Therefore, the local rigidity in molecular solids may be hardly related to the reorganization energy for charge transfer. Therefore, ΔE and λ do not properly explain the large increase in k_q(RT) in the amorphous, compared with the crystalline, 5 wt% (*S*)-BINAP-doped (*S*)-H_8-BINAP.

Another potential reason to change k_q(RT) independently of ΔE and λ may be *D*(RT). Diffusion depends on Brownian motion. It is a different physical phenomenon from the vibrations and coordination changes that take place in molecules during reorganization (Brown, 1828; Einstein, 1905). The theory underlying Brownian motion was established in the early 1900s (von Smoluchowski, 1906). Because molecules in an amorphous state generally have a large free volume compared with those in a crystalline state, the local diffusion of molecules is allowed, even when the solids are below the glass transition temperature (Horie and Mita, 1982; Horie et al., 1984). The *D*(RT) of a side group in a representative amorphous polymer—i.e., polymethylmethacrylate—was reported to have a magnitude of 10^{-14} cm^2/s (Horie et al., 1984), which is less than the *D*(RT) of a general liquid molecule, i.e., $1/10^8$ (Monguzzi et al., 2013). The *D*(RT) in the amorphous state may be large compared with that in the crystalline state for solid materials at RT. To enable triplet–triplet energy transfer, two molecular orbitals must overlap. In the amorphous state, a large *D*(RT) increases the possibility of the overlap of two molecular orbitals enabling triplet–triplet energy transfer (**Figure 6B**; (i)). However, stronger intermolecular interactions decrease *D*(RT), reducing the possibility of orbital overlap (**Figure 6B**; (ii)). Molecular dynamics (MD) analysis indicates that the simulated *D*(RT) of (*S*)-H_8-BINAP in the amorphous state is approximately 10 times larger than it is in the crystalline state (**Supplementary Figure S13**). The magnitude of the difference in the calculated *D*(RT) between the amorphous and crystalline states is comparable to that of the k_q(RT) between those states. Thus, the similar increase of magnitude of the enhanced *D*(RT) of crystalline (*S*)-H_8-BINAP solid compared with amorphous (*S*)-H_8-BINAP solid was observed between optically estimated *D*(RT) and simulated *D*(RT). To date there has been no discussion of ΔE, λ, and *D*(RT) with regard to k_q(RT). By investigating large differences in k_q(RT) between two solid materials with comparable ΔE and λ values, we attempted to confirm that the control of *D*(RT) is also a dominant factor in increasing the triplet quenching caused by endothermic triplet energy transfer. Therefore, more detailed discussions about molecular diffusion in solid materials are essential. The contribution of *D*(RT) to k_q(RT) has not been addressed in research into organic electronics. The contribution made by ΔE to k_q(RT) has not been investigated in research on aggregated chromophores that generate *p*RTP, and the relationship between rigidity and vibrations and intermolecular interactions remains unclear. The controlled results reported in the present paper indicate that discussions about both ΔE and *D*(RT) are crucial for the intrinsic control of k_q(RT) and the long-lived RT triplet state of heavy atom-free and/or metal-free solid materials.

CONCLUSION

In the present study, a thermo-reversible phase change of an (*S*)-H_8-BINAP host doped with (*S*)-BINAP was induced. The (*S*)-BINAP produced a *p*RTP spectrum that was comparable to the spectra of the (*S*)-H_8-BINAP host in the two phases. The molecularly dispersed (*S*)-BINAP had a Φ_p(RT) of 6.7% in the crystalline (*S*)-H_8-BINAP host and a Φ_p(RT) of 0.31% in the amorphous host. Detailed photophysical analyses indicated that the triplet generation of (*S*)-BINAP and the magnitude of the difference in k_q(RT) between the (*S*)-BINAP guest and the (*S*)-H_8-BINAP host both differed between the amorphous and crystalline states. This caused a large difference in the Φ_p(RT) of (*S*)-BINAP between those states. Differing ΔE, λ, and *D*(RT) values were considered as a potential explanation for the difference in k_q(RT) values between the amorphous and crystalline states. Comparable ΔE and λ values in both the amorphous and crystalline states indicated that the *D*(RT) is the reason for the large discrepancy in k_q(RT). The large difference in the magnitude of *D*(RT) between the amorphous and crystalline states was supported by MD simulations. The suppression of vibrations by intermolecular interactions is often used to explain the decrease in nonradiative deactivation from T_1. However, analysis of ΔE, λ, and *D*(RT) from all perspectives clarifies that the small *D*(RT) in the solid state makes a large contribution to the control of k_q(RT), and intermolecular interactions could be used to suppress molecular diffusion in the solid state, thereby reducing the k_q(RT). Because the significantly low rate of diffusion in molecular solids is also logically related to solid-state chemical reactions, analysis of slow local diffusion may be crucial to the control of chemical conversion in the solid state (Kubota et al., 2019). Because an accurate estimation of the small diffusion constant in molecular solids is difficult, the analysis introduced in the present paper is important for the construction of a variety of materials that allow long-lived RT triplet excitons, and for the control of electron transfer and chemical reactions in molecular solids.

DATA AVAILABILITY STATEMENT

The datasets presented in this study can be found in online repositories. The names of the repository/repositories and accession number(s) can be found in the article/**Supplementary Material**.

AUTHOR CONTRIBUTIONS

TK and SH wrote the critical parts of the manuscript, performed the photophysical experiments, and analyzed the photophysical data. SH performed the quantum chemical and molecular dynamics calculations.

FUNDING

The present work was supported by the JST FOREST Program (grant number JPMJFR201T, Japan) and JSPS KAKENHI (grant numbers JP18H04507, JP20H04664, JP21H02011, and JP21K18928).

REFERENCES

Adachi, C., Kwong, R. C., Djurovich, P., Adamovich, V., Baldo, M. A., Thompson, M. E., et al. (2001). Endothermic Energy Transfer: A Mechanism for Generating Very Efficient High-Energy Phosphorescent Emission in Organic Materials. *Appl. Phys. Lett.* 79, 2082–2084. doi:10.1063/1.1400076

Bhattacharjee, I., Hayashi, K., and Hirata, S. (2021). Key of Suppressed Triplet Nonradiative Transition-dependent Chemical Backbone for Spatial Self-Tunable Afterglow. *JACS Au* 1, 945–954. doi:10.1021/jacsau.1c00132

Bhattacharjee, I., and Hirata, S. (2020). Highly Efficient Persistent Room-Temperature Phosphorescence from Heavy Atom-Free Molecules Triggered by Hidden Long Phosphorescent Antenna. *Adv. Mater.* 32, 2001348. doi:10.1002/adma.202001348

Brown, R. (1828). XXVII. A Brief Account of Microscopical Observations Made in the Months of June, July and August 1827, on the Particles Contained in the Pollen of Plants; and on the General Existence of Active Molecules in Organic and Inorganic Bodies. *Philosophical Mag.* 4, 161–173. doi:10.1080/14786442808674769

Chakraborty, A., Chakrabarty, D., Seth, D., Hazra, P., and Sarkar, N. (2006). Photo-Induced Intermolecular Electron Transfer from Electron Donating Solvents to Coumarin Dyes in Bile Salt Aggregates: Role of Diffusion in Electron Transfer Reaction. *Spectrochimica Acta A: Mol. Biomol. Spectrosc.* 63, 594–602. doi:10.1016/j.saa.2005.06.006

Clapp, D. B. (1939). The Phosphorescence of Tetraphenylmethane and Certain Related Substances. *J. Am. Chem. Soc.* 61, 523–524. doi:10.1021/ja01871a504

Closs, G. L., Johnson, M. D., Miller, J. R., and Piotrowiak, P. (1989). A Connection between Intramolecular Long-Range Electron, Hole, and Triplet Energy Transfers. *J. Am. Chem. Soc.* 111, 3751–3753. doi:10.1021/ja00192a044

Deng, Y., Zhao, D., Chen, X., Wang, F., Song, H., and Shen, D. (2013). Long Lifetime Pure Organic Phosphorescence Based on Water Soluble Carbon Dots. *Chem. Commun.* 49, 5751–5753. doi:10.1039/C3CC42600A

Dexter, D. L. (1953). A Theory of Sensitized Luminescence in Solids. *J. Chem. Phys.* 21, 836–850. doi:10.1063/1.1699044

Einstein, A. (1905). Über die von der molekularkinetischen Theorie der Wärme geforderte Bewegung von in ruhenden Flüssigkeiten suspendierten Teilchen. *Ann. Phys.* 322, 549–560. doi:10.1002/andp.19053220806

Fateminia, S. M. A., Mao, Z., Xu, S., Yang, Z., Chi, Z., and Liu, B. (2017). Organic Nanocrystals with Bright Red Persistent Room-Temperature Phosphorescence for Biological Applications. *Angew. Chem. Int. Ed.* 56, 12160–12164. doi:10.1002/ange.20170594510.1002/anie.201705945

Fukuzumi, S., Ohkubo, K., Imahori, H., and Guldi, D. M. (2003). Driving Force Dependence of Intermolecular Electron-Transfer Reactions of Fullerenes. *Chem. Eur. J.* 9, 1585–1593. doi:10.1002/chem.200390182

Hirata, S., and Bhattacharjee, I. (2021). Vibrational Radiationless Transition from Triplet States of Chromophores at Room Temperature. *J. Phys. Chem. A.* 125, 885–894. doi:10.1021/acs.jpca.0c09410

Hirata, S., Hara, H., and Bhattacharjee, I. (2020). Phosphorescence Quenching of Heavy-atom-free Dopant Chromophores Triggered by Thermally Activated Triplet Exciton Diffusion of a Conjugated Crystalline Host. *J. Phys. Chem. C* 124, 25121–25132. doi:10.1021/acs.jpcc.0c07864

Hirata, S. (2017). Recent Advances in Materials with Room-Temperature Phosphorescence: Photophysics for Triplet Exciton Stabilization. *Adv. Opt. Mater.* 5, 1700116. doi:10.1002/adom.201700116

Hirata, S., Totani, K., Zhang, J., Yamashita, T., Kaji, H., Marder, S. R., et al. (2013). Efficient Persistent Room Temperature Phosphorescence in Organic Amorphous Materials under Ambient Conditions. *Adv. Funct. Mater.* 23, 3386–3397. doi:10.1002/adfm.201203706

SUPPLEMENTARY MATERIAL

The Supplementary Material for this article can be found online at: https://www.frontiersin.org/articles/10.3389/fchem.2021.788577/full#supplementary-material

Horie, K., and Mita, I. (1982). Photochemistry in Polymer Solids. Decay of Benzophenone Phosphorescence in Poly(methyl Methacrylate). *Chem. Phys. Lett.* 93, 61–65. doi:10.1016/0009-2614(82)85056-2

Horie, K., Morishita, K., and Mita, I. (1984). Photochemistry in Polymer Solids. 3. Kinetics for Nonexponential Decay of Benzophenone Phosphorescence in Acrylic and Methacrylic Polymers. *Macromolecules* 17, 1746–1750. doi:10.1021/ma00139a020

Köhler, A., and Bässler, H. (2011). What Controls Triplet Exciton Transfer in Organic Semiconductors? *J. Mater. Chem.* 21, 4003–4011. doi:10.1039/C0JM02886J

Kubota, K., Pang, Y., Miura, A., and Ito, H. (2019). Redox Reactions of Small Organic Molecules Using Ball Milling and Piezoelectric Materials. *Science* 366, 1500–1504. doi:10.1126/science.aay8224

Kwon, M. S., Yu, Y., Coburn, C., Phillips, A. W., Chung, K., Shanker, A., et al. (2015). Suppressing Molecular Motions for Enhanced Room-Temperature Phosphorescence of Metal-free Organic Materials. *Nat. Commun.* 6, 8947. doi:10.1038/ncomms9947

Liu, C., Huang, K., Park, W.-T., Li, M., Yang, T., Liu, X., et al. (2017). A Unified Understanding of Charge Transport in Organic Semiconductors: the Importance of Attenuated Delocalization for the Carriers. *Mater. Horiz.* 4, 608–618. doi:10.1039/C7MH00091J

Louis, M., Thomas, H., Gmelch, M., Haft, A., Fries, F., and Reineke, S. (2019). Blue-Light-Absorbing Thin Films Showing Ultralong Room-Temperature Phosphorescence. *Adv. Mater.* 31, 1807887. doi:10.1002/adma.201807887

Marcus, R. A. (1956). On the Theory of Oxidation-Reduction Reactions Involving Electron Transfer. I. *J. Chem. Phys.* 24, 966–978. doi:10.1063/1.1742723

Metz, F., Friedrich, S., and Hohlneicher, G. (1972). What Is the Leading Mechanism for the Nonradiative Decay of the Lowest Triplet State of Aromatic Hydrocarbons? *Chem. Phys. Lett.* 16, 353–358. doi:10.1016/0009-2614(72)80291-4

Metz, F. (1973). Position-Dependent Deuterium Effect on Relative Rate Constants for ISC Processes in Aromatic Hydrocarbons. *Chem. Phys. Lett.* 22, 186–190. doi:10.1016/0009-2614(73)80567-6

Monguzzi, A., Bianchi, F., Bianchi, A., Mauri, M., Simonutti, R., Ruffo, R., et al. (2013). High Efficiency Up-Converting Single Phase Elastomers for Photon Managing Applications. *Adv. Energ. Mater.* 3, 680–686. doi:10.1002/aenm.201200897

Narushima, K., Kiyota, Y., Mori, T., Hirata, S., and Vacha, M. (2019). Suppressed Triplet Exciton Diffusion Due to Small Orbital Overlap as a Key Design Factor for Ultralong-Lived Room-Temperature Phosphorescence in Molecular Crystals. *Adv. Mater.* 31, 1807268. doi:10.1002/adma.201807268

Notsuka, N., Kabe, R., Goushi, K., and Adachi, C. (2017). Confinement of Long-Lived Triplet Excitons in Organic Semiconducting Host-Guest Systems. *Adv. Funct. Mater.* 27, 1703902. doi:10.1002/adfm.201703902

Schlag, E. W., Schneider, S., and Fischer, S. F. (1971). Lifetimes in Excited States. *Annu. Rev. Phys. Chem.* 22, 465–526. doi:10.1146/annurev.pc.22.100171.002341

Totani, K., Okada, Y., Hirata, S., Vacha, M., and Watanabe, T. (2013). Thermoresponsive Persistent Phosphorescent Color Change Using Efficient Thermally Activated Reverse Energy Transfer with a Large Energy Difference. *Adv. Opt. Mater.* 1, 283–288. doi:10.1002/adom.201300013

von Smoluchowski, M. (1906). Zur kinetischen Theorie der Brownschen Molekularbewegung und der Suspensionen. *Ann. Phys.* 326, 756–780. doi:10.1002/andp.19063261405

Zhang, G., Chen, J., Payne, S. J., Kooi, S. E., Demas, J. N., and Fraser, C. L. (2007). Multi-Emissive Difluoroboron Dibenzoylmethane Polylactide Exhibiting Intense Fluorescence and Oxygen-Sensitive Room-

Temperature Phosphorescence. *J. Am. Chem. Soc.* 129, 8942–8943. doi:10.1021/ja0720255

Zhang, X., Xie, T., Cui, M., Yang, L., Sun, X., Jiang, J., et al. (2014). General Design Strategy for Aromatic Ketone-Based Single-Component Dual-Emissive Materials. *ACS Appl. Mater. Inter.* 6, 2279–2284. doi:10.1021/am405209w

Zhao, W., He, Z., and Tang, B. Z. (2020). Room-Temperature Phosphorescence from Organic Aggregates. *Nat. Rev. Mater.* 5, 869–885. doi:10.1038/s41578-020-0223-z

Zhen, X., Tao, Y., An, Z., Chen, P., Xu, C., Chen, R., et al. (2017). Ultralong Phosphorescence of Water-Soluble Organic Nanoparticles for *In Vivo* Afterglow Imaging. *Adv. Mater.* 29, 1606665. doi:10.1002/adma.201606665

Zhou, B., and Yan, D. (2019). Simultaneous Long-Persistent Blue Luminescence and High Quantum Yield within 2D Organic-Metal Halide Perovskite Micro/Nanosheets. *Angew. Chem. Int. Ed.* 58, 15128–15135. doi:10.1002/anie.201909760

Conflict of Interest: The authors declare that the research was conducted in the absence of any commercial or financial relationships that could be construed as a potential conflict of interest.

frontiers in Chemistry

ORIGINAL RESEARCH
published: 23 November 2021
doi: 10.3389/fchem.2021.781294

Highly Efficient Heavy Atom Free Room Temperature Phosphorescence by Host-Guest Doping

Jinzhu Cao[1,2†], Meng Zhang[3†], Manjeet Singh[3], Zhongfu An[3], Lingfei Ji[1], Huifang Shi[3]* and Yijian Jiang[1]

[1]Institute of Laser Engineering, Beijing University of Technology (BJUT), Beijing, China, [2]China Electronics Standardization Institute, Beijing, China, [3]Key Laboratory of Flexible Electronics (KLOFE), Institute of Advanced Materials (IAM), Nanjing Tech University (NanjingTech), Nanjing, China

Recently, there has been remarkable progress of the host-guest doped pure organic room-temperature phosphorescence (RTP) materials. However, it remains a great challenge to develop highly efficient host-guest doping systems. In this study, we have successfully developed a heavy atom free pure organic molecular doped system (benzophenone-thianthrene, respectively) with efficient RTP through a simple host-guest doping strategy. Furthermore, by optimizing the doping ratios, the host-guest material with a molar ratio of 100:1 presented an efficient RTP emission with 46% quantum efficiency and a long lifetime of up to 9.17 ms under ambient conditions. This work will provide an effective way to design new organic doping systems with RTP.

Keywords: host-guest doping, heavy atom free, room temperature phosphorescence (RTP), triplet state, nonradiative transition

Edited by:
Wang Zhang Yuan,
Shanghai Jiao Tong University, China

Reviewed by:
Yunxiang Lei,
Wenzhou University, China
Yosuke Tani,
Osaka University, Japan

***Correspondence:**
Huifang Shi
iamhfshi@njtech.edu.cn

†These authors have contributed equally to this work and share first authorship

Specialty section:
This article was submitted to Physical Chemistry and Chemical Physics,
a section of the journal Frontiers in Chemistry

Received: *22 September 2021*
Accepted: *01 November 2021*
Published: *23 November 2021*

Citation:
Cao J, Zhang M, Singh M, An Z, Ji L, Shi H and Jiang Y (2021) Highly Efficient Heavy Atom Free Room Temperature Phosphorescence by Host-Guest Doping.
Front. Chem. 9:781294.
doi: 10.3389/fchem.2021.781294

1 INTRODUCTION

Recently, purely organic room temperature phosphorescence (RTP) materials are gaining more and more attention because of their long luminescent lifetimes, larger Stokes shift, convenient syntheses, low cost, and so on (Ma et al., 2019; Xiong et al., 2019), showing potential applications in display (Wang et al., 2019), data storage (Xu et al., 2016), encryption (Hirata, 2017), and bioimaging (Qu et al., 2019), and so on. Due to the inherent spin-forbidden and the fast-non-radiative transition of triplet excitons, it is quite hard to obtain RTP based on metal-free organic compounds. So far, in order to increase intersystem crossing (ISC) rate and to suppress non-radiative transitions, many strategies have succeeded to achieve efficient organic RTP materials, such as host-guest doping, heavy-atom effects, intermolecular electronic coupling, supramolecular self-assembly, and so forth (Yang et al., 2016; Chai et al., 2017; Cai et al., 2018; Yang et al., 2018; Shi et al., 2019; Alam et al., 2020; Lee et al., 2020; Li and Li, 2020). Among them, host-guest doping materials containing heavy atoms are an effective way to obtain efficient RTP by constructing a relatively rigid environment to restrain the nonradiative decay of the triplet state and promoting the ISC through the heavy-atom effect (Bolton et al., 2011; Kabe and Adachi, 2017; Zhang et al., 2019a; Zhang et al., 2019b; Lei et al., 2020; Liu et al., 2021a; Wang et al., 2021a). For example, Bolton et al. (2011). have developed an efficient RTP system with efficiency and lifetime up to 55% and 8.3 ms, respectively, through diluting the aldehyde chromophore into a host crystal with a similar halogen-bonding motif. Liu et al. (2021b) have developed an RTP emission of organic host-guest doped system with fluorescence and phosphorescence efficiency up to ~67.5% and ~13.2%, respectively, in a solid state using a phenylamine derivative containing halogen atoms as a guest

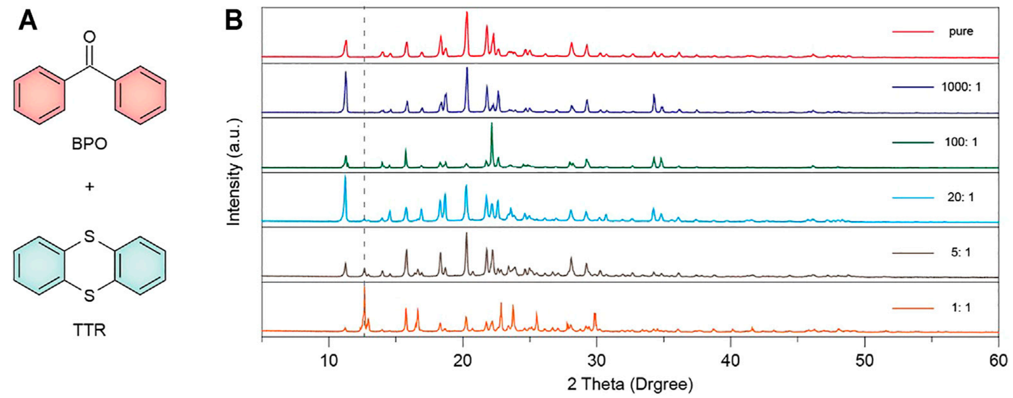

FIGURE 1 | (A) Chemical structures of the host matrices BPO and guest emitter TTR. **(B)** Powder XRD patterns of pure BPO and BPO/TTR doped crystalline materials at different molar ratios (1000:1, 100:1, 20:1, 5:1 and 1:1 Mol %).

and benzophenone as a host. Halogen-bonding is a crucial way to enhance the heavy-atom effect and promote spin-orbit coupling (SOC) to accelerate phosphorescence with high quantum yields in organic materials (Qu et al., 2019). However, the presence or substitution of heavy halogen atoms seriously affects the chemical stability upon thermal and electrical treatments (Zhou et al., 2018).

To avoid or overcome these shortcomings, heavy atom free host-guest interactions are an important approach in this research field. For instance, Lei et al. (2019) have developed a series of heavy-atom-free pure organic host-guest doping systems by using 4-(2-(4-(diphenylamino) -phenyl)-2-oxoethyl) benzonitrile with a donor moiety (triphenylamine, TPA) and an acceptor moiety (benzonitrile) within the same molecule as a guest, and TPA and 4-(cyanomethyl) benzonitrile as a donor host and acceptor host respectively, which lead to an enhanced fluorescence ($\Phi = 63 \sim 76\%$) and RTP ($\Phi = 7.6 \sim 14.5\%$, $\tau = 119 \sim 317$ ms) under ambient conditions. In another instance, Wang et al. (2020) have successfully developed an efficient heat-responsive RTP material with three components by utilizing N,N-dimethylpyridin-4-amine as a host and a blue RTP molecule (N,N,N,N-tetramethylbenzidine as a guest, and energy acceptor (fluorescein) with phosphorescence efficiency and lifetime of up to 13.4% and 2.08 s, respectively, through the simple host-guest doping strategy. Furthermore, Wang et al. (2021b) have also developed a series of efficient pure organic RTP materials by using phenothiazine derivatives (CzS-CH_3 and CzS-C_2H_5) as guests and their corresponding dioxide derivatives (CS-CH_3 and CS-C_2H_5) as hosts, showing high phosphorescence efficiency (43%) as well as a long afterglow of up to 25 min in an aqueous environment. As can be seen from the above analysis, the phosphorescence efficiency of host-guest doping materials without heavy atoms is lower than that of RTP materials containing heavy atoms. Therefore, it remains a challenge to further improve the phosphorescent quantum efficiency of RTP materials without heavy atoms.

In the present study, we have developed a heavy atom free pure organic host-guest doped material, in which thianthrene (TTR) was selected as a guest molecule and benzophenone (BPO) as a host. TTR was selected as the guest because it contains dual-heteroatom of sulfur with abundant lone-pair electrons which can effectively facilitate the SOC and further increase the intersystem crossing (Lei et al., 2019; Zhao et al., 2020). BPO was chosen as the host due to the characteristics of low melting point, good crystallinity, and phosphorescent features. According to the literature (Chen et al., 2020; Liu et al., 2021b), the host matrix is believed to play a synergistic role in energy transfer during the phosphorescence emission of the guest molecule, so the abundant lone-pair electrons of TTR are obviously beneficial for energy transfer. The low melting point of BPO (48.5°C) promotes the preparation of the doped materials by the melt-casting method, and the good crystallinity is beneficial to provide a rigid environment for the guest molecule (Chen et al., 2020). As we expected, a series of host-guest doped crystals all showed excellent room-temperature phosphorescence (RTP). Interestingly, the multi-emission (phosphorescence) peaks of individual guest (BPO) molecules nearly became a single emission peak, especially at a 100:1 molar ratio of the host-guest doped system, which presented an efficient RTP emission with 46% quantum efficiency and a long lifetime of up to 9.17 ms under ambient conditions. This work will provide an effective way to further design new organic doping systems with RTP.

2 MATERIALS AND METHODS

Reagents and materials: Unless otherwise noted, all reagents used in the experiments were purchased from commercial sources without further purification. For flash column chromatography, silica gel with 200–300 mesh was used.

Measurements: The Steady-state luminescence, delayed luminescence spectra, and lifetimes were recorded on an Edinburgh Instruments LTD FLS1000 photoluminescence spectrometer, which is equipped with a xenon arc lamp, xenon flash lamp (μF2), picosecond pulsed diode laser (EPL), and picosecond pulsed led (EPLED). The delayed luminescence spectra were collected with a delay time of 1 or 8 ms. Photoluminescence efficiency was collected on a Hamamatsu

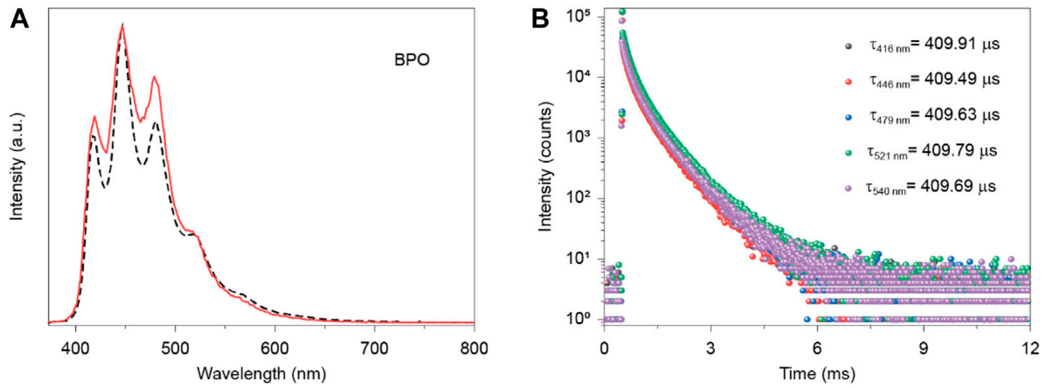

FIGURE 2 | (A) Steady-state PL (dotted line) and decay emission spectra (full line) of the host BPO in crystal excited by 383 nm. Inset image show the photograph under 365 nm UV light. **(B)** Lifetime profiles of decay emission bands at 416, 446, 479, 521 and 540 nm for the host (BPO) excited by 396 nm.

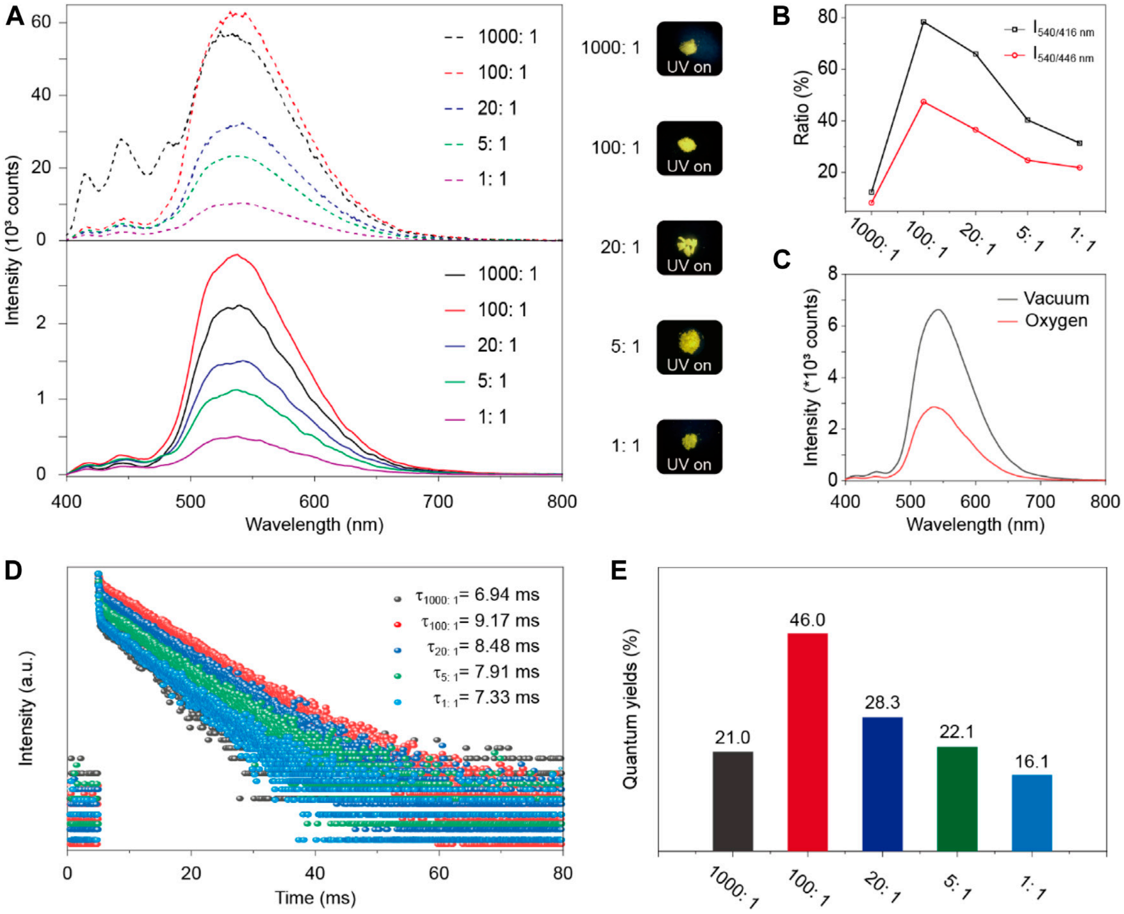

FIGURE 3 | (A) Steady-state PL (dotted line) and decay emission spectra (full line) of BPO/TTR-doped crystalline powders at different molar ratios excited by 390 nm. Insets show photographs under 365 nm UV light. **(B)** The ratio of phosphorescent intensity at 540 nm and fluorescent intensity at 416 or 446 nm of the decay emission spectra in the BPO/TTR doping system with different doping ratios. **(C)** Phosphorescence spectra of BPO/TTR composite (100:1) under oxygen and vacuum atmosphere, respectively. **(D)** Lifetime profiles of decay emission band at 540 nm for the BPO/TTR composites excited by 390 nm. **(E)** Phosphorescence quantum yields of BPO/TTR-doped materials with different molar ratios of guest (1000:1, 100:1, 20:1, 5:1 and 1:1 Mol %).

TABLE 1 | Photophysical properties of the BPO/TTR-doped materials at different molar ratios of guest.

Samples (host:guest)	λ_{em} (nm)	$\Phi_{phos.}$ (%)	τ (ms)
BPO	416	-	0.410
	446	-	0.409
	479	-	0.410
	521	-	0.410
1000:1	416	-	0.142
	446	-	0.156
	540	21%	6.94
100:1	416	-	0.233
	446	-	0.230
	540	46%	9.17
20:1	416	-	0.104
	446	-	0.105
	540	28.3%	8.48
5:1	416	-	0.089
	446	-	0.081
	540	22.1%	7.91
1:1	416	-	0.082
	446	-	0.097
	540	16.1%	7.33

Absolute PL Quantum Yield Spectrometer C11347. Luminescent photos were taken by a Canon EOS 700D camera. Powder X-Ray diffraction (XRD) patterns at room temperature were measured on an X-ray diffractometer (RIGAKU, RINT-ULTIMA III) using Cu Kα radiation (λ = 1.54051 Å). All the measurements of the photophysical properties for emissive materials are made carried out in air.

3 RESULTS AND DISCUSSIONS

The molecular structures of TTR (m. p. 151–155°C) and BPO (m. p. 48.5°C) are shown in **Figure 1A**. Their doped systems were prepared via a melt-casting method (within a temperature range of 453 K to 395 K) by taking different molar ratios of the BPO and TTR in a vacuum. The powder X-ray diffraction (XRD) patterns (**Figure 1B**) reveal that there are no significant changes in the spectra of BPO from 1000:1 to 5:1 molar ratio of BPO/TTR. However, the doped powder with 1:1 molar ratio has some new peaks but there are still all the major peaks (11.2°, 15.8°, 18.3°, 20.3°, 21.7°, 22.2°, 28.1°) of BPO in the spectra. These results suggested that the host and guest molecules are homogeneously cocrystallized in the host lattice at a low doping ratio, while at a high molar ratio of BPO (1:1), both molecules are crystallized individually.

Next, their photophysical properties were studied through steady-state photoluminescence (PL) spectra, and time-resolved emission decay curves in solid state. Pure crystalline BPO powders showed almost identical multiple peaks for steady-state photoluminescence (PL) and phosphorescence with emission peaks at 416 nm (409.91 μs), 446 nm (409.49 μs), 479 nm (409.63 μs) and a shoulder band around 521 nm (409.79 μs) under ambient conditions (**Figures 2A,B**). After doping with TTR, their blend crystalline powders exhibit a new emission band at 540 nm in both steady-state PL and phosphorescence spectra with a slight red shift of pure BPO (**Figure 3A**). Moreover, the phosphorescence spectra of blend crystalline powders became almost a single emission band at 540 nm, indicating that the energy transfer between singlet-triplet states from BPO to TTR may occur. It can significantly improve the phosphorescence properties of the doping system. (Lei et al., 2019; Lei et al., 2020) Besides, the doped materials exhibit bright yellow emission under the UV lamp excitation at 365 nm. Moreover, from the ratio of phosphorescent intensity at 540 nm and steady-state PL intensity (416 nm and 446 nm) in the BPO/TTR systems, we can find that different doping concentrations have different influences on the photophysical properties of organic room temperature phosphorescence (**Figure 3B**). Notably, compared with the phosphorescence in a vacuum, the intensity of the phosphorescence emission band around 540 nm significantly decreased in an oxygen atmosphere, indicating the phosphorescence feature.

It is noteworthy to mention that when guest molecules were doped into the host material with the molar ratio of 1:100, the characteristic steady-state PL and phosphorescence emission peaks (at 416, 446, 479, and 521 nm) of the host material (BPO) were reduced to their lowest level compared to other doped molar ratios (1:1000, 1:20, 1:5 and 1:1). Besides, the phosphorescence lifetime of all doped materials is higher than the individual host (BPO) at their maximum emission peak at 540 nm and the doped material with a 100:1 molar ratio showed the longest emission lifetime of 9.17 ms (**Table 1** and **Figure 3D**). From the performance of 1:100 doped molar ratio, it is not only indicated that the doping system does not disturb the original structure of the host which provides a suitable rigid environment, but also it can form a suitable co-crystallized system that effectively facilitates electron SOC and ISC transitions of molecules, increase the rate of intersystem crossing ($S_1 \rightarrow T_1$) and accelerate the subsequent $T_1 \rightarrow S_0$ phosphorescence processes (Qu et al., 2019).

Moreover, it was surprising to find out that the characteristic peaks of host materials almost disappeared, and a new band at 540 nm appeared after doping the guest materials. This unusual phenomenon can be initially understood by the El-Sayed rule (El Sayed, 1964; Zhou et al., 2018) that the ISC process takes place more easily due to the distinct transition pattern between singlet and triplet states. The dual-heteroatom of sulfur in TTR and carboxylic oxygen in BPO are playing a similar role as that of heavy atoms, which provide the abundant lone pair electrons to strengthen SOC and to facilitate the ISC process between $n \rightarrow \pi^*$ and $\pi \rightarrow \pi^*$ transition states according to the El-Sayed rule˙(El Sayed, 1964; Zhou et al., 2018)

The emission wavelength and quantum yield of phosphorescence can be tuned by optimizing the doping ratio of the guest (TTR) molecule. Among these experiments, the doped material with a molar ratio of 100:1 presented the highest phosphorescence quantum yields of up to 46% (**Figure 3E**), which is consistent with the declining trend of characteristic fluorescence and phosphorescence peaks of BPO, due to the spin-orbit coupling to accelerate both the $S_1 \rightarrow T_1$ and subsequent $T_1 \rightarrow S_0$ phosphorescence processes.

To gain insight into the mechanism of the highly efficient RTP for BPO/TTR composite, we conducted a series of control experiments including excitation and phosphorescence spectra of BPO, TTR, and composites, as well as luminescent lifetime

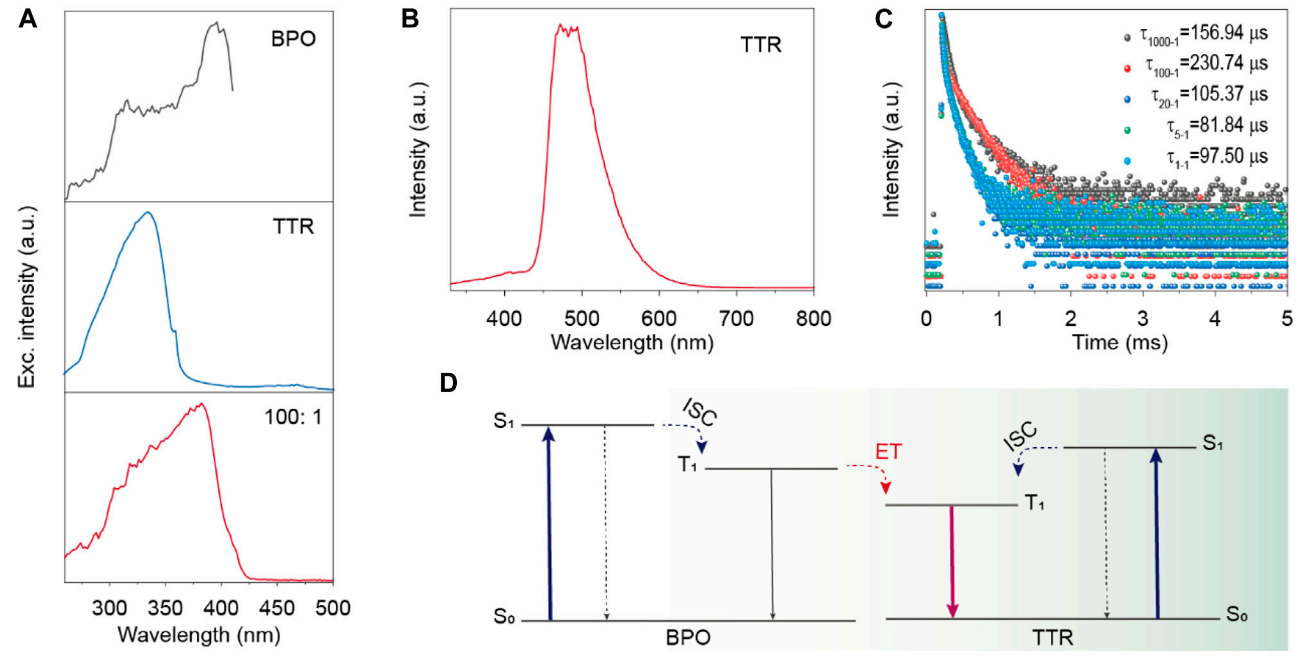

FIGURE 4 | (A) Excitation spectra of the BPO, TTR and BPO/TTR composite (1000:1) in solid state under ambient conditions. **(B)** Phosphorescence spectrum of the TTR molecules in dilute *m*-THF solution at 77 K. **(C)** Lifetime profiles of decay emission band at 446 nm for the BPO/TTR composite excited by 390 nm. **(D)** A plausible mechanism for the RTP in BPO/TTR composite.

change. From **Figure 4A**, it is easily found that the excitation spectra of the BPO and BPO/TTR doped systems were similar, which is different from that of TTR in solid state, indicating the phosphorescence emission band around 540 nm in BPO/TTR composite was related to the BPO host material. Taking the different lifetimes of the emission bands at 540 nm for BPO host and BPO/TTR composite (**Figures 2B**, **3D**) and the phosphorescence spectrum for TTR in an isolated state (**Figure 4B**) together, we concluded that the phosphorescence emission around 540 nm stemmed from the isolated TTR molecules in BPO/TTR composite. It is worth noting that the lifetimes of emission bands at 446 nm gradually decrease with the ratio of TTR guests increasing (**Figure 4C**), suggesting that there existed energy transfer from BPO host to TTR guest molecules. To sum up, the RTP was ascribed to the phosphorescence emission of the isolated TTR molecules in crystalline BPO/TTR composite (**Figure 4D**). Both crystalline molecular environment and efficient energy transfer between host and guest molecules significantly boost the phosphorescence for high efficiency.

4 CONCLUSION

In conclusion, we have developed an efficient RTP doping material based on two heavy atom free organic small molecules, benzophenone and thianthrene. The doped materials have contained different heteroatoms (TTF contains dual S atoms and BPO contains O atom) with abundant lone pair electrons, which make them promising candidates to enhance SOC, leading to an efficient ISC in pure organic metal-free RTP materials, instead of commonly used heavy atoms. We achieved an efficient RTP emission with phosphorescence efficiency of up to 46% under ambient conditions by tuning the doping molar ratio of the host and guest molecules. Our work not only provides a new approach to develop heavy atom free pure organic host-guest doped RTP materials but also expands the methods to enhance their quantum efficiency.

DATA AVAILABILITY STATEMENT

The original contributions presented in the study are included in the article/supplementary material, further inquiries can be directed to the corresponding author.

AUTHOR CONTRIBUTIONS

JC and MZ conducted the experiments. HS and JC designed the project and wrote the manuscript, MS and ZA revised the manuscript. All the authors discussed the results.

FUNDING

This work has been financially supported by the National Natural Science Foundation of China under Grants 11674018 and 21975120.

REFERENCES

Alam, P., Leung, N. L. C., Liu, J., Cheung, T. S., Zhang, X., He, Z., et al. (2020). Two Are Better Than One: A Design Principle for Ultralong-Persistent Luminescence of Pure Organics. *Adv. Mater.* 32, 2001026. doi:10.1002/adma.202001026

Bolton, O., Lee, K., Kim, H.-J., Lin, K. Y., and Kim, J. (2011). Activating Efficient Phosphorescence from Purely Organic Materials by crystal Design. *Nat. Chem.* 3, 205–210. doi:10.1038/nchem.984

Cai, S., Shi, H., Tian, D., Ma, H., Cheng, Z., Wu, Q., et al. (2018). Enhancing Ultralong Organic Phosphorescence by Effective π-Type Halogen Bonding. *Adv. Funct. Mater.* 28, 1705045. doi:10.1002/adfm.201705045

Chai, Z., Wang, C., Wang, J., Liu, F., Xie, Y., Zhang, Y.-Z., et al. (2017). Abnormal Room Temperature Phosphorescence of Purely Organic boron-containing Compounds: the Relationship between the Emissive Behaviorand the Molecular Packing, and the Potential Related Applications. *Chem. Sci.* 8, 8336–8344. doi:10.1039/c7sc04098a

Chen, Y., Xie, Y., Shen, H., Lei, Y., Zhou, Y., Dai, W., et al. (2020). Tunable Phosphorescence/Fluorescence Dual Emissions of Organic Isoquinoline-Benzophenone Doped Systems by Alkoxy Engineering. *Chem. Eur. J.* 26, 17376–17380. doi:10.1002/chem.202004291

El Sayed, M. A. (1964). Vanishing First- and Second-Order Intramolecular Heavy-Atom Effects on the (π*→n) Phosphorescence in Carbonyls. *J. Chem. Phys.* 41, 2462–2467. doi:10.1063/1.1726288

Hirata, S. (2017). Recent Advances in Materials with Room-Temperature Phosphorescence: Photophysics for Triplet Exciton Stabilization. *Adv. Opt. Mater.* 5, 1700116. doi:10.1002/adom.201700116

Kabe, R., and Adachi, C. (2017). Organic Long Persistent Luminescence. *Nature* 550, 384–387. doi:10.1038/nature24010

Lee, D. R., Lee, K. H., Shao, W., Kim, C. L., Kim, J., and Lee, J. Y. (2020). Heavy Atom Effect of Selenium for Metal-free Phosphorescent Light-Emitting Diodes. *Chem. Mater.* 32, 2583–2592. doi:10.1021/acs.chemmater.0c00078

Lei, Y., Dai, W., Tian, Y., Yang, J., Li, P., Shi, J., et al. (2019). Revealing Insight into Long-Lived Room-Temperature Phosphorescence of Host-Guest Systems. *J. Phys. Chem. Lett.* 10, 6019–6025. doi:10.1021/acs.jpclett.9b02411

Lei, Y., Dai, W., Guan, J., Guo, S., Ren, F., Zhou, Y., et al. (2020). Wide-Range Color-Tunable Organic Phosphorescence Materials for Printable and Writable Security Inks. *Angew. Chem. Int. Ed.* 59, 16054–16060. doi:10.1002/anie.202003585

Li, Q., and Li, Z. (2020). Molecular Packing: Another Key point for the Performance of Organic and Polymeric Optoelectronic Materials. *Acc. Chem. Res.* 53, 962–973. doi:10.1021/acs.accounts.0c00060

Liu, X., Pan, Y., Lei, Y., Liu, N., Dai, W., Liu, M., et al. (2021). Influence of Guest/host Morphology on Room Temperature Phosphorescence Properties of Pure Organic Doped Systems. *J. Phys. Chem. Lett.* 12, 7357–7364. doi:10.1021/acs.jpclett.1c01893

Liu, X., Dai, W., Junjie, Q., Lei, Y., Liu, M. C., Cai, Z., et al. (2021). Pure Room Temperature Phosphorescence Emission of Organic Host-Guest Doped System with Quantum Efficiency of 64%. *J. Mater. Chem. C.* 9, 3391–3395. doi:10.1039/D1TC00403D

Ma, X., Wang, J., and Tian, H. (2019). Assembling-induced Emission: an Efficient Approach for Amorphous Metal-free Organic Emitting Materials with Room-Temperature Phosphorescence. *Acc. Chem. Res.* 52, 738–748. doi:10.1021/acs.accounts.8b00620

Qu, G., Zhang, Y., and Ma, X. (2019). Recent Progress on Pure Organic Room Temperature Phosphorescence Materials Based on Host-Guest Interactions. *Chin. Chem. Lett.* 30, 1809–1814. doi:10.1016/j.cclet.2019.07.042

Shi, H., Song, L., Ma, H., Sun, C., Huang, K., Lv, A., et al. (2019). Highly Efficient Ultralong Organic Phosphorescence through Intramolecular-Space Heavy-Atom Effect. *J. Phys. Chem. Lett.* 10, 595–600. doi:10.1021/acs.jpclett.8b03712

ACKNOWLEDGMENTS

Special thanks to Beijing University of Technology and Nanjing Tech University for their technical help.

Wang, D., Wang, X., Xu, C., and Ma, X. (2019). A Novel Metal-free Amorphous Room-Temperature Phosphorescent Polymer without Conjugation. *Sci. China Chem.* 62, 430–433. doi:10.1007/s11426-018-9383-2

Wang, Y., Yang, J., Gong, Y., Fang, M., Li, Z., and Tang, B. Z. (2020). Host-guest Materials with Room Temperature Phosphorescence: Tunable Emission Color and thermal Printing Patterns. *SmartMat* 1006, 1–9. doi:10.1002/smm2.1006

Wang, D., Xie, Y., Wu, X., Lei, Y., Zhou, Y., Cai, Z., et al. (2021). Excitation-Dependent Triplet-Singlet Intensity from Organic Host-Guest Materials: Tunable Color, White-Light Emission, and Room-Temperature Phosphorescence. *J. Phys. Chem. Lett.* 12, 1814–1821. doi:10.1021/acs.jpclett.1c00188

Wang, Y., Gao., H., Yang, J., Fang, M., Ding, D., Tang, B. Z., et al. (2021). High Performance of Simple Organic Phosphorescence Host-Guest Materials and Their Application in Time-Resolved Bioimaging. *Adv. Mater.* 33, 2007811. doi:10.1002/adma.202007811

Xiong, Q., Xu, C., Jiao, N., Ma, X., Zhang, Y., and Zhang, S. (2019). Pure Organic Room-Temperature Phosphorescent N-Allylquinolinium Salts as Anti-counterfeiting Materials. *Chin. Chem. Lett.* 30, 1387–1389. doi:10.1016/j.cclet.2019.04.010

Xu, S., Chen, R., Zheng, C., and Huang, W. (2016). Excited State Modulation for Organic Afterglow: Materials and Applications. *Adv. Mater.* 28, 9920–9940. doi:10.1002/adma.201602604

Yang, Z., Mao, Z., Zhang, X., Ou, D., Mu, Y., Zhang, Y., et al. (2016). Intermolecular Electronic Coupling of Organic Units for Efficient Persistent Room-Temperature Phosphorescence. *Angew. Chem.* 128, 2221–2225. doi:10.1002/ange.201509224

Yang, J., Zhen, X., Wang, B., Gao, X., Ren, Z., Wang, J., et al. (2018). The Influence of the Molecular Packing on the Room Temperature Phosphorescence of Purely Organic Luminogens. *Nat. Commun.* 9, 840. doi:10.1038/s41467-018-03236-6

Zhang, Z. Y., Chen, Y., and Liu, Y. (2019). Efficient Room-Temperature Phosphorescence of a Solid-State Supramolecule Enhanced by Cucurbit[6]uril. *Angew. Chem. Int. Ed.* 58, 6028–6032. doi:10.1002/anie.201901882

Zhang, X., Du, L., Zhao, W., Zhao, Z., Xiong, Y., He, X., et al. (2019). Ultralong UV/mechano-excited Room Temperature Phosphorescence from Purely Organic Cluster Excitons. *Nat. Commun.* 10, 5161. doi:10.1038/s41467-019-13048-x

Zhao, W., He, Z., and Tang, B. Z. (2020). Room-temperature Phosphorescence from Organic Aggregates. *Nat. Rev. Mater.* 5, 869–885. doi:10.1038/s41578-020-0223-z

Zhou, C., Zhang, S., Gao, Y., Liu, H., Shan, T., Liang, X., et al. (2018). Ternary Emission of Fluorescence and Dual Phosphorescence at Room Temperature: a Single-Molecule white Light Emitter Based on Pure Organic Aza-Aromatic Material. *Adv. Funct. Mater.* 28, 1802407. doi:10.1002/adfm.201802407

Conflict of Interest: The authors declare that the research was conducted in the absence of any commercial or financial relationships that could be construed as a potential conflict of interest.

frontiers
in Chemistry

ORIGINAL RESEARCH
published: 13 January 2022
doi: 10.3389/fchem.2021.812593

Modulating Room-Temperature Phosphorescence-To-Phosphorescence Mechanochromism by Halogen Exchange

*Yoshika Takewaki, Takuji Ogawa and Yosuke Tani**

Department of Chemistry, Graduate School of Science, Osaka University, Toyonaka, Japan

Modulating the stimulus-responsiveness of a luminescent crystal is challenging owing to the complex interdependent nature of its controlling factors, such as molecular structure, molecular conformation, crystal packing, optical properties, and amorphization behavior. Herein, we demonstrate a halogen-exchange approach that disentangles this problem, thereby realizing the modulation of room-temperature phosphorescence-to-phosphorescence mechanochromism. Replacing the bromine atoms in a brominated thienyl diketone with chlorine atoms afforded isostructural crystals; i.e., molecules with different halogen atoms exhibited the same molecular conformation and crystal packing. Consequently, amorphization behavior toward mechanical stimulation was also the same, and the phosphorescence of amorphous states originated from the same conformer of each diketone. In contrast, the phosphorescence properties of each conformer were modulated differently, which is ascribable to heavy atom effects, resulting in the modulation of the mechanochromism. Thus, halogen exchange is a promising approach for modulating the stimulus-responsive photofunctions of crystals involving spin-forbidden processes.

Keywords: mechanochromism, heavy atom effects, isostructural crystals, amorphous, halogen exchange, room-temperature phosphorescence, metal-free

Edited by:
Wang Zhang Yuan,
Shanghai Jiao Tong University, China

Reviewed by:
Zhijian Wang,
Beihang University, China
Huili Ma,
Nanjing Tech University, China
Tomohiro Seki,
Shizuoka University, Japan

****Correspondence:***
Yosuke Tani
y-tani@chem.sci.osaka-u.ac.jp

Specialty section:
This article was submitted to Physical Chemistry and Chemical Physics,
a section of the journal Frontiers in Chemistry

Received: *10 November 2021*
Accepted: *10 December 2021*
Published: *13 January 2022*

Citation:
Takewaki Y, Ogawa T and Tani Y (2022) Modulating Room-Temperature Phosphorescence-To-Phosphorescence Mechanochromism by Halogen Exchange. Front. Chem. 9:812593. doi: 10.3389/fchem.2021.812593

INTRODUCTION

Mechanochromic luminescence is a phenomenon in which the luminescence color changes when mechanical stimulus is applied and is recovered by other external stimuli, such as heat (Sagara et al., 2016; Ito, 2021). Such phenomena have received significant interest not only because they visualize otherwise invisible force histories, but also because of their mechanism involved in transducing macroscopic force to the molecular level. Basically, the color change is due either to a change in the molecular environment, the intermolecular arrangement, the molecular conformation, or a combination thereof.

Phosphorescent organic molecules are particularly promising mechanochromic materials because phosphorescence is highly sensitive to changes in the molecular environment (Xue et al., 2016; Huang et al., 2020). Phosphorescence is a spin-forbidden form of luminescence that involves a change in the spin multiplicity. Unlike metal complexes, such as Ir and Pt, which benefit from the heavy atom effect that accelerates spin-forbidden processes, metal-free organic molecules seldom show room-temperature phosphorescence (RTP) (Hirata, 2017; Kenry et al., 2019). However, the crystalline states of some metal-free organic molecules were reported to exhibit RTP as early as 1939

(Clapp, 1939; Bilen et al., 1978). More recently, significant interest has been directed toward "crystallization-induced phosphorescence" (CIP) following the seminal report published in 2010 by Tang et al. (Yuan et al., 2010) A rigid environment is generally regarded to be crucial for observing RTP from a metal-free organic molecule; otherwise, RTP is quenched by molecular motions (Baroncini et al., 2017). Indeed, the conventional RTP of an organic crystal is quenched by applying mechanical stimulation, which amorphizes the crystal. While such mechanoresponsive RTP turn-off behavior has been used to achieve RTP-to-fluorescence mechanochromism, (Gong et al., 2015; Mao et al., 2015; Xu et al., 2017; He et al., 2019; Huang et al., 2019; Ma et al., 2019; Wang et al., 2019a; Liu et al., 2021a; Liu et al., 2021b) the RTP mechanoresponse is largely limited to the turn-off type, with a molecular design that modulates mechanochromic RTP behavior remaining elusive.

To establish design principles for mechanochromism, two types of structure–mechanochromic-property relationship are important: the molecular-structure–property and the crystal-structure–property relationship. However, in many cases, the molecular structure and crystal structure are strongly interdependent, which prevents revealing the essential causal relationship. Polymorphic crystals, in which the same molecule forms different crystal structures, provide practical bases for studying the crystal-structure–property relationship (Wang and Li, 2017). On the other hand, the molecular-structure–property relationship can be elucidated when different molecules form isostructural crystals; i.e., crystals with the same space group, lattice constants, crystal packing, and molecular conformations (Fábián and Kálmán, 1999; Kálmán et al., 1993). The differences in isostructural crystal structures are so small that they usually do not disturb the properties derived from the molecular structure itself.

Previously, we reported the thienyl diketone **BrTn** (**Figure 1A**), the first metal-free organic molecule to exhibit RTP-to-RTP mechanochromism (Tani et al., 2019); in contrast to RTP quenching observed for conventional organic phosphors, mechanical stimulation amorphizes the **BrTn** crystals, resulting in RTP color change. Detailed investigations revealed that mechanical stimulus turns off the initial RTP (from a skew conformer) while providing a small amount of the highly emissive trans-planar (TP) conformer. In addition, we desymmetrized the C_2-symmetrical **BrTn** structure. (Tani et al., 2020; Komura et al., 2021) Notably, replacing one of the two Br atoms with a hydrogen atom led to the formation of a crystal that is isostructural with that of **BrTn** (Tani et al., 2020). Interestingly, the crystal of the unsymmetrical diketone was non-emissive, which was attributed to the presence of voids that result from the volumetric difference between Br and H (**Figure 1B** top). Hence, the difference in the crystal structures were highly localized, facilitating the stringent crystal-structure–property relationship study.

Herein, we report the first RTP-to-RTP mechanochromism modulated by halogen-atom exchange. We envisaged that halogen-atom exchange in **BrTn** (e.g., bromine to chlorine) would afford isostructural crystals (Reddy et al., 2006; Saidykhan et al., 2021; He et al., 2017; Wen et al., 2019; Lai et al., 2021) that retained the mechanoresponsive nature of **BrTn**, as observed for our previous system (**Figure 1B** top). On the other hand, altering the heavy atoms is expected to affect the molecular phosphorescence properties, thereby modulating the responsiveness to RTP color. Heavy atom effect—the enhancement of the rate of a spin-forbidden process by the presence of an atom of high atomic number—has been widely used to modulate or achieve phosphorescence from metal-free organic molecules. (He et al., 2017; Wen et al., 2019; Lai et al., 2021; Wang et al., 2019b; Liao et al., 2021) With these aims in mind, we designed new diketone **ClTn**, in which the Br atoms in **BrTn** are replaced with Cl atoms (**Figure 1B** bottom). As a result, the fundamental stimulus-responsive nature of **BrTn** is retained, while the sensitivities of RTP color to mechanical/thermal stimuli are modulated. Our study demonstrates the usefulness of the halogen-exchange strategy for modulating the stimulus-responsive photofunctions of crystals that involve spin-forbidden processes.

EXPERIMENTAL SECTION

Instrumentation and Chemicals

^{1}H and ^{13}C{^{1}H} NMR spectra were recorded on a JEOL ECS400 spectrometer. Chemical shift values (δ) are reported in ppm and are calibrated to tetramethylsilane (0.00 ppm) for ^{1}H and to $CDCl_3$ (77.0 ppm) for ^{13}C NMR. Melting points were measured between cover glasses with Yanaco MP-S3. Elemental analysis (EA) was conducted on a Yanaco MT-6 recorder. Analytical thin-layer chromatography (TLC) was performed on aluminum plates bearing a layer of Merck silica gel 60 F_{254}. Column chromatography was carried out on silica-gel 60N (Kanto Chemical Co., Inc., spherical, 63–210 μm). Unless otherwise noted, chemicals were obtained from commercial suppliers and used without further purification.

Synthesis of ClTn

To a heat gun-dried Schlenk flask under Ar were added **BrTn** (69.9 mg, 0.101 mmol) (Tani et al., 2019), copper chloride (I) (50.2 mg, 0.507 mmol), and *N,N*-dimethylformamide/*o*-dichlorobenzene (3:1, 2.4 ml). The solution was degassed by typical freeze-pump-thaw cycling three times. Then, the mixture was stirred at 140°C overnight, quenched by adding aq. NH_4Cl, and extracted with $CHCl_3$ (10 ml × 3). The combined organic extracts were washed with aq. NH_4Cl (10 ml × 2) and water (10 ml × 2), dried over $MgSO_4$, and concentrated under reduced pressure. The crude product was passed through a silica-gel column (eluent: $CHCl_3$), and all the volatiles were removed. The residue was further purified in refluxing MeOH (5 ml) at 75°C (bath temperature) for 20 min, and then filtered at room temperature. The solid was then suspended in hexane (2 ml) and refluxed at 80°C (bath temperature) for 20 min, cooled in a freezer, and filtered to give 34.5 mg (57.1 μmol, 57%) of **ClTn** as a yellowish-white powder. **m. p.** 156–158°C. **^{1}H NMR** (400 MHz, $CDCl_3$) δ: 7.17 (2H, s), 1.38 (6H, sep, *J* = 7.3 Hz), 1.12 (36H, d, *J* = 7.3 Hz). **^{13}C NMR** (100 MHz, $CDCl_3$) δ: 182.21, 148.75, 137.33, 134.64, 133.89, 18.38, 11.51. **EA** Calcd for $C_{28}H_{44}Cl_2O_2S_2Si_2$: C, 55.69; H, 7.34. Found: C, 55.79; H, 7.41.

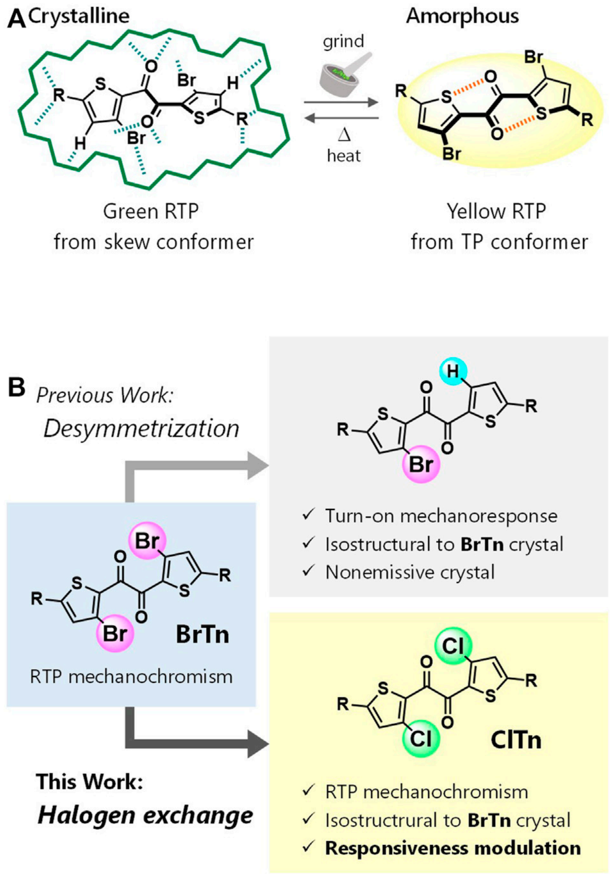

FIGURE 1 | (A) Schematic depicting the RTP-to-RTP mechanochromism of **BrTn**. Green hashed lines represent intermolecular interactions, whereas orange ones represent intramolecular chalcogen bonds. **(B)** Molecular design for modulating mechanoresponsive RTP. R, triisopropylsilyl.

Single-Crystal X-Ray Structure Analysis of ClTn

A single-crystal of **ClTn** suitable for X-ray structure analysis was obtained by a liquid-liquid diffusion of $CHCl_3$/MeOH solution. Data were collected on a Rigaku XtaLab P200 diffractometer with graphite monochromated MoKα radiation (λ = 0.71075 Å) in the ω-scan mode. The crystals were cooled by a stream of cold N_2 gas. Collection, indexing, peak integration, cell refinement, and scaling of the diffraction data were performed using the CrystalClear software (Rigaku). The structures were solved by direct methods (SIR97) and refined by full-matrix least-square refinement on F^2 (SHELXL2014). The non-hydrogen atoms were refined anisotropically. All hydrogen atoms were placed on the calculated positions and refined using the riding model. The crystallographic data have been deposited at the Cambridge Crystallographic Data Centre (CCDC) under deposition number CCDC-2119698, and can be obtained free of charge via www.ccdc.cam.ac.uk/data_request/cif.

Preparing and Characterizing ClTn-G and ClTn-Y

Typical procedure: to a stirred solution of **ClTn** (70.2 mg) in $CHCl_3$ (4 ml) was added dropwise MeOH (30 ml). The precipitate was collected by vacuum filtration and washed with MeOH to obtain **ClTn-G**, which was then uniformly ground for 1 hour with an agate mortar and pestle to give **ClTn-Y**. The materials were characterized at room temperature in air. The steady-state photoluminescence (PL) spectra of **ClTn-G** and **ClTn-Y** were acquired using a JASCO FP-8200 spectrofluorometer with an L37 sharp-cut filter (HOYA, long pass, >370 nm) and a U340 band-pass filter (HOYA). Powder X-ray diffraction (PXRD) patterns were collected on a Rigaku MiniFlex 600 diffractometer with CuKα radiation (λ = 1.5418 Å). The PL quantum yields of **ClTn-G** and **ClTn-Y** were determined by the absolute method using a Hamamatsu photonics C11347-01 spectrometer augmented with an integrating sphere while excited at (λ_{ex}) 368 nm. The PL decay curves were acquired with a HORIBA DeltaFlex multichannel scaling system using a DeltaDiode for excitation (368 nm). The PL intensity decay curves were recorded at 520 nm for **ClTn-G** and 560 nm for **ClTn-Y**. The area-weighted average lifetimes τ were determined with EzTime software (HORIBA) using a single-exponential fit for **ClTn-G** and a double-exponential fit for **ClTn-Y**.

Evaluating Reversibility and Sensitivity

To evaluate reversibility of mechano/thermochromism and heat-induced recovery, **ClTn-G** was placed between two quartz plates and rubbed for 1 min, after which the PL spectrum was acquired (λ_{ex} = 320 nm). The plates were placed on a preheated copper plate and heated on a hot plate (IKA C-MAG HS 7) for 1 h, with the temperature of the copper plate maintained at 138–143°C. The sample was cooled to room temperature while on the plate (with the heater turned off), after which the PL spectrum was acquired (λ_{ex} = 320 nm). This treatment protocol was repeated four times to test repeatability. PL spectral change was evaluated as the color change ratio: First, the normalized difference in intensity $D = (I_{520} - I_{560})/(I_{520} + I_{560})$ was determined for each spectrum to provide the relative intensity of the skew/TP emission, where I_x is the intensity at x nm. The color change ratio was then calculated as $(D - D_G)/(D_Y - D_G) \times 100$ (%), where D_G and D_Y are the D values for the **ClTn-G** and **ClTn-Y**, respectively. All photographic images were acquired using a SONY NEX-5N camera while irradiated with a hand-held UV light (365 nm). Temperature was controlled in a similar manner to evaluate sensitivity toward thermal stimulation. The recovery ratio is defined as $(D - D_{h0})/(D_G - D_{h0}) \times 100$ (%), where D_{h0} is the D value for sample h0 (**ClTn-G** rubbed for 1 min between two quartz plates). The color change and recovery ratios of **BrTn** were determined using I_{570} instead of I_{560}.

Constructing the Φ_P-Weighted PL Spectrum of ClTn-Y

The spectrum of **ClTn-G**, which is purely derived from the skew conformer, was subtracted from that of **ClTn-Y** after normalizing the intensity at λ_{max} (the emission maximum) of **ClTn-G**. The

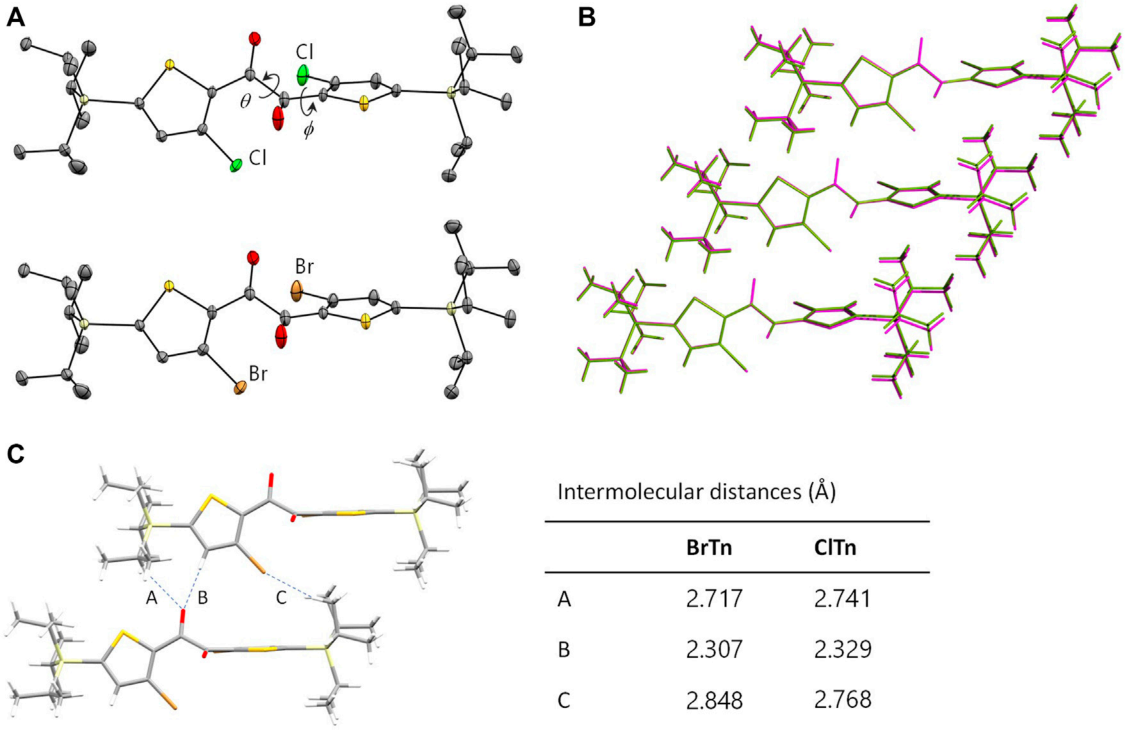

Intermolecular distances (Å)

	BrTn	ClTn
A	2.717	2.741
B	2.307	2.329
C	2.848	2.768

FIGURE 2 | (A) ORTEP drawings of the X-ray crystal structures of **ClTn (top)** and **BrTn (bottom)**. Hydrogen atoms are omitted for clarity and the thermal ellipsoids are set at the 50% probability level. **(B)** Overlaying three successive molecules in the crystals of **ClTn** (green) and **BrTn** (magenta). **(C)** Intermolecular short contact distances (Å) found in the crystal structures of **BrTn** and **ClTn**.

TABLE 1 | Crystallographic data for **ClTn** and **BrTn**.

	Space group	*a*/Å	*b*/Å	*c*/Å	*α*/o	*β*/o	*γ*/o	*θ*/o	*ϕ*/o
ClTn	*C2/c*	12.0873(13)	9.4966(10)	27.677(3)	90	91.255(3)	90	114.0(1)	−19.1(2)
BrTn	*C2/c*	12.0795(9)	9.5698(6)	27.9836(17)	90	92.019(7)	90	109.5(2)	−17.2(3)

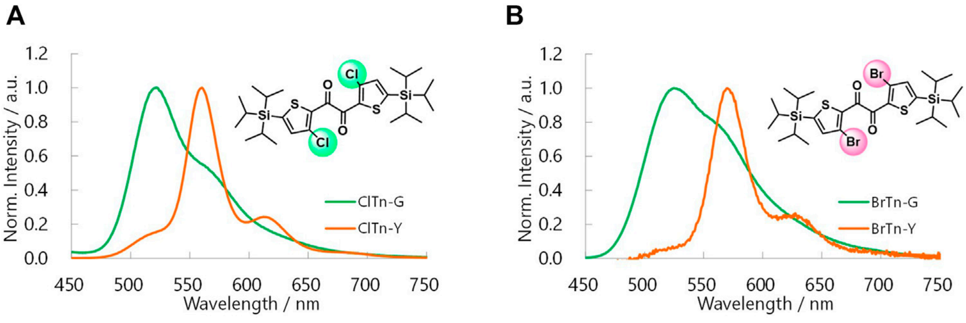

FIGURE 3 | Steady-state PL spectra of **(A) ClTn** and **(B) BrTn** at room temperature in air. λ_{ex} = 320 and 360 nm for the G and Y phase samples, respectively.

difference spectrum corresponds to the pure PL spectrum of the TP conformer. The difference spectrum and the spectrum of **ClTn-G** were multiplied by α_Y = [Φ_p of **BrTn-Y**]/[Φ_p of **ClTn-Y**] and α_G = [Φ_p of **BrTn-G**]/[Φ_p of **ClTn-G**], respectively, and summed to construct the Φ_p-weighted PL spectrum of **ClTn-Y**.

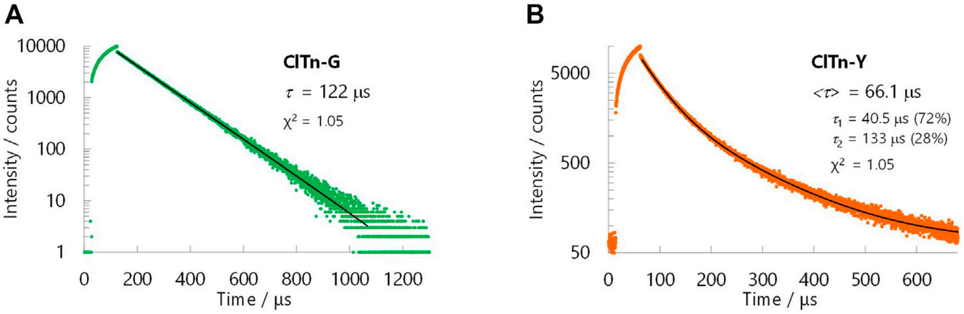

FIGURE 4 | PL decay curves for **(A) ClTn-G** and **(B) ClTn-Y** at room temperature in air. The black lines are fitted curves. PL intensities were recorded at 520 nm for **ClTn-G** and 560 nm for **ClTn-Y** (λ_{ex} = 368 nm). The bracketed lifetime $<\tau>$ is the area-weighted lifetime.

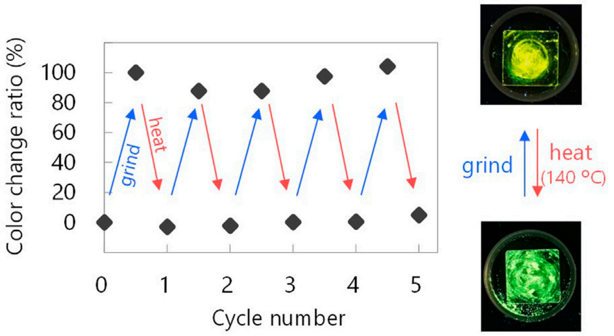

FIGURE 5 | Showing reversibility of the mechano/thermoresponsive RTP chromism of **ClTn**. Photographic images were acquired under UV light (365 nm). See Experimental Section for definition of the color change ratio.

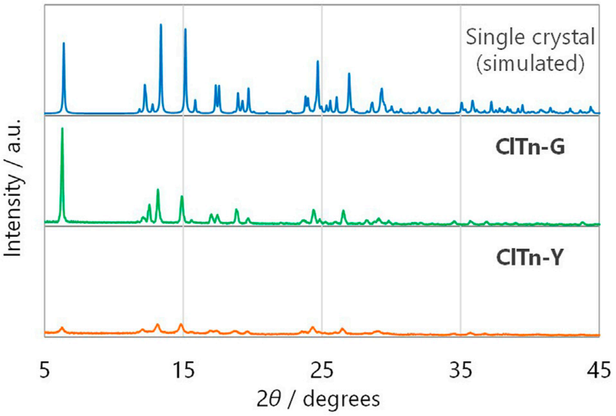

FIGURE 6 | Powder X-ray diffraction patterns of (from **top** to **bottom**) single-crystals of **ClTn** (simulated), **ClTn-G**, and **ClTn-Y**.

RESULTS AND DISCUSSION

Diketone **ClTn** was synthesized by reacting **BrTn** with CuCl. The X-ray structure of a single-crystal of **ClTn** revealed that it is isostructural to that of **BrTn** (CCDC), with superimposable molecular geometries, the same space group, and very similar lattice constants (**Figure 2** and **Table 1**). The conformation of aromatic 1,2-diketones is well represented by two torsion angles: the vicinal-dicarbonyl torsion angle θ and the thiophene–carbonyl torsion angle ϕ (Mukai et al., 1992; Singh et al., 2002). A comparison of these angles in **ClTn** and **BrTn** highlights their almost identical crystal conformations (θ: 114.0(1) vs. 109.5(2)°; ϕ: −19.1(2) vs. −17.2(3)°). In addition, the diketones have three kinds of intermolecular interactions (a total of 12 interactions from one molecule), which are also comparable in both systems due to their identical crystal packing (**Figure 2C**). Hence, these isostructural crystals provide both conformationally and environmentally consistent systems that are ideal for investigating structure–property relationships.

ClTn was found to exhibit RTP-to-RTP mechanochromism in a qualitatively similar manner to **BrTn** (Tani et al., 2019); the RTP color changed from green (G-phase) to yellow (Y-phase) upon grinding. To investigate these photophysical properties in detail, we prepared samples of **ClTn-G** and **ClTn-Y**; **ClTn-G** is a crystalline powder reprecipitated from $CHCl_3$/MeOH, while **ClTn-Y** was prepared by uniformly grinding **ClTn-G** using an agate mortar and a pestle (see Experimental Section for details). The photoluminescence (PL) emission maximum of **ClTn-Y** (λ_{PL} = 560 nm) was observed to be redshifted by ~40 nm compared to that of **ClTn-G** (λ_{PL} = 522 nm) (**Figure 3A**). By comparing the behavior of **BrTn** with that of **ClTn** (**Figure 3B**), (Tani et al., 2019) we conclude that the PL spectrum of **ClTn-Y** consists of an emerging emission from the TP conformer and a remaining small emission from the skew conformer (vide infra). The PL lifetimes of **ClTn-G** and **ClTn-Y** were determined to be 66 and 122 μs, respectively, without any nanosecond-order decay component, confirming that these are phosphorescence emissions (**Figure 4**). Moreover, the yellow RTP of **ClTn-Y** returned to green upon heating (**Figure 5**); this color-change cycle was repeated for five-times, thereby demonstrating reversible mechano/thermoresponsiveness. The observed RTP mechanochromism is based on crystal amorphization, because the PXRD pattern of **ClTn-G** reveals sharp diffraction peaks, while that of **ClTn-Y** shows peak broadening (**Figure 6**). Overall, the RTP-to-RTP mechanochromism of **BrTn** was well reproduced by **ClTn**;

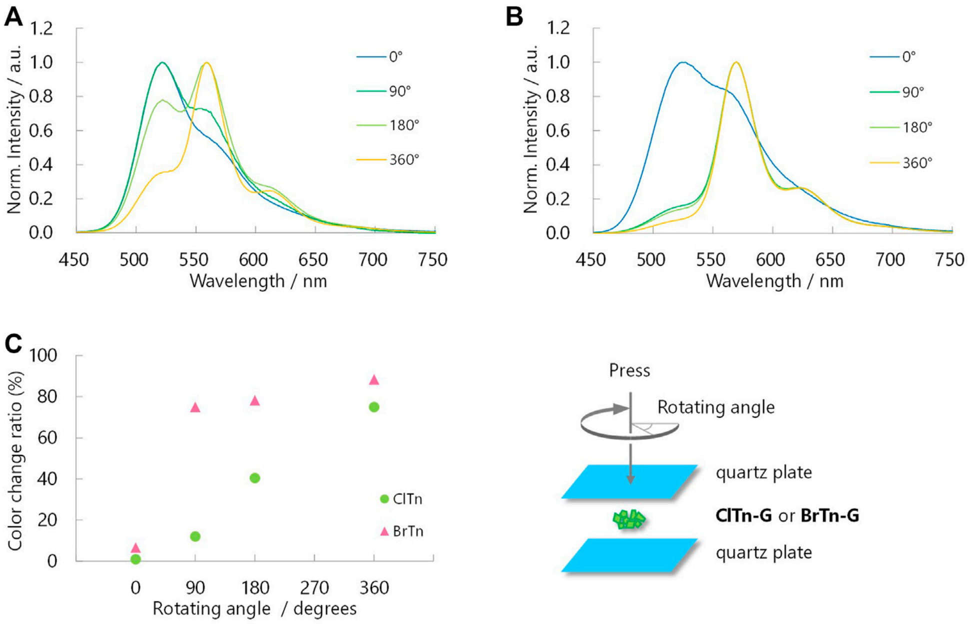

FIGURE 7 | Normalized PL spectra of **(A) ClTn-G** and **(B) BrTn-G** upon mechanical stimulation (λ_{ex} = 320 nm). Angles in the legends are the rotating angles as depicted in the bottom right. **(C)** Sensitivity of RTP color to mechanical stimulation. See Experimental Section for definition of the color change ratio.

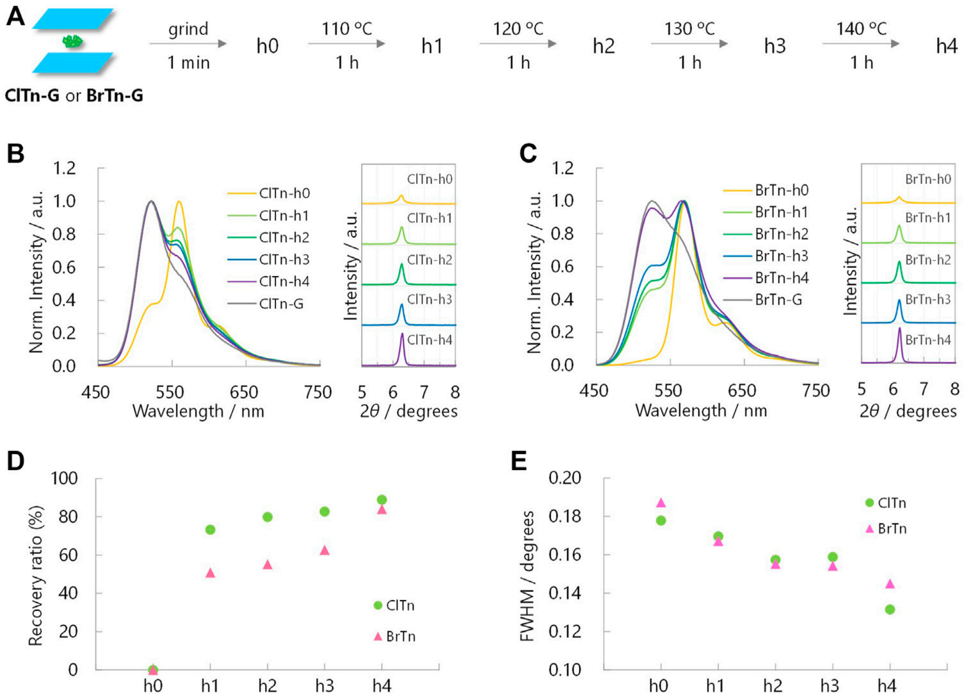

FIGURE 8 | (A) Sample preparation for heat-induced-recovery experiments. **(B, C)** Normalized PL spectra **(left,** λ_{ex} = 320 nm) and corresponding PXRD profiles **(right)** of **(B) ClTn-Y** and **(C) BrTn-Y** upon heating. **(D)** Sensitivity of the RTP color and **(E)** FWHMs of the PXRD peaks at 2θ = ~6° toward the thermal stimulation. See Experimental Section for definition of the recovery ratio.

TABLE 2 | Phosphorescence maxima, quantum yields, and lifetimes.

	λ_p/nm	Φ_p (%)	τ/μs
ClTn-G	522	1.7	122
BrTn-G	527	3.9	103
ClTn-Y	560	1.4	66
BrTn-Y	571	10	51

however, close inspection revealed notable differences in stimulus-responsiveness that are compared and mechanistically rationalized below.

Despite its isostructural nature, the RTP color of **ClTn** responds to mechanical stimulus more slowly than that of **BrTn**. For comparison, crystalline powder (**ClTn-G** or **BrTn-G**) was placed between two quartz plates, ground by rotating the upper plate while being pressed, with PL spectra acquired at rotating angles of 0, 90, 180, and 360° (**Figure 7**). The RTP color of **ClTn** changed gradually; the relative intensity of the emission from the TP conformer (λ_{PL} = 560 nm) continuously increased with the application of the mechanical stimulus. On the other hand, the TP emission of **BrTn** emerged rapidly; its RTP color changed dramatically during the first quarter turn and remained almost unchanged thereafter (**Figure 7C**). These results may seem to suggest that **BrTn-G** is more easily amorphized than **ClTn-G**; however, we note that what responds faster in **BrTn** is the RTP color, for which the ease of amorphization is just one of the possible factors. Evaluating/monitoring the rate of amorphization (loss of crystallinity) during mechanical stimulation is difficult because the preferred orientation may also affect the PXRD peak, the full-width at half-maximum (FWHM) of which is a measure of crystallinity, and can be alleviated by mechanical stimulation.

Monitoring the heat-induced recovery from the Y phase to the G phase is expected to provide a better understanding of the crystallinity–RTP color relationship, as heating does not disturb the orientation of the powder. With this in mind, PL spectra and PXRD profiles were acquired after heating the Y phase samples (h0) at the temperatures and times indicated in **Figures 8A–C**. In contrast to the mechanical response observed for **ClTn**, its PL spectrum responded faster to temperature than the spectrum of **BrTn**. More interestingly, **ClTn** and **BrTn** exhibited the same crystallinity response; the FWHMs of the PXRD peaks at $2\theta = 6°$ were observed to decrease at the same rate (**Figures 8D,E**). These results indicate that, while the crystallinity of the powder is important for determining the RTP color, the stimulus-responsiveness of RTP color is not associated with ease of amorphization.

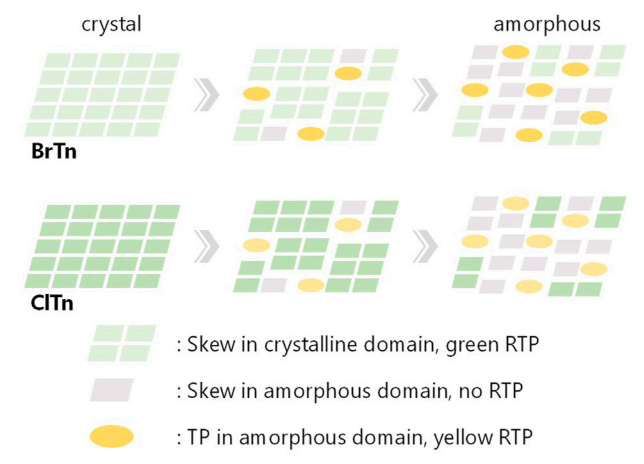

FIGURE 10 | Schematic representation of the proposed mechanism for different mechanoresponse of RTP color, describing the change in conformation and RTP color along amorphization. The relative color depth represents relative PL efficiency.

We hypothesize that the difference in the stimulus-responsiveness of the RTP color originates from a conformation-dependent heavy atom effect. To test this hypothesis, we determined the phosphorescence quantum yields Φ_p of each compound/phase and constructed the Φ_p-weighted PL spectrum of **ClTn-Y**. As expected from the weaker heavy atom effect of Cl compared to Br, the Φ_p of **ClTn** is smaller than that of **BrTn** (**Table 2**). Interestingly, the amorphous Y phase exhibited a larger quantum yield ratio (α = [Φ_p of **BrTn**]/[Φ_p of **ClTn**]) than the crystalline G phase, implying that the extent of the heavy atom effect depends on conformation. Next, we subtracted the PL spectrum of **ClTn-G**, which is purely derived from the skew conformer, from that of **ClTn-Y** (**Figure 9A**). The difference spectrum corresponds to the pure PL spectrum of the TP conformer. Indeed, other PL spectra of **ClTn** with partial amorphization (e.g., 180° in **Figure 7A**) can be reconstructed from the obtained spectra of the skew and TP conformers (**Figure 9B**), which indicates that the PL spectra are

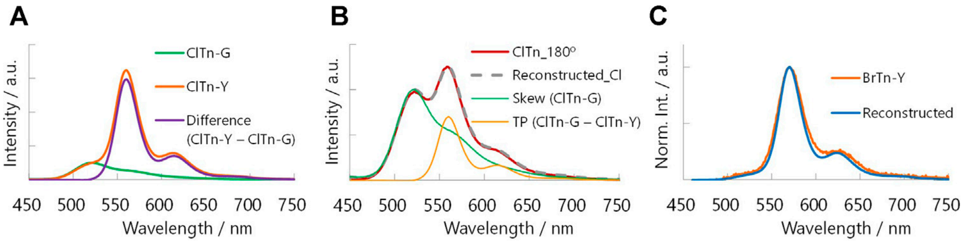

FIGURE 9 | (A) Deconvolution of the PL spectrum of **ClTn-Y** (orange) by subtracting that of **ClTn-G** (green). **(B)** Reconstructing the PL spectrum of partially ground **ClTn** (red, 180° in **Figure 7A**) from those of the skew (green) and TP conformer (orange). **(C)** Reconstructed Φ_p-weighted PL spectrum of **ClTn-Y** (blue, shifted by −10 nm) and the PL spectrum of **BrTn-Y** (orange).

composed of the two emissions. Finally, we corrected the PL spectrum of **ClTn-Y** by multiplying the spectra of each conformer by α and then recombining them. The Φ_P-weighted PL spectrum of **ClTn-Y** (**Figure 9C**, blue trace) obtained in this manner matches the PL spectrum of **BrTn-Y**; therefore, we concluded that the conformational composition of amorphous **ClTn-Y** is similar to that of **BrTn-Y**, and that the differences in spectral shape are attributable to the difference in PL efficiency. A proposed mechanism for the different stimulus-responsivenesses of RTP color is described in **Figure 10**. Even though the ease of amorphization is similar as expected for the isostructural crystals, different PL efficiency (represented by color depth) makes the RTP color response different. Upon amorphization, the PL quantum yields are increased in **BrTn-G/Y** (3.9/10%) while slightly decreased in **ClTn-G/Y** (1.7/1.4%) (**Table 2**). Thus, the mechanoresponse in the RTP color is different. We emphasize that, in the present system, isostructural crystals exhibited a similar amorphization behavior, enabling the stimulus-responsiveness of the bulk solid to be modulated by tuning the molecular properties.

CONCLUSION

The RTP-to-RTP mechanochromism of a thienyl diketone was successfully modulated by Br-to-Cl halogen exchange. Modulating the molecular structure does not disturb the crystal structure, with both diketones forming isostructural crystals. The stimuli-responsiveness of the crystallinity is also retained, as evidenced by PXRD peak widths. In contrast, relative RTP efficiency is affected, which is ascribable to a conformation-dependent heavy-atom effect. Consequently, we were able to successfully modulate the stimulus-responsiveness of RTP color. We are currently investigating the conformation-dependent heavy atom effect, which will be reported in due course.

DATA AVAILABILITY STATEMENT

The datasets presented in this study can be found in online repositories. The names of the repository is Cambridge Crystallographic Data Centre. Following are the accession numbers CCDC-2119698 CCDC-1906440.

AUTHOR CONTRIBUTIONS

YT (last author) conceived the idea and designed research. YT (1st author) synthesized and characterized the materials. All authors analysed data and wrote the paper. All authors contributed to the article and approved the submitted version.

FUNDING

This work was financially supported by JSPS KAKENHI (grant number JP19K15542). YT is grateful to the Chubei Itoh Foundation, the ENEOS Tonengeneral Research/Development Encouragement and Scholarship Foundation, and the Izumi Science and Technology Foundation for financial support. The authors declare that this study received funding from The Toyota Physical and Chemical Research Institute. This funder was not involved in the study design, collection, analysis, interpretation of data, the writing of this article or the decision to submit it for publication.

ACKNOWLEDGMENTS

Theoretical calculations were performed at the Research Center for Computational Science, Okazaki, Japan. Some of experiments were performed at the Analytical Instrument Facility, Graduate School of Science, Osaka University.

SUPPLEMENTARY MATERIAL

The Supplementary Material for this article can be found online at: https://www.frontiersin.org/articles/10.3389/fchem.2021.812593/full#supplementary-material

REFERENCES

Baroncini, M., Bergamini, G., and Ceroni, P. (2017). Rigidification or Interaction-Induced Phosphorescence of Organic Molecules. *Chem. Commun.* 53, 2081–2093. doi:10.1039/c6cc09288h

Bilen, C. S., Harrison, N., and Morantz, D. J. (1978). Unusual Room Temperature Afterglow in Some Crystalline Organic Compounds. *Nature* 271, 235–237. doi:10.1038/271235a0

Clapp, D. B. (1939). The Phosphorescence of Tetraphenylmethane and Certain Related Substances. *J. Am. Chem. Soc.* 61, 523–524. doi:10.1021/ja01871a504

Fábián, L., and Kálmán, A. (1999). Volumetric Measure of Isostructurality. *Acta Crystallogr. Sect B* 55, 1099–1108. doi:10.1107/S0108768199009325

Gong, Y., Chen, G., Peng, Q., Yuan, W. Z., Xie, Y., Li, S., et al. (2015). Achieving Persistent Room Temperature Phosphorescence and Remarkable Mechanochromism from Pure Organic Luminogens. *Adv. Mater.* 27, 6195–6201. doi:10.1002/adma.201502442

He, Z., Zhao, W., Lam, J. W. Y., Peng, Q., Ma, H., Liang, G., et al. (2017). White Light Emission from a Single Organic Molecule with Dual Phosphorescence at Room Temperature. *Nat. Commun.* 8, 416. doi:10.1038/s41467-017-00362-5

He, G., Du, L., Gong, Y., Liu, Y., Yu, C., Wei, C., et al. (2019). Crystallization-Induced Red Phosphorescence and Grinding-Induced Blue-Shifted Emission of a Benzobis(1,2,5-Thiadiazole)-Thiophene Conjugate. *ACS Omega* 4, 344–351. For recent examples of mechanoresponsive organic molecules involving RTP turn-off, see. doi:10.1021/acsomega.8b02805

Hirata, S. (2017). Recent Advances in Materials with Room-Temperature Phosphorescence: Photophysics for Triplet Exciton Stabilization. *Adv. Opt. Mater.* 5, 1700116. doi:10.1002/adom.201700116

Huang, L., Liu, L., Li, X., Hu, H., Chen, M., Yang, Q., et al. (2019). Crystal-State Photochromism and Dual-Mode Mechanochromism of an Organic Molecule with Fluorescence, Room-Temperature Phosphorescence, and Delayed Fluorescence. *Angew. Chem. Int. Ed.* 58, 16445–16450. doi:10.1002/anie.201908567

Huang, L., Qian, C., and Ma, Z. (2020). Stimuli-Responsive Purely Organic Room-Temperature Phosphorescence Materials. *Chem. Eur. J.* 26, 11914–11930. doi:10.1002/chem.202000526

Ito, S. (2021). Recent Advances in Mechanochromic Luminescence of Organic Crystalline Compounds. *Chem. Lett.* 50, 649–660. doi:10.1246/cl.200874

Kálmán, A., Párkányi, L., and Argay, G. (1993). Classification of the Isostructurality of Organic Molecules in the Crystalline State. *Acta Crystallogr. Sect B* 49, 1039–1049. doi:10.1107/S010876819300610X

KenryChen, C., and Liu, B. (2019). Enhancing the Performance of Pure Organic Room-Temperature Phosphorescent Luminophores. *Nat. Commun.* 10, 2111. doi:10.1038/s41467-019-10033-2

Komura, M., Ogawa, T., and Tani, Y. (2021). Room-temperature Phosphorescence of a Supercooled Liquid: Kinetic Stabilisation by Desymmetrisation. *Chem. Sci.* 12, 14363–14368. doi:10.1039/D1SC03800A

Lai, L., Fang, B., Fan, M., Cheng, W., and Yin, M. (2021). Modulating Room-Temperature Phosphorescence through the Synergistic Effect of Heavy-Atom Effect and Halogen Bonding. *J. Phys. Chem. C* 125, 16350–16357. doi:10.1021/acs.jpcc.1c04989

Liao, Q., Li, Q., and Li, Z. (2021). Substituent Effects in Organic Luminogens with Room Temperature Phosphorescence. *ChemPhotoChem* 5, 694–701. doi:10.1002/cptc.202100016

Liu, Y., Ma, Z., Cheng, X., Qian, C., Liu, J., Zhang, X., et al. (2021). Regulating Force-Resistance and Acid-Responsiveness of Pure Organics with Persistent Phosphorescence via Simple Isomerization. *J. Mater. Chem. C* 9, 5227–5233. doi:10.1039/D1TC00501D

Liu, Y., Ma, Z., Liu, J., Chen, M., Ma, Z., and Jia, X. (2021). Robust White-Light Emitting and Multi-Responsive Luminescence of a Dual-Mode Phosphorescence Molecule. *Adv. Opt. Mater.* 9, 2001685. doi:10.1002/adom.202001685

Ma, X., Li, J., Lin, C., Chai, G., Xie, Y., Huang, W., et al. (2019). Reversible Two-Channel Mechanochromic Luminescence for a Pyridinium-Based white-light Emitter with Room-Temperature Fluorescence-Phosphorescence Dual Emission. *Phys. Chem. Chem. Phys.* 21, 14728–14733. doi:10.1039/C9CP02451D

Mao, Z., Yang, Z., Mu, Y., Zhang, Y., Wang, Y.-F., Chi, Z., et al. (2015). Linearly Tunable Emission Colors Obtained from a Fluorescent-Phosphorescent Dual-Emission Compound by Mechanical Stimuli. *Angew. Chem. Int. Ed.* 54, 6270–6273. doi:10.1002/anie.201500426

Mukai, M., Yamauchi, S., Hirota, N., and Higuchi, J. (1992). Time-resolved EPR and Phosphorescence Studies of the Lowest Excited Triplet State of Benzil. *J. Phys. Chem.* 96, 9328–9331. doi:10.1021/j100202a050

Reddy, C. M., Kirchner, M. T., Gundakaram, R. C., Padmanabhan, K. A., and Desiraju, G. R. (2006). Isostructurality, Polymorphism and Mechanical Properties of Some Hexahalogenated Benzenes: The Nature of Halogen···Halogen Interactions. *Chem. Eur. J.* 12, 2222–2234. doi:10.1002/chem.200500983

Sagara, Y., Yamane, S., Mitani, M., Weder, C., and Kato, T. (2016). Mechanoresponsive Luminescent Molecular Assemblies: An Emerging Class of Materials. *Adv. Mater.* 28, 1073–1095. doi:10.1002/adma.201502589

Saidykhan, A., Fenwick, N. W., Bowen, R. D., Telford, R., and Seaton, C. C. (2021). Isostructurality of Quinoxaline crystal Phases: the Interplay of Weak Hydrogen Bonds and Halogen Bonding. *CrystEngComm* 23, 7108–7117. doi:10.1039/D1CE00878A

Singh, A. K., Palit, D. K., and Mittal, J. P. (2002). Conformational Relaxation Dynamics in the Excited Electronic States of Benzil in Solution. *Chem. Phys. Lett.* 360, 443–452. doi:10.1016/S0009-2614(02)00891-6

Tani, Y., Terasaki, M., Komura, M., and Ogawa, T. (2019). Room-temperature Phosphorescence-To-Phosphorescence Mechanochromism of a Metal-free Organic 1,2-diketone. *J. Mater. Chem. C* 7, 11926–11931. doi:10.1039/C9TC04176A

Tani, Y., Komura, M., and Ogawa, T. (2020). Mechanoresponsive Turn-On Phosphorescence by a Desymmetrization Approach. *Chem. Commun.* 56, 6810–6813. doi:10.1039/D0CC01949F

Wang, C., and Li, Z. (2017). Molecular Conformation and Packing: Their Critical Roles in the Emission Performance of Mechanochromic Fluorescence Materials. *Mater. Chem. Front.* 1, 2174–2194. doi:10.1039/C7QM00201G

Wang, X., Ma, H., Gu, M., Lin, C., Gan, N., Xie, Z., et al. (2019). Multicolor Ultralong Organic Phosphorescence through Alkyl Engineering for 4D Coding Applications. *Chem. Mater.* 31, 5584–5591. doi:10.1021/acs.chemmater.9b01304

Wang, X.-F., Xiao, H., Chen, P.-Z., Yang, Q.-Z., Chen, B., Tung, C.-H., et al. (2019). Pure Organic Room Temperature Phosphorescence from Excited Dimers in Self-Assembled Nanoparticles under Visible and Near-Infrared Irradiation in Water. *J. Am. Chem. Soc.* 141, 5045–5050. doi:10.1021/jacs.9b00859

Wen, Y., Liu, H., Zhang, S., Gao, Y., Yan, Y., and Yang, B. (2019). One-dimensional π-π Stacking Induces Highly Efficient Pure Organic Room-Temperature Phosphorescence and Ternary-Emission Single-Molecule white Light. *J. Mater. Chem. C* 7, 12502–12508. doi:10.1039/C9TC04580E

Xu, B., Wu, H., Chen, J., Yang, Z., Yang, Z., Wu, Y.-C., et al. (2017). White-light Emission from a Single Heavy Atom-free Molecule with Room Temperature Phosphorescence, Mechanochromism and Thermochromism. *Chem. Sci.* 8, 1909–1914. doi:10.1039/c6sc03038f

Xue, P., Ding, J., Wang, P., and Lu, R. (2016). Recent Progress in the Mechanochromism of Phosphorescent Organic Molecules and Metal Complexes. *J. Mater. Chem. C* 4, 6688–6706. doi:10.1039/c6tc01503d

Yuan, W. Z., Shen, X. Y., Zhao, H., Lam, J. W. Y., Tang, L., Lu, P., et al. (2010). Crystallization-Induced Phosphorescence of Pure Organic Luminogens at Room Temperature. *J. Phys. Chem. C* 114, 6090–6099. doi:10.1021/jp909388y

Conflict of Interest: The authors declare that the research was conducted in the absence of any commercial or financial relationships that could be construed as a potential conflict of interest.

frontiers in Chemistry

ORIGINAL RESEARCH
published: 27 January 2022
doi: 10.3389/fchem.2021.810304

Efficient Room-Temperature Phosphorescence from Discrete Molecules Based on Thianthrene Derivatives for Oxygen Sensing and Detection

Zhiqiang Yang, Shuaiqiang Zhao, Xiangyu Zhang, Meng Liu, Haichao Liu and Bing Yang**

State Key Laboratory of Supramolecular Structure and Materials, College of Chemistry, Jilin University, Changchun, China

In this work, two thianthrene (TA) derivatives, 1-phenylthianthrene (TA1P) and 2-phenylthianthrene (TA2P), were synthesized with single-phenyl modification for pure organic discrete-molecule room-temperature phosphorescence (RTP). They both show the dual emission of fluorescence and RTP in amorphous polymer matrix after deoxygenation, as a result of a new mechanism of folding-induced spin-orbit coupling (SOC) enhancement. Compared with TA1P, TA2P exhibits a higher RTP efficiency and a larger spectral separation between fluorescence and RTP, which is ascribed to the substituent effect of TA at the 2-position. With decreasing oxygen concentration from 1.61% to 0%, the discrete-molecule TA2P shows an about 18-fold increase in RTP intensity and an almost constant fluorescence intensity, which can make TA2P as a self-reference ratiometric optical oxygen sensing probe at low oxygen concentrations. The oxygen quenching constant (K_{SV}) of TA2P is estimated as high as 10.22 KPa^{-1} for polymethyl methacrylate (PMMA)-doped film, and even reach up to 111.86 KPa^{-1} for Zeonex$^{®}$-doped film, which demonstrates a very high sensitivity in oxygen sensing and detection. This work provides a new idea to design pure organic discrete-molecule RTP materials with high efficiency, and TA derivatives show a potential to be applied in quantitative detection of oxygen as a new-generation optical oxygen-sensing material.

Keywords: pure organic room-temperature phosphorescence, discrete molecule, thianthrene, ratiometric optical oxygen sensing, polymer film, folding geometry, spin-orbit coupling

Edited by:
Wang Zhang Yuan,
Shanghai Jiao Tong University, China

Reviewed by:
Zhiyong Yang,
Sun Yat-sen University, China
Wei Jun Jin,
Beijing Normal University, China

***Correspondence:**
Haichao Liu
hcliu@jlu.edu.cn
Bing Yang
yangbing@jlu.edu.cn

Specialty section:
This article was submitted to Physical Chemistry and Chemical Physics,
a section of the journal Frontiers in Chemistry

Received: *06 November 2021*
Accepted: *15 December 2021*
Published: *27 January 2022*

Citation:
Yang Z, Zhao S, Zhang X, Liu M, Liu H and Yang B (2022) Efficient Room-Temperature Phosphorescence from Discrete Molecules Based on Thianthrene Derivatives for Oxygen Sensing and Detection. Front. Chem. 9:810304. doi: 10.3389/fchem.2021.810304

1 INTRODUCTION

Due to high efficiency and long lifetime of luminescence, phosphorescent materials have received increasing attention, resulting in their broad applications in light-emitting devices (Higginbotham et al., 2021; Wang J. et al., 2021; Zhang et al., 2021), information encryption and storage (Bian et al., 2018; Gu et al., 2018; She et al., 2021), biological imaging (Yang J. et al., 2018; Yang et al., 2021), photodynamic therapy (Shi et al., 2014; Wang et al., 2020), molecular detection and sensing (Yu et al., 2017; Zhou et al., 2019; Liu et al., 2020), etc. Most of the phosphorescent materials are focused on metal complexes [such as Os (Omar et al., 2018), Ir (Idris et al., 2021; Mao et al., 2021), and Pt (Yang X. et al., 2018; Stipurin and Strassner, 2021)], due to the strong spin-orbit coupling (SOC) from the heavy-atom effect of metal atoms. However, they still have some drawbacks from high cost, resource scarcity, and potential toxicity of these noble metals, so the pure organic metal-free room-temperature phosphorescence (RTP) material becomes an ideal alternative. Limited by the weak SOC in pure organic materials, their phosphorescence radiation experiences an extremely slow process (Zhao et al., 2020), which leads to very easy deactivation of triplet excitons by molecular thermal motions or external oxygen quenching. In this case, two pathways are commonly used to obtain the efficient pure organic RTP: one is to promote the generation of triplet excitons by enhancing SOC effect with an introduction of heavy atoms (e.g., Br, I, and Se) (Wen et al., 2019; Lee et al., 2020) or heteroatoms (e.g., O, N, and S) (Xu et al., 2017; Wen et al., 2020; Xu et al., 2020; Wen et al., 2021) in molecular systems; the other one is to suppress the non-radiative decay of triplet excitons by strengthening the system rigidity from crystallization and host–guest interactions (Gu et al., 2019; Qu et al., 2019). However, this crystalline state greatly increases the difficulty of material processing and limits the practical applications of pure organic RTP materials. As a matter of fact, it is more convenient for organic emitters to be widely used in the form of amorphous film comparing with crystalline state, especially for the doped film with discrete molecules in polymer matrix, showing excellent processability. Nevertheless, the efficient discrete-molecule RTP materials in amorphous film have been rarely reported (Li et al., 2018; Ma et al., 2018; Ma et al., 2019; Zhang et al., 2020), because the discrete-molecule RTP in amorphous state frequently encounters a competitive non-radiative decay of triplet excitons. As for the reasons, on the one hand, the environmental rigidity is not large enough to effectively suppress the molecular vibrational quenching; on the other hand, triplet state oxygen can sensitively quench RTP through non-radiative energy transfer *via* molecular collisions under ambient conditions (Lee et al., 2013).

Using this unique oxygen-sensitive property, the pure organic RTP materials can be also applied in the optical oxygen sensing and detection, which involves many aspects of the application, such as physiological and pathological detection (Zhang et al., 2009; Spencer et al., 2014; Zhang et al., 2018), food packaging and storage (Smiddy et al., 2002; Mills, 2005; O'Mahony et al., 2006), and so on. Commonly, the ratiometric measurement method is used to improve the accuracy of optical oxygen detection, which combines an oxygen-insensitive fluorophore and an oxygen-sensitive phosphor into the same polymer matrix, and the oxygen concentration can be quantitatively detected by the ratio of emission intensities between fluorescence and phosphorescence (Feng et al., 2012). For the ratiometric measurement, the metal complex material with single phosphorescence usually needs to be used together with a fluorescence material (Xu et al., 2001), which easily leads to complex problems from multi-components, including sophisticated processing and physical separation (Huang et al., 2018). Thus, the pure organic discrete-molecule RTP material can be a good candidate for ratiometric measurement, because its moderate SOC enables simultaneous and comparable dual-emission between fluorescence and RTP. In addition, such a discrete-molecule dual-emission material is doped in polymer matrix, which surely facilitates the oxygen sensing and detection as a result of good oxygen permeability, unlike the difficult oxygen diffusion in tightly packed molecular crystals (Zhou et al., 2019).

In this work, we designed and synthesized two pure organic compounds, showing the efficient RTP of discrete molecule in polymer film for oxygen sensing and detection. Two compounds, 1-phenylthianthrene (TA1P) and 2-phenylthianthrene (TA2P), were obtained by a simple chemical modification of TA at 1- and 2-positions by using a single-phenyl group. When these two compounds were dispersed in polymethyl methacrylate (PMMA) matrix to form the discrete-molecule-doped film, they exhibit a strong RTP emission band after deoxygenation along with an almost constant fluorescence emission. The efficient RTP emission can be ascribed to the mechanism of folding-induced SOC enhancement (Liu et al., 2018). As a result, the fluorescence intensity can be directly used as a reference signal and RTP intensity can act as an analysis signal, which enable single-component ratiometric optical oxygen sensing and detection without any internal standard substance. Compared with TA1P, the π-conjugation of TA2P is enhanced due to the phenyl substitution at the 2-position of TA, resulting in a larger separation between fluorescence and RTP emission spectra, which substantially decreases the intensity interference between fluorescence and RTP. TA2P demonstrates a better linearity and a larger quenching constant than those of TA1P in oxygen-sensing experiment, which greatly improves the accuracy of oxygen sensing and detection. This work mainly presents a molecular design strategy of the efficient discrete-molecule RTP material, as well as their potential application in terms of oxygen sensing and detection.

2 MATERIALS AND METHODS

2.1 Materials and General Methods

All the reagents and solvents used for the synthesis were purchased commercially. The prepared compounds were characterized by ^1H and ^{13}C Nuclear magnetic resonance (NMR) spectra using tetramethylsilane (TMS) as the internal standard (Bruker AVANCE 500 spectrometer), mass spectra (Thermo Fisher ITQ1100 instrument), and elemental analysis (Flash EA 1112, CHNS elemental analysis instrument). UV-vis spectra of films were recorded on a Shimadzu UV-3100 Spectrophotometer. Emission spectra and time-resolved emission spectra were carried out on a FLS980 Spectrometer. Photoluminescence quantum yields under ambient conditions were measured by using an integrating sphere apparatus on a FLS980 Spectrometer, and the excitation wavelength was 300 nm. RTP efficiency was obtained by a comparison between fluorescence and RTP spectra areas under the same experimental conditions. Grayscale images and grayscale values were obtained by using a MATLAB program. The density functional theory (DFT) was adopted for the ground-state geometry optimization at the level of CAM-B3LYP/6-31G(d, p) using Gaussian 09 (version D.01) package (Frisch et al., 2013). The natural transition orbitals (NTOs) were calculated by using time-dependent DFT (TD-DFT) at the

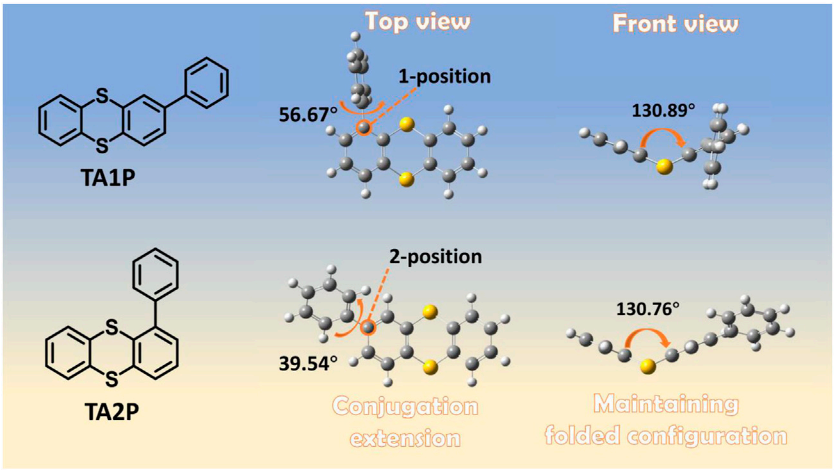

SCHEME 1 | Chemical structures and molecular geometries of TA1P and TA2P.

level of CAM-B3LYP/6-31G(d, p). SOC coefficients were quantitatively estimated at the level of CAM-B3LYP/6-31G(d, p) by using the Beijing Density Functional (BDF) program (Liu et al., 2003; Li et al., 2012; Quaranta et al., 2012; Li et al., 2013; Li et al., 2014).

2.2 Preparation of Film

Firstly, 1 mg TA derivative and 100 mg PMMA particles were weighed, and then both of them were put into a sample tube, followed by a solvent addition of 1.5 ml chloroform; the mixture was left for 30 min until the PMMA was completely dissolved; the mixture of TA derivative and PMMA was further well dispersed by sonicated treatment for 5 min to prepare a homogeneous stock solution. The stock solution was spin-coated on a quartz glass substrate, and a thin film for oxygen sensing and detection was successfully obtained after solvent evaporation and film drying in the air for 30 min.

2.3 Synthesis

2.3.1 The Synthesis of 1-Phenylthianthrene

A mixture of 1-thianthrenylboronic acid (520 mg, 2.00 mmol), bromobenzene (471 mg, 3.00 mmol), K_2CO_3 (2.48 g, 18.00 mmol), 6 ml distilled water, and 9 ml toluene was degassed and recharged with nitrogen. Then, $Pd(PPh_3)_4$ (69 mg, 0.06 mmol) was added in the mixture as catalyst, and the mixture was degassed and recharged with nitrogen again. After being stirred and refluxed at 90°C for 48 h under nitrogen atmosphere, the mixture was extracted with dichloromethane (DCM). The organic phase was dried with anhydrous sodium sulfate, filtered, and concentrated in vacuum. It was purified *via* silica gel chromatography by the mixture of petroleum ether/DCM and was recrystallized from DCM/methanol to give the product as white powder in 66% yield (385 mg). ^1H NMR (500 MHz, DMSO-d_6, 25°C, TMS): δ=7.62 (ddd, J = 16.5, 7.7, and 1.4 Hz, 2H), 7.53 (dd, J = 8.0 and 6.5 Hz, 2H), 7.50–7.44 (m, 1H), 7.48–7.39 (m, 4H), 7.39–7.32 (m, 2H), and 7.28 (td, J = 7.5 and 1.4 Hz, 1H); ^{13}C NMR (126 MHz, $CDCl_3$-d, 25°C, TMS): δ = 142.52 (C), 140.21 (C), 136.35 (C), 135.98 (C), 135.40 (C), 135.05 (C), 129.44 (CH), 129.28 (CH), 128.88 (CH), 128.52 (CH), 128.22 (CH), 128.15 (CH), 127.83 (CH), 127.77 (CH), 127.54 (CH), and 127.06 (CH). GC-MS, EI, mass m/z: 292.42 [M^+]; anal. calculated for $C_{12}H_{18}S_2$: C 73.94, H 4.14, and S 21.93; found: C 73.97, H 4.20, and S 21.61.

2.3.2 The Synthesis of 2-Phenylthianthrene

According to a previous report, 2-bromothianthrene was synthesized (Liu et al., 2016). TA2P was synthesized by a procedure similar to that of TA1P, and the detail is shown in the **Supplementary Material**. TA2P product was obtained as white powder in 72% yield (420 mg). ^1H NMR (500 MHz, DMSO-d_6, 25°C, TMS): δ = 7.87 (d, J = 1.3 Hz, 1H), 7.74–7.69 (m, 2H), 7.66 (d, J = 1.2 Hz, 2H), 7.61 (ddd, J = 5.5, 3.3, and 1.7 Hz, 2H), 7.48 (t, J = 7.6 Hz, 2H), and 7.39 (ddd, J = 13.1, 6.6, and 2.3 Hz, 3H); ^{13}C NMR (126 MHz, $CDCl_3$-d, 25°C, TMS): δ = 141.09 (C), 139.69 (C), 136.14 (C), 135.57 (C), 135.46 (C), 134.39 (C), 128.91 (CH), 128.81 (CH), 128.76 (CH), 127.75 (CH), 127.28 (CH), 127.00 (CH), and 126.51 (CH). GC-MS, EI, mass m/z: 292.42 [M^+]; anal. calculated for $C_{12}H_{18}S_2$: C 73.94, H 4.14, and S 21.93; found: C 74.22, H 4.04, and S 21.02.

3 RESULTS AND DISCUSSION

In our previous work, efficient RTP of TA was reported with a novel mechanism of folding-induced SOC enhancement. TA exhibits not only bright RTP in the crystalline state but also discrete-molecule RTP emission in the doped film of PMMA after deoxygenation. However, under ambient conditions, the discrete-molecule RTP emission cannot be observed in its doped film (**Supplementary Figure S1**), owing to the complete quenching of triplet state of TA by molecular oxygen in the air. Such a high oxygen sensitivity of TA-doped film inspires us to explore a unique application of TA and its derivatives in oxygen sensing and detection. However, for TA emission, due to the inadequate

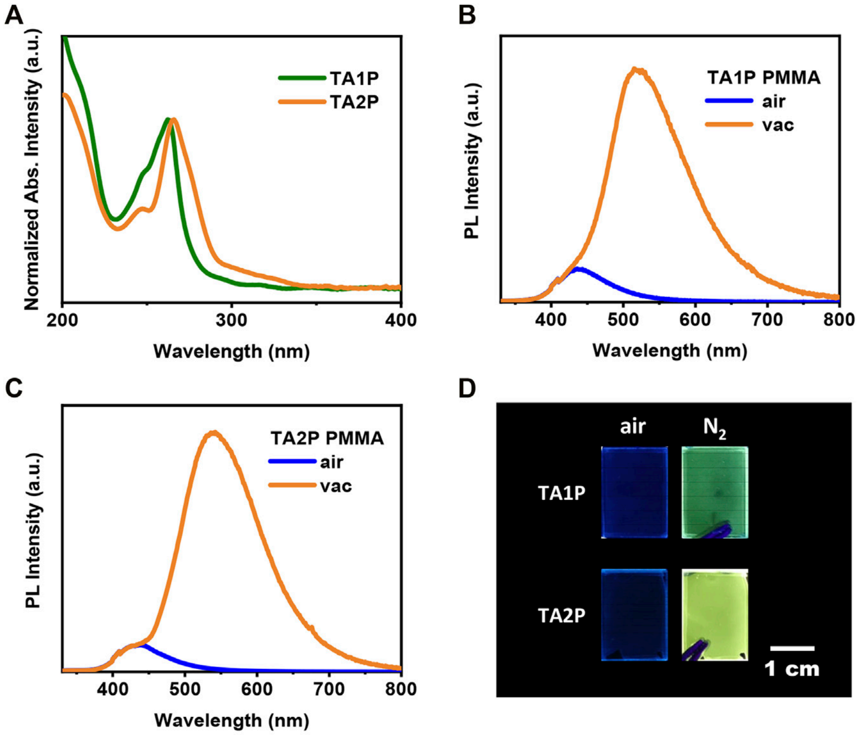

FIGURE 1 | (A) UV-vis absorption spectra of 1-phenylthianthrene (TA1P) and 2-phenylthianthrene (TA2P) polymethyl methacrylate (PMMA) films. **(B)**, **(C)** Fluorescence spectra and room-temperature phosphorescence (RTP) spectra of 1 wt.% PMMA-doped films for TA1P and TA2P, respectively. **(D)** Luminous images of TA1P and TA2P PMMA films in the air and purged by nitrogen (N_2).

separation between fluorescence and RTP spectra, the fluorescence intensity is easily affected by the RTP intensity with the decrease of oxygen concentration, which will cause a serious error in ratiometric optical oxygen detection. How to achieve good separation between fluorescence and RTP spectra while maintaining high efficiency of discrete-molecule RTP is a primary focus for molecular design of oxygen-sensitive materials. As regards TA, its high-efficiency discrete-molecule RTP comes from the substantial SOC brought by the folded configuration. Therefore, we can obtain the impressive SOC by maintaining the folded configuration of TA and achieve good separation of fluorescence and RTP spectra by chemical modification of TA. For this reason, TA was further chemically modified at two main sites (1- and 2-position) to design two TA derivatives (TA1P and TA2P), respectively (**Scheme 1**; **Supplementary Scheme S1**).

For the oxygen sensing and detection, the polymer matrix is a key factor to determine its working performance. As a priority, PMMA was chosen as the polymer matrix for good film-forming ability, proper oxygen permeability, good UV transmittance, etc. (Wang and Wolfbeis, 2014) The experimental operation process is described in detail in the *Preparation of Film* section (**Supplementary Scheme S2**).

Compared with TA, both TA1P and TA2P exhibit different degrees of redshift in their absorption spectra, as a result of the different conjugation effect between phenyl group and TA unit (**Figure 1A**; **Supplementary Figures S2, S3**). Obviously, the substitution of phenyl at the 2-position of TA is more effective for conjugation extension than that at the 1-position, and this difference can be clearly understood by theoretical calculations. In the ground state of TA1P (**Supplementary Figure S4**), the dihedral angle between phenyl group and TA unit is as large as 56.67° due to the steric hindrance. Although the phenyl group participates in the electronic transition of $S_0 \rightarrow S_1$, the degree of participation is very low, indicating a weak conjugation effect between the phenyl group and TA unit. However, for TA2P (**Supplementary Figure S5**), the small steric hindrance between phenyl group and TA unit results in a small dihedral angle of 39.54°, and the phenyl group obviously participates in the electronic transition of $S_0 \rightarrow S_1$, corresponding to an enhanced conjugation. As for emission, both compounds show almost the same blue emission under ambient conditions (the wavelength maximum is at 436 nm in PMMA-doped films). The time-resolved emission spectra demonstrate a short-lived characteristic, indicating the blue fluorescence for the discrete molecules in the doped films (**Supplementary Figures S6, S7**). As shown in **Figures 1B,C**, when the doped films are deoxygenated in a vacuum, both materials exhibit a new emission band (peaking at 519 and 533 nm for TA1P and TA2P, respectively) at the long wavelength in addition to the original weak fluorescence emission, and the new emission intensity far exceeds the fluorescence intensity in a vacuum. Time-resolved emission spectra reveal a long-lived characteristic of the long-wavelength emission bands (**Supplementary Figure S8**), corresponding to the RTP emission. Furthermore, when the

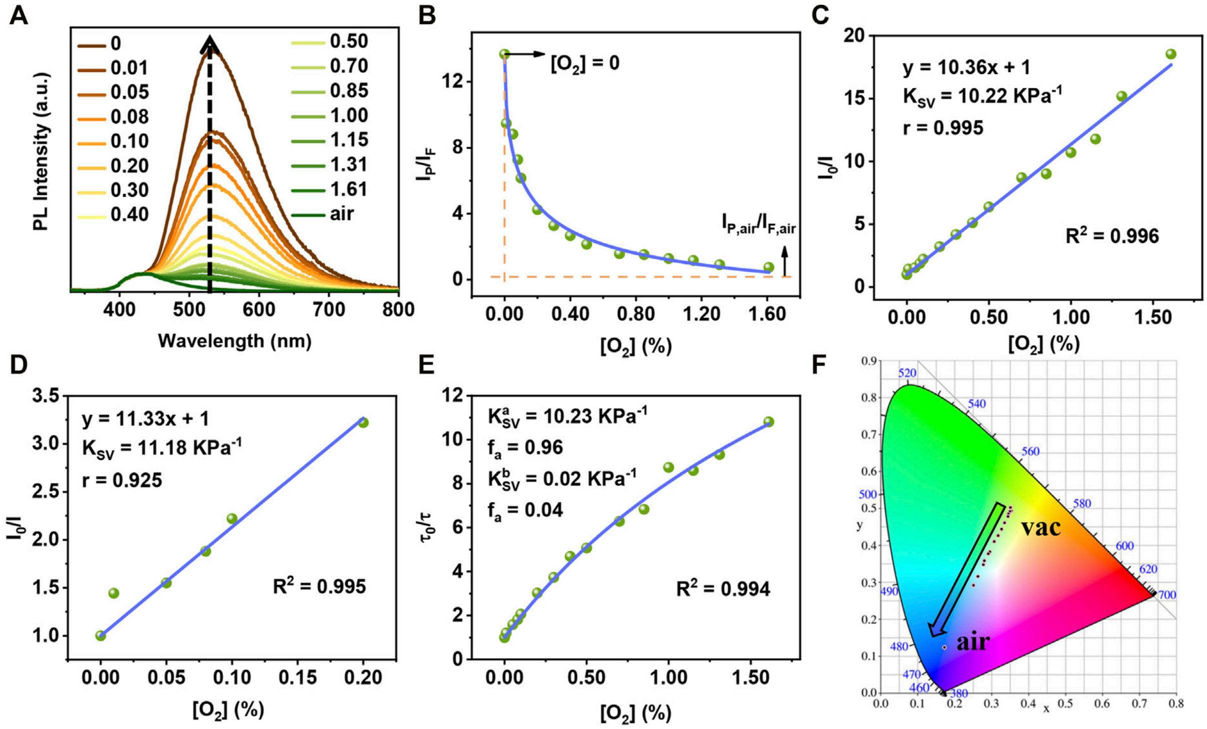

FIGURE 2 | (A) Emission spectra of TA2P-PMMA film at different oxygen concentrations (excited by 300 nm). **(B)** The plot of I_P/I_F against oxygen concentration for TA2P PMMA film. **(C)** Stern–Volmer curve of TA2P PMMA film based on the emission spectrum method (fitting range: 0%–1.61%). **(D)** The Stern–Volmer curve of TA2P PMMA film based on the emission spectrum method (fitting range: 0%–0.20%). **(E)** the "Demas model" curve of TA2P PMMA film based on the lifetime method. **(F)** The Commission Internationale del'Eclairage (CIE) coordinates of TA2P PMMA film with varying oxygen concentrations.

film was purged by using a nitrogen stream to simulate the deoxygenation environment, it is obvious that the emission color changes from faint blue to bright green or yellow for these two films (**Figure 1D**), in good agreement with the spectral measurement in the air and in a vacuum, respectively. Photoluminescence (PL) efficiency is an important performance parameter to evaluate RTP materials for ratiometric optical oxygen sensing and detection. Under ambient conditions, the PL efficiencies of TA1P and TA2P films are measured to be 0.89% and 1.73%, which correspond to their fluorescence efficiencies, respectively. Their RTP efficiencies are estimated to be 8.44% for TA1P and 22.73% for TA2P, which are very high values for pure organic discrete-molecule RTP materials. Compared with TA1P, TA2P has a much higher efficiency of RTP, which is surely more advantageous to be used for oxygen sensing and detection as a detection signal. To understand the origin of RTP of these two materials, the excited states and SOC coefficients were calculated between singlet and triplet states, respectively. Owing to the folding geometry of TA1P and TA2P (the folding dihedral angle is 130.89° and 130.76° for TA units in TA1P and TA2P, respectively), the SOC coefficients are estimated to be very sizeable between singlet and triplet manifolds, which are much higher than those of usual pure organic materials as a result of a new mechanism of folding-induced SOC enhancement. These large SOC coefficients provide very rich intersystem crossing (ISC) channels for the effective generation of triplet excitons, and then the great SOC between T_1 and S_0 can ensure the efficient radiation of triplet excitons to produce efficient RTP emission (from **Supplementary Figures S9–S12**).

From qualitative sensing to quantitative detection of oxygen, the detection range should be taken into account firstly. For this reason, a series of nitrogen and oxygen mixtures were prepared with different oxygen concentrations. Considering the complete RTP quenching of discrete-molecule-doped film in the air, the mixed gas should be prepared with an oxygen concentration of less than 21% in later experiments. After careful optimization of conditions, the oxygen concentration range was selected from 0% to 1.61% for subsequent experiments of oxygen detection. For ratiometric oxygen detection, the stability of reference signal is an important factor that affects the accuracy of detection. As shown in **Figures 1B,C**, the fluorescence intensities of these two films are affected very little, even negligibly, when the RTP intensity is increased dramatically during deoxygenation. This property allows them to be used for single-component ratiometric optical oxygen detection, where the fluorescence emission can directly serve as the reference signal without the addition of an internal standard substance. With increasing oxygen concentration, the fluorescence intensities of the three films (TA, TA1P, and TA2P) were plotted together for the purpose of comparison (**Supplementary Figure S13**). Among them, the fluorescence intensity of TA2P has the smallest fluctuation with the change of oxygen concentration, demonstrating the best stability of fluorescence intensity as the reference signal for ratiometric optical oxygen detection, which is ascribed to the largest spectral separation between fluorescence (peaking at 436 nm) and RTP (peaking at 533 nm) in essence.

Next, TA2P was taken as an example to carry out oxygen detection experiment. When exposed to the air, the RTP emission of TA2P-doped film is completely quenched, showing pure fluorescence emission. With the decrease of oxygen concentration, the RTP emission is enhanced gradually, while the fluorescence intensity remains almost the same during this process (**Figure 2A**). For ratiometric optical oxygen detection, a new variable I is defined as I_P/I_F, corresponding to a ratio of the RTP emission intensity (I_P) to the fluorescence emission intensity (I_F) at different oxygen concentrations. As shown in **Figure 2B**, an inverse proportional relation can be obtained for I as a function of oxygen concentration. With increasing oxygen concentration, the value of I gradually approaches to $I_{P,air}/I_{F,air}$, where $I_{P,air}$ and $I_{F,air}$ represent the actual spectral intensity at 533 and 436 nm in the air, respectively. When the oxygen concentration is zero, the variable I is equal to I_0 in a vacuum. In order to quantitatively evaluate oxygen sensitivity, a linear relationship can be well fitted between I_0/I and oxygen concentration according to the Stern–Volmer **Eq. 1** (Feng et al., 2012; Wang and Wolfbeis, 2014), as shown in **Figure 2C**:

$$\frac{I_0}{I} = \frac{\tau_0}{\tau} = 1 + K_{SV}[O_2] = 1 + k_q \tau_0 [O_2] \quad (1)$$

where K_{SV} is the Stern–Volmer quenching constant, k_q is quenching rate constant, $[O_2]$ is the oxygen concentration, and τ_0 is the RTP lifetime when $[O_2] = 0$.

As a result, the linear fitting of TA2P-doped film shows excellent correlation in the $[O_2]$ range of 0%–1.61%, and the correlation coefficient (R^2) is as high as 0.996, corresponding to the Pearson correlation coefficient (Pearson's r) of 0.995. The Stern–Volmer constant (K_{SV}) is estimated to be 10.22 KPa^{-1}, which reflects very high oxygen sensitivity of TA2P film. When the linear fitting was done at an oxygen concentration lower than 0.2%, the correlation coefficient and K_{SV} are still as high as 0.994 and 11.18 KPa^{-1}, respectively (**Figure 2D**). This result can guarantee the accuracy of oxygen detection even at a very low oxygen concentration. In the meantime, to verify the dynamic quenching mechanism of oxygen detection, the RTP lifetimes of TA2P film were recorded at different oxygen concentrations. The Stern–Volmer curve of the τ_0/τ shows a slight curvature, which is common in most optical oxygen sensors due to the inevitable heterogeneity of materials. In fact, it can be rationalized that there are different micro-zones for the material in different micro-environments. And thus, the quenching constants may be different in different micro-environments, causing a linear deviation of the Stern–Volmer curve. In this case, it can be well described using the "two-site model" by Demas and co-workers, which is also called the "Demas model" **Eq. 2** (Carraway et al., 1991; Borisov et al., 2006; Medina-Castillo et al., 2007):

$$\frac{I_0}{I} = \frac{\tau_0}{\tau} = \frac{1}{\frac{f_a}{1+K_{SV}^a[O_2]} + \frac{f_b}{1+K_{SV}^b[O_2]}} \quad (2)$$

where, K_{SV}^a and K_{SV}^b are Stern–Volmer constants of different micro-zone components and f_a and f_b are their corresponding component proportions ($f_a + f_b = 1$), respectively.

As shown in **Figure 2E**, the Demas model is used for Stern–Volmer curve fitting, resulting in $K_{SV}^a = 10.23\ \text{KPa}^{-1}$ with a large component ratio of 96% ($f_a = 0.96$) as well as $K_{SV}^b = 0.02\ \text{KPa}^{-1}$ with a small proportion of only 4% ($f_b = 0.04$). Thus, the overall K_{SV} can be replaced with K_{SV}^a approximatively, and K_{SV}^a is almost equal to the K_{SV} based on I_0/I from Stern–Volmer linear fitting according to **Eq. 1** (**Supplementary Figure S14**), which further validates a dynamic quenching mechanism of RTP in oxygen detection. Besides, the quenching rate constant (k_q) can be calculated as 213.8 $\text{KPa}^{-1}\ \text{s}^{-1}$ by **Eq. 1**, which is one of the highest values among all oxygen-sensing materials (Zhou et al., 2019; Liu et al., 2020; Wang S. et al., 2021). For another key parameter for oxygen detection, the limit of detection (LOD) can be estimated as the oxygen concentration when I_P/I_F is changed by 0.1% (Guo et al., 2021). For TA2P-doped film, the LOD is calculated to be 0.0979 Pa (equal to 0.966 ppm at atmospheric pressure), which is among one of the best values for oxygen detection.

Owing to the significant difference between fluorescence and RTP spectra, the emission color change of TA2P can be observed with different oxygen concentrations. This color change can be expressed through the Commission Internationale del'Eclairage (CIE) coordinates, as shown in **Figure 2F**. As the oxygen concentration gradually increases, the CIE coordinate points move along a line from yellow-green to blue region. Such a linear change gives us an inspiration to conduct the colorimetric detection of oxygen concentration, which is similar to the pH measurement using pH test strips. A simple home-made device was designed to detect the oxygen concentration of nitrogen–oxygen mixed gas stream (**Supplementary Figure S15**). As shown in **Figure 3**, when the TA2P film is purged by the mixture of nitrogen and oxygen with different oxygen contents, the color change can be obviously observed with the naked eye. At the same time, the luminous image can be transformed into a grayscale one, and the grayscale value is obtained with the help of computer software (Zhou et al., 2019). In the fitting range of 0.08%–1.15%, a good correlation linearity was found between grayscale value and oxygen concentration (**Supplementary Figure S16**), which provides a simple method for on-site detection of oxygen concentration in the absence of spectral measurement instrument.

Moreover, the PMMA polymer matrix was replaced with Zeonex® for optimizing oxygen detection (Tomkeviciene et al., 2019), in which Zeonex® is more oxygen-permeable and more rigid than PMMA. Due to the better oxygen permeability, the RTP of TA2P Zeonex® film can be greatly quenched at a lower oxygen concentration, (**Figure 4A**). Different from PMMA matrix, the Stern–Volmer curve obtained based on I_0/I with decreasing oxygen concentration shows an obvious non-linear change in the way of first flat and then steep, instead of a good linear fitting like that in PMMA matrix. Likewise, the Demas model was also used to fit the Stern–Volmer curve and to estimate K_{SV} (**Figure 4B**). As a result, its K_{SV}^a is calculated as high as 111.86 KPa^{-1} (f_a = 0.99, an almost complete contribution to K_{SV}). Such a high K_{SV} is very rare in

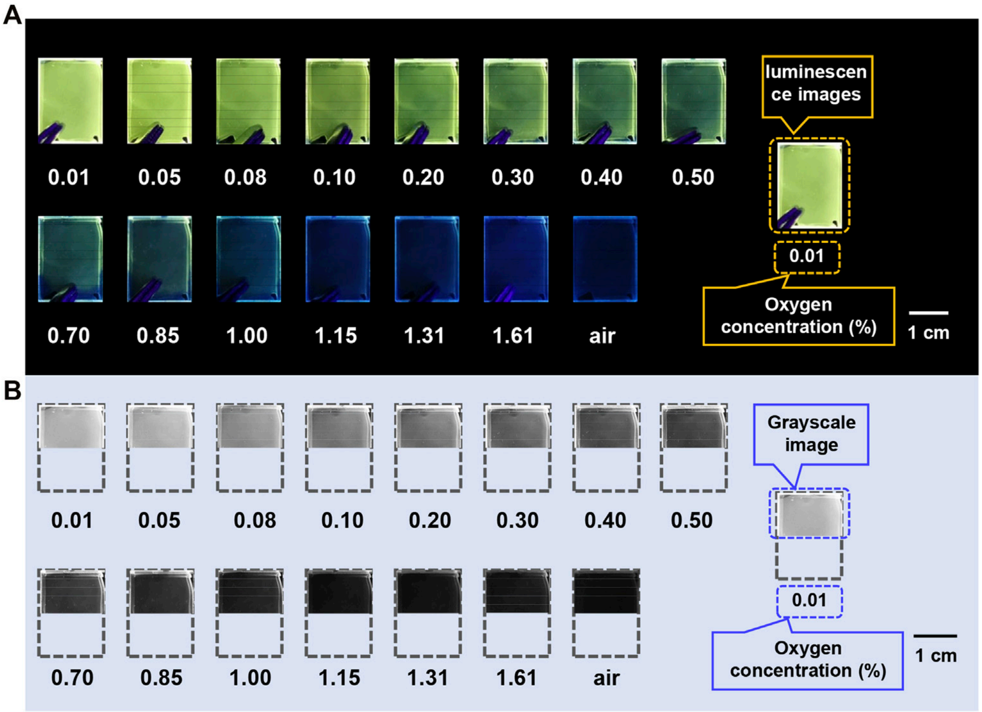

FIGURE 3 | (A) Luminescence images of TA2P PMMA-doped films at different oxygen concentrations. **(B)** Grayscale images corresponding to luminescence images at different oxygen concentrations.

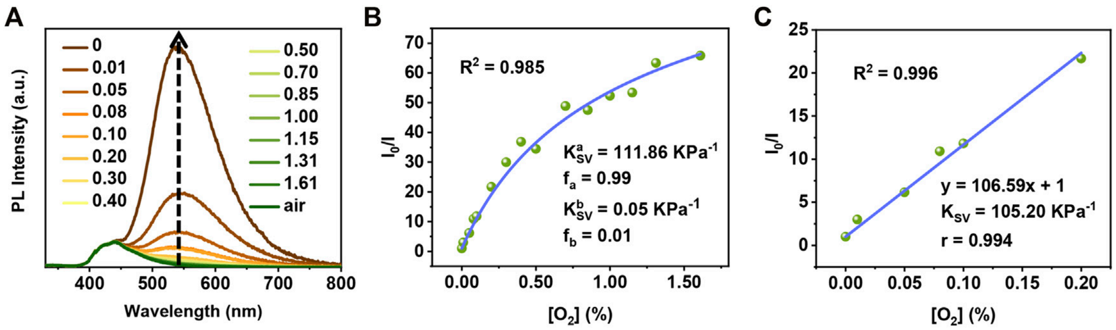

FIGURE 4 | (A) Emission spectra of TA2P Zeonex® film at different oxygen concentrations. **(B)** The Demas model curve of TA2P Zeonex® film (fitting range: 0%–1.61%). **(C)** The Stern–Volmer curve of TA2P Zeonex® film (fitting range: 0%–0.20%).

oxygen-sensing materials, and what is more, the Stern–Volmer curve still exhibits excellent linearity when the oxygen concentration is below 0.20% (**Figure 4C**). Also, the K_{SV} was obtained as 104.62 KPa^{-1} by direct linear fitting according to the Stern–Volmer **Eq. 1**, which is very close to the fitting result using the Demas model. Such a high sensitivity provides a feasible alternative to use TA2P Zeonex® film for an accurate detection of trace oxygen in the future (Borisov et al., 2011).

Relative to TA2P, TA1P shows an inferior performance in oxygen detection, and the detailed data is shown in **Supplementary Figures S17, S18**.

4 CONCLUSION

In summary, two phenyl-substituted derivatives of TA (TA1P and TA2P) were designed and synthesized for the efficient pure organic discrete-molecule RTP and the featured application of oxygen sensing and detection. These two compounds display the dual emission of fluorescence and RTP in discrete-molecule-doped film after deoxygenation, in which the efficient RTP is ascribed to the mechanism of folding-induced SOC enhancement. As a comparison, TA2P exhibits a higher RTP efficiency and more red-shifted RTP emission than those of TA1P, indicating a more significant electron conjugation effect between TA and phenyl group. Thus, TA2P has merits of both high efficiency of RTP and large spectral separation between dual emissions, which is more suitable for discrete-molecule ratiometric optical oxygen sensing and detection. As a result, TA2P demonstrates a Stern–Volmer quenching constant as high as 10.22 KPa^{-1} and the LOD can reach as low as 0.966 ppm in PMMA-doped film, which is one of the best results among oxygen-sensing materials. Additionally, PMMA was replaced with Zeonex® as a polymer matrix for further performance optimization. The Stern–Volmer constant of TA2P is estimated to be 111.86 KPa^{-1} in Zeonex® matrix, which is a very high value. These results present a feasible way for the optimization design of pure organic discrete-molecule RTP materials based on TA derivatives, as well as provide a class of dual-emission materials for a promising application in ratiometric optical oxygen sensing and detection.

DATA AVAILABILITY STATEMENT

The original contributions presented in the study are included in the article/**Supplementary Material**; further inquiries can be directed to the corresponding authors.

AUTHOR CONTRIBUTIONS

ZY and HL provided the molecular design and performed the synthesis experiment. ZY, SZ, XZ, and ML carried out the photophysical characterizations and image collection. ZY carried out the theoretical calculations. HL and BY supervised the whole work. All authors contributed to the article and approved the submitted version.

FUNDING

This work was supported by the National Natural Science Foundation of China (51873077, 91833304, 52073117, and 52103209), the National Key Research and Development Program of China (2020YFA0714603), and the China Postdoctoral Science Foundation (2018M641767).

SUPPLEMENTARY MATERIAL

The Supplementary Material for this article can be found online at: https://www.frontiersin.org/articles/10.3389/fchem.2021.810304/full#supplementary-material

REFERENCES

Bian, L., Shi, H., Wang, X., Ling, K., Ma, H., Li, M., et al. (2018). Simultaneously Enhancing Efficiency and Lifetime of Ultralong Organic Phosphorescence Materials by Molecular Self-Assembly. *J. Am. Chem. Soc.* 140 (34), 10734–10739. doi:10.1021/jacs.8b03867

Borisov, S. M., Lehner, P., and Klimant, I. (2011). Novel Optical Trace Oxygen Sensors Based on Platinum(II) and Palladium(II) Complexes with 5,10,15,20-Meso-Tetrakis-(2,3,4,5,6-Pentafluorphenyl)-Porphyrin Covalently Immobilized on Silica-Gel Particles. *Analytica Chim. Acta.* 690 (1), 108–115. doi:10.1016/j.aca.2011.01.057

Borisov, S. M., Vasylevska, A. S., Krause, C., and Wolfbeis, O. S. (2006). Composite Luminescent Material for Dual Sensing of Oxygen and Temperature. *Adv. Funct. Mater.* 16 (12), 1536–1542. doi:10.1002/adfm.200500778

Carraway, E. R., Demas, J. N., DeGraff, B. A., and Bacon, J. R. (1991). Photophysics and Photochemistry of Oxygen Sensors Based on Luminescent Transition-Metal Complexes. *Anal. Chem.* 63 (4), 337–342. doi:10.1021/ac00004a007

Feng, Y., Cheng, J., Zhou, L., Zhou, X., and Xiang, H. (2012). Ratiometric Optical Oxygen Sensing: a Review in Respect of Material Design. *Analyst.* 137 (21), 4885–4901. doi:10.1039/C2AN35907C

Frisch, M. J., Trucks, G. W., Schlegel, H. B., Scuseria, G. E., Robb, M. A., Cheeseman, J. R., et al. (2013). *Gaussian 09, Revision D.01.* Wallingford CT: Gaussian, Inc.

Gu, L., Shi, H., Bian, L., Gu, M., Ling, K., Wang, X., et al. (2019). Colour-Tunable Ultra-Long Organic Phosphorescence of a Single-Component Molecular crystal. *Nat. Photon.* 13 (6), 406–411. doi:10.1038/s41566-019-0408-4

Gu, L., Shi, H., Gu, M., Ling, K., Ma, H., Cai, S., et al. (2018). Dynamic Ultralong Organic Phosphorescence by Photoactivation. *Angew. Chem. Int. Ed.* 57 (28), 8425–8431. doi:10.1002/anie.201712381

Guo, W.-J., Chen, Y.-Z., Tung, C.-H., and Wu, L.-Z. (2021). Ultralong Room-Temperature Phosphorescence of Silicon-Based Pure Organic Crystal for Oxygen Sensing. *CCS Chem.* 3, 1384–1392. doi:10.31635/ccschem.021.202100932

Higginbotham, H. F., Okazaki, M., de Silva, P., Minakata, S., Takeda, Y., and Data, P. (2021). Heavy-Atom-Free Room-Temperature Phosphorescent Organic Light-Emitting Diodes Enabled by Excited States Engineering. *ACS Appl. Mater. Inter.* 13 (2), 2899–2907. doi:10.1021/acsami.0c17295

Huang, X., Song, J., Yung, B. C., Huang, X., Xiong, Y., and Chen, X. (2018). Ratiometric Optical Nanoprobes Enable Accurate Molecular Detection and Imaging. *Chem. Soc. Rev.* 47 (8), 2873–2920. doi:10.1039/C7CS00612H

Idris, M., Kapper, S. C., Tadle, A. C., Batagoda, T., Muthiah Ravinson, D. S., Abimbola, O., et al. (2021). Blue Emissive Fac/Mer -Iridium (III) NHC Carbene Complexes and Their Application in OLEDs. *Adv. Opt. Mater.* 9 (8), 2001994. doi:10.1002/adom.202001994

Lee, D., Bolton, O., Kim, B. C., Youk, J. H., Takayama, S., and Kim, J. (2013). Room Temperature Phosphorescence of Metal-Free Organic Materials in Amorphous Polymer Matrices. *J. Am. Chem. Soc.* 135 (16), 6325–6329. doi:10.1021/ja401769g

Lee, D. R., Lee, K. H., Shao, W., Kim, C. L., Kim, J., and Lee, J. Y. (2020). Heavy Atom Effect of Selenium for Metal-Free Phosphorescent Light-Emitting Diodes. *Chem. Mater.* 32 (6), 2583–2592. doi:10.1021/acs.chemmater.0c00078

Li, D., Lu, F., Wang, J., Hu, W., Cao, X.-M., Ma, X., et al. (2018). Amorphous Metal-Free Room-Temperature Phosphorescent Small Molecules with Multicolor Photoluminescence via a Host-Guest and Dual-Emission Strategy. *J. Am. Chem. Soc.* 140 (5), 1916–1923. doi:10.1021/jacs.7b12800

Li, Z., Suo, B., Zhang, Y., Xiao, Y., and Liu, W. (2013). Combining Spin-Adapted Open-Shell TD-DFT with Spin-Orbit Coupling. *Mol. Phys.* 111 (24), 3741–3755. doi:10.1080/00268976.2013.785611

Li, Z., Xiao, Y., and Liu, W. (2012). On the Spin Separation of Algebraic Two-Component Relativistic Hamiltonians. *J. Chem. Phys.* 137 (15), 154114. doi:10.1063/1.4758987

Li, Z., Xiao, Y., and Liu, W. (2014). On the Spin Separation of Algebraic Two-Component Relativistic Hamiltonians: Molecular Properties. *J. Chem. Phys.* 141 (5), 054111. doi:10.1063/1.4891567

Liu, H., Gao, Y., Cao, J., Li, T., Wen, Y., Ge, Y., et al. (2018). Efficient Room-Temperature Phosphorescence Based on a Pure Organic Sulfur-Containing Heterocycle: Folding-Induced Spin-Orbit Coupling Enhancement. *Mater. Chem. Front.* 2 (10), 1853–1858. doi:10.1039/c8qm00320c

Liu, H., Yao, L., Li, B., Chen, X., Gao, Y., Zhang, S., et al. (2016). Excimer-Induced High-Efficiency Fluorescence Due to Pairwise Anthracene Stacking in a Crystal with Long Lifetime. *Chem. Commun.* 52 (46), 7356–7359. doi:10.1039/C6CC01993E

Liu, W., Wang, F., and Li, L. (2003). The Beijing Density Functional (BDF) Program Package: Methodologies and Applications. *J. Theor. Comput. Chem.* 02 (02), 257–272. doi:10.1142/s0219633603000471

Liu, X. Q., Zhang, K., Gao, J. F., Chen, Y. Z., Tung, C. H., and Wu, L. Z. (2020). Monochromophore-Based Phosphorescence and Fluorescence from Pure Organic Assemblies for Ratiometric Hypoxia Detection. *Angew. Chem. Int. Ed.* 59 (52), 23456–23460. doi:10.1002/anie.202007039

Ma, X., Wang, J., and Tian, H. (2019). Assembling-Induced Emission: An Efficient Approach for Amorphous Metal-Free Organic Emitting Materials with Room-Temperature Phosphorescence. *Acc. Chem. Res.* 52 (3), 738–748. doi:10.1021/acs.accounts.8b00620

Ma, X., Xu, C., Wang, J., and Tian, H. (2018). Amorphous Pure Organic Polymers for Heavy-Atom-Free Efficient Room-Temperature Phosphorescence Emission. *Angew. Chem. Int. Ed.* 57 (34), 10854–10858. doi:10.1002/anie.201803947

Mao, M.-X., Li, F.-L., Shen, Y., Liu, Q.-M., Xing, S., Luo, X.-F., et al. (2021). Simple Synthesis of Red Iridium(III) Complexes with Sulfur-Contained Four-Membered Ancillary Ligands for OLEDs. *Molecules.* 26 (9), 2599. doi:10.3390/molecules26092599

Medina-Castillo, A. L., Fernández-Sánchez, J. F., Klein, C., Nazeeruddin, M. K., Segura-Carretero, A., Fernández-Gutiérrez, A., et al. (2007). Engineering of Efficient Phosphorescent Iridium Cationic Complex for Developing Oxygen-Sensitive Polymeric and Nanostructured Films. *Analyst.* 132 (9), 929–936. doi:10.1039/B702628E

Mills, A. (2005). Oxygen Indicators and Intelligent Inks for Packaging Food. *Chem. Soc. Rev.* 34 (12), 1003–1011. doi:10.1039/B503997P

O'Mahony, F. C., O'Riordan, T. C., Papkovskaia, N., Kerry, J. P., and Papkovsky, D. B. (2006). Non-Destructive Assessment of Oxygen Levels in Industrial Modified Atmosphere Packaged Cheddar Cheese. *Food Control.* 17 (4), 286–292. doi:10.1016/j.foodcont.2004.10.013

Omar, S. A. E., Scattergood, P. A., McKenzie, L. K., Jones, C., Patmore, N. J., Meijer, A. J. H. M., et al. (2018). Photophysical and Cellular Imaging Studies of Brightly Luminescent Osmium(II) Pyridyltriazole Complexes. *Inorg. Chem.* 57 (21), 13201–13212. doi:10.1021/acs.inorgchem.8b01627

Qu, G., Zhang, Y., and Ma, X. (2019). Recent Progress on Pure Organic Room Temperature Phosphorescence Materials Based on Host-Guest Interactions. *Chin. Chem. Lett.* 30 (10), 1809–1814. doi:10.1016/j.cclet.2019.07.042

Quaranta, M., Borisov, S. M., and Klimant, I. (2012). Indicators for Optical Oxygen Sensors. *Bioanal. Rev.* 4 (2-4), 115–157. doi:10.1007/s12566-012-0032-y

She, P., Qin, Y., Ma, Y., Li, F., Lu, J., Dai, P., et al. (2021). Lifetime-Tunable Organic Persistent Room-Temperature Phosphorescent Salts for Large-Area Security Printing. *Sci. China Mater.* 64 (6), 1485–1494. doi:10.1007/s40843-020-1544-6

Shi, H., Ma, X., Zhao, Q., Liu, B., Qu, Q., An, Z., et al. (2014). Ultrasmall Phosphorescent Polymer Dots for Ratiometric Oxygen Sensing and Photodynamic Cancer Therapy. *Adv. Funct. Mater.* 24 (30), 4823–4830. doi:10.1002/adfm.201400647

Smiddy, M., Papkovskaia, N., Papkovsky, D. B., and Kerry, J. P. (2002). Use of Oxygen Sensors for the Non-Destructive Measurement of the Oxygen Content in Modified Atmosphere and Vacuum Packs of Cooked Chicken Patties; Impact of Oxygen Content on Lipid Oxidation. *Food Res. Int.* 35 (6), 577–584. doi:10.1016/S0963-9969(01)00160-0

Spencer, J. A., Ferraro, F., Roussakis, E., Klein, A., Wu, J., Runnels, J. M., et al. (2014). Direct Measurement of Local Oxygen Concentration in the Bone Marrow of Live Animals. *Nature.* 508 (7495), 269–273. doi:10.1038/nature13034

Stipurin, S., and Strassner, T. (2021). Phosphorescent Cyclometalated Platinum(II) Imidazolinylidene Complexes. *Eur. J. Inorg. Chem.* 2021 (9), 804–813. doi:10.1002/ejic.202001077

Tomkeviciene, A., Dabulienė, A., Matulaitis, T., Guzauskas, M., Andruleviciene, V., Grazulevicius, J. V., et al. (2019). Bipolar Thianthrene Derivatives Exhibiting Room Temperature Phosphorescence for Oxygen Sensing. *Dyes Pigm.* 170, 107605. doi:10.1016/j.dyepig.2019.107605

Wang, J., Liang, B., Wei, J., Li, Z., Xu, Y., Yang, T., et al. (2021). Highly Efficient Electrofluorescence Material Based on Pure Organic Phosphor Sensitization. *Angew. Chem. Int. Ed.* 60 (28), 15335–15339. doi:10.1002/anie.202104755

Wang, S., Shu, H., Han, X., Wu, X., Tong, H., and Wang, L. (2021). A Highly Efficient Purely Organic Room-Temperature Phosphorescence Film Based on a Selenium-Containing Emitter for Sensitive Oxygen Detection. *J. Mater. Chem. C.* 9 (31), 9907–9913. doi:10.1039/D1TC02324A

Wang, S., Xu, M., Huang, K., Zhi, J., Sun, C., Wang, K., et al. (2020). Biocompatible Metal-Free Organic Phosphorescent Nanoparticles for Efficiently Multidrug-Resistant Bacteria Eradication. *Sci. China Mater.* 63 (2), 316–324. doi:10.1007/s40843-019-1191-9

Wang, X.-d., and Wolfbeis, O. S. (2014). Optical Methods for Sensing and Imaging Oxygen: Materials, Spectroscopies and Applications. *Chem. Soc. Rev.* 43 (10), 3666–3761. doi:10.1039/C4CS00039K

Wen, Y., Liu, H., Zhang, S.-T., Pan, G., Yang, Z., Lu, T., et al. (2021). Modulating Room Temperature Phosphorescence by Oxidation of Thianthrene to Achieve Pure Organic Single-Molecule White-Light Emission. *CCS Chem.* 3 (7), 1940–1948. doi:10.31635/ccschem.020.202000433

Wen, Y., Liu, H., Zhang, S., Cao, J., De, J., and Yang, B. (2020). Achieving Highly Efficient Pure Organic Single-Molecule White-Light Emitter: The Coenhanced Fluorescence and Phosphorescence Dual Emission by Tailoring Alkoxy Substituents. *Adv. Opt. Mater.* 8 (7), 1901995. doi:10.1002/adom.201901995

Wen, Y., Liu, H., Zhang, S., Gao, Y., Yan, Y., and Yang, B. (2019). One-dimensional π-π Stacking Induces Highly Efficient Pure Organic Room-Temperature Phosphorescence and Ternary-Emission Single-Molecule White Light. *J. Mater. Chem. C.* 7 (40), 12502–12508. doi:10.1039/c9tc04580e

Xu, B., Wu, H., Chen, J., Yang, Z., Yang, Z., Wu, Y.-C., et al. (2017). White-light Emission from a Single Heavy Atom-free Molecule with Room Temperature Phosphorescence, Mechanochromism and Thermochromism. *Chem. Sci.* 8 (3), 1909–1914. doi:10.1039/C6SC03038F

Xu, H., Aylott, J. W., Kopelman, R., Miller, T. J., and Philbert, M. A. (2001). A Real-Time Ratiometric Method for the Determination of Molecular Oxygen inside Living Cells Using Sol–Gel-Based Spherical Optical Nanosensors with Applications to Rat C6 Glioma. *Anal. Chem.* 73 (17), 4124–4133. doi:10.1021/ac0102718

Xu, L., Zhou, K., Qiu, X., Rao, B., Pei, D., Li, A., et al. (2020). Tunable Ultralong Organic Phosphorescence Modulated by Main-Group Elements with Different Lewis Acidity and Basicity. *J. Mater. Chem. C* 8 (42), 14740–14747. doi:10.1039/d0tc02953j

Yang, J., Zhang, Y., Wu, X., Dai, W., Chen, D., Shi, J., et al. (2021). Rational Design of Pyrrole Derivatives with Aggregation-Induced Phosphorescence Characteristics for Time-Resolved and Two-Photon Luminescence Imaging. *Nat. Commun.* 12 (1). doi:10.1038/s41467-021-25174-6

Yang J, J., Zhen, X., Wang, B., Gao, X., Ren, Z., Wang, J., et al. (2018). The Influence of the Molecular Packing on the Room Temperature Phosphorescence of Purely Organic Luminogens. *Nat. Commun.* 9 (1), 1–10. doi:10.1038/s41467-018-03236-6

Yang, X., Jiao, B., Dang, J.-S., Sun, Y., Wu, Y., Zhou, G., et al. (2018). Achieving High-Performance Solution-Processed Orange OLEDs with the Phosphorescent Cyclometalated Trinuclear Pt(II) Complex. *ACS Appl. Mater. Inter.* 10 (12), 10227–10235. doi:10.1021/acsami.7b18330

Yu, Y., Kwon, M. S., Jung, J., Zeng, Y., Kim, M., Chung, K., et al. (2017). Room-Temperature-Phosphorescence-Based Dissolved Oxygen Detection by Core-Shell Polymer Nanoparticles Containing Metal-Free Organic Phosphors. *Angew. Chem. Int. Ed.* 56 (51), 16207–16211. doi:10.1002/anie.201708606

Zhang, G., Palmer, G. M., Dewhirst, M. W., and Fraser, C. L. (2009). A Dual-Emissive-Materials Design Concept Enables Tumour Hypoxia Imaging. *Nat. Mater.* 8 (9), 747–751. doi:10.1038/nmat2509

Zhang, K. Y., Yu, Q., Wei, H., Liu, S., Zhao, Q., and Huang, W. (2018). Long-Lived Emissive Probes for Time-Resolved Photoluminescence Bioimaging and Biosensing. *Chem. Rev.* 118 (4), 1770–1839. doi:10.1021/acs.chemrev.7b00425

Zhang, T., Ma, X., Wu, H., Zhu, L., Zhao, Y., and Tian, H. (2020). Molecular Engineering for Metal-Free Amorphous Materials with Room-Temperature Phosphorescence. *Angew. Chem. Int. Ed.* 59 (28), 11206–11216. doi:10.1002/anie.201915433

Zhang, Y., Su, Y., Wu, H., Wang, Z., Wang, C., Zheng, Y., et al. (2021). Large-Area, Flexible, Transparent, and Long-Lived Polymer-Based Phosphorescence Films. *J. Am. Chem. Soc.* 143 (34), 13675–13685. doi:10.1021/jacs.1c05213

Zhao, W., He, Z., and Tang, B. Z. (2020). Room-temperature Phosphorescence from Organic Aggregates. *Nat. Rev. Mater.* 5 (12), 869–885. doi:10.1038/s41578-020-0223-z

Zhou, Y., Qin, W., Du, C., Gao, H., Zhu, F., and Liang, G. (2019). Long-Lived Room-Temperature Phosphorescence for Visual and Quantitative Detection of Oxygen. *Angew. Chem. Int. Ed.* 58 (35), 12102–12106. doi:10.1002/anie.201906312

Conflict of Interest: The authors declare that the research was conducted in the absence of any commercial or financial relationships that could be construed as a potential conflict of interest.

The handling Editor declared a past co-authorship with one of the authors BY.

ORIGINAL RESEARCH
published: 02 February 2022
doi: 10.3389/fchem.2021.810458

Room Temperature Phosphorescence Emission From Multi-States

Xiaofeng Zhang, Beibei Zhang, Ji Luo, Song Guo, Chun Wei* and Yongyang Gong**

Guangxi Key Laboratory of Optical and Electronic Materials and Devices, College of Materials Science and Engineering, Guilin University of Technology, Guilin, China

Organic room temperature phosphorescence (RTP) materials have received considerable attention due to their fascinating photophysical properties. During the past decade, various organic luminogens exhibiting RTP emission in solid states were reported. However, the phosphorescence emission of organic compounds can hardly be observed in their solutions at room temperature. Herein, we reported two fluorene derivatives that can emit RTP in degassed organic solvents, polymer doped film, and crystalline states. Furthermore, those RTP luminogens emitted different colors with different phosphorescence lifetimes in multi-states. These results indicated that the phosphorescence performance can be adjusted flexibly in different condensed states. To our knowledge, this is the first example possessing diverse organic RTP at multi-states, including solution state.

Keywords: room temperature phosphorescence, solution state, organic small molecule, fluorene derivative, triplet state

Edited by:
Abhijit Patra,
Indian Institute of Science Education and Research, Bhopal, India

Reviewed by:
Subi Jacob George,
Jawaharlal Nehru Centre for Advanced Scientific Research, India
Renren Deng,
Zhejiang University, China

****Correspondence:***
Song Guo
529801643@qq.com
Chun Wei
1986024@glut.edu.cn
Yongyang Gong
yygong@glut.edu.cn

Specialty section:
This article was submitted to Physical Chemistry and Chemical Physics,
a section of the journal Frontiers in Chemistry

Received: *07 November 2021*
Accepted: *31 December 2021*
Published: *02 February 2022*

Citation:
Zhang X, Zhang B, Luo J, Guo S, Wei C and Gong Y (2022) Room Temperature Phosphorescence Emission From Multi-States. Front. Chem. 9:810458. doi: 10.3389/fchem.2021.810458

INTRODUCTION

Organic RTP attracts tremendous attention because of its unique characters, especially the long-lived triplet states, and exhibits immense potential applications in optoelectronic devices, information encryption, emergency exit sign, chemical sensors, bioimaging, and so on (Lin et al., 2018; Wang et al., 2019b; Gu et al., 2019; He et al., 2019; Yang J. et al., 2020; Yang Z. et al., 2020; Zhao et al., 2020; Liu R. et al., 2021; Garain et al., 2021; Zhu et al., 2021). In recent years, various strategies have been utilized to achieve RTP luminogens; for example, the introduction of heavy atom or aromatic carbonyl can effectively boost the spin-orbit coupling (SOC) constant and then facilitate the intersystem crossing (ISC) rates between the excited singlet (S_1) and triplet states (T_n), which is one of the most widely used strategy (Zhao et al., 2020; Zhang et al., 2021). Besides, host-guest doping (Notsuka et al., 2017; Qu et al., 2019; Lei et al., 2020; Liu X. et al., 2021; Guo et al., 2021), crystallization (Yuan et al., 2010; Gong et al., 2015; Wu et al., 2019; Nitti et al., 2020), H-aggregation (An et al., 2015; Yuan et al., 2019; Zhang L. et al., 2020; Li et al., 2021), polymer skeleton (Wang et al., 2019a; Du et al., 2019; Gao and Ma, 2021; Meng et al., 2021; Yan et al., 2021; Zhang et al., 2021), and other methods (Baroncini et al., 2017; Li et al., 2019; Wen et al., 2019), which can strengthen the rigidity of the structure, were also proposed towards the high-efficiency of RTP.

However, the most reported organic luminogens emitting phosphorescence are in solid states at room temperature or in solution state at 77 K, owing to the unstable triplet excited states, which can be easily quenched by molecular vibration and the collision with other media. Although several literature has reported efficient RTP in the common organic solvents at 77 K, these solvents are not completely liquid at 77 K. Thus, it is extremely difficult and of great attractiveness to exploit novel purely organic single molecular phosphorescence not only in the solid state but also in the solvent state at room temperature. In 1978, Turro et al. reported phosphorescence of naphthalene and triphenylene in purified and degassed solutions of 1, 2-dibromoethane. In addition, 1, 4-dibromonaphthalene in common solvent acetonitrile (nitrogen purged) can exhibit obvious phosphorescence at room temperature (Turro et al., 1978). In 2018, George et al. reported a supramolecular assembly using inorganic layered silicate and bromine substituted naphthalene derivatives, which showed bright phosphorescence in dilute aqueous solution and amorphous films under ambient conditions. Liu group reported enhancement ultralong bright RTP in solution by host-guest complexation interaction between phosphors and cucurbit[6, 7, 8]urils (Zhang Z. Y. et al., 2020).

Most recently, various luminogens exhibiting ambient phosphorescence in the aqueous phase were reported. Hisaeda et al. reported naphthalenediimide halobenzoate triad molecules, which exhibited evident red RTP in the suspended aqueous solution (Ono et al., 2021). However, because of the hydrophobicity of these molecules, the solution was not true solution. Ma group developed a flexible porous water-soluble supramolecular organic framework, which could efficiently exhibit phosphorescence in both the aqueous phase and film state at room temperature (Xu et al., 2021). Yang group reported a water-resistant carbon dot with a high phosphorescent quantum yield of 23% in aqueous environment and this material was successfully applied for the fingerprint recognition and advanced information encryption (Su et al., 2021). Su et al. prepared a kind of carbon dot composites using a molten salt method, which exhibited bright RTP with a quantum yield of 26.4% and a lifetime of 1.28 s. In particular, their aqueous dispersion showed obvious RTP behaviors, and then these phosphors were utilized to detect temperature and pH in the aqueous phase (Su et al., 2021). Liang et al. reported a kind of silica capsulated water-soluble carbon nanodots with the lifetime and phosphorescence quantum yield of 1.86 s and 11.6%, respectively. These features allowed them to apply for afterglow imaging *in vivo*/*in vitro* (Liang et al., 2020). In spite of extensive efforts which have been contributed to developing RTP in both solvent and solid state, including crystal and amorphousness, up to now, very few species, especially purely organic molecule, can achieve the requirements, let alone the effective regulation of the photophysical properties in different states.

Fluorene and its derivatives are a kind of very important organic chromophores with π conjugation, which have been often used in organic semiconductor devices (Xie et al., 2012). Rational modification of fluorene derivatives can achieve extraordinary photophysical properties [delayed fluorescence (Liang et al., 2018; Liu et al., 2020; Zhu et al., 2020), RTP (Bruzzone and Badía, 1990; Wang et al., 2018; Chen et al., 2021), mechanochromism (Matsuo et al., 2019; Tan et al., 2020), and so forth]. In 2013, Takeuchi et al. reported a fluorene derivative substituted by bromo and formyl groups, exhibiting distinct phosphorescence in some common organic solvents at room temperature with the phosphorescence quantum yield of 5.9% in chloroform at 298 K under N_2 atmosphere (Xu et al., 2013). However, this derivative was a colorless viscous liquid at room temperature (Vijayakumar et al., 2011).

Herein, two traditional and frequently used intermediates of photoelectric materials, 2-bromo-9,10-diphenylfluorene (**BDF**) and 2,7-dibromo-9,10-diphenylfluorene (**DBDF**), were carefully selected to investigate their phosphorescent properties. In these two compounds, the twisted structure and large steric hindrance effect of 9,10-diphenylfluorene can suppress the detrimental π-π stacking and reinforce the rigidity of the molecules. In addition, the modified bromine atom can promote the ISC process and increase SOC constant on account of the heavy-atom effect. Interestingly, two compounds exhibited obvious RTP not merely in crystalline state and amorphous film, but also in the solution state. Impressively, emitter **BDF** showed different maximum phosphorescent emission peaks at different states. In brief, the generation and efficacious adjustment of triplet energy level at multi-states, especially the solution state, was achieved successfully. To our knowledge, this is the first purely organic molecule possessing diverse RTP at multi-states, including solution state.

RESULTS AND DISCUSSION

Compounds **BDF** and **DBDF** (**Figure 1A**) were purchased commercially and purified by recrystallization. Then, the chemical structures were fully characterized and confirmed by nuclear magnetic resonance (NMR) spectroscopy, high-performance liquid chromatography (HPLC), thin-layer chromatography (TLC), and X-ray crystallography (CCDC: 2109386-2109387) (**Supplementary Figures S1–S9**; **Supplementary Table S1**).

The absorption spectra of **BDF** and **DBDF** in chloroform at the concentration of 2×10^{-5} M exhibited the character of spin-allowed π-π* transition with the maximal peak at 312 and 317 nm (**Figure 1**), respectively. Then, the emission behaviors of **BDF** and **DBDF** in chloroform solutions (2.0×10^{-5} M) at room temperature were investigated. The prompt (FL) spectra were carried out as shown in **Figure 1B**. The emission cannot be observed with the naked eye for the two solutions when excited at 290 nm under air atmosphere. However, the FL spectra for **BDF** and **DBDF** showed one peak at 320 and 325 nm, with the corresponding quantum efficiency of 0.54 and 0.64%, respectively, assigned to the ultraviolet fluorescence unambiguously. Then, the FL spectra of **BDF** and **DBDF** in different common solvents under air atmosphere were measured in detail. As shown in **Supplementary Figure S10**, the peak profile is almost corresponding to that of the chloroform solution. Subsequently, the FL behaviors of their solutions bubbled argon gas (Ar) for 30 min were studied. **BDF** and **DBDF** in chloroform solution deaerated with Ar showed bright blue and green emission color, respectively, when excited at 365 nm as shown in **Figure 1A**. Delayed emission (PL) spectra (delay time, t_d = 0.1 ms) of **BDF** and **DBDF** (**Supplementary Figure S11**) peaked at 416 and 440 nm with the corresponding lifetimes/quantum efficiency of 5.61 μs/1.51% and 6.49 μs/1.32%, respectively. This phenomenon cannot be observed under air conditions, which can be ascribed to the phosphorescent emission without doubt. It is important to note that there exist very rare organic compounds

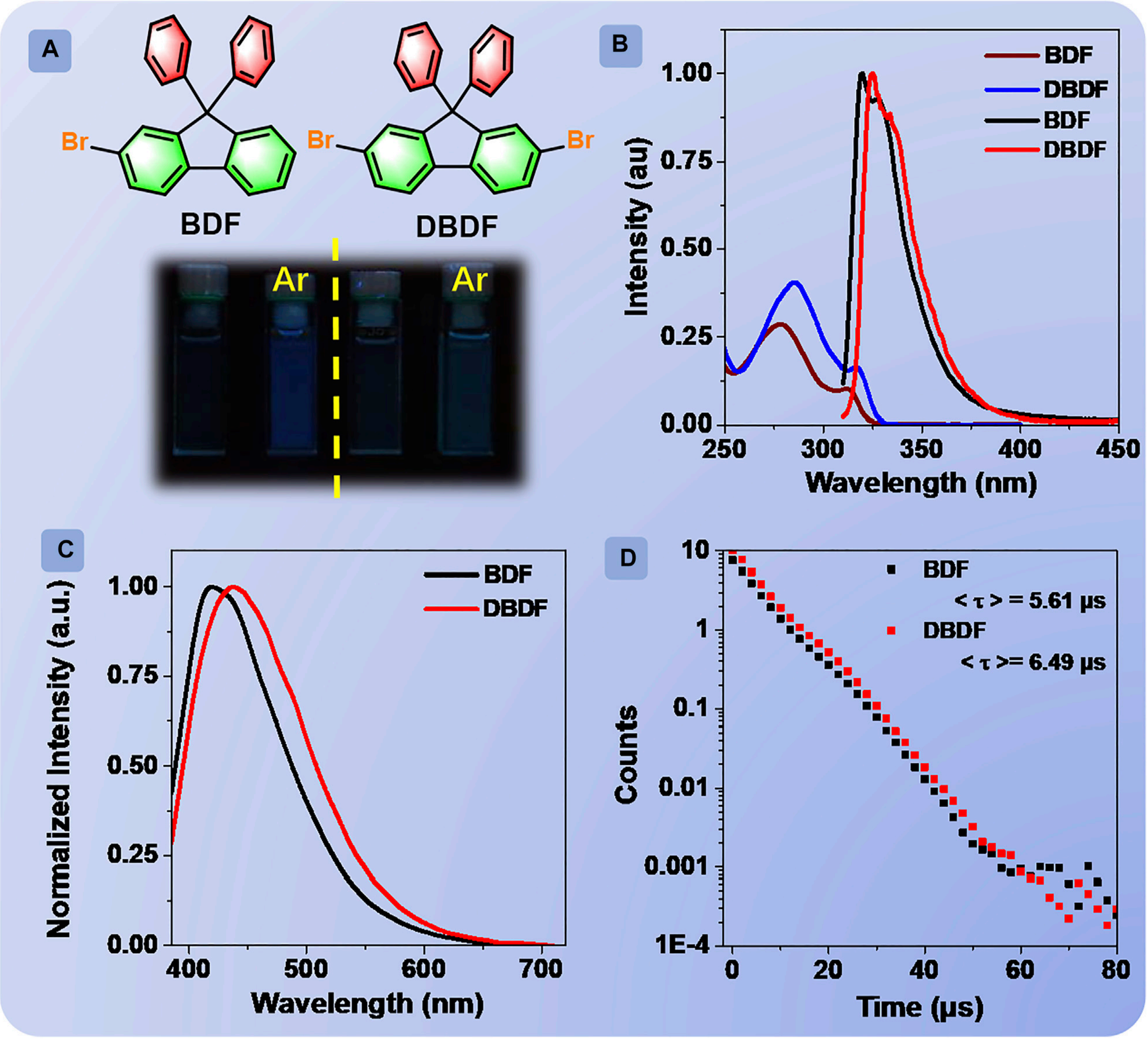

FIGURE 1 | Chemical structures of **BDF** and **DBDF (A)**; absorption (blue and brown line) and emission (black and red line) spectra of **BDF** and **DBDF** in distilled chloroform solution **(B)**; emission spectra of **BDF** and **DBDF** in Ar degassed chloroform solution **(C)**; phosphorescence decay curves of **BDF** and **DBDF** in Ar degassed chloroform solution **(D)**; luminescent photographs of **BDF** (left) and **DBDF** (right) in chloroform and Ar degassed chloroform solutions under irradiation at 365 nm UV light, concentration: 2.0 × 10^{-5} M **(A)**.

emitting phosphorescence in solution at room temperature (Shu et al., 2020). The excitation spectra of two compounds for the phosphorescent peak showed that the optimal excitation wavelengths for **BDF** and **DBDF** were both 365 nm as shown in **Supplementary Figure S12**. In addition, the phosphorescent intensity of the two compounds at the maximum emission peak is proportional to the concentration of the solutions (**Supplementary Figure S13**), suggesting that the phosphorescent emission originates from the monomeric species and no molecular interactions existed in solution. Besides, the onset of the phosphorescence spectra of BDF and DBDF can be observed in **Figure 1C**, peaking at 660 and 675 nm, respectively. The onset of the fluorescence spectra of BDF and DBDF can be observed in **Figure 1B**, peaking at 440 and 425 nm, respectively. Then, ΔE_{ST} of BDF and DBDF can be calculated as 0.94 and 1.08 eV, respectively.

Then, the properties of the excited state in crystals were studied systematically. The XRD patterns of **BDF** and **DBDF** exhibited evident diffraction peaks as shown in **Supplementary Figure S14**, confirming the excellent crystallinity. **BDF** and **DBDF** showed blue (**Figure 2A**) and green colors under 312 nm UV lamp, respectively. The FL spectrum of **BDF** (**Figure 2B**, black line) peaked at 411 nm with the lifetime/ quantum efficiency of 0.81 ns/7.93% (**Supplementary Figure**

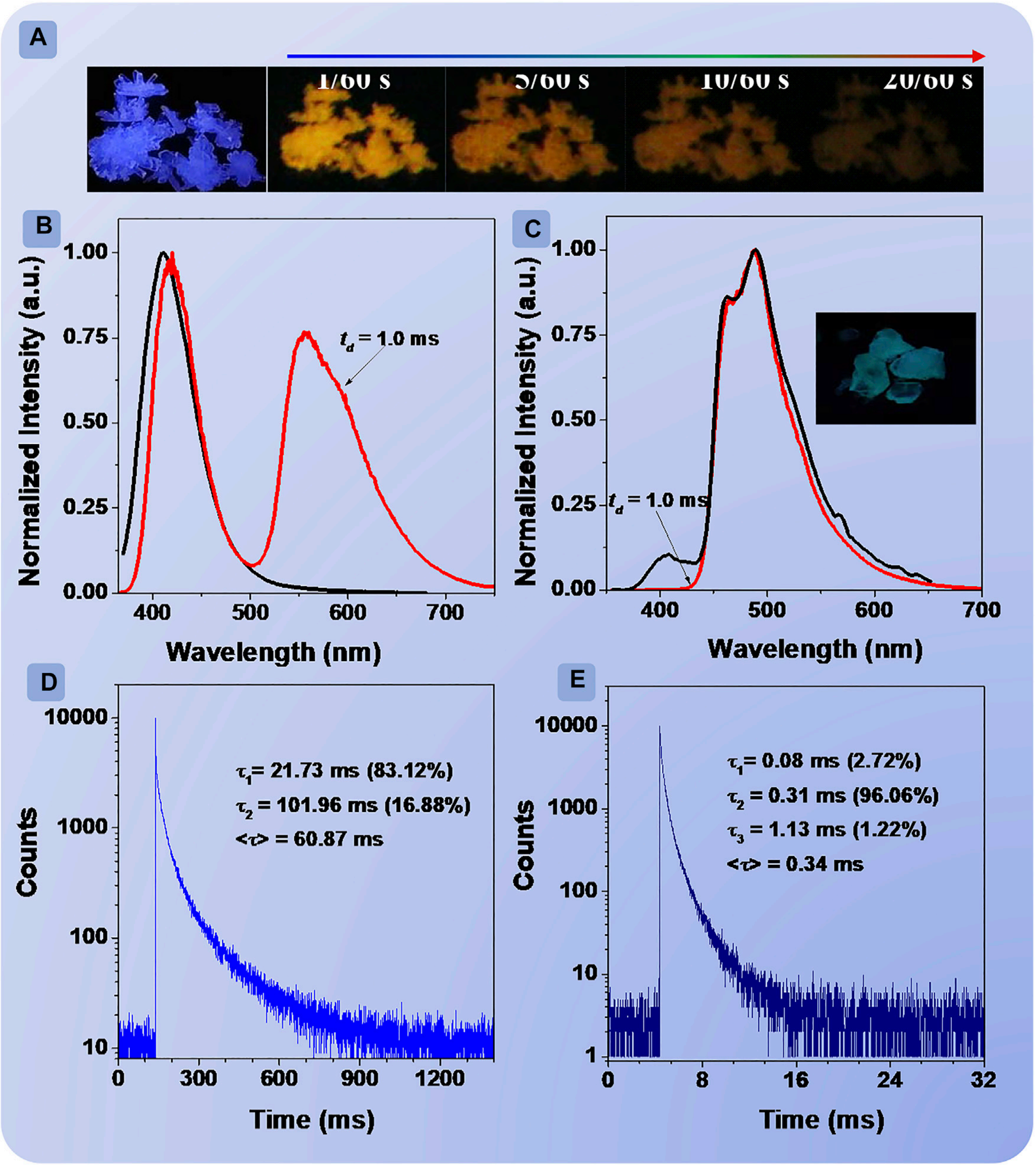

FIGURE 2 | Photographs of **BDF** crystals under irradiation of 312 nm UV light at different delay times after turning off the UV lamp **(A)**; prompt (black line) and delay (red line) spectra of **BDF (B)** and **DBDF (C)**, delay time = 1.0 ms; phosphorescence decay curves of crystalline powders of **BDF (D)** and **DBDF (E)** monitored at 556 and 489 nm, respectively.

S15, black line), and **DBDF** (**Figure 2C**, black line) showed a weak peak at 408 nm (0.66 ns/1.38%) (**Supplementary Figure S15**, red line) and an intense peak at 491 nm. After ceasing the 365 nm UV lamp, **BDF** exhibited orange phosphorescence that could be observed with the naked eye (**Figure 2A**). However, no obvious emission can be observed from **DBDF** (**Figure 2C**). Next, the PL spectrum (t_d = 1.0 ms) of **BDF** was carried out (**Figure 2B**, red line), which exhibited two peaks at 417 and 556 nm, respectively. The peak at 417 nm with a lifetime of 5.72 μs was similar to the prompt spectra of **BDF**. The temperature-dependent lifetime experiment of BDF crystal at 417 nm was carried out as shown in **Supplementary Figure S16**. Overall, results showed that the lifetime declined accompanied by an increase in temperature, which may be assigned to the delayed fluorescent (DF). Meanwhile, the peak at 556 nm was ascribed to the phosphorescent emission with a lifetime of 60.87 ms. Besides, the PL spectra (t_d = 1.0 ms) of **DBDF** (**Figure 2C**, red line), similar to its FL spectra, showed one peak at 489 nm with a

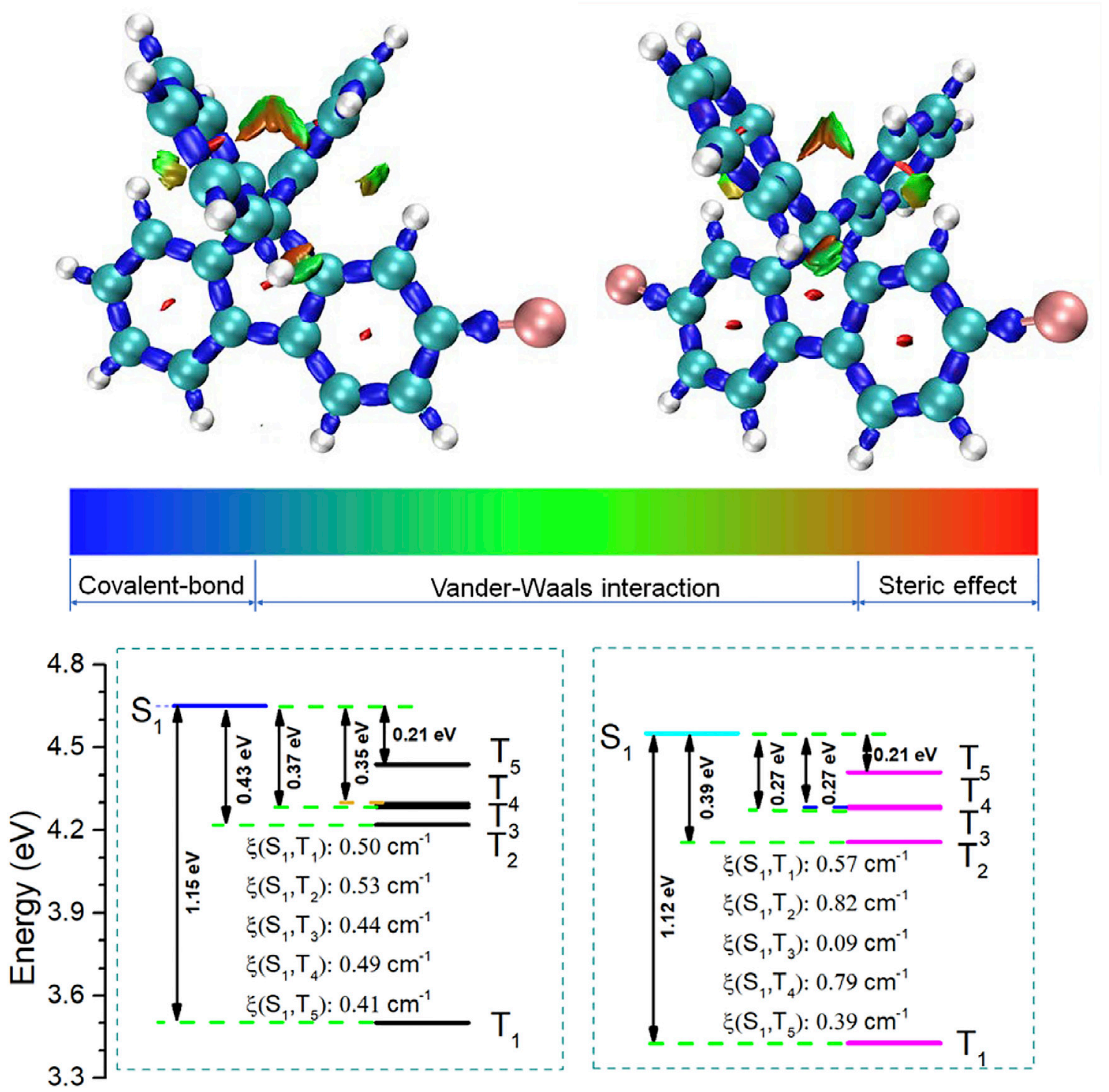

FIGURE 3 | Isosurface maps of IRI = 1.0; the grid spacing for IRI is 0.12 Bohr; and red, green, and blue colors mean steric hindrance, van der Waals force, and covalent bond intramolecular, respectively (top). The energy level diagrams of **BDF** and **DBDF** (S_0 = 0 eV). SOC: ξ (S_1–T_n) (cm^{-1}) (bottom).

lifetime of 0.34 ms, indicating that the prompt emission of **DBDF** was mainly composed of the phosphorescent emission. Such a relatively short lifetime resulted in no obvious afterglow visible to the naked eye for **DBDF**. Compared with **BDF**, it was unexpected that the introduction of an extra bromine atom had a great impact on the phosphorescence behaviors.

Furthermore, the FL and PL spectra of **BDF** and **DBDF** at crystalline state under various temperatures were investigated as shown in **Supplementary Figure S16**. The FL and PL spectra of **BDF** shared similar outline peaking at 412 and 508 nm at 78 K, at the excitation of 300 nm under vacuum. The intensity of the peak at 412 nm assigned to DF emission increased when the temperature raised to 150 K from 78 K. Then, it gradually decreased with the increase in temperature due to the violent vibration and collision of the excitons. Impressively, the intensity of phosphorescent emission decreased dramatically as the temperature increased to 400 K from 78 K, accompanied by a great redshift of the wavelength from 508 to 570 nm. Meanwhile, the intensity is in inverse proportion to the increase in temperature. As for compound **DBDF**, the phosphorescent emission also decreased along with the increase in temperature. Interestingly, the phosphorescent wavelength showed a blueshift from 507 to 461/487 nm when the temperature increased to about 200 K from 78 K. This phenomenon may result from the destruction of the balance between conjugation effect and inductive effect of the halogen atom bromine as the variation of the temperature.

To gain further insights into the phosphorescent mechanism in solution and crystalline state, crystal structures of the **BDF** and **DBDF** were studied as shown in **Supplementary Figures S8, S9**

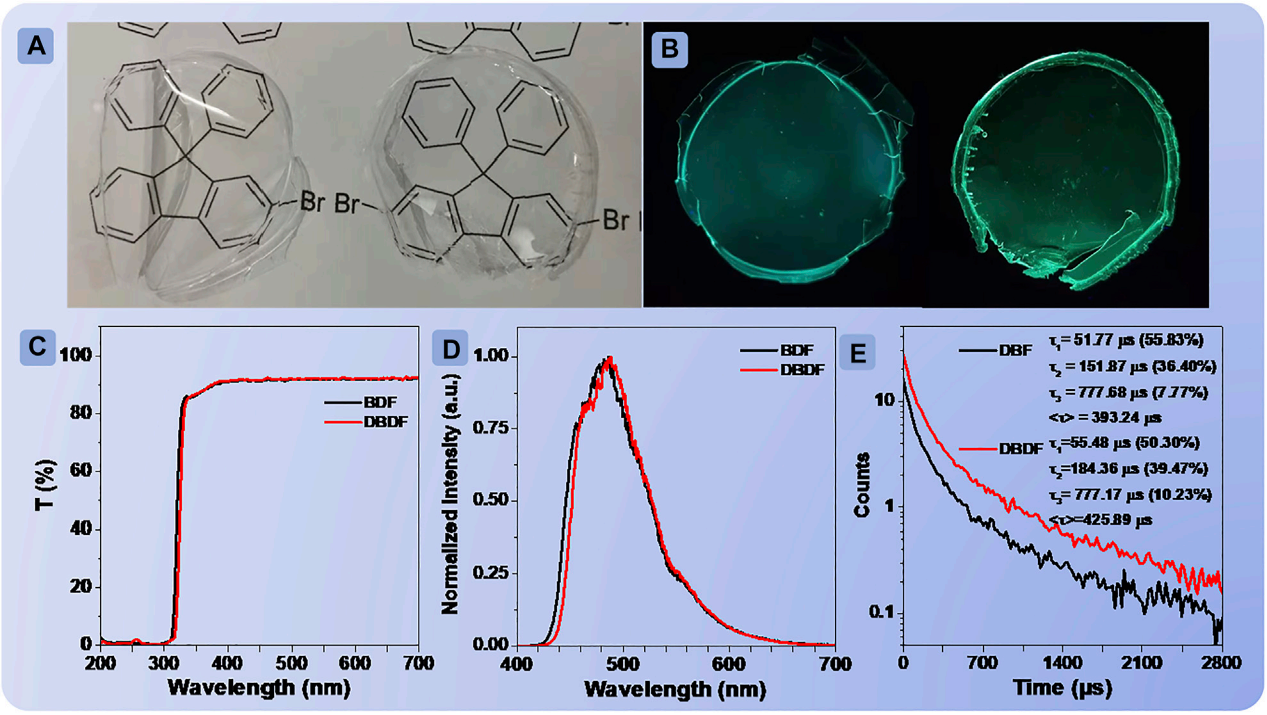

FIGURE 4 | Photographs of **BDF** and **DBDF (A)** doped into PMMA films under sunlight; transmittance curves of the PMMA films doped with **BDF** and **DBDF (C)**; photographs of PMMA films doped with **BDF** and **DBDF (B)** under irradiation at 312 nm UV light; phosphorescence emission spectra **(D)** and lifetimes **(E)** of the two films at room temperature.

and **Supplementary Table S1**. In the crystalline state, they both exhibited C-H···π (2.859 Å) interaction. In addition, **BDF** possessed C-H···H-C (2.358 Å) interaction, and **DBDF** showed numerous Br···π interactions with a distance from 3.394 to 3.541 Å. These short contacts can effectively enhance the rigidity of the structure and decrease the non-radiative transition of the triplet state excitons, thereby boosting the ISC process, increasing the SOC constant, and then promoting the phosphorescent emission. Additionally, the dihedral angles between two benzene rings connected by the sp^3 carbon at 9/10 position of fluorine for **BDF** and **DBDF** were 114.71° and 111.83°, respectively, which can avoid the π-π stacking.

In order to further understand the RTP behaviors, theory calculation was conducted using a recently reported method, a new real space function named interaction region indicator (IRI) (Lu and Chen, 2021), which can visually reveal chemical bonding and weak interaction regions by Multiwfn (Lu and Chen, 2012). As shown in **Figure 3**, the IRI analysis results indicated that steric hindrance and van der Waals force restricted the free rotation of the benzene ring at the 9 and 10 positions of fluorene. Therefore, in addition to the heavy atom effect of Br atoms, the RTP performance in solution is also closely related to the steric hindrance, which was disadvantageous to the emission via the generation of excimers, and it may be responsible for the effective RTP in solutions. Moreover, the SOC constants and energy gap (Eg) between single and triplet states in the gas state calculated by the time-dependent density functional theory (TD-DFT) are shown in **Figure 3** (**Supplementary Figure S17**; **Supplementary Tables S2–S4**). According to the Franck–Condon principle, the ISC rate is mainly determined by the E_g and SOC constants between excited singlet and triplet states (Gong et al., 2015). Small energy gaps and large SOC constants are favorable for the ISC process. There are five excited triplet states ($T_1 \sim T_5$) lying below the first excited singlet state (S_1), suggesting the possible occurrence of ISC process of $S_1 \leftrightarrow T_1$, $S_1 \leftrightarrow T_2$, $S_1 \leftrightarrow T_3$, $S_1 \leftrightarrow T_4$, $S_1 \leftrightarrow T_5$. Taking compound **BDF** for example, the SOC constants and the corresponding E_g of the **BDF** are S_1–T_1 (0.50 cm^{-1}, 1.15 eV) and S_1–T_5 (0.41 cm^{-1},0.21 eV), respectively. Appropriate SOC constant and low energy level gap in S_1-T_n made the ISC process possible to achieve RTP emission. These calculation results were in good agreement with the experimental results.

Then, the films fabricated by doping the phosphors into polymethyl methacrylate (PMMA) with a mass ratio of 1:100 were presented to investigate the monomolecular phosphorescent performance. The photographs of the films are shown in **Figure 4A**. It can be seen that the films did not block the information behind them. Subsequently, the transmittance spectra of the films were measured, as shown in **Figure 4E**. The results showed that few percentages of the light could be absorbed, and they exhibited excellent transmittance (≥87%) from the visible light regions of 336–700 nm. The XRD patterns of the films (**Supplementary Figure S18**) were recorded and showed no evident diffraction peaks, confirming the amorphous state. The fluorescent and phosphorescent behaviors of the two films were carried out at ambient conditions. Interestingly, the FL/PL spectra and phosphorescence lifetime of **BDF** and **DBDF** both exhibited similar emission performance as shown in **Figures 4D,E** and **Supplementary Figure S19**, peaking at 480/480 and 490/490 nm, with the corresponding lifetimes/quantum efficiency of 393.24 ms/4.96% and 425.89 ms/6.31%, respectively. The low-temperature FL/PL spectra of the two compounds at 78 K showed the same profile but with fine structure (**Supplementary Figure S20**). On the one hand, the polymer matrix restricts intramolecular rotation and enhances the radiation transition. On the other hand, PMMA doped film can avoid the invasion of water and oxygen to the matrix effectively. This is similar to the previously reported RTP emission from small molecules that doped polymer films (Cheng et al., 2018; Garain et al., 2021).

CONCLUSION

In summary, in this work, we reported two fluorene derivatives that can emit RTP in degassed organic solvents: polymer doped film and crystalline states. Furthermore, compound **BDF** emitted blue, green, and yellow RTP in solution, film, and crystal states. The phosphorescence lifetime at room temperature ranges from microseconds to milliseconds. These results indicate that the emission color and lifetime of RTP can be adjusted flexibly by different condensed states. In addition to the heavy atom effect of Br, the intra-molecular steric effect and van der Waals force, which can restrict intramolecular rotation, played a vital role in the phosphorescence emission of the solution. To our knowledge, this is the first example of organic RTP at multi-states, including solution. The present organic RTP emission from multi-states would be beneficial for the exploitation of novel RTP luminogens and capable of being applied in the fields of organic optoelectronic devices, biosensors, data storage, and so forth.

DATA AVAILABILITY STATEMENT

The original contributions presented in the study are included in the article/**Supplementary Material**. Further inquiries can be directed to the corresponding authors.

AUTHOR CONTRIBUTIONS

XZ, BZ, JL synthesized and characterized materials; SG, CW, YG conceived the idea, designed research and wrote the manuscript.

FUNDING

This research was funded by the National Natural Science Foundation of China (51863006, 52163017); the Project of Guangxi Natural Science Foundation (2020GXNSFBA297098, 2021GXNSFAA220047); the Project of Thousand Outstanding Young Teachers' Training in Higher Education Institutions of Guangxi; and the Open Project Program of Guangxi Key Laboratory of Optical and Electronic Materials and Devices (20AA-2, 20AA-10).

ACKNOWLEDGMENTS

The authors acknowledge the National Natural Science Foundation and Key Laboratory of New Processing Technology for Nonferrous Metal & Materials, Ministry of Education/Guangxi Key Laboratory of Optical and Electronic Materials and Devices, Guilin University of Technology, Guilin 541004, China.

SUPPLEMENTARY MATERIAL

The Supplementary Material for this article can be found online at: https://www.frontiersin.org/articles/10.3389/fchem.2021.810458/full#supplementary-material

REFERENCES

An, Z., Zheng, C., Tao, Y., Chen, R., Shi, H., Chen, T., et al. (2015). Stabilizing Triplet Excited States for Ultralong Organic Phosphorescence. *Nat. Mater* 14 (7), 685–690. doi:10.1038/nmat4259

Baroncini, M., Bergamini, G., and Ceroni, P. (2017). Rigidification or Interaction-Induced Phosphorescence of Organic Molecules. *Chem. Commun.* 53 (13), 2081–2093. doi:10.1039/c6cc09288h

Bruzzone, L., and Badía, R. (1990). Room-temperature Phosphorescence of Impure Fluorene. *Anal. Lett.* 23 (6), 1113–1121. doi:10.1080/00032719008053450

Chen, X., Dai, W., Wu, X., Su, H., Chao, C., Lei, Y., et al. (2021). Fluorene-based Host-Guest Phosphorescence Materials for Information Encryption. *Chem. Eng. J.* 426, 131607. doi:10.1016/j.cej.2021.131607

Cheng, Z., Shi, H., Ma, H., Bian, L., Wu, Q., Gu, L., et al. (2018). Ultralong Phosphorescence from Organic Ionic Crystals under Ambient Conditions. *Angew. Chem. Int. Ed.* 57 (3), 678–682. doi:10.1002/anie.201710017

Du, L.-L., Jiang, B.-L., Chen, X.-H., Wang, Y.-Z., Zou, L.-M., Liu, Y.-L., et al. (2019). Clustering-triggered Emission of Cellulose and its Derivatives. *Chin. J. Polym. Sci.* 37 (4), 409–415. doi:10.1007/s10118-019-2215-2

Gao, H., and Ma, X. (2021). Recent Progress on Pure Organic Room Temperature Phosphorescent Polymers. *Aggregate* 2 (4), e38. doi:10.1002/agt2.38

Garain, S., Kuila, S., Garain, B. C., Kataria, M., Borah, A., Pati, S. K., et al. (2021). Arylene Diimide Phosphors: Aggregation Modulated Twin Room Temperature Phosphorescence from Pyromellitic Diimides. *Angew. Chem. Int. Ed.* 60 (22), 12323–12327. doi:10.1002/anie.202101538

Gong, Y., Zhao, L., Peng, Q., Fan, D., Yuan, W. Z., Zhang, Y., et al. (2015). Crystallization-induced Dual Emission from Metal- and Heavy Atom-free Aromatic Acids and Esters. *Chem. Sci.* 6 (8), 4438–4444. doi:10.1039/c5sc00253b

Gu, L., Shi, H., Bian, L., Gu, M., Ling, K., Wang, X., et al. (2019). Colour-tunable Ultra-long Organic Phosphorescence of a Single-Component Molecular crystal. *Nat. Photon.* 13 (6), 406–411. doi:10.1038/s41566-019-0408-4

Guo, S., Dai, W., Chen, X., Lei, Y., Shi, J., Tong, B., et al. (2021). Recent Progress in Pure Organic Room Temperature Phosphorescence of Small Molecular Host-

Guest Systems. *ACS Mater. Lett.* 3 (4), 379–397. doi:10.1021/acsmaterialslett.1c00062

He, G., Du, L., Gong, Y., Liu, Y., Yu, C., Wei, C., et al. (2019). Crystallization-Induced Red Phosphorescence and Grinding-Induced Blue-Shifted Emission of a Benzobis(1,2,5-Thiadiazole)-Thiophene Conjugate. *ACS Omega* 4 (1), 344–351. doi:10.1021/acsomega.8b02805

Lei, Y., Dai, W., Guan, J., Guo, S., Ren, F., Zhou, Y., et al. (2020). Wide-Range Color-Tunable Organic Phosphorescence Materials for Printable and Writable Security Inks. *Angew. Chem. Int. Ed.* 59 (37), 16054–16060. doi:10.1002/anie.202003585

Li, F., Guo, S., Qin, Y., Shi, Y., Han, M., An, Z., et al. (2019). Achieving Dual Persistent Room-Temperature Phosphorescence from Polycyclic Luminophores via Inter-/Intramolecular Charge Transfer. *Adv. Optical Mater.* 7 (19), 1900511. doi:10.1002/adom.201900511

Li, S., Fu, L., Xiao, X., Geng, H., Liao, Q., Liao, Y., et al. (2021). Regulation of Thermally Activated Delayed Fluorescence to Room-Temperature Phosphorescent Emission Channels by Controlling the Excited-States Dynamics via J- and H-Aggregation. *Angew. Chem. Int. Ed.* 60 (33), 18059–18064. doi:10.1002/anie.202103192

Liang, J.-J., Li, Y., Yuan, Y., Li, S.-H., Zhu, X.-D., Barlow, S., et al. (2018). A Blue Thermally Activated Delayed Fluorescence Emitter Developed by Appending a Fluorene Moiety to a Carbazole Donor with Meta-Linkage for High-Efficiency OLEDs. *Mater. Chem. Front.* 2 (5), 917–922. doi:10.1039/c7qm00605e

Liang, Y.-C., Gou, S.-S., Liu, K.-K., Wu, W.-J., Guo, C.-Z., Lu, S.-Y., et al. (2020). Ultralong and Efficient Phosphorescence from Silica Confined Carbon Nanodots in Aqueous Solution. *Nano Today* 34, 100900. doi:10.1016/j.nantod.2020.100900

Lin, Z., Kabe, R., Nishimura, N., Jinnai, K., and Adachi, C. (2018). Organic Long-Persistent Luminescence from a Flexible and Transparent Doped Polymer. *Adv. Mater.* 30 (45), 1803713. doi:10.1002/adma.201803713

Liu, H., Liu, H., Fan, J., Guo, J., Zeng, J., Qiu, F., et al. (2020). An Effective Design Strategy for Robust Aggregation-Induced Delayed Fluorescence Luminogens to Improve Efficiency Stability of Nondoped and Doped OLEDs. *Adv. Optical Mater.* 8 (21), 2001027. doi:10.1002/adom.202001027

Liu, R., Ding, B., Liu, D., and Ma, X. (2021). Switchable Circularly Polarized Room-Temperature Phosphorescence Based on Pure Organic Amorphous Binaphthyl Polymer. *Chem. Eng. J.* 421, 129732. doi:10.1016/j.cej.2021.129732

Liu, X., Dai, W., Qian, J., Lei, Y., Liu, M., Cai, Z., et al. (2021). Pure Room Temperature Phosphorescence Emission of an Organic Host-Guest Doped System with a Quantum Efficiency of 64. *J. Mater. Chem. C* 9 (10), 3391–3395. doi:10.1039/d1tc00403d

Lu, T., and Chen, F. (2012). Multiwfn: a Multifunctional Wavefunction Analyzer. *J. Comput. Chem.* 33 (5), 580–592. doi:10.1002/jcc.22885

Lu, T., and Chen, Q. (2021). Interaction Region Indicator: A Simple Real Space Function Clearly Revealing Both Chemical Bonds and Weak Interactions**. *Chem. Methods* 1 (5), 231–239. doi:10.1002/cmtd.202100007

Matsuo, Y., Wang, Y., Ueno, H., Nakagawa, T., and Okada, H. (2019). Mechanochromism, Twisted/Folded Structure Determination, and Derivatization of (N -Phenylfluorenylidene)acridane. *Angew. Chem.* 131 (26), 8854–8859. doi:10.1002/anie.20190263610.1002/ange.201902636

Meng, Y., Guo, S., Jiang, B., Zhang, X., Zou, L., Wei, C., et al. (2021). Boosting the Humidity Resistance of Nonconventional Luminogens with Room Temperature Phosphorescence via Enhancing the Strength of Hydrogen Bonds. *J. Mater. Chem. C* 9 (27), 8515–8523. doi:10.1039/d1tc01271a

Nitti, A., Botta, C., Forni, A., Cariati, E., Lucenti, E., and Pasini, D. (2020). Crystallization-induced Room-Temperature Phosphorescence in Fumaramides. *CrystEngComm* 22 (45), 7782–7785. doi:10.1039/D0CE01253J

Notsuka, N., Kabe, R., Goushi, K., and Adachi, C. (2017). Confinement of Long-Lived Triplet Excitons in Organic Semiconducting Host-Guest Systems. *Adv. Funct. Mater.* 27 (40), 1703902. doi:10.1002/adfm.201703902

Ono, T., Kimura, K., Ihara, M., Yamanaka, Y., Sasaki, M., Mori, H., et al. (2021). Room-Temperature Phosphorescence Emitters Exhibiting Red to Near-Infrared Emission Derived from Intermolecular Charge-Transfer Triplet States of Naphthalenediimide–Halobenzoate Triad Molecules. *Chem. Eur. J.* 27 (37), 9535–9541. doi:10.1002/chem.202100906

Qu, G., Zhang, Y., and Ma, X. (2019). Recent Progress on Pure Organic Room Temperature Phosphorescence Materials Based on Host-Guest Interactions. *Chin. Chem. Lett.* 30 (10), 1809–1814. doi:10.1016/j.cclet.2019.07.042

Shu, H., Li, H., Rao, J., Chen, L., Wang, X., Wu, X., et al. (2020). Room-temperature Phosphorescence from a Purely Organic Tetraphenylmethane Derivative with Formyl Groups in Both Solution and Crystalline States. *J. Mater. Chem. C* 8 (41), 14360–14364. doi:10.1039/D0TC04070C

Su, Q., Gan, L., and Yang, X. (2021). Achieving Room Temperature Phosphorescence in Aqueous Phase through Rigidifying the Triplet State and Information Encryption. *Appl. Surf. Sci.* 566, 150726. doi:10.1016/j.apsusc.2021.150726

Tan, S., Yin, Y., Chen, W., Chen, Z., Tian, W., and Pu, S. (2020). Carbazole-based Highly Solid-State Emissive Fluorene Derivatives with Various Mechanochromic Fluorescence Characteristics. *Dyes Pigm.* 177, 108302. doi:10.1016/j.dyepig.2020.108302

Turro, N. J., Lru, K.-C., Chow, M.-F., and Lee, P. (1978). Convenient and Simple Methods for the Observation of Phosphorescence in Fluid Solutions. Internal and External Heavy Atom and Micellar Effects. *Photochem. Photobiol.* 27 (5), 523–529. doi:10.1111/j.1751-1097.1978.tb07641.x

Vijayakumar, C., Sugiyasu, K., and Takeuchi, M. (2011). Oligofluorene-based Electrophoretic Nanoparticles in Aqueous Medium as a Donor Scaffold for Fluorescence Resonance Energy Transfer and white-light Emission. *Chem. Sci.* 2 (2), 291–294. doi:10.1039/C0SC00343C

Wang, D., Wang, X., Xu, C., and Ma, X. (2019a). A Novel Metal-free Amorphous Room-Temperature Phosphorescent Polymer without Conjugation. *Sci. China Chem.* 62 (4), 430–433. doi:10.1007/s11426-018-9383-2

Wang, J., Wang, C., Gong, Y., Liao, Q., Han, M., Jiang, T., et al. (2018). Bromine-Substituted Fluorene: Molecular Structure, Br-Br Interactions, Room-Temperature Phosphorescence, and Tricolor Triboluminescence. *Angew. Chem.* 130 (51), 17063–17068. doi:10.1002/anie.20181166010.1002/ange.201811660

Wang, X.-F., Xiao, H., Chen, P.-Z., Yang, Q.-Z., Chen, B., Tung, C.-H., et al. (2019b). Pure Organic Room Temperature Phosphorescence from Excited Dimers in Self-Assembled Nanoparticles under Visible and Near-Infrared Irradiation in Water. *J. Am. Chem. Soc.* 141 (12), 5045–5050. doi:10.1021/jacs.9b00859

Wen, Y., Liu, H., Zhang, S., Gao, Y., Yan, Y., and Yang, B. (2019). One-dimensional π-π Stacking Induces Highly Efficient Pure Organic Room-Temperature Phosphorescence and Ternary-Emission Single-Molecule white Light. *J. Mater. Chem. C* 7 (40), 12502–12508. doi:10.1039/C9TC04580E

Wu, H., Chen, Z., Chi, W., Bindra, A. K., Gu, L., Qian, C., et al. (2019). Structural Engineering of Luminogens with High Emission Efficiency Both in Solution and in the Solid State. *Angew. Chem. Int. Ed.* 58 (33), 11419–11423. doi:10.1002/anie.201906507

Xie, L.-H., Yin, C.-R., Lai, W.-Y., Fan, Q.-L., and Huang, W. (2012). Polyfluorene-based Semiconductors Combined with Various Periodic Table Elements for Organic Electronics. *Prog. Polym. Sci.* 37 (9), 1192–1264. doi:10.1016/j.progpolymsci.2012.02.003

Xu, C., Lin, X., Wu, W., and Ma, X. (2021). Room-temperature Phosphorescence of a Water-Soluble Supramolecular Organic Framework. *Chem. Commun.* 57 (79), 10178–10181. doi:10.1039/D1CC04786H

Xu, J., Takai, A., Kobayashi, Y., and Takeuchi, M. (2013). Phosphorescence from a Pure Organic Fluorene Derivative in Solution at Room Temperature. *Chem. Commun.* 49 (76), 8447–8449. doi:10.1039/C3CC44809F

Yan, Z. A., Lin, X., Sun, S., Ma, X., and Tian, H. (2021). Activating Room-Temperature Phosphorescence of Organic Luminophores via External Heavy-Atom Effect and Rigidity of Ionic Polymer Matrix**. *Angew. Chem. Int. Ed.* 60 (36), 19735–19739. doi:10.1002/anie.202108025

Yang, J., Fang, M., and Li, Z. (2020). Organic Luminescent Materials: The Concentration on Aggregates from Aggregation-induced Emission. *Aggregate* 1 (1), 6–18. doi:10.1002/agt2.2

Yang, Z., Xu, C., Li, W., Mao, Z., Ge, X., Huang, Q., et al. (2020). Boosting the Quantum Efficiency of Ultralong Organic Phosphorescence up to 52 % via Intramolecular Halogen Bonding. *Angew. Chem. Int. Ed.* 59 (40), 17451–17455. doi:10.1002/anie.202007343

Yuan, J., Wang, S., Ji, Y., Chen, R., Zhu, Q., Wang, Y., et al. (2019). Invoking Ultralong Room Temperature Phosphorescence of Purely Organic Compounds through H-Aggregation Engineering. *Mater. Horiz.* 6 (6), 1259–1264. doi:10.1039/c9mh00220k

Yuan, W. Z., Shen, X. Y., Zhao, H., Lam, J. W. Y., Tang, L., Lu, P., et al. (2010). Crystallization-Induced Phosphorescence of Pure Organic Luminogens at Room Temperature. *J. Phys. Chem. C* 114 (13), 6090–6099. doi:10.1021/jp909388y

Zhang, L., Li, M., Gao, Q.-Y., and Chen, C.-F. (2020). An Ultralong Room-Temperature Phosphorescent Material Based on the Combination of Small Singlet-Triplet Splitting Energy and H-Aggregation. *Chem. Commun.* 56 (31), 4296–4299. doi:10.1039/c9cc09636a

Zhang, T., Wu, Y., and Ma, X. (2021). Tunable Multicolor Room-Temperature Phosphorescence Including white-light Emission from Amorphous Copolymers. *Chem. Eng. J.* 412, 128689. doi:10.1016/j.cej.2021.128689

Zhang, Z. Y., Xu, W. W., Xu, W. S., Niu, J., Sun, X. H., and Liu, Y. (2020). A Synergistic Enhancement Strategy for Realizing Ultralong and Efficient Room-Temperature Phosphorescence. *Angew. Chem.* 132 (42), 18907–18913. doi:10.1002/ange.202008516

Zhao, W., He, Z., and Tang, B. Z. (2020). Room-temperature Phosphorescence from Organic Aggregates. *Nat. Rev. Mater.* 5 (12), 869–885. doi:10.1038/s41578-020-0223-z

Zhu, X.-D., Peng, C.-C., Kong, F.-C., Yang, S.-Y., Li, H.-C., Kumar, S., et al. (2020). Acceptor Modulation for Improving a spiro-type Thermally Activated Delayed Fluorescence Emitter. *J. Mater. Chem. C* 8 (25), 8579–8584. doi:10.1039/d0tc00743a

Zhu, Y., Guan, Y., Niu, Y., Wang, P., Chen, R., Wang, Y., et al. (2021). Ultralong Polymeric Room Temperature Phosphorescence Materials Fabricated by Multiple Hydrogen Bondings Resistant to Temperature and Humidity. *Adv. Optical Mater.* 9 (21), 2100782. doi:10.1002/adom.202100782

Conflict of Interest: The authors declare that the research was conducted in the absence of any commercial or financial relationships that could be construed as a potential conflict of interest.

frontiers in Chemistry

ORIGINAL RESEARCH
published: 17 March 2022
doi: 10.3389/fchem.2022.812602

Room Temperature Phosphorescence of Chlorine Doped Carbon Nitride Dots

Khemnath Patir[1,2] *and Sonit Kumar Gogoi*[1]*

[1]*Department of Chemistry, Gauhati University, Guwahati, India,* [2]*Department of Applied Science and Humanities, Assam University, Silchar, India*

Metal free room temperature phosphorescent materials have been the subject of considerable attention due to their potential applications in optoelectronic devices sensing, and security and safety signage. This study discusses how efficient fluorescent and phosphorescent chlorine doped carbon nitride dots (Cl-CNDs) were prepared by thermal treatment of guanidine hydrochloride. The Cl-CNDs prepared were characterized by field emission scanning electron microscope, dynamic light scattering, PXRD, EDX, Thermo gravimetric analysis, FT-IR, and UV-Visible spectroscopy. The Cl-CNDs exhibit a long phosphorescence lifetime of 657 ms and the phosphorescence quantum yield was found to be 2.32% upon being excited at 360 nm in ambient conditions. Formation of compact coreparticles via condensation along with hydrogen bonding of Cl-CNDs by its functional groups facilitate intersystem crossing and stabilizes the triplet states, favoring room temperature phosphorescence. The cost effective preparation and tunable optical properties of Cl-CNDs may find applications in security encryption and optoelectronic devices.

Keywords: guanidine hydrochloride, carbon nitride dots, blue fluorescence, room temperature phosphorescence, security encryption

Edited by:
Abhijit Patra,
Indian Institute of Science Education and Research, Bhopal, India

Reviewed by:
Anindya Datta,
Indian Institute of Technology Bombay, India
Wei Zeng,
Northwest Normal University, China

Correspondence:
Sonit Kumar Gogoi
skgogoi@gauhati.ac.in

Specialty section:
This article was submitted to Physical Chemistry and Chemical Physics,
a section of the journal Frontiers in Chemistry

Received: *10 November 2021*
Accepted: *31 January 2022*
Published: *17 March 2022*

Citation:
Patir K and Gogoi SK (2022) Room Temperature Phosphorescence of Chlorine Doped Carbon Nitride Dots.
Front. Chem. 10:812602.
doi: 10.3389/fchem.2022.812602

INTRODUCTION

Room temperature phosphorescence (RTP) materials with efficient luminescence have received a great deal of attention due to their potential applications in photocatalysis, security features, sensing and optoelectronic devices, etc. due to the longer lifetime of the triplet states (Braun and Heeger, 1991; Zhang et al., 2010; Meruga et al., 2012; Gan et al., 2018). Until the recent reports on carbon nanoparticle based organic phosphorescent materials, most of the materials with desirable RTP were metal doped inorganic and organometallic compounds (Chakraborty et al., 2016; Yang and Yan, 2016; Hu et al., 2020; Wei et al., 2021). However, these materials are inevitably expensive with low stability, and were toxic in nature.

Contrary to its metal based counterpart, the RTP phenomenon from organic materials is difficult to come by as it involves a spin-forbidden process of intersystem crossing (ISC) between the singlet and triplet states (Yuan et al., 2010). As a way of resolving these issues, two methodologies have been developed. The first approach aims to facilitate spin-orbit coupling by incorporating heteroatoms/groups such as phosphorus, nitrogen, aromatic carbonyl or heterocycles, heavy atoms, etc. This helps in adjusting the singlet and triplet state energy gaps to promote efficient ISC. Furthermore, it also helps in inducing non-covalent interactions like hydrogen and halogen bonding, etc. among the phosphorescing species, thus increasing the efficiency of the RTP process (Li et al., 2016; Gao et al., 2018; Long et al., 2018; Patir and Gogoi, 2019). In the second method, RTP is achieved by embedding the luminescent species in solid matrices such as polymer, silica, filter paper, crystals, etc., which again introduces weak interactions suppressing the non-radiative transitions, stabilizes the triplet excited states, and creates a good oxygen barrier in the composite systems (Zhao et al., 2011; Li et al., 2016; Chen et al., 2017).

Carbon nitride quantum dots (CNQD) as an emerging class of luminescent materials have stimulated extensive research in various fields, including bioimaging, chemical sensing, fluorescent marking, optoelectronic devices, etc. due to their excellent optical properties, simple synthesis process, low toxicity, and easy miscibility in different solvents (Liu et al., 2012; Song et al., 2016; Wang et al., 2016; Wang et al., 2017; Patir and Gogoi, 2018). Even though the fluorescent properties of CNQD have been extensively studied, its phosphorescence phenomenon and related applications remain lesser explored. On the other hand, similar luminescent carbon-based nanoparticles, carbon dots (CDs) have been extensively studied as phosphorescent materials in various matrix such as polyvinylalcohol (PVA), urea/biuret, polyurethane, potash alum, silica gel, double layer hydroxides, boric acid, etc. (Deng et al., 2013; Ding et al., 2015; Li et al., 2016; Tan et al., 2016; Bai et al., 2017; Joseph and Anappara, 2017; Li et al., 2019).

The quest for a brighter long-lasting afterglow drives the exploration of RTP materials. At the same time, easy and economic synthetic routes from benign precursors are much desired. Among the two strategies mentioned above, the heteroatom introduction strategy seems advantageous at present as it not only induces phosphorescence by providing mechanical rigidity and oxygen barrier but also the energy tunability of the electronic states; thus allowing control over the emission color of the phosphor.

The present study reports on a facile one step thermal method for synthesizing phosphorescent chlorine doped carbon nitride dots (Cl-CNDs) using low-cost guanidine hydrochloride as the precursor. The Cl-CNDs is highly miscible in water giving a clear dispersion with violet-blue fluorescence under UV irradiation. In powder form, Cl-CNDs show green RTP with an average lifetime of 657 ms along with blue fluorescence. Based on the Cl-CNDs phosphorescence, it is efficiently applied in security marking. Guanidine hydrochloride is a commonly used precursor for the synthesis of bulk graphitic carbon nitride and carbon nitride quantum dots due to its easy availability, low cost, and benign nature (Tang et al., 2013; Tang et al., 2014).

EXPERIMENTAL SECTION

Materials

For this experiment, guanidine hydrochloride and ethanol were purchased from Merck Specialties Private Limited. Transparent liquid paper gum was bought from a local market. Double distilled water was used throughout the experiments.

Methods

Synthesis of phosphorescent chlorine doped carbon nitride dots (Cl-CNDs)

In an optimized synthetic process, 1 g guanidine hydrochloride is transferred to silica crucible with lid and heated at 260°C in an oven from Biocraft Scientific System Pvt. Ltd. for 6 h and allowed to cool to room temperature: a yellowish solid product (Cl-CNDs) is obtained. The solid product so obtained is washed several times with 10 mL portions of ethanol and filtered through Whatman 40 filter paper several times. The washed and dried powder Cl-CNDs is then used for further experiments.

Preparation of Cl-CNDs phosphorescent ink

0.01 g of Cl-CNDs is thoroughly mixed to a transparent liquid paper gum and characters ‘CHEM’is written on non-reflecting filter paper.

Characterization

The scanning electron microscopy (SEM) images of the sample are recorded with a field emission scanning electron microscope (FESEM), Carl Zeiss, Gemini, Model-Sigma 300. The elemental composition of the sample is determined with EDX spectroscopy (EDAX system attached with FESEM) and Thermo Scientific Flash 2000 elemental analyzer. The particle size of the Cl-CNDs is measured through dynamic light scattering (DLS) with a zeta seizer, Nano series Nano-ZS90 (Malvern, United Kingdom). UV 1800 spectrophotometer (SHIMADZU, Japan) is used for

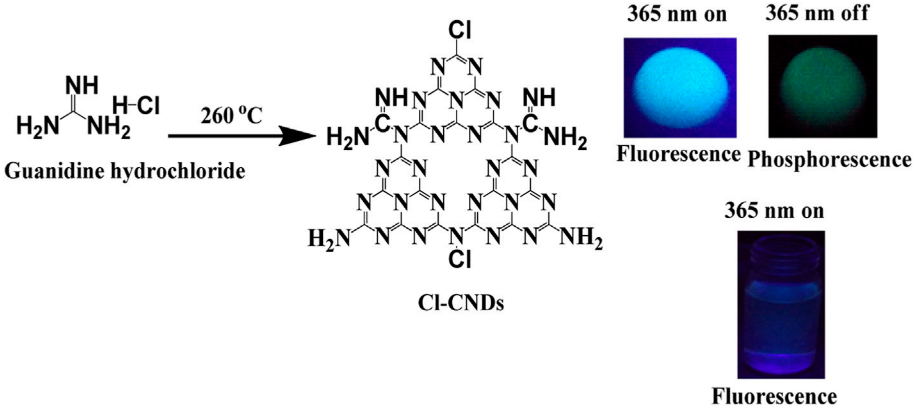

SCHEME 1 | Synthetic scheme of Cl-CNDs and its optical properties.

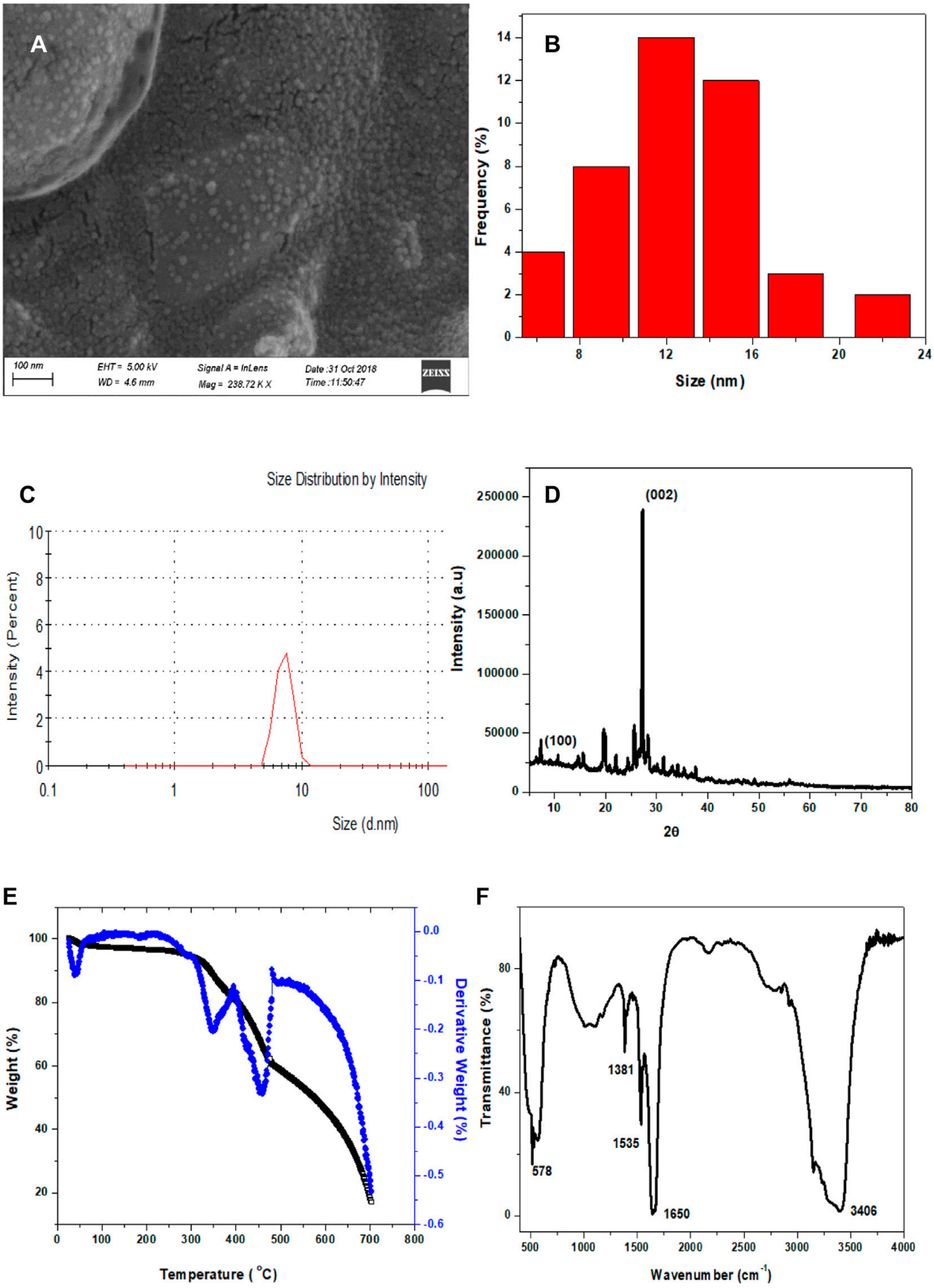

FIGURE 1 | (A) FESEM image of Cl-CNDs. **(B)** Particle size distribution from the FESEM image, calculated by using ImageJ software. **(C)** DLS of Cl-CNDs. **(D)** PXRD pattren of Cl-CNDs. **(E)** TGA (black line) and DTG (blue line) of Cl-CNDs. **(F)** FT-IR spectrum of Cl-CNDs.

recording the UV-visible absorption of the sample, in the range from 200 to 800 nm. The powder X-ray diffraction (PXRD) pattern of the sample is recorded from 5° to 80° 2θ with a scanning speed of 10° per minute in a Rigaku Ultima IV instrument with CuK$_\alpha$ radiation (λ = 1.54Å). Fourier transform infrared (FT-IR) spectrum of the sample is recorded in SHIMADZU IR Affinity equipment in the range from 400 to 4,000 cm^{-1} in KBr pellets. Thermo gravimetric analysis (TGA) is

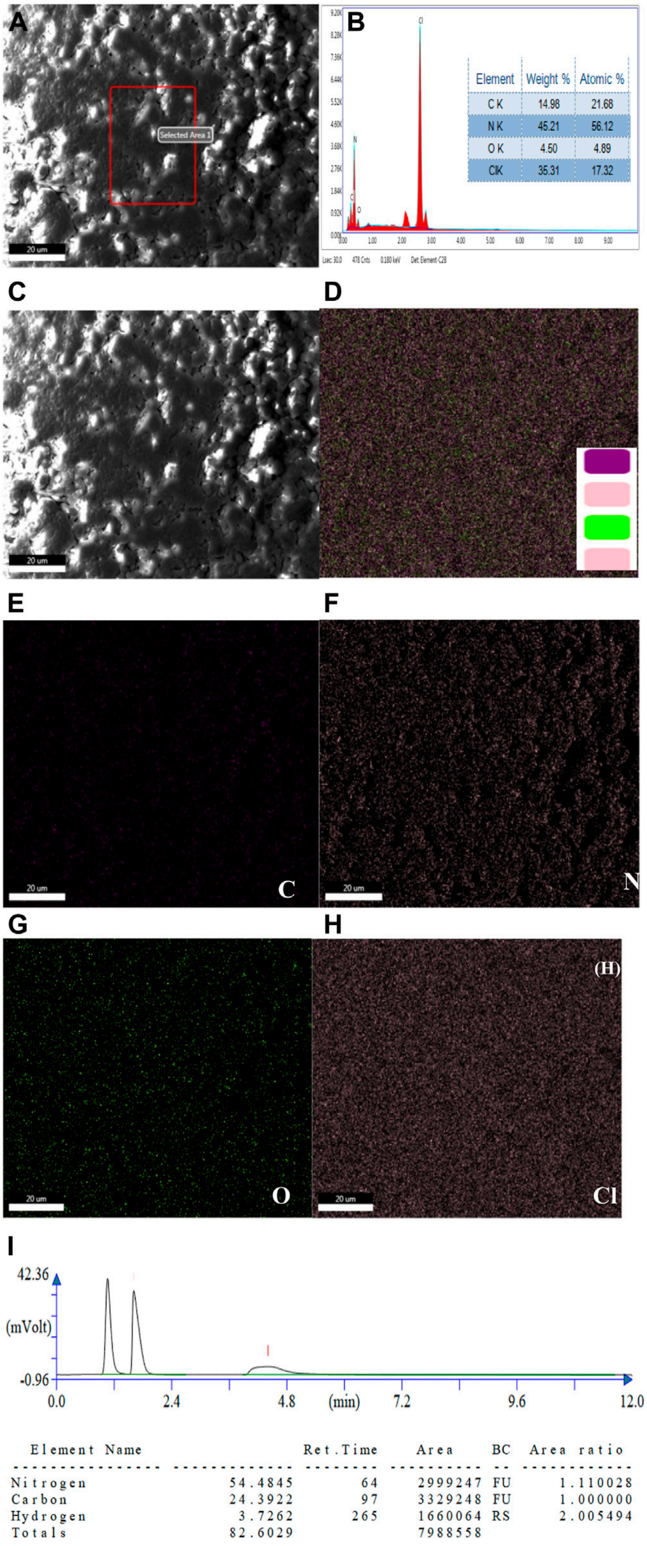

Element	Weight %	Atomic %
C K	14.98	21.68
N K	45.21	56.12
O K	4.50	4.89
ClK	35.31	17.32

```
  Element Name                         Ret.Time      Area     BC  Area ratio
----------------- -------------- --------- ----------- -- --------------
Nitrogen                    54.4845        64    2999247 FU      1.110028
Carbon                      24.3922        97    3329248 FU      1.000000
Hydrogen                     3.7262       265    1660064 RS      2.005494
Totals                      82.6029              7988558
```

FIGURE 2 | (A) FESEM image of Cl-CNDs with selected area for collecting the elements present **(B)** corresponding EDX spectrum along with *(Continued)*

FIGURE 2 | their elemental composition table. **(C)** FESEM image of Cl-CNDs. **(D)** EDX elemental mapping of Cl-CNDs with their corresponding individual mapping **(E)** carbon **(F)** nitrogen **(G)** oxygen **(H)** chlorine. **(I)** Elemental analysis chromatogram with elemental composition table.

carried out in a METTLER TOLEDO STAR thermal analysis system. Photoluminescence measurements (fluorescence and phosphorescence spectra) and phosphorescence lifetime decay profile is measured with Hitachi F-7000 spectrophotometer. The time resolved photoluminescence (TRPL) decay of the sample is recorded using the FSP920 Edinburgh Instrument. The chromaticity diagram along with CIE coordinates of the samples are analyzed with OSRAM color calculator software. The phosphorescence quantum yield measurement of the sample is determined in a Horiba Fluoromax-4CP equipped with an integrating sphere.

RESULTS AND DISCUSSION

The phosphorescent Cl-CNDs is directly obtained by heating guanidine hydrochloride at 260 °C in an oven, as illustrated in **Scheme 1**. The morphology and size of Cl-CNDs are analyzed by FESEM and DLS, **Figure 1**. The FESEM image of Cl-CNDs shows the uniform particle distribution with sizes below 30 nm, **Figure 1A**.

The particle distribution of Cl-CNDs from the FESEM image was found to be between 6 and 22 nm, with an average diameter of about 12 nm, **Figure 1B**. The DLS analysis of Cl-CNDs shows its particle size was 8 nm, which is in agreement with the FESEM results, **Figure 1C**. The PXRD pattern of Cl-CNDs has peaks at 14.87° 2θ (100) and 27.39° 2θ (200) due to the triazine repeating unit and layered graphitic structure, respectively, which is similar to previous reports, **Figure 1D** (Deng et al., 2013; Tang et al., 2013; Yuan et al., 2019).

The TGA and DTG curves of Cl-CNDs are shown in **Figure 1E**. A small weight loss was observed at 38 °C due to the removal of gaseous matter, which may be adsorbed on the Cl-CNDs. The weight losses at approximately 347 and 456 °C are due to the further condensation processes of Cl-CNDs with the elimination of gases like NH_3 and HCl leading to the formation of bulk carbon nitride (Tang et al., 2013; Rangel et al., 2015).

The FT-IR spectrum of Cl-CNDs, **Figure 1F**, provides information about the different functional groups present in Cl-CNDs. The broad peak observed at 3,406 cm^{-1} is assigned to–NH/OHstretching vibration while peaks at 1,650 cm^{-1} and 1,381 cm^{-1} are due to C=N and C-N stretching vibrations respectively. 1,535 cm^{-1} and 578 cm^{-1}peaks are assigned to C=C and C-Cl vibrations.

EDX analysis and elemental mapping were used to determine the composition of Cl-CNDs, as shown in **Figure 2**. A typical elemental composition of C = 14.98%, N = 45.21%, O = 4.50% and Cl = 35.31%, **Figure 2B**, is observed for the Cl-CNDs.The

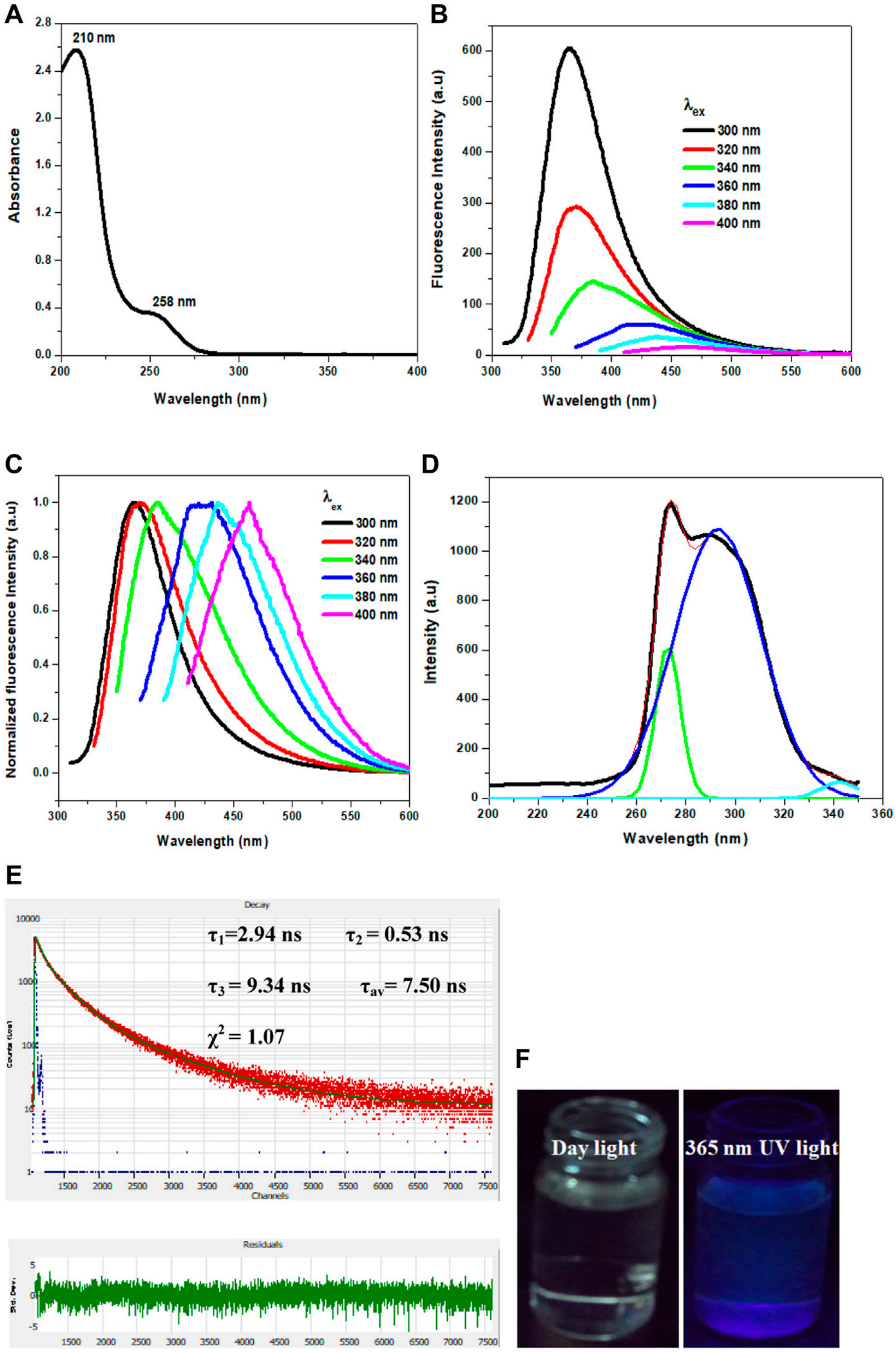

FIGURE 3 | (A) UV-visible spectrum of Cl-CNDs in aqueous medium. **(B)** Fluorescence spectra of Cl-CNDs with variation of excitation wavelength from 300 to 400 nm in aqueous medium **(C)** corresponding normalized plot of **(B)**.**(D)** Fluorescence excitation spectra of Cl-CNDs monitored at 360 nm emission in aqueous medium with deconvolution showing the multiple peaks. **(E)** Time resolved fluorescence decay curve of Cl-CNDs with residual fitting. **(F)** Photograph of fluorescence of Cl-CNDs in aqueous dispersion under daylight and 365 nm UV light irradiation respectively.

elemental mapping of the samples confirmed the homogeneity of the Cl-CNDs in terms of evenly distributed carbon, nitrogen, oxygen, and chlorine atoms, **Figures 2C–H**. The elemental composition of the Cl-CNDs determined by the elemental analyzer, **Figure 2I**, resulted in a composition of C = 24.39%, N = 54.48% and H = 3.72%, which closely matches the results from the EDX analysis.

The optical properties of Cl-CNDs were studied with UV-visible and fluorescence spectroscopy. The absorption peak at 210 nm was due to the π-π* transition originating from an

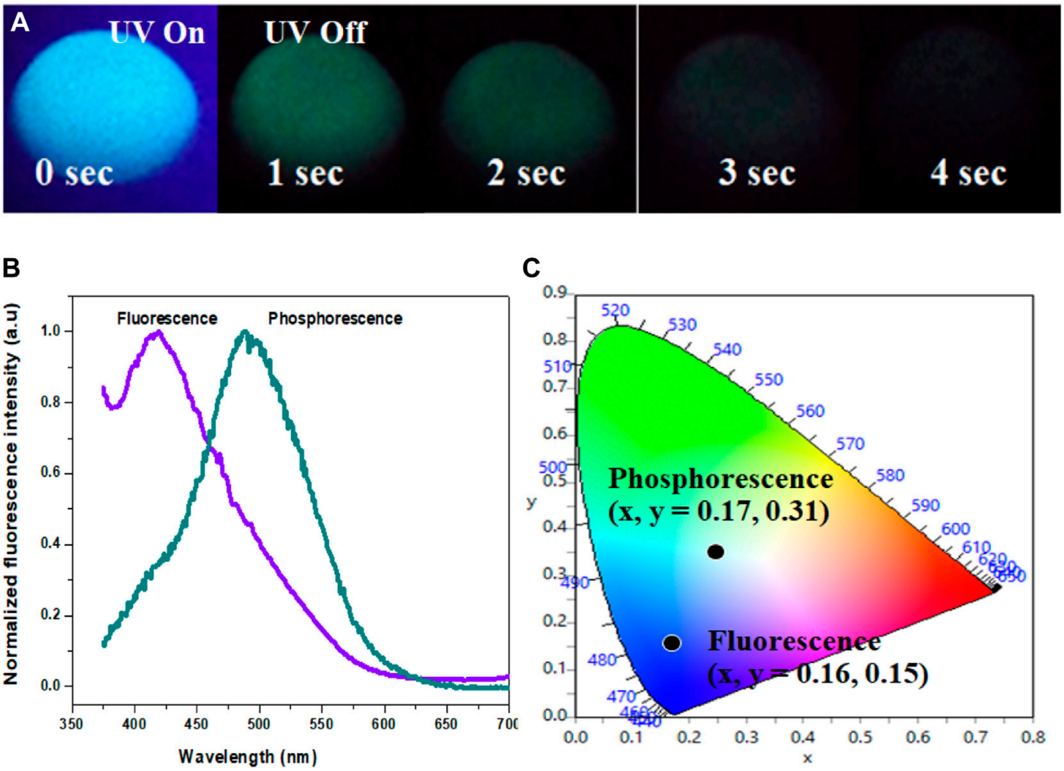

FIGURE 4 | (A) Photograph showing luminescence (fluorescence and phsophorescence) of Cl-CNDs (solid state) under 365 nm UV light on and off. **(B)** Fluorescence and phosphorescence spectra of Cl-CNDs **(C)** corresponding CIE chromaticity diagram with color coordinates of **(B)**.

aromatic ring while the peak observed at 258 nm was assigned to the n-π* transition, (Liu et al., 2011) **Figure 3A**. The aqueous dispersion of Cl-CNDs shows the excitation dependent shift of fluorescence emission maxima, indicating the presence of multiple emissive states. The fluorescence emission center of Cl-CNDs had a red shift from 360 to 460 nm on variation of the excitation wavelength from 300 to 400 nm, which is characteristic of carbon nitride nanoparticles (Ding et al., 2015; Patir and Gogoi, 2018), **Figure 3B**-C. The excitation spectrum of Cl-CNDs is recorded by monitoring the emission center at 360 nm, **Figure 3D**. This shows a broad spectrum that can be deconvoluted to three peaks at 270 nm, 295 nm, and 342 nm, which is indicative of there being at least three excitation centers involved in the emission process. The time resolved fluorescence decay curve of Cl-CNDs, **Figure 3E**, fits to three exponential models giving fluorescence life times of $\tau_1 = 2.94$ ns, $\tau_2 = 0.53$ ns, $\tau_3 = 9.34$ ns, with an average fluorescence life time of $\tau_{av} = 7.50$ ns. These results further confirm the presence of multiple emitters. Commonly observed wavelength dependent red shift of emission spectrum in carbogenic nanoparticles has been attributed to diverse phenomena like quantum confinement, a single particle with multiple functional groups, the composition of individual emitters within a particle, and the ensemble of emissive states (Baker and Baker, 2010; Hsu and Chang, 2012, Dekaliuk et al., 2014, Khan et al., 2015, Demchenko, 2019). Here, the observation of excitation wavelength dependent fluorescence shift is assigned to the presence of multiple excitation centers, which are generated due to the difference in the local environment around individual emitters. These emission centers are excited at different excitation wavelengths and emit subsequently (Dekaliuk et al., 2014). Blue fluorescence is observed for the clear aqueous dispersion of Cl-CNDs under 365 nm UV irradiation, **Figure 3F**.

The Cl-CNDs in a solid state also show blue fluorescence under 365 nm UV light irradiation and green phosphorescence afterglow for a few seconds after the light is turned off, **Figure 4A**. The phosphorescence emission is centered at 490 nm while the fluorescence is at 419 nm, **Figure 4B**. The visual perception of the fluorescence and phosphorescence is obtained from the CIE chromaticity diagram, **Figure 4C**. The shift of fluorescence to phosphorescence emission centers is 71 nm, implying the difference between the singlet-triplet energy levels to be ~0.48 eV (Deng et al., 2013).

Interestingly, the Cl-CNDs powder also shows an excitation wavelength dependent fluorescence similar to the aqueous solution, **Figures 5A,B**. With the variation of the excitation wavelength from 300 to 400 nm, the fluorescence intensity of Cl-CNDs powder decreases continuously with red shift from 355 to 450 nm. The fluorescence excitation spectrum of Cl-CNDs in a solid state can again be deconvoluted to bands at 270 nm, 302 nm, and 337 nm **Figure 5C**, indicating the presence of three excited energy states contributing to the fluorescence process. Compared with the excitation peaks of Cl-CNDs in liquid dispersion, as

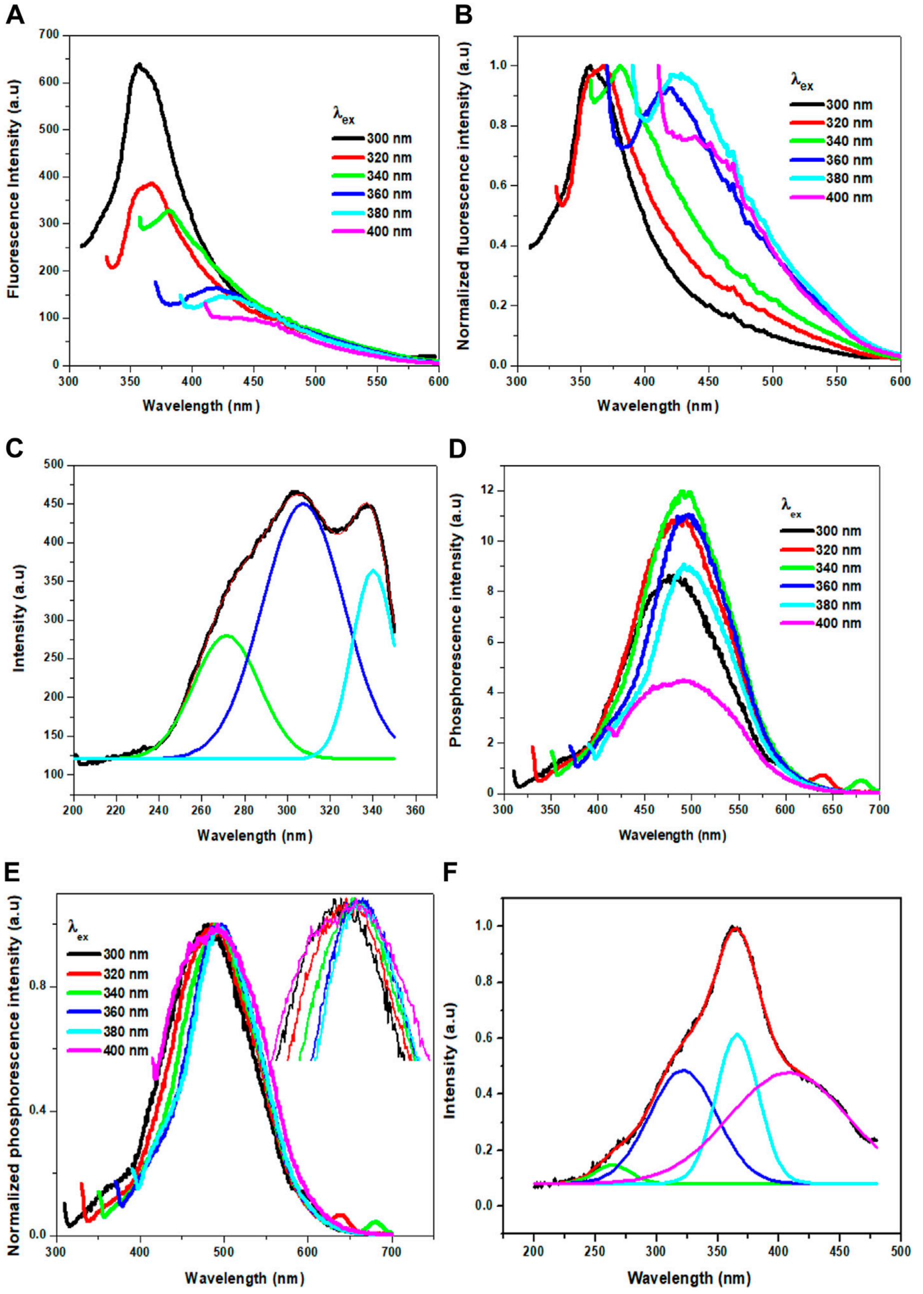

FIGURE 5 | (A) Fluorescence of Cl-CNDs (solid state) with a variation of excitation wavelength from 300 to 400 nm **(B)** corresponding normalized spectra of **(A)**. **(C)** Fluorescence excitation spectra of Cl-CNDs monitored under 360 nm emission with deconvolution showing the multiple peaks. **(D)** Phosphorescence of Cl-CNDs with a variation of excitation wavelength from 300 to 400 nm **(E)** corresponding normalized spectra of **(D)** (inset: expansion of peaks to visualized the shifting). **(F)** Phosphorescence excitation spectra of Cl-CNDs monitored under 490 nm emission with deconvolution showing the multiple peaks.

shown in **Figure 3D**, the excitation peaks at 270 nm, 295 nm, and 342 nm are at similar wavelengths in both solid and liquid phases. Thus the observation of similar excitation dependent red shift of emission maxima in liquid and solid phases rules out the ensemble of states generated by competitive solvent relaxation and fluorescence emission as the origin of the red shift observed. Rather, our experimental findings point towards the presence of emission centers in different local environments, leading to multiple excited states emitting at different wavelengths. Similarly, we have also recorded the phosphorescence spectra of the Cl-CNDs powder under different excitation wavelengths, **Figures 5D,E.** On increasing the excitation wavelength from 300 to 400 nm, the phosphorescence emission center is red-shifted from 480 to 490 nm with increasing phosphorescence intensity until 340 nm excitation wavelength, thereafter the phosphorescence intensity decreases till 400 nm with phosphorescence emission

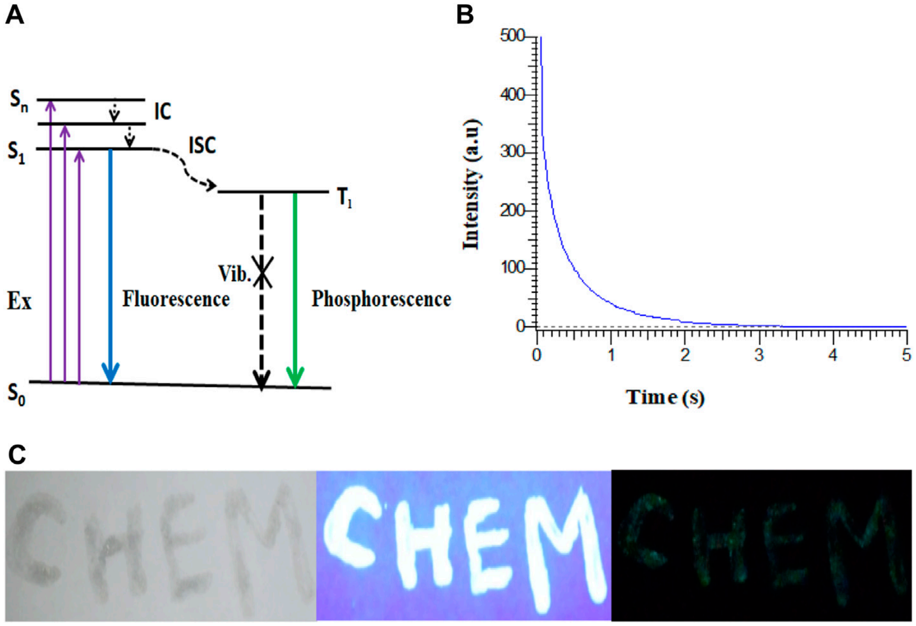

FIGURE 6 | (A) Probable mechanism of RTP in Cl-CNDs. **(B)** Phosphorescence lifetime decay profile of Cl-CNDs under 360 nm excitation wavelength and emission monitored at 490 nm. **(C)** Application of Cl-CNDs as a phosphorescent ink for anti-counterfeiting (from left to right under daylight, 365 nm UV light on and off).

centre red shift from 490 to 500 nm (Li et al., 2019). Thus the excitation wavelength dependent red shift of phosphorescence emission maxima is a confirmation of the red edge effect due to the emission from the lowest triplet states of luminogens at different rigid polar environments rather than the emission from different triplet states of the same luminogen. Since the lifetime of the phosphorescence process is considerably longer, the possibility of emission from higher triplet states is negated. This is an indication that stabilization of the electronic states of Cl-CNDs in a solid state leads to the observation of phosphorescence.

The phosphorescence excitation spectrum of Cl-CNDs, **Figure 5F**, is deconvoluted to four peaks centered at 261, 318, 366, and 418 nm. This indicates that the excitation states contribute to the phosphorescence. Comparing Cl-CNDs phosphorescence excitation spectrum with the solid-state fluorescence excitation spectrum, as observed in **Figure 5C**, it can be said that the same states have contributed to the fluorescence and the phosphorescence process. Thus the fluorescence and the phosphorescence have the same origin: the Cl-CNDs. The shift of the lowest fluorescence excitation center 337 nm to the lowest phosphorescence excitation center 418 nm, is about 81 nm, suggesting their singlet-triplet energy gap to be ~0.54 eV. The phosphorescence excitation spectrum overlaps with the UV-visible absorbance peak for C=O/N, **Figure 3A**, suggesting that the phosphorescence originates from the C=O/N groups of the Cl-CNDs (Li et al., 2016; Long et al., 2018). The C-Cl or C-NH_2 groups present on the surface of the Cl-CNDs and provide rigidity via hydrogen bonding, stabilizing the triplet states, which in turn enhance phosphorescence. Furthermore, the hydrogen bonding of C-Cl or C-NH_2 bonds of Cl-CNDs also prevents the oxygen or moisture-induced quenching of phosphorescence at room temperature.

The probable mechanism of phosphorescence in Cl-CNDs is shown in **Figure 6A**. The electrons are raised from the ground state (S_o) to higher excited states (S_n) on absorption, followed by the electrons coming back to the lowest excited state (S_1) by the internal conversion (IC) process. The S_1 electrons are then transferred to the excited triplet state (T_1) via the intersystem crossing process (ISC) from where electrons fall to S_o, resulting in phosphorescence. The phosphorescence quantum yield of the Cl-CNDs was determined with the integrating sphere method and was found to be 2.32%, which is comparable to existing literature (Li et al., 2016; Long et al., 2018; Li et al., 2019).

The time resolved phosphorescence decay profile of the Cl-CNDs is measured under 360 nm excitation wavelength with emission monitored at 490 nm, as shown in **Figure 6B**. The phosphorescence lifetime of Cl-CNDs is found to be 657 ms. The phosphorescent Cl-CNDs are applied as a long afterglow ink. The Cl-CNDs powder is mixed with a transparent liquid paper gum and the characters 'CHEM' are written on non-reflecting filter paper, **Figure 6C**. These characters show fluorescence under 365 nm UV light irradiation and display green phosphorescence after the 365 nm UV light is turned off. The Cl-CNDs may find applications in different fields such as fluorescent sensors, phosphorescent glow-in-the-dark materials, and security encryption (Long et al., 2018; Wang et al., 2021).

CONCLUSION

The present study presents a simple and cost-effective thermal strategy to synthesize an efficient matrix free carbon based phosphorescent nanomaterial using guanidine hydrochloride as the starting material. The obtained Cl-CNDs are highly miscible in an aqueous medium and display fluorescence and phosphorescence (solid state) under ambient conditions. The heteroatom bonds of the Cl-CNDs facilitate the effective intersystem crossing to triplet state from lowest singlet state, hence phosphorescence is observed. In addition, C-Cl or C-NH_2 presence on Cl-CNDs inhibited the non-radiative decay from the triplet states as well as excluded the atmospheric oxygen via hydrogen bond formation. The average phosphorescence lifetime of Cl-CNDs is observed to be 657 ms. The phosphorescence quantum yield of Cl-CNDs is determined to be 2.32% by using the integrating sphere method. Moreover, Cl-CNDs are also demonstrated as phosphorescent ink on non-reflecting paper for the purpose of security marking. Hence, this work may help understanding and future applications of carbon nitride nanoparticles based on room temperature phosphorescent materials.

DATA AVAILABILITY STATEMENT

The original contributions presented in the study are included in the article.

AUTHOR CONTRIBUTIONS

KP: Methodology, validation, Data curation, Formal analysis, Investigation, Writing—original draft, review and editing. SG: Writing—review and editing, supervision.

FUNDING

This work was supported by the DST SERB project SB/S1/PC-105/2012 and UGC-NFST-2015-17-ST-ASS-2321, Government of India.

ACKNOWLEDGMENTS

KP and SG thank the Department of Chemistry, Gauhati University-Guwahati, CIF-Gauhati University, SIC-IIT-Indore and CIF-IIT-Guwahati for sample analyses. The authors are also thankful to Dr.Shanta Singh Naorem and Ranjoy Wangkhem, Department of Physics, Nagaland University for helping in recording the phosphorescent quantum yield. Authors would also like to express gratitude to DST-FIST support to Department of Chemistry, Gauhati University for the PXRD facility.

REFERENCES

Bai, L. Q., Xue, N., Wang, X. R., Shi, W. Y., and Lu, C. (2017). Activating Efficient Room Temperature Phosphorescence of Carbon Dots by Synergism of Orderly Non-noble Metals and Dual Structural Confinements. *Nanoscale* 9 (20), 6658–6664. doi:10.1039/C6NR09648D

Baker, S. N., and Baker, G. A. (2010). Luminescent Carbon Nanodots: Emergent Nanolights. *Angew. Chem. Int. Edition* 49 (38), 6726–6744. doi:10.1002/anie.200906623

Braun, D., and Heeger, A. J. (1991). Visible Light Emission from Semiconducting Polymer Diodes. *Appl. Phys. Lett.* 58, 1982–1984. doi:10.1063/1.105039

Chakraborty, A., Debnath, G. H., Saha, N. R., Chattopadhyay, D., Waldeck, D. H., and Mukherjee, P. (2016). Identifying the Correct Host-Guest Combination to Sensitize Trivalent Lanthanide (Guest) Luminescence: Titanium Dioxide Nanoparticles as a Model Host System. *J. Phys. Chem. C* 120 (41), 23870–23882. doi:10.1021/ACS.JPCC.6B08421

Chen, Y., He, J., Hu, C., Zhang, H., Lei, B., and Liu, Y. (2017). Room Temperature Phosphorescence from Moisture-Resistant and Oxygen-Barred Carbon Dot Aggregates. *J. Mater. Chem. C* 5 (25), 6243–6250. doi:10.1039/C7TC01615H

Dekaliuk, M. O., Viagin, O., Malyukin, Y. V., and Demchenko, A. P. (2014). Fluorescent Carbon Nanomaterials: "quantum Dots" or Nanoclusters. *Phys. Chem. Chem. Phys.* 16 (30), 16075–16084. doi:10.1039/C4CP00138A

Demchenko, A. (2019). Excitons in Carbonic Nanostructures. *C* 5 (4), 71. doi:10.3390/c5040071

Deng, Y., Zhao, D., Chen, X., Wang, F., Song, H., and Shen, D. (2013). Long Lifetime Pure Organic Phosphorescence Based on Water Soluble Carbon Dots. *Chem. Commun.* 49 (51), 5751–5753. doi:10.1039/C3CC42600A

Dong, X., Wei, L., Su, Y., Li, Z., Geng, H., Yang, C., et al. (2015). Efficient Long Lifetime Room Temperature Phosphorescence of Carbon Dots in a Potash Alum Matrix. *J. Mater. Chem. C* 3 (12), 2798–2801. doi:10.1039/C5TC00126A

Gan, N., Shi, H., An, Z., and Huang, W. (2018). Recent Advances in Polymer-Based Metal-free Room-Temperature Phosphorescent Materials. *Adv. Funct. Mater.* 28 (51), 1802657. doi:10.1002/adfm.201802657

Gao, Y., Han, H., Lu, W., Jiao, Y., Liu, Y., Gong, X., et al. (2018). Matrix-Free and Highly Efficient Room-Temperature Phosphorescence of Nitrogen-Doped Carbon Dots. *Langmuir* 34 (43), 12845–12852. doi:10.1021/acs.langmuir.8b00939

Hsu, P.-C., and Chang, H.-T. (2012). Synthesis of High-Quality Carbon Nanodots from Hydrophilic Compounds: Role of Functional Groups. *Chem. Commun.* 48 (33), 3984–3986. doi:10.1039/C2CC30188A

Hu, R., Zhang, Y., Zhao, Y., Wang, X., Li, G., and Wang, C. (2020). UV-Vis-NIR Broadband-Photostimulated Luminescence of LiTaO3:Bi3+ Long-Persistent Phosphor and the Optical Storage Properties. *Chem. Eng. J.* 392, 124807. doi:10.1016/j.cej.2020.124807

Joseph, J., and Anappara, A. A. (2017). Cool white, Persistent Room-Temperature Phosphorescence in Carbon Dots Embedded in a Silica Gel Matrix. *Phys. Chem. Chem. Phys.* 19 (23), 15137–15144. doi:10.1039/C7CP02731A

Khan, S., Gupta, A., Verma, N. C., and Nandi, C. K. (2015). Time-Resolved Emission Reveals Ensemble of Emissive States as the Origin of Multicolor Fluorescence in Carbon Dots. *Nano Lett.* 15 (12), 8300–8305. doi:10.1021/acs.nanolett.5b03915

Li, Q., Zhou, M., Yang, Q., Wu, Q., Shi, J., Gong, A., et al. (2016). Efficient Room-Temperature Phosphorescence from Nitrogen-Doped Carbon Dots in Composite Matrices. *Chem. Mater.* 28 (22), 8221–8227. doi:10.1021/acs.chemmater.6b03049

Li, W., Zhou, W., Zhou, Z., Zhang, H., Zhang, X., Zhuang, J., et al. (2019). A Universal Strategy for Activating the Multicolor Room-Temperature Afterglow of Carbon Dots in a Boric Acid Matrix. *Angew. Chem.* 131 (22), 7356–7361. doi:10.1002/ange.201814629

Liu, S., Tian, J., Wang, L., Luo, Y., and Sun, X. (2012). A General Strategy for the Production of Photoluminescent Carbon Nitride Dots from Organic Amines and Their Application as Novel Peroxidase-like Catalysts for Colorimetric Detection of H2O2and Glucose. *RSC Adv.* 2 (2), 411–413. doi:10.1039/C1RA00709B

Liu, S., Tian, J., Wang, L., Luo, Y., Zhai, J., and Sun, X. (2011). Preparation of Photoluminescent Carbon Nitride Dots from CCl4 and 1,2-ethylenediamine: a Heat-Treatment-Based Strategy. *J. Mater. Chem.* 21 (32), 11726–11729. doi:10.1039/C1JM12149A

Long, P., Feng, Y., Cao, C., Li, Y., Han, J., Li, S., et al. (2018). Self-protective Room-Temperature Phosphorescence of Fluorine and Nitrogen Codoped Carbon Dots. *Adv. Funct. Mater.* 28 (37), 1800791. doi:10.1002/adfm.201800791

Meruga, J. M., Cross, W. M., Stanley May, P., Luu, Q., Crawford, G. A., and Kellar, J. J. (2012). Security Printing of covert Quick Response Codes Using

Upconverting Nanoparticle Inks. *Nanotechnology* 23, 395201. doi:10.1088/0957-4484/23/39/395201

Patir, K., and Gogoi, S. K. (2018). Facile Synthesis of Photoluminescent Graphitic Carbon Nitride Quantum Dots for Hg2+ Detection and Room Temperature Phosphorescence. *ACS Sustain. Chem. Eng.* 6 (2), 1732–1743. doi:10.1021/acssuschemeng.7b03008

Patir, K., and Gogoi, S. K. (2019). Long Afterglow Room-Temperature Phosphorescence from Nanopebbles: A Urea Pyrolysis Product. *Chem. Asian J.* 14 (15), 2573–2578. doi:10.1002/asia.201900454

Rangel, L. S., Rivera de la Rosa, J., Lucio Ortiz, C. J., and Castaldi, M. J. (2015). Pyrolysis of Urea and Guanidinium Salts to Be Used as Ammonia Precursors for Selective Catalytic Reduction of NOx. *J. Anal. Appl. Pyrolysis* 113, 564–574. doi:10.1016/j.jaap.2015.04.007

Song, Z., Lin, T., Lin, L., Lin, S., Fu, F., Wang, X., et al. (2016). Invisible Security Ink Based on Water-Soluble Graphitic Carbon Nitride Quantum Dots. *Angew. Chem.* 128 (8), 2823–2827. doi:10.1002/ange.201510945

Tan, J., Zou, R., Zhang, J., Li, W., Zhang, L., and Yue, D. (2016). Large-scale Synthesis of N-Doped Carbon Quantum Dots and Their Phosphorescence Properties in a Polyurethane Matrix. *Nanoscale* 8 (8), 4742–4747. doi:10.1039/C5NR08516K

Tang, Y., Song, H., Su, Y., and Lv, Y. (2013). Turn-on Persistent Luminescence Probe Based on Graphitic Carbon Nitride for Imaging Detection of Biothiols in Biological Fluids. *Anal. Chem.* 85 (24), 11876–11884. doi:10.1021/ac403517u

Tang, Y., Su, Y., Yang, N., Zhang, L., and Lv, Y. (2014). Carbon Nitride Quantum Dots: A Novel Chemiluminescence System for Selective Detection of Free Chlorine in Water. *Anal. Chem.* 86 (9), 4528–4535. doi:10.1021/ac5005162

Wang, A.-J., Li, H., Huang, H., Qian, Z.-S., and Feng, J.-J. (2016). Fluorescent Graphene-like Carbon Nitrides: Synthesis, Properties and Applications. *J. Mater. Chem. C* 4 (35), 8146–8160. doi:10.1039/C6TC02330D

Wang, Y., Wang, J., Ma, P., Yao, H., Zhang, L., and Li, Z. (2017). Synthesis of Fluorescent Polymeric Carbon Nitride Quantum Dots in Molten Salts for Security Inks. *New J. Chem.* 41 (24), 14918–14923. doi:10.1039/C7NJ03423G

Wang, Z., Shen, J., Sun, J., Xu, B., Gao, Z., Wang, X., et al. (2021). Ultralong-lived Room Temperature Phosphorescence from N and P Codoped Self-Protective Carbonized Polymer Dots for Confidential Information Encryption and Decryption. *J. Mater. Chem. C* 9 (14), 4847–4853. doi:10.1039/D0TC05845A

Wei, X., Yang, J., Hu, L., Cao, Y., Lai, J., Cao, F., et al. (2021). Recent Advances in Room Temperature Phosphorescent Carbon Dots: Preparation, Mechanism, and Applications. *J. Mater. Chem. C* 9 (13), 4425–4443. doi:10.1039/D0TC06031C

Yang, X., and Yan, D. (2016). Long-afterglow Metal-Organic Frameworks: Reversible Guest-Induced Phosphorescence Tunability. *Chem. Sci.* 7 (7), 4519–4526. doi:10.1039/C6SC00563B

Yuan, T., Yuan, F., Li, X., Li, Y., Fan, L., and Yang, S. (2019). Fluorescence-phosphorescence Dual Emissive Carbon Nitride Quantum Dots Show 25% white Emission Efficiency Enabling Single-Component WLEDs. *Chem. Sci.* 10 (42), 9801–9806. doi:10.1039/c9sc03492g

Yuan, W. Z., Shen, X. Y., Zhao, H., Lam, J. W. Y., Tang, L., Lu, P., et al. (2010). Crystallization-induced Phosphorescence of Pure Organic Luminogens at Room Temperature. *J. Phys. Chem. C* 114 (13), 6090–6099. doi:10.1021/jp909388y

Zhang, S., Hosaka, M., Yoshihara, T., Negishi, K., Iida, Y., Tobita, S., et al. (2010). Phosphorescent Light-Emitting Iridium Complexes Serve as a Hypoxia-Sensing Probe for Tumor Imaging in Living Animals. *Cancer Res.* 70 (11), 4490–4498. doi:10.1158/0008-5472.CAN-09-3948

Zhao, L., Ming, T., Chen, H., Gong, L., Chen, J., and Wang, J. (2011). Room-temperature Metal-activator-free Phosphorescence from Mesoporous Silica. *Phys. Chem. Chem. Phys.* 13 (6), 2387–2393. doi:10.1039/C0CP01981J

Conflict of Interest: The authors declare that the research was conducted in the absence of any commercial or financial relationships that could be construed as a potential conflict of interest.

frontiers | Frontiers in Physics

BRIEF RESEARCH REPORT
published: 25 April 2022
doi: 10.3389/fphy.2022.841413

Impact of Fabrication Processes of Small-Molecule-Doped Polymer Thin-Films on Room-Temperature Phosphorescence

Heidi Thomas[1], Katherina Haase[2], Tim Achenbach[1], Toni Bärschneider[1], Anton Kirch[1], Felix Talnack[2], Stefan C. B. Mannsfeld[2] and Sebastian Reineke[1]*

[1]Dresden Integrated Center for Applied Physics and Photonic Materials (IAPP), Technische Universität Dresden, Dresden, Germany, [2]Center for Advancing Electronics Dresden (cfaed) and Faculty of Electrical and Computer Engineering, Technische Universität Dresden, Dresden, Germany

The development of organic materials displaying room-temperature phosphorescence is a research field that has attracted more and more attention in the last years. Most studies focus on designing or optimizing emitter molecules to increase the phosphorescent performance in host:emitter systems. Rarely, the overall thin-film preparation routines are compared with respect to their triplet-state luminescence yield. Herein, different film preparation techniques are investigated using the very same emitter molecule. A variation of host polymer, post-annealing temperature, and fabrication procedure is evaluated with respect to the obtained phosphorescent lifetime, photoluminescent quantum yield, and phosphorescence-to-luminescence ratio. This study elaborates the importance of different film preparation techniques and gathers a concise set of data which is helpful to anyone optimizing the phosphorescence of a particular system.

Keywords: room-temperature phosphorescence, host-guest system, wet thin-film processing, persistent phosphorescence, UV excitation, persistent luminescence, organic emitter, triplet state

Edited by:
Rene A. Nome,
State University of Campinas, Brazil

Reviewed by:
Zhenghuan Lin,
Fujian Normal University, China
Ahmed Al-Masoodi,
American University of Kurdistan, Iraq

***Correspondence:**
Sebastian Reineke
sebastian.reineke@tu-dresden.de

Specialty section:
This article was submitted to Physical Chemistry and Chemical Physics,
a section of the journal Frontiers in Physics

***Received:** 22 December 2021*
***Accepted:** 01 April 2022*
***Published:** 25 April 2022*

Citation:
Thomas H, Haase K, Achenbach T, Bärschneider T, Kirch A, Talnack F, Mannsfeld SCB and Reineke S (2022) Impact of Fabrication Processes of Small-Molecule-Doped Polymer Thin-Films on Room-Temperature Phosphorescence. Front. Phys. 10:841413. doi: 10.3389/fphy.2022.841413

1 INTRODUCTION

Organic room temperature phosphorescence (RTP), an optical phenomenon originating from the radiative transition of molecular excitations from the triplet excited state to the ground state, has attracted a lot of interest among scientists [1–4]. Its use in information and optical storage, bio-imaging, data encryption, as well as organic light-emitting diodes (OLEDs), and displays [5–12] makes this group of materials indispensable nowadays. To achieve efficient organic RTP, both a substantial intersystem crossing (ISC) between the lowest singlet and the triplet state manifold, as well as the effective suppression of the non-radiative relaxations of triplet excitons are essential [13–15].

According to Yan et.al, [3] one of the key parameters to efficient phosphorescence is the phosphorescence lifetime. There are several pathways to increase it. Among those, host-guest doping [16–18], crystal engineering [19, 20], H-aggregation [21–23], metal-organic and supramolecular frameworks [24, 25], self-assembly [26], as well as luminescent polymers [14, 27–29], and carbon dots [30, 31], just to name a few, can be found. However, phosphorescence is not only characterized by the excited triplet state lifetime, but also by its photoluminescence quantum yield (PLQY) and the phosphorescence-to-luminescence (P2L) ratio (defined later in the text).

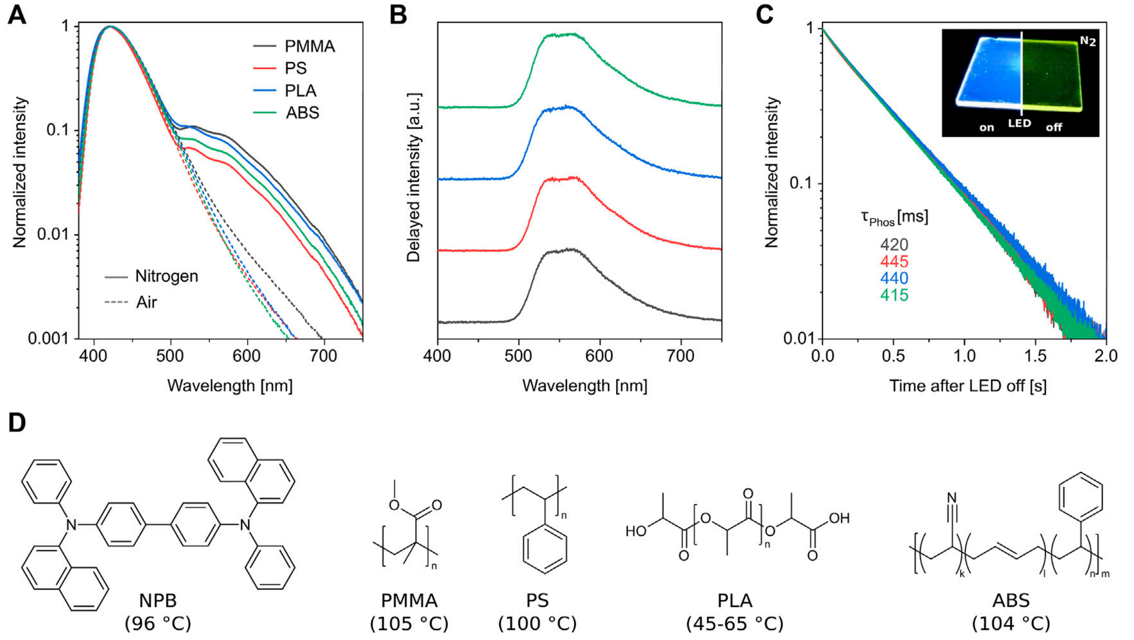

FIGURE 1 | (A) Continuous wave (cw) emission spectra of drop-cast host:NPB films in air (dashed line) and nitrogen atmosphere (solid line). **(B)** Delayed emission spectra showing the respective phosphorescence. **(C)** Phosphorescence decays and lifetimes, inset: PMMA:NPB sample excited with 365 nm showing blue prompt and green delayed emission. **(D)** Molecular structures of NPB and the host polymers used in this work, glass transition temperatures of the polymers given in brackets.

Numerous research groups focused on improving these parameters by employing specially designed emitter molecules like boronic acid esters or carbazoles or rigid polymer matrices such as cyclodextrines [3, 4]. It is, however, equally important to optimize the phosphorescence lifetime, P2L ratio, and PLQY for already existing emitters. This is particularly interesting when different RTP applications may require different processing techniques. It then needs to be elaborated how employing different processing might alter the phosphorescence performance. For fabricating thin films where the emitter is embedded in a polymer matrix, there are a few adjusting screws that can be turned. On the one hand, the nature of the polymer can be important. Polarity, chain length, and side groups can not only promote the interaction of the emitter with the polymer but also rigidify the polymer itself, e.g., by forming intermolecular hydrogen bonds [32, 33] or by a denser packing [1]. This leads to a reduction of the non-radiative decay rate, thus enhancing the phosphorescence lifetime and efficiency. On the other hand, the same effect might probably be achieved by varying the deposition technique since for slower or directed deposition, the packing density can be increased [34]. A similar behavior can be expected by thermal post-treatment of the films [35].

In this report, we study the interplay of the process parameters, host materials, deposition and post-treatment techniques regarding their impact on phosphorescence lifetime, P2L ratio, and PLQY. We utilize a poly (methyl methacrylate) (PMMA):*N*,*N*′-di (1-naphthyl)-*N*,*N*′-diphenyl-(1,1′-biphenyl)-4,4′-diamine (NPB) blend as the material system benchmark, as our group has used it extensively throughout the recent years. We developed rewritable photoluminescent tags, PLTs [6], synthesized microparticles [36], and prooved dual-state Förster Resonance Energy Transfer [37] using that system.

2 RESULTS AND DISCUSSION

The thin films studied in this report are comprised of PMMA, polystyrene (PS), polylactic acid (PLA), or acrylonitrile butadiene styrene (ABS) (**Figure 1D**) as host materials and two weight percent (wt%) NPB as guest molecule. The latter is not only a well-known hole transport material in OLED technology [38–40] but also a widely used phosphorescent emitter when embedded into a polymer matrix [37, 41]. We used either spin-coating (sc), drop-casting (dc), or blade-coating (bc) onto quartz substrates under ambient conditions as deposition techniques. The samples were either used as fabricated or were subject to additional post-treatment annealing at 40, 60, 80, 100, or 120°C, respectively, for 24 h in ambient air. These temperatures have been chosen to identify potential changes in the material system exceeding a certain threshold. During this heating step (unheated films were subject to a 24 h waiting time), the films were allowed to reorganize/find their equilibrium over a longer period of time. Except for PLA, the glass transition temperatures (T_G, see **Figure 1D**) are around 100°C. We have chosen the post-annealing temperature range to span from room temperature to slightly above T_G. A further increase in temperature leads to the decomposition of the emitter first, closely followed by the polymer decomposition. PMMA for example starts to

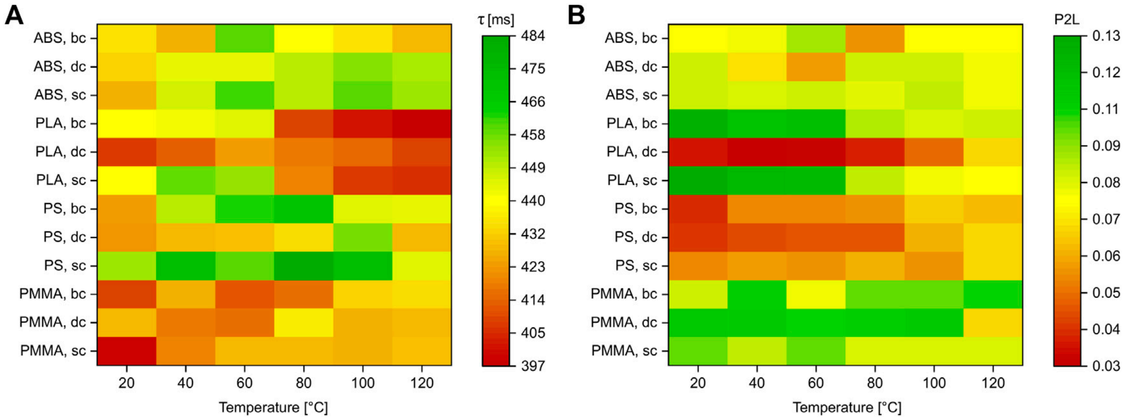

FIGURE 2 | Heat maps of **(A)** phosphorescence lifetime (τ) and **(B)** phosphorescence-to-luminescence ratio (P2L) of spin-coated (sc), drop-cast (dc) as well as blade-coated (bc) polymer:NPB samples for different post annealing temperatures.

decompose already at 180°C. For all 72 samples, the emission spectra in air and nitrogen, as well as the PLQY were measured under 365 nm excitation. The phosphorescence lifetime τ was determined from the transient of the delayed emission (see **Supplementary Tables S1, S2**).

Figure 1 exemplarily shows the spectra of blade-coated samples post-treated at 40°C. In ambient conditions (**Figure 1A**, dashed line), only the blue fluorescence with a peak wavelength of 420 nm is visible, since the phosphorescence is quenched by oxygen [6, 42, 43]. In nitrogen atmosphere (**Figure 1A**, solid line), the green phosphorescence with maximum intensity at 555 nm appears. Taking delayed spectra of the films shows the isolated phosphorescence spectrum (**Figure 1B**). The inset in **Figure 1C** shows a photograph of such a sample during excitation and shortly after the LED is turned off. The lifetimes of the latter are given in **Figure 1C**.

To identify the P2L values, the integral of the emission curves in air (fluorescence, F_{air}) and nitrogen (fluorescence + phosphorescence, $F_{N2} + P = L$) between 380 and 800 nm were determined. With $(L\text{-}F_{air})/L$, the P2L ratio can be calculated. Here, the spectra in nitrogen were recorded at low excitation intensities to prevent nonlinear effects such as singlet-triplet annihilation (STA), triplet-triplet annihilation (TTA) [44], and excited-state saturation. PLQY was measured in an integrating sphere at 340 nm excitation. More details of the procedure are given in the supplementary material. **Figure 2** gives an overview of the measurement results.

2.1 Phosphorescence Lifetime

Figure 2A shows the phosphorescence lifetime (τ) of the samples after the respective temperature treatment (see **Supplementary Table S1**). In a first experiment (**Supplementary Table S2**), we used an equal polymer concentration for all three deposition techniques. Here, the spin-coated samples were about ten times thinner than the one of drop-cast or blade-coated samples [e.g., for PMMA samples: 210 nm (sc), 3,150 nm (dc), and 1,835 nm (bc)]. For that reason, we prepared samples by spin-coating with film thicknesses in the range of 150–5,600 nm and measured the respective phosphorescence lifetime. **Supplementary Figure S2** shows, that there is an increase of the lifetime with increasing film thickness.

We therefore decided to increase the film thickness by a second spin-coating series with higher polymer concentration to match the film thickness values of the other coating techniques. Here, we adjusted the film thickness to be in between the ones obtained by drop-casting and blade-coating. Analyzing this series we found that the lifetimes of the thin spin-coated samples are around 15 ms (PMMA), 140 ms (PS), 80 ms (PLA), and 50 (ABS) ms shorter, in case of unheated substrates, compared to the thicker samples.

It has been shown before that polymer chains align during the drying process following a drop-casting or blade-coating fabrication [45]. This change of the nanostructure might influence the overall luminescence and the phosphorescence in particular by decreasing the non-radiative rates. The slow process usually leads to more ordered and less defective films as compared to spin-coated ones. Also, blade-coating can facilitate molecule alignment through applied directional shear stress and likewise results in less defective films with enhanced structural order [46]. As already mentioned, an increase in stiffness of the polymer and consequent suppression of non-radiative rates is supposed to increase the phosphorescence lifetime. We, therefore, performed GIWAXS measurements of samples with PS in order to observe if the different processing methods change the packing of either the NPB or the PS matrix. A summary of the collected data is shown in **Supplementary Figure S3**. For all PS:NPB films we observe a broad ring located at $q \sim 1.38$ $Å^{-1}$ that we associate with the polystyrene matrix. The corresponding real space distance is approximately 4.55 Å, which coincides with the PS monomer length and thus the average distance of the phenyl rings in PS. Due to the intense, broad scattering signal of the PS matrix, and the tendency to form amorphous films, no scattering signal of NPB could be observed for the PS:NPB films. However, compared to a plain PS film, slight changes in the PS matrix are seen in the blended films, with

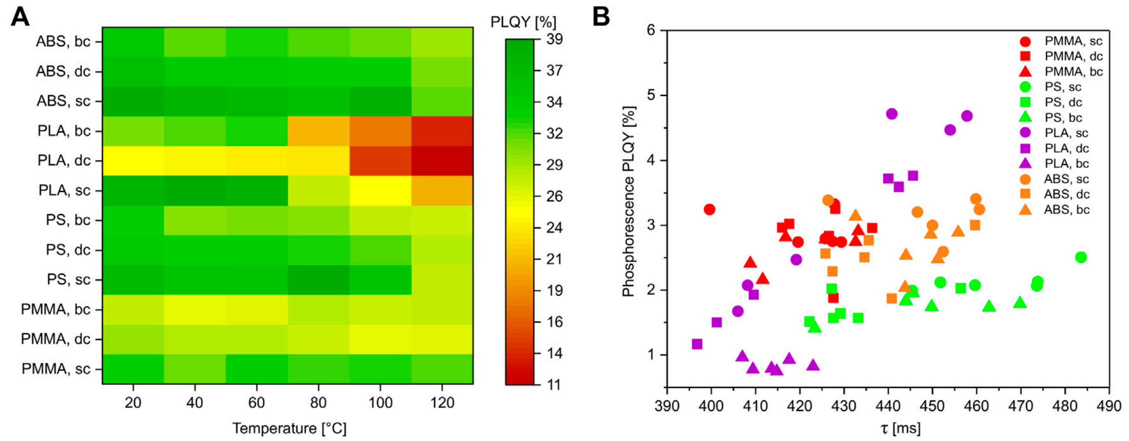

FIGURE 3 | (A) Heat map of PLQY of spin-coated (sc), drop-cast (dc) as well as blade-coated (bc) polymer:NPB samples for different post annealing temperatures. **(B)** Correlation of phosphorescence PLQY and τ for spin-coated (dot), drop-cast (square), and blade-coated (triangle) samples of NPB in PMMA (red), PS (green), PLA (purple), and ABS (orange), respectively.

the PS ring position shifting to smaller *q*-values. We think that the addition of NPB increases the distance between the phenyl rings, either by a coordination of the NPB molecules at positions in-between the PS phenyl rings or by an increase of the PS chain curvature (**Supplementary Figure S3**). This change of the PS matrix scattering signal also shows that the NPB molecules are well dispersed in the PS matrix and that no phase separation occurs. Furthermore, the position of the ring in the GIWAXS images seems to depend on the processing technique with the most evident change occurring for the drop-cast samples. One may speculate that this trend correlates with the processing and film formation velocity, respectively. Indeed, the deposition time is longest in the case of drop-casting, since the solvent needs several hours to evaporate.

Upon heating of the samples after the deposition, the lifetimes show only an increase of up to 20 ms for drop-cast and blade-coated samples. In addition, there is nearly no change for the thin spin-coated PMMA samples. The glass transition temperatures (T_G) of the used polymers are around 100°C, except for PLA (50–80°C). Up to this temperature, the lifetimes are more or less in the same range. By reaching T_G, they start to decrease which is most prominent for the whole PLA series as well as for thin spin-coated ABS and PS samples. It is remarkable though, that by heating the thick spin-coated samples, the lifetime can be increased by impressive 50 ms (PMMA, 80 and 100°C), 230 ms (PS, 40°C), 250 ms (PLA, 100°C), and 135 ms (ABS, 100°C), compared to the corresponding thin samples. A possible reason could be remaining solvent that was trapped in between the unordered polymer chains and can be released only by heating of the film. It is possible that the order of the chains and the stiffness of the film does not necessarily correlate. In case of spin-coating, the chains are very much unordered but nevertheless the film could be very stiff if the remaining solvent is removed. On the other hand, the ordered chains in drop-cast and blade-coated films might be less stiff due to flexible intermolecular hydrogen bonds.

2.2 Phosphorescence-to-Luminescence Ratio

The phosphorescence-to-luminescence ratio (P2L) indicates the proportion of the phosphorescence in the total emission. This is not only interesting in the case of afterglow applications but also for the visibility of the phosphorescence in continuous wave (cw) photoluminescence in nitrogen atmosphere. If the P2L ratio is over 0.5, the intensity of the phosphorescence is higher than the one of the fluorescence, thus enabling the detection of the phosphorescence signal clearly by eye even under cw illumination [47, 48].

From the data presented in **Figure 2B** we cannot deduce any systematic influence of post-annealing or fabrication technique, but it can be shown, that PS as well as the drop-cast PLA samples show the lowest P2L ratio.

2.3 Photoluminescence Quantum Yield

The PLQY is the ratio of emitted to absorbed photons and is quantified in photoluminescence experiments [49]. **Figure 3A** depicts the PLQY values of the samples and looks very similar to **Figure 2A**. By multiplication of the P2L with the PLQY values, the phosphorescence PLQY ($\mathrm{PLQY_{phos}}$) can be obtained. **Figure 3B** shows that $\mathrm{PLQY_{phos}}$ correlates with the phosphorescence lifetime. This behavior seems to have different trends for each of the tested polymer hosts. We therefore account it to the suppression of non-radiative triplet decay, which influences both the PLQY and lifetime of the excited state and is mediated by the host polymer.

2.4 Global Phosphorescence Performance

To achieve an overall and easy-to-read figure of merit, we define a parameter called global phosphorescence performance (GPP). Each parameter set (phosphorescence lifetime, P2L ratio, and PLQY) is normalized to [0:1], which gives 1 for the best and 0 for the worst value. For each sample, the values of the three

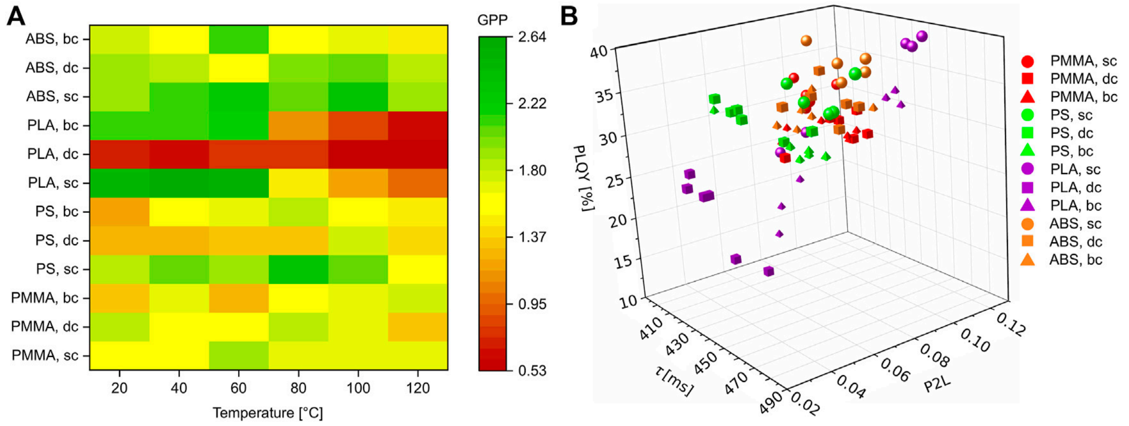

FIGURE 4 | (A) Heat map of the global phosphorescence performance for all 72 samples. **(B)** The same data shown as 3D plot.

parameters were added up, resulting in a score between 0 and 3. The overall GPP for each sample is shown in **Figure 4A** as a heat map and in **Figure 4B** as 3D plot. For the sake of clarity, we decided to not mark each individual point with the respective temperature. The GPP values are provided in **Supplementary Table S1**. As can be seen, there are three PLA samples (purple spheres) in the top-right corner of the plot, indicating the highest GPP. The values correspond to the spin-coated samples post-treated at 40 and 60°C, as well as the untreated one.

Another parameter that might be important is the chain length of the polymeric hosts. Shorter chains might form a denser packing, thus increasing the lifetime by suppressing the non-radiative rates. We have chosen PS with five different chain lengths and four types of PMMA (see **Supplementary Figure S4**). However, there were no dependencies observable. We repeated the same experiment with a different emitter [4,4′-bis(diethylphosphonomethyl)biphenyl (BDPB)] which is known to interact with PMMA by forming intermolecular hydrogen bonds [50], confirming that the lifetime indeed increases with decreasing the PMMA chain length (see **Supplementary Figure S5**). This indicates that NPB does not interact with the polymer matrix in the same way and without measurable changes.

3 MATERIALS AND METHODS

3.1 Chemicals

NPB and PS [MW 280,000 (photophysical measurements) and 35,000 (GIWAXS)] were purchased from Sigma Aldrich, PMMA (MW 550,000) as well as anisole from Alfa Aesar, PLA and ABS from Smart Advanced Systems GmbH.

3.2 Film Fabrication

Both emitter and respective polymer were dissolved in anisole to reach a solution containing 2 wt% NPB and 98 wt% polymer. The polymer concentration was 40 mg/ml (PMMA) and 80 mg/ml (PS, PLA, ABS), respectively. For thick spin-coated samples, concentrations of 120 (PMMA), 250 (PS), 110 (PLA), and 220 mg/ml were used. Cleaned quartz glass substrates of a size of 25 mm by 25 mm were used.

3.2.1 Spin-Coating

A spin coater SCE-150 from Novocontrol Technologies was used. 150 µL of the respective solution was applied to a quartz substrate and spun at 33 rps for 60 s with a ramp of 3 s in case of thin films. The thick films were spun at 20 rps for 180 s.

3.2.2 Drop-Casting

50 µL of the respective solution has been drop-cast onto the quartz substrate and was kept at ambient conditions over night for the solvent to evaporate.

3.2.3 Blade-Coating

Blade coating was carried out with a home-build coating setup consisting of a sample stage that can be heated and a movable blade. The ODTMS-treated [51] blade was kept at a substrate-blade distance of 100 µm with an angle of 8°. All samples were coated with 25 µl at 30 mm/s at normal ambient conditions in air. After coating, they were kept on a hotplate at 40°C for 5 min.

3.2.4 Post-Annealing

To heat the samples to a defined temperature, a hotplate VWR VMS-C7 was used. A 160 × 160 × 10 mm aluminum block with 16 squares (30 × 30 mm, 1 mm depth) and a drilled hole for a temperature sensor were used to ensure an equal temperature distribution over the whole area. Twelve samples have been heated to the dedicated temperature simultaneously and kept there for 24 h.

3.3 Emission Measurements

Direct and delayed emission measurements were performed using a CAS 140CTS from Instrument Systems. To trigger the detection and the 365 nm (Thorlabs, M365 L2) LED, a TGP3122 pulse generator (AIM-TTI Instruments) was used. All measurements were performed in darkness under nitrogen or ambient conditions. The control software SweepMe! was used for automated data acquisition [A. Fischer, F. Kaschura, SweepMe! A multi-tool measurement software, www.sweep-me.net (accessed: 2021–12–20)].

3.4 Lifetime Measurements

The phosphorescent lifetime was determined using a silicon photodetector PDA100A by Thorlabs. The decay was recorded and fitted using a two-exponential fit resulting in an intensity-averaged lifetime. The prodecure and details can be found in Refs. [41, 52]. The measurement error is ±5 ms.

3.5 PLQY Measurements

The PLQY values were determined using the method proposed by de Mello et al. [53], improved by F. Fries. [49] As excitation source, a 300 W xenon lamp in combination with a monochromator (LOT Quantum Design MSH300) was used. The samples were placed in a calibrated integration sphere (Labsphere RTC-060-SF) and the spectra were acquired with an array spectrometer (CAS 140CT, Instrument Systems).

3.6 GIWAXS Measurements

GIWAXS investigations were performed at the NCD-SWEET beamline at the ALBA synchrotron. An area detector (LX255-HS, Rayonix) was placed approximately 20 cm behind the sample. The beam size was 80 μm horizontally and 30 μm vertically, and the beam energy was 12.4 keV. The incidence angle was 0.12°. The collected images were calibrated using a chromium oxide calibration standard and background-subtracted using background images obtained from a plain quartz sample.

3.7 Film Thickness

Film thickness was determined using a profilometer Veeco Dektak 150 from Bruker. A groove has been cut into the film in the middle of the sample using a cannula. A line scan was done at three different positions and the thickness values were averaged.

4 CONCLUSION

This study compares the phosphorescence performance of differently produced thin films employing all the same RTP emitter. The host polymer, the annealing temperature, and the fabrication technique were varied. Every combination was evaluated with regard to phosphorescence lifetime, PLQY, and P2L ratio. In terms of the host polymer, the most significant change was detected reaching annealing temperatures above the glass transition temperature. PLA, which has the lowest T_G, clearly showed a performance drop above 80 °C annealing temperature. Apart from PLA, reasonable annealing temperatures below T_G do not seem to change the overall phosphorescence performance in case of drop-cast and blade-coated samples. With respect to the fabrication technique, spin-coated films that are thinner by an order of magnitude, showed the poorest performance, while blade-coating and drop-casting yielded comparable results. This behavior might be induced by a higher net excitation intensity in thin films but is not yet fully understood at this stage and subject to further ongoing experiments. Going from thin to thick spin-coated films, the phosphorescence lifetime could be increased by a factor of up to 2.5 (PLA, sc).

DATA AVAILABILITY STATEMENT

The original contributions presented in the study are included in the article/**Supplementary Material**, further inquiries can be directed to the corresponding author.

AUTHOR CONTRIBUTIONS

HT prepared the samples, performed all measurements and wrote the manuscript. TB prepared the thick spin-coated samples. HT and KH did the blade-coating experiment. KH, FT and SM contributed GIWAXS data/analysis, TA, TB, AK, KH, and FT revised the manuscript and helped with data evaluation. SR supervised the project and revised the manuscript.

FUNDING

This work has received funding from the European Social Fund (Project OrgNanoMorph, proposal no. 100382168) and from the European Research Council (ERC) under the European Union's Horizon 2020 research and innovation program (Grant Agreement No. 679213 "BILUM"). The GIWAXS experiments were performed at the BL11 NCDSWEET beamline at ALBA Synchrotron with the collaboration of ALBA staff. The research leading to this result has been supported by the project CALIPSOplus under Grant Agreement 730872 from the EU Framework Program for Research and Innovation HORIZON 2020.

ACKNOWLEDGMENTS

HT and KH acknowledge the funding of the European Social Fund. FT acknowledges financial support from the German Research Foundation (DFG, MA 3342/6-1). AK acknowledges financial support from DFG project HEFOS (grant no. FI 2449/1-1). KH, FT and SM would like to acknowledge support by the German Excellence Initiative via the Cluster of Excellence EXC 1056 "Center for Advancing Electronics Dresden (cfaed)".

SUPPLEMENTARY MATERIAL

The Supplementary Material for this article can be found online at: https://www.frontiersin.org/articles/10.3389/fphy.2022.841413/full#supplementary-material

REFERENCES

1. Reineke S, Baldo MA. Room Temperature Triplet State Spectroscopy of Organic Semiconductors. *Sci Rep* (2015) 4:3797–804. doi:10.1038/srep03797
2. Xu S, Chen R, Zheng C, Huang W. Excited State Modulation for Organic Afterglow: Materials and Applications. *Adv Mater* (2016) 28:9920–40. doi:10.1002/adma.201602604
3. Yan X, Peng H, Xiang Y, Wang J, Yu L, Tao Y, et al. Recent Advances on Host-Guest Material Systems toward Organic Room Temperature Phosphorescence. *Small* (2021) 18:2104073. doi:10.1002/smll.202104073
4. Hirata S. Recent Advances in Materials with Room-Temperature Phosphorescence: Photophysics for Triplet Exciton Stabilization. *Adv Opt Mater* (2017) 5:1700116. doi:10.1002/adom.201700116
5. Ding L, Wang X-d. Luminescent Oxygen-Sensitive Ink to Produce Highly Secured Anticounterfeiting Labels by Inkjet Printing. *J Am Chem Soc* (2020) 142:13558–64. doi:10.1021/jacs.0c05506
6. Gmelch M, Thomas H, Fries F, Reineke S. Programmable Transparent Organic Luminescent Tags. *Sci Adv* (2019) 5:5. doi:10.1126/sciadv.aau7310
7. Li H, Li H, Wang W, Tao Y, Wang S, Yang Q, et al. Stimuli-Responsive Circularly Polarized Organic Ultralong Room Temperature Phosphorescence. *Angew Chem Int Ed* (2020) 59:4756–62. doi:10.1002/anie.201915164
8. Xu Y, Xu R, Wang Z, Zhou Y, Shen Q, Ji W, et al. Recent Advances in Luminescent Materials for Super-resolution Imaging via Stimulated Emission Depletion Nanoscopy. *Chem Soc Rev* (2021) 50:667–90. doi:10.1039/d0cs00676a
9. Jayabharathi J, Goperundevi G, Thanikachalam V, Panimozhi S. Regulation of Singlet and Triplet Excitons in a Single Emission Layer: Efficient Fluorescent/Phosphorescent Hybrid White Organic Light-Emitting Diodes. *ACS Omega* (2019) 4:15030–42. doi:10.1021/acsomega.9b01815
10. Kabe R, Notsuka N, Yoshida K, Adachi C. Afterglow Organic Light-Emitting Diode. *Adv Mater* (2016) 28:655–60. doi:10.1002/adma.201504321
11. Huang Q, Gao H, Yang S, Ding D, Lin Z, Ling Q. Ultrastable and Colorful Afterglow from Organic Luminophores in Amorphous Nanocomposites: Advanced Anti-counterfeiting and *In Vivo* Imaging Application. *Nano Res* (2020) 13:1035–43. doi:10.1007/s12274-020-2740-x
12. Kirch A, Fischer A, Liero M, Fuhrmann J, Glitzky A, Reineke S. Electrothermal Tristability Causes Sudden Burn-In Phenomena in Organic LEDs (Adv. Funct. Mater. 47/2021). *Adv Funct Mater* (2021) 31:2170349. doi:10.1002/adfm.202170349
13. Hirata S, Totani K, Yamashita T, Adachi C, Vacha M. Large Reverse Saturable Absorption under Weak Continuous Incoherent Light. *Nat Mater* (2014) 13:938–46. doi:10.1038/nmat4081
14. Kwon MS, Yu Y, Coburn C, Phillips AW, Chung K, Shanker A, et al. Suppressing Molecular Motions for Enhanced Room-Temperature Phosphorescence of Metal-free Organic Materials. *Nat Commun* (2015) 6:8947. doi:10.1038/ncomms9947
15. Sun Y, Liu S, Sun L, Wu S, Hu G, Pang X, et al. Ultralong Lifetime and Efficient Room Temperature Phosphorescent Carbon Dots through Multi-Confinement Structure Design. *Nat Commun* (2020) 11:5591. doi:10.1038/s41467-020-19422-4
16. Hirata S, Totani K, Zhang J, Yamashita T, Kaji H, Marder SR, et al. Efficient Persistent Room Temperature Phosphorescence in Organic Amorphous Materials under Ambient Conditions. *Adv Funct Mater* (2013) 23:3386–97. doi:10.1002/adfm.201203706
17. Mieno H, Kabe R, Notsuka N, Allendorf MD, Adachi C. Long-Lived Room-Temperature Phosphorescence of Coronene in Zeolitic Imidazolate Framework ZIF-8. *Adv Opt Mater* (2016) 4:1015–21. doi:10.1002/adom.201600103
18. Baroncini M, Bergamini G, Ceroni P. Rigidification or Interaction-Induced Phosphorescence of Organic Molecules. *Chem Commun* (2017) 53:2081–93. doi:10.1039/c6cc09288h
19. Bolton O, Lee K, Kim H-J, Lin KY, Kim J. Activating Efficient Phosphorescence from Purely Organic Materials by crystal Design. *Nat Chem* (2011) 3:205–10. doi:10.1038/nchem.984
20. Hamzehpoor E, Perepichka DF. Crystal Engineering of Room Temperature Phosphorescence in Organic Solids. *Angew Chem Int Ed* (2020) 59:9977–81. doi:10.1002/anie.201913393
21. An Z, Zheng C, Tao Y, Chen R, Shi H, Chen T, et al. Stabilizing Triplet Excited States for Ultralong Organic Phosphorescence. *Nat Mater* (2015) 14:685–90. doi:10.1038/nmat4259
22. Lucenti E, Forni A, Botta C, Carlucci L, Giannini C, Marinotto D, et al. Cyclic Triimidazole Derivatives: Intriguing Examples of Multiple Emissions and Ultralong Phosphorescence at Room Temperature. *Angew Chem Int Ed* (2017) 56:16302–7. doi:10.1002/anie.201710279
23. Gu L, Shi H, Bian L, Gu M, Ling K, Wang X, et al. Colour-tunable Ultra-long Organic Phosphorescence of a Single-Component Molecular crystal. *Nat Photon* (2019) 13:406–11. doi:10.1038/s41566-019-0408-4
24. Bian L, Shi H, Wang X, Ling K, Ma H, Li M, et al. Simultaneously Enhancing Efficiency and Lifetime of Ultralong Organic Phosphorescence Materials by Molecular Self-Assembly. *J Am Chem Soc* (2018) 140:10734–9. doi:10.1021/jacs.8b03867
25. Wang Z, Zhu C-Y, Wei Z-W, Fan Y-N, Pan M. Breathing-Ignited Long Persistent Luminescence in a Resilient Metal-Organic Framework. *Chem Mater* (2020) 32:841–8. doi:10.1021/acs.chemmater.9b04440
26. Ma X, Wang J, Tian H. Assembling-Induced Emission: An Efficient Approach for Amorphous Metal-free Organic Emitting Materials with Room-Temperature Phosphorescence. *Acc Chem Res* (2019) 52:738–48. doi:10.1021/acs.accounts.8b00620
27. DeRosa CA, Samonina-Kosicka J, Fan Z, Hendargo HC, Weitzel DH, Palmer GM, et al. Oxygen Sensing Difluoroboron Dinaphthoylmethane Polylactide. *Macromolecules* (2015) 48:2967–77. doi:10.1021/acs.macromol.5b00394
28. Al-Attar HA, Monkman AP. Room-Temperature Phosphorescence from Films of Isolated Water-Soluble Conjugated Polymers in Hydrogen-Bonded Matrices. *Adv Funct Mater* (2012) 22:3824–32. doi:10.1002/adfm.201200814
29. Ogoshi T, Tsuchida H, Kakuta T, Yamagishi Ta., Taema A, Ono T, et al. Ultralong Room-Temperature Phosphorescence from Amorphous Polymer Poly(Styrene Sulfonic Acid) in Air in the Dry Solid State. *Adv Funct Mater* (2018) 28:1707369. doi:10.1002/adfm.201707369
30. Tang G, Zhang K, Feng T, Tao S, Han M, Li R, et al. One-step Preparation of Silica Microspheres with Super-stable Ultralong Room Temperature Phosphorescence. *J Mater Chem C* (2019) 7:8680–7. doi:10.1039/c9tc02353d
31. Wang C, Chen Y, Hu T, Chang Y, Ran G, Wang M, et al. Color Tunable Room Temperature Phosphorescent Carbon Dot Based Nanocomposites Obtainable from Multiple Carbon Sources via a Molten Salt Method. *Nanoscale* (2019) 11:11967–74. doi:10.1039/c9nr03038g
32. Su Y, Phua SZF, Li Y, Zhou X, Jana D, Liu G, et al. Ultralong Room Temperature Phosphorescence from Amorphous Organic Materials toward Confidential Information Encryption and Decryption. *Sci Adv* (2018) 4:eaas9732. doi:10.1126/sciadv.aas9732
33. Kwon MS, Lee D, Seo S, Jung J, Kim J. Tailoring Intermolecular Interactions for Efficient Room-Temperature Phosphorescence from Purely Organic Materials in Amorphous Polymer Matrices. *Angew Chem Int Ed* (2014) 53:11177–81. doi:10.1002/anie.201404490
34. Lantz KR, Pate R, Stiff-Roberts AD, Duffell AG, Smith ER, Everitt HO. Comparison of Conjugated Polymer Deposition Techniques by Photoluminescence Spectroscopy. *J Vac Sci Technol B* (2009) 27:2227–31. doi:10.1116/1.3222855
35. Bora MÖ. The Influence of Heat Treatment on Scratch Behavior of Polymethylmethacrylate (PMMA). *Tribology Int* (2014) 78:75–83. doi:10.1016/j.triboint.2014.04.030
36. Thomas H, Fries F, Gmelch M, Bärschneider T, Kroll M, Vavaleskou T, et al. Purely Organic Microparticles Showing Ultralong Room Temperature Phosphorescence. *ACS Omega* (2021) 6:13087–93. doi:10.1021/acsomega.1c00785
37. Kirch A, Gmelch M, Reineke S. Simultaneous Singlet-Singlet and Triplet-Singlet Förster Resonance Energy Transfer from a Single Donor Material. *J Phys Chem Lett* (2019) 10:310–5. doi:10.1021/acs.jpclett.8b03668
38. Reineke S, Lindner F, Schwartz G, Seidler N, Walzer K, Lüssem B, et al. White Organic Light-Emitting Diodes with Fluorescent Tube Efficiency. *Nature* (2009) 459:234–8. doi:10.1038/nature08003
39. Fries F, Fröbel M, Lenk S, Reineke S. Transparent and Color-Tunable Organic Light-Emitting Diodes with Highly Balanced Emission to Both Sides. *Org Electro* (2017) 41:315–8. doi:10.1016/j.orgel.2016.11.022

40. Adamovich VI, Cordero SR, Djurovich PI, Tamayo A, Thompson ME, D'Andrade BW, et al. New Charge-Carrier Blocking Materials for High Efficiency OLEDs. *Org Electro* (2003) 4:77–87. doi:10.1016/j.orgel.2003.08.003
41. Salas Redondo C, Kleine P, Roszeitis K, Achenbach T, Kroll M, Thomschke M, et al. Interplay of Fluorescence and Phosphorescence in Organic Biluminescent Emitters. *J Phys Chem C* (2017) 121:14946–53. doi:10.1021/acs.jpcc.7b04529
42. Wilson DF. Oxygen Dependent Quenching of Phosphorescence: A Perspective. *Adv Exp Med Biol* (1992) 317:195–201. doi:10.1007/978-1-4615-3428-0_20
43. Borisov SM. CHAPTER 1. Fundamentals of Quenched Phosphorescence O2 Sensing and Rational Design of Sensor Materials. In: *Quenched-phosphorescence Detection of Molecular Oxygen: Applications in Life Science*. Cambridge, MA: Royal Society of Chemistry (2018). p. 1–18. doi:10.1039/9781788013451-00001
44. Köhler A, Bässler H. *Decay of Excitations" in: Electronic Processes in Organic Semiconductors*. Weinheim: Wiley-VCH Verlag GmbH and Co. KGaA (2015). p. 287
45. Chang M, Lim G, Park B, Reichmanis E. Control of Molecular Ordering, Alignment, and Charge Transport in Solution-Processed Conjugated Polymer Thin Films. *Polymers* (2017) 9:212–37. doi:10.3390/polym9060212
46. Gu X, Shaw L, Gu K, Toney MF, Bao Z. The Meniscus-Guided Deposition of Semiconducting Polymers. *Nat Commun* (2018) 9:534. doi:10.1038/s41467-018-02833-9
47. Tomkeviciene A, Dabulienė A, Matulaitis T, Guzauskas M, Andruleviciene V, Grazulevicius JV, et al. Bipolar Thianthrene Derivatives Exhibiting Room Temperature Phosphorescence for Oxygen Sensing. *Dyes Pigm* (2019) 170: 107605. doi:10.1016/j.dyepig.2019.107605
48. Gmelch M, Achenbach T, Tomkeviciene A, Reineke S. High-Speed and Continuous-Wave Programmable Luminescent Tags Based on Exclusive Room Temperature Phosphorescence (RTP). *Adv Sci* (2021) 8:2102104. doi:10.1002/advs.202102104
49. Fries F, Reineke S. Statistical Treatment of Photoluminescence Quantum Yield Measurements. *Sci Rep* (2019) 9:15638. doi:10.1038/s41598-019-51718-4
50. Thomas H, Pastoetter DL, Gmelch M, Achenbach T, Schlögl A, Louis M, et al. Aromatic Phosphonates: A Novel Group of Emitters Showing Blue Ultralong Room Temperature Phosphorescence. *Adv Mater* (2020) 32:2000880. doi:10.1002/adma.202000880
51. Ito Y, Virkar AA, Mannsfeld S, Oh JH, Toney M, Locklin J, et al. Crystalline Ultrasmooth Self-Assembled Monolayers of Alkylsilanes for Organic Field-Effect Transistors. *J Am Chem Soc* (2009) 131:9396–404. doi:10.1021/ja9029957
52. Lakowicz JR. *Principles of Fluorescence Spectroscopy*. New York, NY: Springer Science+Business Media, LLC (1983).
53. de Mello JC, Wittmann HF, Friend RH. An Improved Experimental Determination of External Photoluminescence Quantum Efficiency. *Adv Mater* (1997) 9:230–2. doi:10.1002/adma.19970090308

Conflict of Interest: The authors declare that the research was conducted in the absence of any commercial or financial relationships that could be construed as a potential conflict of interest.

frontiers | Frontiers in Chemistry

ORIGINAL RESEARCH
published: 26 April 2022
doi: 10.3389/fchem.2022.809863

Tetrathienothiophene Porphyrin as a Metal-Free Sensitizer for Room-Temperature Triplet–Triplet Annihilation Upconversion

Aleksey Vasilev*[1,2]*, Anton Kostadinov*[2]*, Meglena Kandinska*[1]*, Katharina Landfester*[2]** and Stanislav Baluschev*[2,3]**

[1]University of Sofia "Saint Kliment Ohridski", Faculty of Chemistry and Pharmacy, Sofia, Bulgaria, [2]Max Planck Institute for Polymer Research, Mainz, Germany, [3]University of Sofia "Saint Kliment Ohridski", Faculty of Physics, Sofia, Bulgaria

Optically excited triplet states of organic molecules serve as an energy pool for the subsequent processes, either photon energy downhill, such as room temperature phosphorescence, or photon energy uphill process—the triplet–triplet annihilation upconversion (TTA-UC). Manifestation of a high intersystem crossing coefficient is an unavoidable requirement for triplet state formation, following the absorption of a single photon. This requirement is even more inevitable if the excitation light is non-coherent, with moderate intensity and extremely low spectral power density, when compared with the light parameters of 1 Sun (1.5 AM). Coordination of a heavy atom increases substantially the probability of intersystem crossing. Nevertheless, having in mind the global shortage in precious and rare-earth metals, identification of metal-free organic moieties able to form triplet states becomes a prerequisite for environmental friendly optoelectronic technologies. This motivates us to synthesize a metal-free thienothiophene containing porphyrin, based on a condensation reaction between thienothiophene-2-carbaldehyde and pyrrole in an acidic medium by modified synthetic protocol. The upconversion couple tetrathienothiophene porphyrin/rubrene when excited at $\lambda = 658$ nm demonstrates bright, delayed fluorescence with a maximum emission at $\lambda = 555$ nm. This verifies our hypothesis that the ISC coefficient in thienothiophene porphyrin is efficient in order to create even at room temperature and low-intensity optical excitation densely populated organic triplet ensemble and is suitable for photon energy uphill processes, which makes this type of metal-free sensitizers even more important for optoelectronic applications.

Keywords: triplet state formation, room temperature, metal-free triplet–triplet annihilation, acidification, inter system crossing

Edited by:
Shuzo Hirata,
The University of Electro-Communications, Japan

Reviewed by:
Yasunori Matsui,
Osaka Prefecture University, Japan
Angelo Monguzzi,
University of Milano-Bicocca, Italy

****Correspondence:***
Katharina Landfester
landfester@mpip-mainz.mpg.de
Stanislav Baluschev
balouche@phys.uni-sofia.bg

Specialty section:
This article was submitted to Physical Chemistry and Chemical Physics,
a section of the journal Frontiers in Chemistry

Received: *05 November 2021*
Accepted: *18 March 2022*
Published: *26 April 2022*

Citation:
Vasilev A, Kostadinov A, Kandinska M, Landfester K and Baluschev S (2022) Tetrathienothiophene Porphyrin as a Metal-Free Sensitizer for Room-Temperature Triplet–Triplet Annihilation Upconversion.
Front. Chem. 10:809863.
doi: 10.3389/fchem.2022.809863

INTRODUCTION

Optically created molecular triplet organic ensembles serve as an energy pool for numerous succeeding processes and technological applications, such as photocatalytic organic reactions, all-optical sensing of metabolic activity of cell cultures, bio-imaging, and sunlight concentrators for organic solar cells. As an unavoidable prerequisite for all these applications, the requirements to create the organic triplet states at low excitation intensity and at room temperature are stated. The creation of excited triplet states depends drastically on the ISC-parameter of the sensitizer molecule.

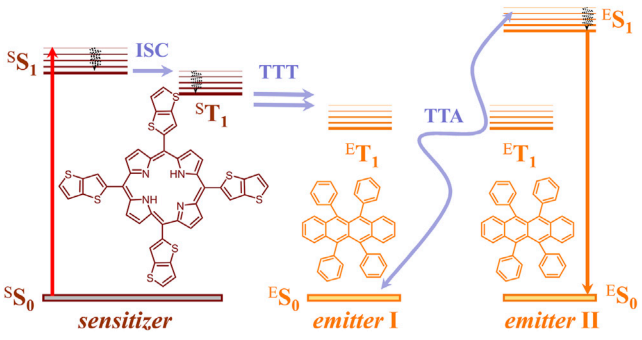

FIGURE 1 | Simplified energetic scheme of the TTA–UC process in the multicomponent organic system in a molecular oxygen-free environment. Left—structures of the sensitizer (TTP, *meso*-5,10,15,20-tetrathieno[*3,2-b*] thienyl porphyrin) and right—structure of the emitter (rubrene).

Furthermore, the ability to relax the accumulated triplet energy *via* an emissive process, such as the phosphorescence, depends also on the ISC parameter: if it is low, no phosphorescence at room temperature is observable. Nevertheless, the process of TTA-UC allows not only to use partially the sensitizer triplet states for an emissive process, such as the delayed fluorescence of the emitter molecules, but also to overcome the destructive influence of the rising sample temperature on the intensity of the emitted light. If the rising sample temperature leads to a significant decrease of the sensitizer phosphorescence, in contrary, the TTA-UC ensures a remarkable increase in the intensity of the delayed fluorescence.

Originally synthesized BODIPY triads (Guo et al., 2014), excited at room temperature by broadband visible light, function efficiently as triplet photosensitizers with enhanced intramolecular resonance energy transfer. Recently (Pristash et al., 2020), heavy-atom–free photon upconversion in a thiosquaraine composite was demonstrated. Hybrid photocatalysts based on C60 molecules, deposited on mesoporous silica, operating at room temperature were demonstrated (Kyriakopoulos et al., 2014). Stable functioning of a heterogeneous photocatalyst (Mori et al., 2013), consisting of iridium and rhodium complexes embedded in a macroreticular acidic resin, was evidenced for visible light–driven H_2 production. A systematic summary of the advances (Jin et al., 2021) in phosphorescence-based ratiometric sensing of physical parameters and chemical characteristics of living systems, including bioimaging and medical therapy, was recently presented. Iridium(III), ruthenium(II), and rhenium(I) rare-earth metal complexes, phosphorescent at room temperature (Tan et al., 2021) able to monitor the dynamic behavior of subcellular organelles and serving additionally as multifunctional antitumor compounds and integrating imaging and antitumor functions in a single molecule, were reported. Combination of Ir (III)–porphyrins with cell-penetrating and tumor-targeting peptides (Koren et al., 2012) allows sensing the oxygen saturation in various mammalian cell types. Modified phosphorescent materials, combined with amphiphilic or hydrophilic polymers in order to increase their biocompatibility and to allow *in vitro* and *in vivo* bioimaging (Zhen et al., 2021), were recently reviewed. Molecular systems, demonstrating even at highly efficient room temperature thermally activated delayed fluorescence (TADF), were recently (Yang et al., 2017) reviewed. Banu Iyisan (Iyisan et al., 2020) demonstrated minimally invasive and real-time temperature sensing in HeLa cell cultures, based on the process of triplet–triplet annihilation photon energy upconversion, performed in the ambient environment without loss of sensitivity: the sensing organic ensemble was embedded in core/shell nanoparticles, hosting also sacrificial singlet oxygen scavenging oils (FDA-approved as food additives).

Excited organic triplet ensembles interact with the environment much more intensively than the organic singlet states. Therefore, in order to observe bright phosphorescence at room temperature or efficient triplet–triplet annihilation photon energy upconversion (TTA-UC), it is essential to build up a densely populated organic triplet ensemble. In other words, the number of molecules in the excited triplet state should be comparable with the total number of molecules (belonging to the studied species). Importantly, all molecular energy levels, involved in the processes of phosphorescence or TTA-UC should be real molecular levels, i.e., no virtual energetic levels are involved. This structural feature, combined with the relatively long excited state lifetime, allows accumulation of optically excited triplet states as a result of linear absorption of light with very low intensity. Therefore only organic molecules possessing enough high intersystem crossing coefficient (ISC) are able to form an excited triplet state, following absorption of a single photon. Coordination of a heavy atom increases substantially the probability of intersystem crossing. The major experimental demonstrations of densely populated excited triplet ensembles are related to application of precious or rare-earth metals. There are few examples of metal-free TTA-UC (Zhou et al., 2017; Pristash et al., 2020). Nevertheless, having in mind the global shortage in precious and rare-earth metals, identification of metal-free organic moieties able to form triplet states becomes a prerequisite for environmental friendly optoelectronic technologies. This motivates us to synthesize a metal-free thienothiophene containing porphyrin, serving as a sensitizer for the process of TTA-UC.

The process of TTA–UC performed in fluidic organic systems (volatile or nonvolatile organic solvents) or in a hydrophobic soft matter environment relays on optically created densely populated organic triplet ensembles. The driving force for TTA-UC is the intermolecular triplet energy transfer, including the subsequent processes of triplet–triplet energy transfer (TTT) and triplet–triplet annihilation (TTA). All existing TTA-UC models Zhou J et al. (2015); Askes et al. (2017); Gray et al. (2018), state that the annihilation process is diffusion-limited, indirectly assuming the molecular mass transport of excited molecular species as a main physical process behind it, i.e., in order to observe the TTA-UC process, the sensitizer and emitter molecules must be closely arranged; thus, Dexter energy transfer occurs. Therefore in a soft matter matrix, the TTA-UC process demonstrates essential dependences on the material and environmental parameters,

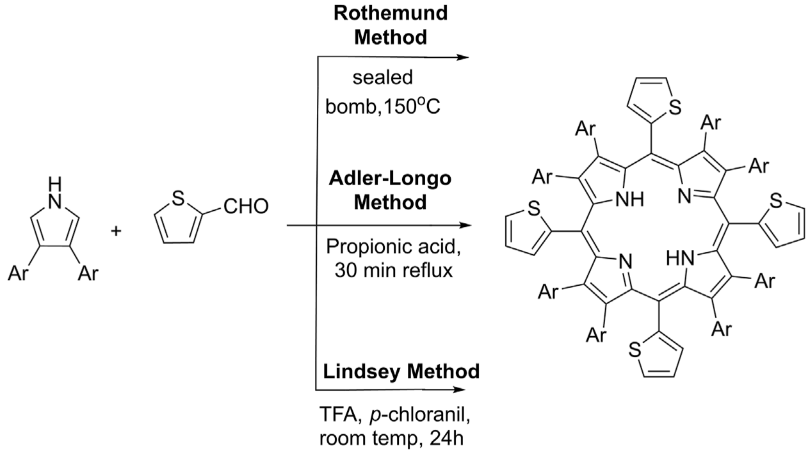

SCHEME 1 | Synthetic methods and the general structure of substituted thienyl-porphyrins.

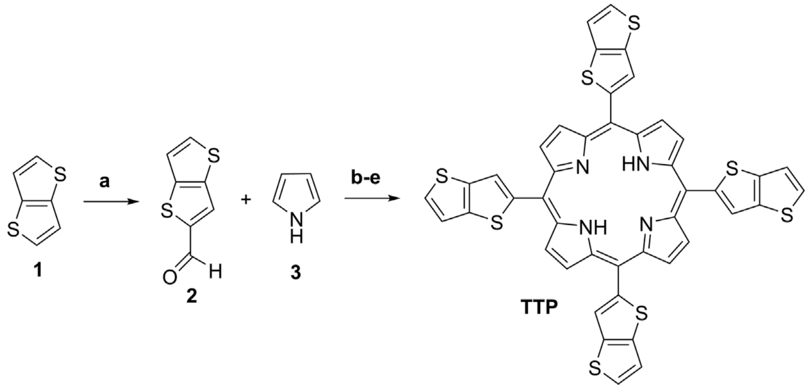

SCHEME 2 | Reaction conditions and yields: **(A)** Preparation of intermediate 2: 1, DMF, POCl3, 80°C, 2 h, and Yield: 81%; **(B)** Adler's method procedure A: 2, 3, acetic acid, 60°C, 2 h, and Yield: 2%; **(C)** Adler's method procedure B: 2, 3, acetic acid, reflux 30 min, and Yield: 2.4%; **(D)** Adler's method procedure C: 2, 3, Propionic acid, reflux 1 h, 3.3%; and **(E)** Lindsey's method procedure D: 2, 3, r. t., dry DCM, TFA, DDQ, TEA, and Yield: 5.1%.

such as the degree of overlapping of the interacting energy states, matrix temperature, matrix viscosity, and presence of molecular oxygen, dissolved into the solvent or adsorbed on the soft matter film. It is important to notice that all these materials and environmental parameters are strongly inter-related, and their impact on the densely populated triplet ensembles is not a linear combination of its partial impacts.

Our aim in this regard is to explore the effect of second thienyl core attached to the tetra meso-thienyl function of the porphyrin and to investigate its application as a sensitizer molecule in metal-free TTA-UC systems. To the best of our knowledge, the synthesis of meso-5,10,15,20-tetrathieno[3,2-b]thienyl porphyrin (TTP, **Scheme 2**) is not reported. Therefore, it was necessary to find the most easy, reliable, and accessible reaction procedures and to adjust the reaction conditions to the needs of the synthetic method of choice.

EXPERIMENTAL

Materials and Methods

General

Dimethylformamide (DMF), dichloromethane (DCM), acetic acid, propionic acid, triethylamine (TEA), thieno[*3,2-b*] thiophene (**1**), phosphorus oxychloride ($POCl_3$), trifluoroacetic acid (TFA), 2,3-dichloro-5,6-dicyano-1,4-benzoquinone (DDQ), *1H*-pyrrole, and glacial acetic acid are purchased from Sigma-Aldrich, TCI Europe or ABCR and are used as supplied. Melting points were determined on a Büchi MP B-545 apparatus and are uncorrected. NMR spectra (^1H-, ^{13}C-NMR) were obtained on a Bruker Avance II + NMR spectrometer operating at 500 MHz for ^1H- and 125 MHz for ^{13}C-NMR using DMSO-d_6 as a solvent. The chemical shifts are given in ppm (δ) using tetramethylsilane (TMS) as an internal standard. MALDI-TOF mass spectra were recorded on a Bruker iontof TOF.SIMS NCS Mass Spectrometer, at the Max Planck Institute for Polymer Research, Mainz, Germany. The UV-VIS spectra were measured using a Unicam 530 UV-Vis spectrophotometer.

Synthesis of thieno[3,2-b] thiophene-2-Carbaldehyde (2)

A solution of 14 g (0.1 mol) of thieno[*3,2-b*]thiophene in 22 ml DMF was cooled in ice water. To the solution, 15.3 g (0.1 mol) of phosphorus oxychloride was added during 15 min, followed by vigorous stirring. During the addition of phosphorous oxychloride, the temperature in the reaction vessel was not allowed to exceed 20°C. The reaction mixture was stirred for 15 min at 0°C, 30 min at room temperature, and then heated to 60–65°C, at which temperature an exothermic reaction started. When the exothermic reaction had ceased, the reaction mixture was heated for 45 min on a steam bath, cooled, and poured on ice. The pH was adjusted to 5–6 with solid sodium acetate, and the reaction mixture was left overnight. The reaction product was extracted with ether, and the ether was washed with water, then with saturated sodium bicarbonate solution, and dried with anhydrous magnesium sulfate. Yield 81%; ^{1}H-NMR (500 MHz, $CDCl_3$; δ (ppm): 7.36 d (1H, CH, $^3J_{HH} = 5.0$ Hz); 7.73 d (1H, CH, $^3J_{HH} = 5.3$ Hz); and 7.97 s (1H, CH), 10.00 s (1H, CHO). ^{13}C NMR (135 MHz, $CDCl_3$ δ(ppm)): 120.19, 129.09, 133.90, 139.22, 145.49, 145.76, and 183.59. Mp = 54–56°C (lit. 52–55°C).

Synthesis of 5,10,15,20-tetrakis(thieno [3,2-b]thiophen-2-yl)porphyrin (TTP)

Procedure A

In a 50-ml round bottom flask, equipped with an electromagnetic stirrer and a reflux condenser, 0.5 g (0.0297 mol) thieno[*3,2-b*] thiophene-2-carbaldehyde (**2**), 0.21 g (0.00312 mol, 0.22 ml) *1H*-pyrrole (**3**) and 10 ml glacial acetic acid were added, and the mixture was heated at 60°C for 3 h. The reaction mixture was cooled to room temperature, and 20 ml methanol was added. The formed precipitate was suction filtered and washed with methanol three times. The residue was purified on a short path silica column with eluent TEA: n-heptane: DCM = 0.2: 2: 3. The product was isolated as a first position on the column. The analytical sample was obtained after subsequent recrystallization from DCM: MeOH. Yield: 0.051 g (2%). ^{1}H-NMR (500 MHz, CD_2ClCD_2Cl; d, ppm): 2.64 s (2H, NH); 7.54 d (4H, CH, $^3J_{HH}$ = 5.2 Hz); 7.66 d (4H, CH, $^3J_{HH}$ = 5.0 Hz); 8.11 s (4H, CH); and 9.15 s (8H, CH). ^{13}C NMR DEPT (135 MHz, CD_2ClCD_2Cl δ(ppm)): 112.8 CH, 119.3 CH, 126.2 CH, 127.4 CH, 138.7 CH, 141.6 CH, and 144.3 CH (MALDI-TOF (*m/z*): found 861.9509, calcd 861.96 for $C_{44}H_{22}N_4S_8$. IR (nujol) ν_{max}: 2395, 2305, 1190, 1110, 1495, 1340, 1190, and 580 cm^{-1}; and UV–vis [toluene, λ_{max} (nm), ε (l.mol^{-1}. cm^{-1}]: 437 (152000), 526 (8990), 567 (5390), 597 (3880), and 665 (2510)].

Procedure B

In a 50-ml round bottom flask, equipped with an electromagnetic stirrer and a reflux condenser, 0.5 g (0.0297 mol) thieno[*3,2-b*] thiophene-2-carbaldehyde (**2**), 0.21 g (0.00312 mol, 0.22 ml) *1H*-pyrrole (**3**), and 10 ml glacial acetic acid were added, and the mixture was heated at reflux for 30 min. The reaction mixture was cooled to room temperature, and 20 ml methanol was added. The formed precipitate was suction filtered and washed with methanol three times. The residue was purified on a short path silica column with eluent TEA: n-heptane: DCM = 0.2: 2: 3. The product was isolated as a first spot. The analytical sample was obtained after subsequent recrystallization from DCM: MeOH. Yield: 0.063 g (2.4%).

Procedure C

In a 50-ml round bottom flask, equipped with an electromagnetic stirrer and a reflux condenser, 0.5 g (0.00297 mol) thieno[*3,2-b*] thiophene-2-carbaldehyde (**2**), 0.21 g (0.00312 mol, 0.22 ml) *1H*-pyrrole (**3**), and 10 ml propionic acid were added, and the mixture was heated at reflux for 1 h. The reaction mixture was cooled to room temperature, and 20 ml methanol was added. The formed precipitate was suction filtered and washed with methanol three times. The residue was purified on a short path silica column with eluent TEA: n-heptane: DCM = 0.2: 4: 1. The product was isolated as a first spot by TLC. The analytical sample was obtained after subsequent recrystallization from DCM: MeOH. Yield: 0.085 g (3.3%).

Procedure D

In a 1000-ml, round bottom flask, equipped with an electromagnetic stirrer, 1 g (0.00684 mol) thieno[*3,2-b*] thiophene-2-carbaldehyde (**2**), 0.47 ml (0.46 g, 0.00684 mol), and *1H*-pyrrole (**3**) were dissolved in 500 ml dry dichloromethane. Then, 0.35 ml (0.52 g, 0.0046 mol) trifluoroacetic acid (TFA) was added dropwise by syringe for about 15 min, and the reaction solution was vigorously stirred at room temperature for 4 h in the dark. Furthermore, 2.64 g (0.01163 mol) of DDQ was added, and the mixture was stirred for 30 min at the same conditions. In addition, 4 ml of triethylamine was added, and the solvent was removed using a rotary evaporator to volume of 15 ml. To the dark-colored residue, 30 ml methanol was added. The precipitate was suction filtered and washed with methanol. The analytical sample was obtained after silica flash column chromatography with eluent ethyl acetate: petrol ether = 3:2. Yield: 0.03 g (5.1%).

TTA-UC

The process of TTA-UC is the only upconversion process realized up to now with non-coherent, ultra-low intensity sunlight (Baluschev et al., 2006). A key advantage of the TTA-UC using techniques is that the conversion processes and devices can be considered and optimized independently, without affecting the particular properties of the operating photochemical material or device architecture. The TTA-UC takes place in multi-chromophore systems consisting of energetically optimized pairs of emitter molecules (typically aromatic hydrocarbons) and sensitizer molecules (usually, metalled macrocycles, such as porphyrins and phthalocyanines), as shown in **Figure 1**. Shortly, the photon energy absorbed by a sensitizer is stored in its metastable triplet state, formed in the process of intersystem crossing (ISC).

Furthermore, this energy is transferred to an emitter triplet state *via* the process of TTT. Next, the excited triplet states of two emitter molecules undergo TTA, in which one emitter molecule returns back to its singlet ground state and the other molecule gains the energy of both triplet states and is excited to the higher singlet state. As the singlet state emitter decays radiation back to the ground state, a delayed fluorescence photon (the blue arrow, **Figure 1**) bearing a higher energy than that of the excitation photons is emitted.

RESULTS AND DISCUSSION

Synthesis

Functionalized thienyl-appended porphyrins are significant compounds in many high technology applications, owing to their important physicohemical properties: in a recent comprehensive review, Boyle et al., (2010) demonstrated applications of meso-tetrathienylporphyrins, based on its convenient preparation and ease of functionalization, allowing a large variety of energy transfer reactions, excellent film-forming and pronounced electro-conductivity behavior.

Different modifications of the main synthetic methods demonstrated on **Scheme 1** for the preparation of meso-5,10,15,20-thienyl porphyrins and their derivatives were reported in the literature. The first reported synthesis of meso-tetra (thien-2-yl)porphyrin (**Scheme 1**) was presented by Triebs and Haeberie et al. (1968) by the condensation of pyrrole and 2-thiophenecarboxaldehyde by a modified Rothemund method giving 9% yield. The Adler-Longo's method was later applied (Torrens et al., 1972) by allowing the reaction of equimolar amounts of 2-thiophenecarboxaldehyde and pyrrole in refluxing propionic acid, but the reaction yields were not reported (**Scheme 1**). The main efforts to date were focused to adapt the so-called Lindsey's method for the synthesis of the commented here type of porphyrins (**Scheme 1**). Lindsey's conditions are much milder in comparison to previous methods. Normally, such Lindsey-type synthesis requires room temperature, dehydrogenation reagent (such as p-chloranil or DDQ), and acid. The mixture is subsequently treated with a basic reagent. Thus, Lindsey's method for the preparation of porphyrins provides higher reaction yields and higher purity of the crude reaction products (Lindsey et al., 1987; Ono et al., 1998). Using the commented synthetic strategies, a large variety of polythiophenyl-substituted porphyrins were synthesized and their photophysical and electrochemical properties have been explored (Boyle et al., 2010).

First, the starting thieno[3,2-b]thiophene-2-carbaldehyde (2) (**Scheme 2**) was prepared by the Vilsmeier–Haack-Arnold formylation reaction of thieno[3,2-b]thiophene in DMF as a reagent and as a reaction media in the presence of a slight molar excess of phosphorus oxychloride (Bugge, 1971). The structure of the compound was proved by thin-layer chromatography (TLC), ^{1}H-NMR, 13C-NMR spectroscopy, and observing the melting point. For the synthesis of the target meso-5,10,15,20-tetrathieno[3,2-b]thienyl porphyrin (**Scheme 2**), a large number of reaction conditions were examined by varying the reaction temperature, changing the solvents, and the molar quantities of the reagents and the reaction time as well.

Herein, we described the reaction conditions ensuring the best reaction yields in our hands. In a series of experiments, the best molar quantities for the reactants ensuring optimal reaction yields were observed. The most promising procedures with the optimal molar quantities of the starting materials are based on Adler-Longo's method and Lindsey's method (**Scheme 2**). In procedure A, was used glacial acetic acid for reaction media because of the lowest boiling temperature in comparison with the propionic acid. The mild reaction temperature at 60°C does not lead to higher yields but significantly decreases the amounts of tarry side products formed during the reaction, thus providing facile purification.

Heating the reaction mixture at 120°C for 30 min afforded a slight increase in the reaction yield (**Scheme 2C**, Procedure B). Changing the solvent to propionic acid and ensuring 1 h reflux (141°C) in an open-air system afforded 3.3% reaction yield (Procedure C, Adler-Longo's method). Finally, by modifying Lindsey's procedure by leading the reaction in an optimized volume of dry DCM in the presence of TFA and using the milder dehydrogenating reagent DDQ instead of p-chloranil (classical Lindsey's conditions), we obtained the higher for the given compound reaction yield (5.1%) with the best purity among the mentioned ones (**Scheme 2E**, Procedure D). The chemical structure of the target porphyrin TTP was proved by several analytical methods. The proton NMR spectra demonstrated typical for the meso-tetrathienyl porphyrins signals for the aromatic protons (Bhyrappa and Bhavana, 2001). Typically, the imine protons NH from the porphyrin cycle appear as a singlet with integral intensity for two protons at -2.64 ppm (**Supplementary Material**). Two doublets at 7.53 and 7.65 with an integral intensity for four protons each and with J-constants around 5 Hz can be assigned to the thienyl protons from the theino[3,2-b]thiophene functionality. The

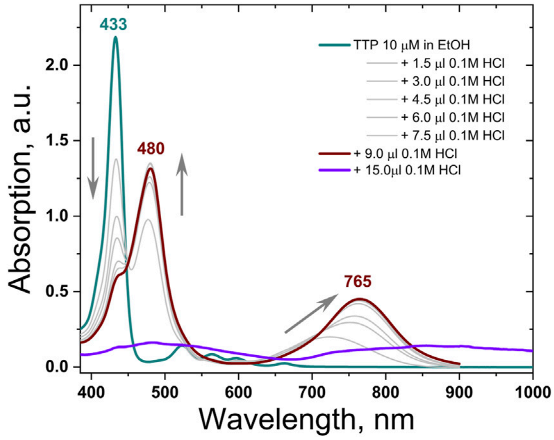

FIGURE 2 | Absorption spectra of TTP in ethanol neat (the dark cyan line) and in the presence of 3×10^{-4} M HCl (the wine line) and in the presence of 5×10^{-3} M HCl (the violet line). For clarity, all intermediate absorption spectra are in light gray.

singlet at 8.11 ppm with the integral intensity corresponding to four protons is assigned to the CH-proton from the theino[3,2-b] thiophene moiety as well. Typically for the unsubstituted pyrrole part of the meso-substituted porphyrin, the broad singlet appeared at 9.15 ppm with an integral intensity for eight protons. The carbon NMR spectra (SI), the UV-VIS spectra, and the MALDI-TOF spectra unequivocally prove the chemical structure and the purity of the final compound TTP (**Supplementary Material**). The relation between the chemical structure and the photo-physical properties of the target porphyrin TTP is described in the next section.

Optical Properties

The UV-VIS absorption spectra of TTP demonstrate the typical for all *meso*-tetrathienyl porphyrin absorption bands. The highly intensive absorption Soret-band is attributed to the higher energy $S_0 \rightarrow S_2$ electron transitions, and it appears at $\lambda = 433$ nm followed by four quite lower intensity Q-bands relative to $S_0 \rightarrow S_1$ electron transitions (**Figure 2**, the dark cyan line). The red shifted band in the absorption spectra of TTP at $\lambda = 665$ nm is bathochromically shifted in comparison with the same in the regular *meso*-tetrathienyl porphyrins $\lambda = 613$ nm (Zhou Y et al., 2015) probably due to the enhanced electron-donating properties of the thienothienyl function in comparison with thien-2-yl one. Titration of ethanol solution of TTP with successive steps of 0.1 M HCl demonstrates pronounced halochromic behavior: the Soret-band of the porphyrin at $\lambda = 437$ nm decreases substantially; simultaneously, a new absorption band grows up with a central wavelength at $\lambda = 480$ nm. Additionally, stepwise appearance and monotonic increase of the intensity of the absorption Q-band with the central wavelength at $\lambda = 760$ nm (**Figure 2**, the wine line) was observed (up to 3×10^{-4} M HCl). Further increase of acidity leads to a dramatic decrease of the total absorption (**Figure 2**, the violet line).

In a strong acid media, the Q-band and S-band of the thienothienyl porphyrins shift bathochromically; additionally, the multiple Q-bands of the free base thienothienyl porphyrin grow together and re-build in an intensive and substantially red shifted Q-band (for more than $\Delta\lambda = 100$ nm). This demonstrates that the absorption spectrum of the studied TTP can be tuned significantly toward the near IR spectral range, without any additional synthetic steps. The direct demonstration of TTA-UC in an acidic medium was not possible since the used emitter rubrene is not directly soluble in ethanol. We intend to decorate emitter molecules in order to increase their solubility in such media and to observe TTA-UC.

Supplementary Figure S6 (SI -part) shows the fluorescence spectrum of the studied TTP-sensitizer in strong acidic media, excited at $\lambda_{exc} = 785$ nm. This wavelength is completely outside the TTP spectrum in hydrophobic media (**Figure 2**, the dark cyan line).

The emitter molecule rubrene (**Figure 1**) possesses a very broad excited triplet state, having energies between 1.04 and 1.29 eV (Liu and Larry, 1977). As mentioned earlier, metal-free TTP does not show phosphorescence at room temperature. We studied the TTA-UC efficiency of the metal-free TTP by testing different perylene and perylene monoimide derivatives, working well with mixed benzo-naphtho and tetranaphtho porphyrins (Heinrich et al., 2018). However, the studied metal-free TTP works efficiently only with rubrene: therefore, its triplet state can be comparable with those of tetraanthraporphyrins, i.e., 0.95 eV.

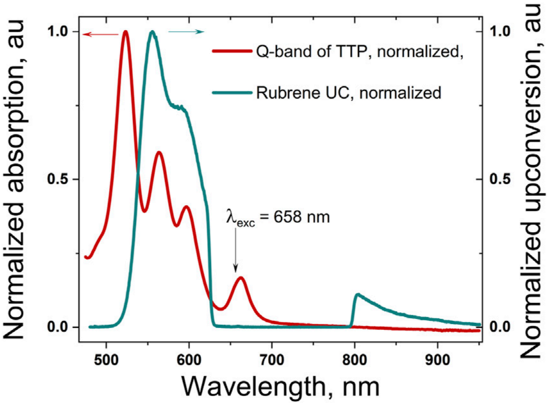

FIGURE 3 | Normalized Q-band absorption spectrum of the meso-5,10,15,20-tetrathieno[3,2-b]thienyl porphyrin, dissolved in 98 toluene/2 vol% squalene (the dark red line); normalized delayed fluorescence of rubrene (the cyan curve) excited in UC regime, whose excitation wavelength λ_{exc} = 658 nm. The excitation wavelength is suppressed by using a super broadband notch filter (rejection: more than 10^4 for the wavelength range centered at $\Delta\lambda$ = 705 nm, with FWHM = 175 nm, and transparency, for all other wavelengths, better than 0.99).

The TTA-UC process suffers doubly by the presence of even a small concentration of molecular oxygen; first, corresponding to the oxygen concentration and/or the rate of molecular oxygen diffusion throughout the sealing materials, significant amounts of optically excited sensitizer triplet states are lost, and second (which is an even more destructive consequence), a considerable amount of the photoactive molecules are being damaged, and they fail out from the UC process. Linear polyunsaturated triterpene, such as squalene (Shimizu et al., 2018), is proved to be a very efficient sacrificial singlet oxygen scavenger (SSOS). This SSOS material introduces a huge excess of "sacrificial" double bonds, combined with low viscosity (at room temperature), essential for high molecular mobility of the UC molecules, ensuring relatively high efficiency of the TTA-UC process.

Figure 3 shows the normalized Q-band absorption spectrum of the TTP, dissolved in a mixture of toluene and squalene. The sample is prepared and sealed in a nitrogen-filled glove box (residual oxygen concentration, 2ppm). The addition of 2 % vol. of squalene ensures the complete scavenging of the residual molecular oxygen; thus, the UC sample could be defined as oxygen-free.

The quantum yield ($Q.Y._{TTA-UC}$) of the TTA-UC process is certainly of decisive importance. The IUPAC definition of quantum yield (Q.Y.) for the arbitrary emissive process defines it as a ratio of the number of emitted photons to the number of absorbed photons. It has to be pointed out explicitly that such a classical term (i.e., $Q.Y._{TTA-UC} = N^{photons}_{emitted}/N^{photons}_{absorbed}$) is attributed to a complex process such as the diffusion controlled TTA-UC

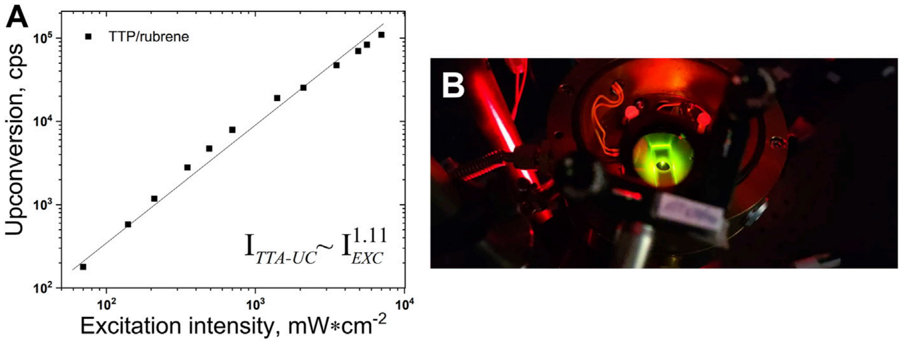

FIGURE 4 | (A)–Dependence of the UC intensity on the excitation intensity. *Experimental conditions*: UC couple, TTP (2×10^{-5} M)/rubrene (4×10^{-4} M); ratio sensitizer/emitter - C_S/C_E = 1/20; room temperature; sample thickness – 1000 µm; single-mode laser diode, λ_{exc} = 658 nm; optical registration–*via* fiber–spectrometer (C10083CA, Hamamatsu Inc.) with absolute wavelength calibration and corrected spectral response; integration time, 100 ms; excitation beam diameter, d_{EXC} = 1600 µm; Vitrotube® glass sample, sealed in a nitrogen-filled glove-box, residual oxygen < 2 ppm; each measurement is performed on a neat sample spot; solvent, 98 vol% toluene/2 vol% squalene; Q.Y.$_{TTA\text{-}UC}$ = 0.018 (following the IUPAC definition). **(B)**–Photograph of a working metal-free TTA-UC sample. In order to suppress the diffuse scattered excitation light, a super broadband notch filter was used.

(consisting of a chain of intramolecular and intermolecular energy transfer processes, namely, ISC, TTT, TTA, and diffusion of excited triplet states). Here, $N_{absorbed}^{photons}$ represents the number of photons absorbed by the UC sensitizer molecules, and $N_{emitted}^{photons}$ represents the number of photons emitted by the UC emitter molecules. The main outcome of such a simplified definition is that clear and noncontradictive knowledge about a real UC photon flux is expected for the given excitation conditions.

The sub-quadratic dependence of the UC fluorescence on the excitation intensity, demonstrated for many UC systems (Baluschev et al., 2016; Askes and Bonnet, 2018) dissolved in organic solvents in oxygen-free conditions is reproduced here for the UC systems dissolved in 98 vol% toluene/2 vol% squalene (**Figure 4**). The experimental data are well approximated with a power law $I_{TTA-UC} = a \times I_{exc}^{b}$, where the parameter **b** = 1.11.

CONCLUSION

We demonstrated the effective formation of densely populated optically excited triplet ensembles, by means of metal-free thienothiophene-containing porphyrins operating at room temperature and low excitation intensity (as low as 100 mW×cm^{-2}). Furthermore, we observed efficient triplet–triplet annihilation upconversion with Q.Y. as high as 0.018, following the IUPAC definition for quantum yield. Manifestation of a high intersystem crossing coefficient is an unavoidable requirement for triplet state formation, following absorption of a single photon. We synthesized a metal-free thienothiophene-containing porphyrin based on a condensation reaction between thienothiophene-2-carbaldehyde and pyrrole in an acidic medium. This proves that thienothiophene porphyrins exhibit ISC coefficients high enough to perform photon energy uphill processes, which makes this type of metal-free sensitizers even more important for optoelectronic applications.

DATA AVAILABILITY STATEMENT

The original contributions presented in the study are included in the article/**Supplementary Material**, further inquiries can be directed to the corresponding authors.

AUTHOR CONTRIBUTIONS

All authors listed have made a substantial, direct, and intellectual contribution to the work and approved it for publication.

FUNDING

This research was supported by the Bulgarian National Science Fund under the fund grant number КП-06-Н37/15-06.12.19 SunUp and Max Planck Society, Germany.

ACKNOWLEDGMENTS

SB, AV, and MK acknowledge the КП-06-Н37/15-06.12.19 SunUp-project of the Bulgarian National Science Fund for the financial support.

SUPPLEMENTARY MATERIAL

The Supplementary Material for this article can be found online at: https://www.frontiersin.org/articles/10.3389/fchem.2022.809863/full#supplementary-material

REFERENCES

Askes, S. H. C., and Bonnet, S. (2018). Solving the Oxygen Sensitivity of Sensitized Photon Upconversion in Life Science Applications. *Nat. Rev. Chem.* 2 (12), 437–452. doi:10.1038/s41570-018-0057-z

Askes, S. H. C., Leeuwenburgh, V. C., Pomp, W., Arjmandi-Tash, H., Tanase, S., Schmidt, T., et al. (2017). Water-Dispersible Silica-Coated Upconverting Liposomes: Can a Thin Silica Layer Protect TTA-UC against Oxygen Quenching? *ACS Biomater. Sci. Eng.* 3, 322–334. doi:10.1021/acsbiomaterials.6b00678

Baluschev, S., Katta, K., Avlasevich, Y., and Landfester, K. (2016). Annihilation Upconversion in Nanoconfinement: Solving the Oxygen Quenching Problem. *Mater. Horiz.* 3, 478–486. doi:10.1039/c6mh00289g

Baluschev, S., Miteva, T., Yakutkin, V., Nelles, G., Yasuda, A., and Wegner, G. (2006). Up-Conversion Fluorescence: Noncoherent Excitation by Sunlight. *Phys. Rev. Lett.* 97 (14), 143903. doi:10.1103/PhysRevLett.97.143903

Bhyrappa, P., and Bhavana, P. (2001). Meso-tetrathienylporphyrins: Electrochemical and Axial Ligation Properties. *Chem. Phys. Lett.* 349, 399–404. doi:10.1016/S0009-2614(01)01189-7

Boyle, N. M., Rochford, J., and Pryce, M. T. (2010). Thienyl-Appended Porphyrins: Synthesis, Photophysical and Electrochemical Properties, and Their Applications. *Coord. Chem. Rev.* 254, 77–102. doi:10.1016/j.ccr.2009.09.001

Bugge, A., Tveita, P. O., Reistad, K. R., Sjöstrand, E., Lagerlund, I., and Ehrenberg, L. (1971). Preparation of Some Methyl- and Formylthieno[2,3-B]thiophenes and Thieno[3,2-B]thiophenes. *Acta Chem. Scand.* 25, 27–34. doi:10.3891/acta.chem.scand.25-0027

Gray, V., Moth-Poulsen, K., Albinsson, B., and Abrahamsson, M. (2018). Towards Efficient Solid-State Triplet-Triplet Annihilation Based Photon Upconversion: Supramolecular, Macromolecular and Self-Assembled Systems. *Coord. Chem. Rev.* 362, 54–71. doi:10.1016/j.ccr.2018.02.011

Guo, S., Ma, L., Zhao, J., Küçüköz, B., Karatay, A., Hayvali, M., et al. (2014). BODIPY Triads Triplet Photosensitizers Enhanced with Intramolecular Resonance Energy Transfer (RET): Broadband Visible Light Absorption and Application in Photooxidation. *Chem. Sci.* 5, 489–500. doi:10.1039/C3SC52323C

Heinrich, E., Avlasevich, Y., Landfester, K., and Baluschev, S. (2018). Annihilation Upconversion: Harvesting the Entire Deep-Red Spectral Range of the Sun Irradiation. *J. Photonics Energy* 8 (2), 022002. doi:10.1117/1.JPE.8.022002

Iyisan, B., Thiramanas, R., Nazarova, N., Avlasevich, Y., Mailänder, V., Baluschev, S., et al. (2020). Temperature Sensing in Cells Using Polymeric Upconversion Nanocapsules. *Biomacromolecules* 21, 4469–4478. doi:10.1021/acs.biomac.0c00377

Jin, H., Jiang, X., Sun, Z., and Gui, R. (2021). Phosphorescence-based Ratiometric Probes: Design, Preparation and Applications in Sensing, Imaging and Biomedicine Therapy. *Coord. Chem. Rev.* 431, 213694. doi:10.1016/j.ccr.2020.213694

Koren, K., Dmitriev, R. I., Borisov, S. M., Papkovsky, D. B., and Klimant, I. (2012). Complexes of IrIII-Octaethylporphyrin with Peptides as Probes for Sensing Cellular O2. *ChemBioChem* 13, 1184–1190. doi:10.1002/cbic.201200083

Kyriakopoulos, J., Papastavrou, A. T., Panagiotou, G. D., Tzirakis, M. D., Triantafyllidis, K. S., Alberti, M. N., et al. (2014). Deposition of Fullerene C60 on the Surface of MCM-41 via the One-step Wet Impregnation Method: Active Catalysts for the Singlet Oxygen Mediated Photooxidation of Alkenes. *J. Mol. Catal. A: Chem.* 381, 9–15. doi:10.1016/j.molcata.2013.09.03610.1016/j.molcata.2013.09.036

Lindsey, J. S., Schreiman, I. C., Hsu, H. C., Kearney, P. C., and Marguerettaz, A. M. (1987). Rothemund and Adler-Longo Reactions Revisited: Synthesis of Tetraphenylporphyrins under Equilibrium Conditions. *J. Org. Chem.* 52, 827–836. doi:10.1021/jo00381a022

Liu, D. K. K., and Faulkner, L. R. (1977). P-type Delayed Fluorescence from Rubrene. *J. Am. Chem. Soc. j* 99, 14. doi:10.1021/ja00456a011

Mori, K., Kubota, Y., and Yamashita, H. (2013). Iridium and Rhodium Complexes within a Macroreticular Acidic Resin: A Heterogeneous Photocatalyst for Visible-Light Driven H2Production without an Electron Mediator. *Chem. Asian J.* 8, 3207–3213. doi:10.1002/asia.201301016

Ono, N., Miyagawa, H., Ueta, T., Ogawa, T., and Tani, H. (1998). Synthesis of 3,4-diarylpyrroles and Conversion into Dodecaarylporphyrins; a New Approach to Porphyrins with Altered Redox Potentials. *J. Chem. Soc. Perkin Trans. 1* 1, 1595–1602. doi:10.1039/A801185K

Pristash, S. R., Corp, K. L., Rabe, E. J., and Schlenker, C. W. (2020). Heavy-Atom-Free Red-To-Yellow Photon Upconversion in a Thiosquaraine Composite. *ACS Appl. Energ. Mater.* 3, 19–28. doi:10.1021/acsaem.9b01808

Shimizu, N., Ito, J., Kato, S., Otoki, Y., Goto, M., Eitsuka, T., et al. (2018). Oxidation of Squalene by Singlet Oxygen and Free Radicals Results in Different Compositions of Squalene Monohydroperoxide Isomers. *Sci. Rep.* 8, 9116. doi:10.1038/s41598-018-27455-5

Tan, C.-P., Zhong, Y.-M., Ji, L.-N., and Mao, Z.-W. (2021). Phosphorescent Metal Complexes as Theranostic Anticancer Agents: Combining Imaging and Therapy in a Single Molecule. *Chem. Sci.* 12, 2357–2367. doi:10.1039/d0sc06885c

Torréns, M. A., Straub, T. K., and Epstein, L. M. (1972). Moessbauer Studies on Oxo-Bridged Iron(III) Porphines. *J. Am. Chem. Soc.* 94, 4160.

Treibs, A., and Haeberie, N. (1968). Concerning the Synthesis and the Electron Spectrum of Ms-Substituted Porphine. *Justus Liebigs Ann. Chem.* 718, 183–207. doi:10.1002/jlac.19687180118

Yang, Z., Mao, Z., Xie, Z., Zhang, Y., Liu, S., Zhao, J., et al. (2017). Recent Advances in Organic Thermally Activated Delayed Fluorescence Materials. *Chem. Soc. Rev.* 46, 915–1016. doi:10.1039/c6cs00368k

Zhen, X., Qu, R., Chen, W., Wu, W., and Jiang, X. (2021). The Development of Phosphorescent Probes for *In Vitro* and *In Vivo* Bioimaging. *Biomater. Sci.* 9, 285–300. doi:10.1039/D0BM00819B

Zhou, J., Liu, Q., Feng, W., Sun, Y., and Li, F. (2015). Upconversion Luminescent Materials: Advances and Applications. *Chem. Rev.* 115 (1), 395–465. doi:10.1021/cr400478f

Zhou, Q., Zhou, M., Wei, Y., Zhou, X., Liu, S., Zhang, S., et al. (2017). Solvent Effects on the Triplet-Triplet Annihilation Upconversion of Diiodo-Bodipy and Peryleneffects on the Triplet–Triplet Annihilation Upconversion of Diiodo-Bodipy and Perylene. *Phys. Chem. Chem. Phys.* 19, 1516–1525. doi:10.1039/c6cp06897a

Zhou, Y., Liu, F., Wu, H., Qu, B., and Duan, L. (2015). Synthesis and Optical/Electrochemical Properties of Meso-5,10,15,20-Tetrathienyl Substituted Porphyrins and Their Metal Complexes. *Asian J. Chem.* 27 (No. 2), 616–620. doi:10.14233/ajchem.2015.17089

Conflict of Interest: The authors declare that the research was conducted in the absence of any commercial or financial relationships that could be construed as a potential conflict of interest.

ORIGINAL RESEARCH
published: 28 June 2022
doi: 10.3389/fchem.2022.805252

Tunable Photoluminescence Properties of Cotton Fiber With Gradually Changing Crystallinity

Qing Zhou[1]*, Man Liu[1], Chuchu Li[1], Shijia Lu[1], Bin Lei[2], Jiantang Jiang[1], Ying Yin[1], Yuanchao Zhang[1] and Yifeng Shen[1]*

[1]Engineering Research Center for Eco-Dyeing and Finishing of Textiles, Key Laboratory of Advanced Textile Materials and Manufacturing Technology, Ministry of Education, College of Textile Science and Engineering (International Institute of Silk), Zhejiang Sci-Tech University, Hangzhou, China, [2]Dali Silk (Zhejiang) Co., Ltd., Dali Science and Technology Park, Nanyan Provincial High-tech Development Zone, Shaoxing, China

Edited by:
Shuzo Hirata,
The University of Electro-Communications, Japan

Reviewed by:
Zhengxu Cai,
Beijing Institute of Technology, China
Huifang Shi,
Nanjing Tech University, China
Zhao Chen,
Jiangxi Science and Technology Normal University, China

***Correspondence:**
Qing Zhou
qingzhou1@zstu.edu.cn
Yifeng Shen
syf@zstu.edu.cn

Specialty section:
This article was submitted to Physical Chemistry and Chemical Physics,
a section of the journal Frontiers in Chemistry

Received: *30 October 2021*
Accepted: *13 May 2022*
Published: *28 June 2022*

Citation:
Zhou Q, Liu M, Li C, Lu S, Lei B, Jiang J, Yin Y, Zhang Y and Shen Y (2022) Tunable Photoluminescence Properties of Cotton Fiber With Gradually Changing Crystallinity. Front. Chem. 10:805252. doi: 10.3389/fchem.2022.805252

The alkali mercerizing process of semicrystalline cotton fiber (CF) is widely used in the printing and dyeing industry. The crystallinity change in the mercerizing process has been studied and certain laws have been obtained, but there is still a certain distance between the theoretical research results and the practical applications. CF is almost composed of cellulose, combined with the photoluminescence (PL) phenomenon of cellulose; herein, the varying crystallinity is correlated with its PL behavior after being treated with different concentrations of NaOH. In line with the characteristics of nonconventional luminogens, CF enjoys excitation-dependent emission and persistent room temperature phosphorescence (p-RTP) behavior. The emission spectra of all samples under the same excitation wavelength indicate that the change of CF crystallinity has a significant impact on its fluorescence and p-RTP emission. As the concentration of NaOH increases, the varying trend of quantum efficiency (QY) is consistent with the changed crystallinity of CF. Interestingly, the lifetime of p-RTP is exactly the opposite of the crystallinity change law. Clustering-triggered emission (CTE), crystallization-Induced Phosphorescence (CIP) mechanism, and the swelling due to hydrated sodium ions can reasonably explain these interesting photophysical processes, which also can be supported by theoretical calculations. The above studies have basically clarified the inherent law between the crystalline change of CF and the PL emission behavior during the alkali treatment process, which can be used as a theoretical reference for real-time monitoring of CF crystallinity changes using the spectral method in the actual cotton mercerizing process.

Keywords: cotton fiber, crystallinity, nonconventional luminogens, persistent room temperature phosphorescence, clustering-triggered emission

INTRODUCTION

Cotton fiber (CF) is one of the most common fibers in the textile printing and dyeing industry. In order to obtain excellent gloss and dyeing properties, CF will be alkali-treated through the alkali mercerizing process (Yazdanshenas and Shateri-Khalilabad, 2013; Ramamoorthy et al., 2015; Rajkumar et al., 2016). The cellulose content of CF is more than 90%, which is the source of natural cellulose with the highest purity (Abidi et al., 2014; Moon et al., 2011; Roche et al., 1978). Generally, after the CF is alkali mercerized, due to the fiber puffing, the light reflection behavior of CF is more regular, thus enhancing the luster (Akerholm et al., 2004). At the same time, the increase of the amorphous fixed area of the fiber increases the dye uptake rate during dyeing (Tsuboi, 1957; Okano and Sarko, 1985; Samsudin et al., 2020). In the current process, in addition to some research on the online control system of alkali concentration in the mercerizing process, there is almost no means to accurately monitor the crystallinity conversion of CF during the mercerizing process (Ujhelyiova et al., 2007). In case, sensitive monitoring methods such as light or electricity can be used to accurately control the entire mercerizing process to achieve fiber quality, which is very meaningful. The photoluminescence (PL) property of cellulose discovered in recent years has brought hope and feasibility to the abovementioned solutions (Gong et al., 2013; Du et al., 2019; Jiang et al., 2021; Lee et al., 2004). In 2013, Yuan et al. reported the luminescence behavior of natural polymers such as rice, starch, and cellulose, and found that they can emit bright light under ultraviolet (UV) light, and proposed a clustering-triggered emission mechanism (CTE), namely, the clustering of nonconventional chromophores with π and n electrons, and subsequent through space conjugation result in extended electron delocalization and conformation rigidification, to rationalize the emission, and to explain their intrinsic luminescence (Gong et al., 2013). In 2019, Du et al. (2019) found that microcrystalline cellulose (MCC) and its derivatives have room temperature phosphorescence (RTP) emission and used the CTE mechanism to explain such emission behavior. These substances also exhibit aggregation-induced emission (AIE) property (Dong et al., 2022).

Moreover, the luminescent compounds poly(amidoamine)s (PAMAM) (Lee et al., 2004; Lin et al., 2011; Lu et al., 2015), poly(amino ester)s (PAE) (Wu et al., 2005), poly(ether amide)s (PEA) (Lin et al., 2009), polyethylenimines (PEI) (Pastor-Pérez et al., 2007), and peptides, as (Guan et al., 2017) reported earlier, should be able to explain their luminescence behavior using the CTE mechanism. Subsequently, many researchers used the CTE mechanism to explain a series of newly discovered non-conjugated luminescence phenomena, such as Xylitol (Wang et al., 2018), non-conjugated amino acid (Chen et al., 2018), 1,1,2,2-tetraphenylethane (Zhang et al., 2017), and MDM2 proteins (Liu et al., 2020), this mechanism has been recognized by more and more researchers. Furthermore, persistent room temperature phosphorescence (p-RTP) phenomenon has been observed from many non-conjugated organic compounds, such as poly(acrylic acid) (PAA) (Zhou et al., 2020), polyacrylamide (PAM) (Wang et al., 2020), cyanoacetic acid (Fang et al., 2018), sodium polymethacrylate (PMANa) (Cai et al., 2019), and oxalic acid (Zheng et al., 2020). Moreover, non-conjugated luminescent compounds have a unique excitation wavelength dependence emission property, generally RTP phenomenon and its wide application prospects in multiple anti-counterfeiting and encryption fields have become research hotspots (Liao et al., 2021a; Xu et al., 2021a; Liao et al., 2021b; Xu et al., 2021b). However, at present, the phosphorescence ability of such compounds is weak at room temperature, and it can even be observed only in a vacuum for some compounds, for example, BSA (Wang et al., 2019). In order to enhance the p-RTP emission of such materials it may be possible to learn from the currently more recognized crystallization-induced phosphorescence (CIP) mechanism (Yuan et al., 2010; Shen et al., 2017; Chen et al., 2019; Nitti et al., 2020; Xing et al., 2020), that is, to build a rigid environment by increasing crystallization to inhibit non-radiative transitions (Sudhakar and Radhakrishnan, 2019; Yang et al., 2020). Therefore, the change in crystallinity has a significant impact on its luminescence behavior.

In order to explore the changes in the crystalline structure of CFs during alkali treatment (**Supplementary Figure S1**), the PL detection method is combined with crystallinity changes, so that it can macroscopically characterize the changes in the mercerization process of CFs through luminescence. In order to obtain a variety of CFs with adjustable crystallinity, we use traditional NaOH treatment solutions that cannot be concentrated. A series of CF samples with different crystallinity were prepared *via* different concentrations of NaOH aqueous solution, and the changes in crystallinity with luminescence behavior were carried out. The results showed that with the increase of alkali treatment concentration, the crystallinity of CF showed a trend of first decreasing and then increasing, and the QY change trend was the same as mentioned above. It is very interesting that in this process the p-RTP lifetime of CFs changes in the opposite direction to their crystallinity, and the most probable reason has been proven that the CF gradually swells due to hydrated sodium ions, resulting in the formation of more and stronger triplet emission centers.

RESULTS AND DISCUSSION

As shown in **Figure 1**, the crystallinity of CF calculated from XRD firstly drops and then rises with the increased NaOH concentration (**Supplementary Figure S2**), and then reaches the lowest value at 18 wt% (36.01%) (**Figure 1C**, **Supplementary Table S1**). In the above process, the violently evolved crystallinity is very likely to change the structure of the cluster and the degree of conformation rigidification. Thus, according to the CTE and CIP theory, these changes will have a huge impact on the FL and p-RTP emission of CFs. In order to prove our guess, these CFs were investigated under different UV lamps (254, 312, and 365 nm). It can be seen that all the samples emit blue light under different UV lamps (**Figure 1A**), and the excitation spectra of the emission peak at 410 nm shows that the best excitation of these samples is around 352 nm (**Supplementary Figure S3**). Furthermore, these samples have excitation-dependent emission under different excitation (**Figure 1B**, **Supplementary Figure S4**), which implied the existence of multiple launch centers.

The QY data also revealed a higher consistency of crystallinity, indicating that crystallization can contribute to improve QY (**Figure 1C**). Specifically, the CF-5 enjoys the highest crystallinity and QY (70.70%, 5.19%), and the crystallinity and QY of CF-18 reached the lowest value (36.01%, 2.24%), while the crystallinity and QY of CF-21 increased simultaneously (43.86%, 3.01%) (Table S1). The above observations are macroscopic, and

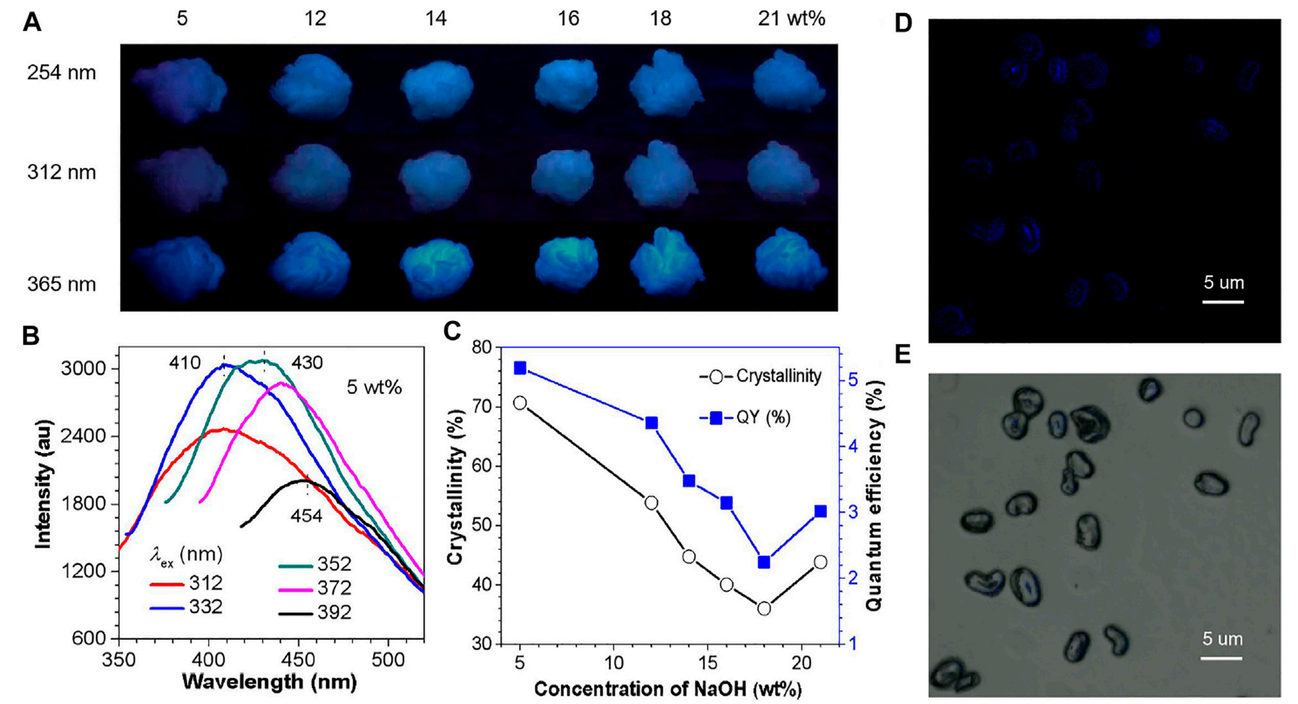

FIGURE 1 | (A) Photographs of CF samples taken under varying UV lights (254, 312, 365 nm) at ambient conditions. **(B)** PL spectra of CF-5 with different λ_{ex} values. **(C)** Trend graph of crystallinity and QY (%) of samples. **(D)** Confocal image recorded under excitation at 405 nm of the CF cross-section and **(E)** bright field image.

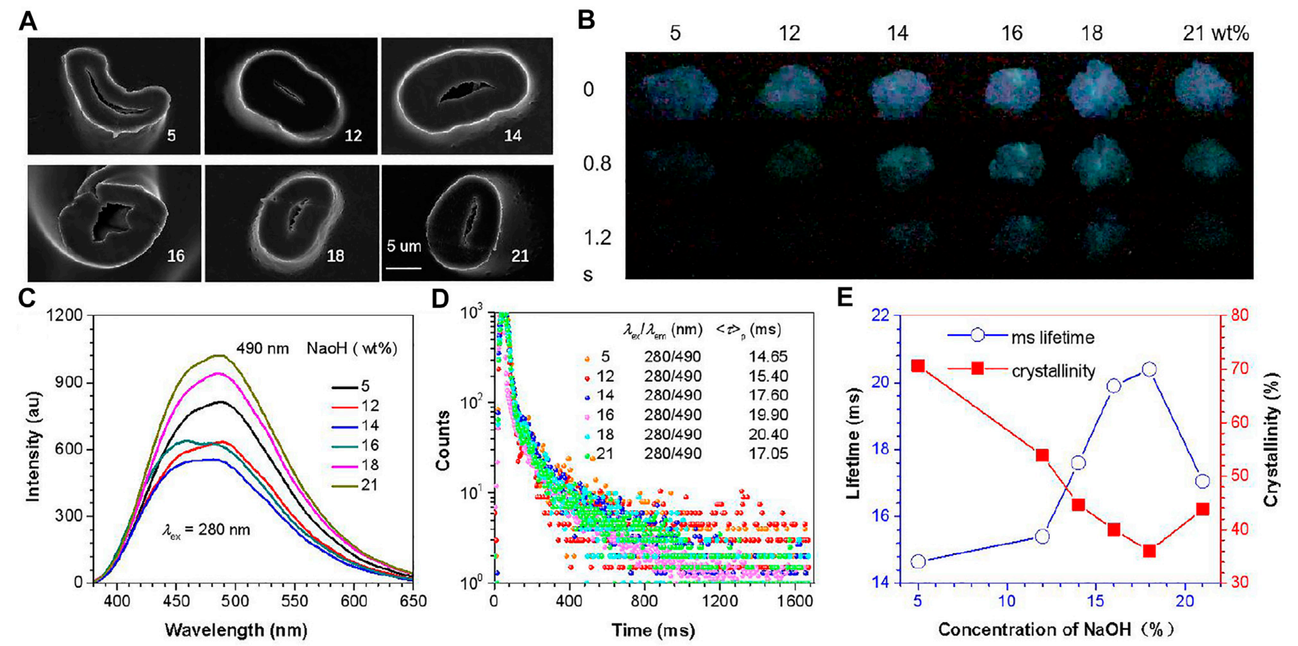

FIGURE 2 | (A) SEM images of CF cross-sections with different crystallinity (scale bar = 5 um). **(B)** Photographs of samples after ceasing the 254 nm irradiation at ambient conditions. **(C)** Phosphorescence of CF sample at excitation wavelength of 280 nm (t_d = 0.1 ms). **(D)** Phosphorescence ms lifetimes of different fiber samples (λ_{ex} = 280 nm). **(E)** Change trend of ms lifetime and crystallinity of samples.

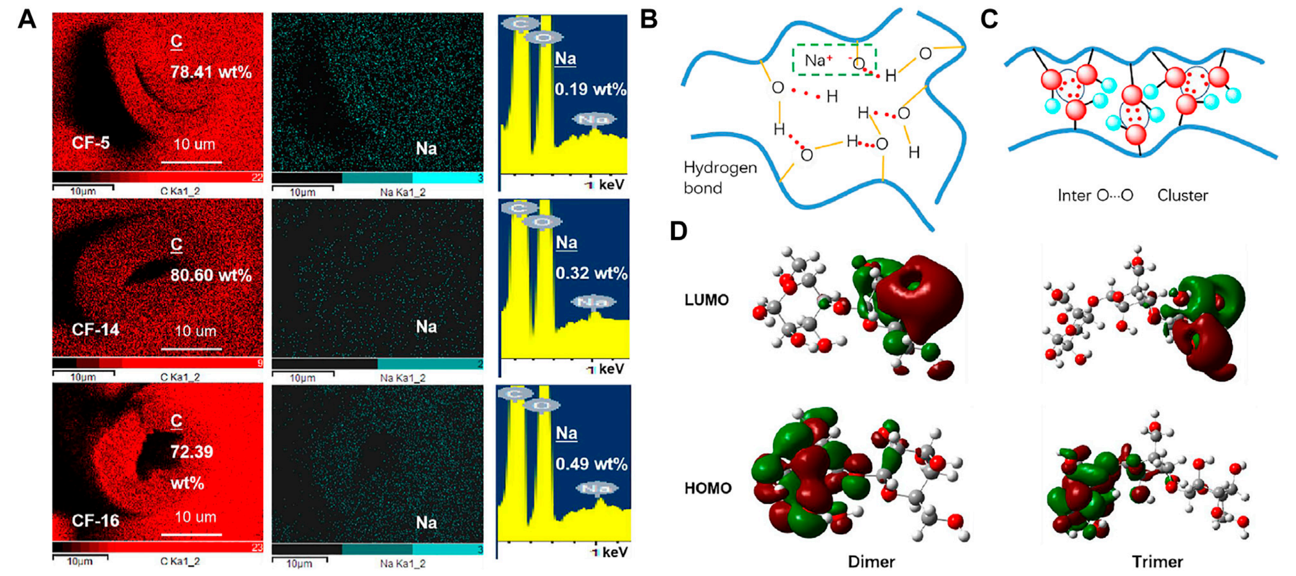

FIGURE 3 | (A) SEM mapping images of CF cross-sections with different crystallinity (scale bar = 10 um), area scans of C and Na elemental distribution. **(B)** Partial hydrogen bond interactions in CFs. **(C)** The oxygen clusters in CFs are mainly formed by the interaction of oxygen atoms. **(D)** LUMO and HOMO electron densities of the dimer and trimer.

the nature of the macro is always determined by the micro structure. Thus, do the internal cross-sections of CF have similar phenomena? The image of the radial cross-section of the CF taken by the laser confocal microscope shows that the inside also has a relatively strong PL behavior (**Figures 1D,E**). Moreover, the PL emission phenomenon of CFs observed in a microscopic scale has hardly been reported.

In the process of alkali treatment, the crystallinity also changes the morphology of the fiber. This can be seen from the SEM images of the cross-sections of these samples (**Figure 2A**). As the alkali treatment concentration increases, the CF gradually swells. The type changes to an elliptical cross-section, which is caused by the swelling of the amorphous region and the transformation of the crystalline region into the amorphous region and the realignment of the molecules. In the above morphological changes, the more important thing is that the changes in molecular arrangement will lead to change in intermolecular interactions, which will affect various physical parameters of CFs, especially the changes in the structure of the cluster emission center, thereby changing its PL behavior. Combining CIP theory and CTE mechanism, changes in crystallinity are likely to affect RTP emission property. Unsurprisingly, after turning off the UV lamp of the same wavelength, the p-RTP emission of samples with different crystallinity have a certain difference in emission peaks and lifetime (**Figures 2B,C**, **Supplementary Figure S5** and **Supplementary Video S1**), which indicates that the emission ability of the emission center is different. The ms lifetimes are greatly increased as the crystallinity decreases until CF-18 (**Figures 2D,E**, **Supplementary Table S2**), and then it increased, basically contrary to the changing trend of crystallinity.

According to the mechanism of CTE and CIP, the increase of crystallinity should increase the emission ability of fluorescence and p-RTP. In general, the arrangement of cellulose molecules in the crystalline region must be denser than that in the amorphous region, resulting in a closer average distance between oxygen atoms in the crystalline region. It is easier for electrons to be delocalized and conjugated to form cluster emission centers with strong emission ability. With the increase of crystallinity, the number and emission ability of the cluster also increase. The above finding can be reasonably understood by the CTE mechanism. The increase of crystallinity makes the distance between some other atoms closer, which leads to the increase of interaction and the rigidity of the conformation of the cluster, and improves the radiation transition probability, which can be reasonably explained by the CIP mechanism.

The change of QY emission ability and the change of crystallinity can support the above conclusion, but p-RTP has the opposite conclusion which is probably because when the crystallinity increases, the per unit volume of CF also increases, and the volume of air decreases, which is defined as the swelling effect (**Figure 3A** and **Supplementary Figure S6**). This effect has been recognized as a phenomenon, and its mechanism is generally believed to be derived from the destruction of the lattice and the reconstruction of bonds by hydrated sodium ions (Gert et al., 2000). Because of the presence of Na^+ ions, which apparently bond with the cellulose hydroxyl groups, almost all of the interchain hydrogen bonds that ordinarily stabilize the cellulose structure have been broken. New types of interchain bonds were formed by the help of Na^+ ions and water molecules present in the system (Klemm et al., 1998). Sodium ions partially remain in the amorphous region due to ionic interactions with oxygen anions, and its content increase with the increase of the amorphous region which can be supported from their mapping elements (carbon, oxygen, and sodium) results calculated by deducting the background and integral area (**Figure 3A**, **Supplementary S7–S9**, **Supplementary Table S3**). The interaction of Na^+ and O^- ions (removal of H from hydroxyl groups on cellulose) to form part of ionic bond greatly increases the molecular conformation rigidity. It can form an emission center with stronger triplet emission capability, so that the CF with low crystallinity has a longer afterglow instead.

The PL phenomenon of CF can be explained by the CTE mechanism, the clustering of oxygen atoms created enriched energy levels and narrowed the energy gaps, thus promoting SOC and allowing the consequent ISC transitions. It can be seen from the above analysis that the influence of crystallinity conversion process on the PL performance of CF has been partially obtained. How do the molecules in the CF affect its emission? In-depth analysis, it can be found that strong hydrogen bond interactions are formed between the hydroxyl groups on the cellulose molecular structure, especially in the crystalline region (**Figure 3B**). The remaining Na ions in the intermolecular and O atoms form partial ionic bonds, resulting in a more rigid cluster emission center. In addition, the interaction between the lone pair of oxygen atoms forms an oxygen cluster structure, which increases the rigidity of the cluster's conformation under the action of hydrogen bonds, and makes it have PL ability. In order to further understand why the cellulose molecule has PL and p-RTP emission capability, the preliminary theoretical calculations were conducted. LUMO and HOMO electron densities of the dimer (the smallest unit of cellulose) and trimer of the cellulose unit were calculated, and their molecular conformations are optimized. Although the results remain preliminary, the electron density distribution clearly indicates the intramolecular O···O electron delocalization for the leftmost single molecule in the dimer and trimer (**Figure 3D**). In addition, the HOMO and LUMO levels of aggregates clearly illustrated the extended delocalization among the neighboring molecules in excited states, which agreed well with the postulated hypothesis.

CONCLUSION

In conclusion, CF enjoys excitation-dependent emission and p-RTP behavior. Moreover, the emission spectra of all samples under the same excitation wavelength indicate that the change of CF crystallinity has a significant impact on its fluorescence and p-RTP emission. The increased QY is attributed to the increase in crystallinity, whereas the emission ability of p-RTP exhibits a negative correlation. These interesting phenomena can be reasonably explained by CTE and the swelling due to hydrated sodium ions. Furthermore, these findings, in turn, offer more fundamental implications to the underlying mechanism of nonconventional chromophores. The exploration of the CIP and CTE laws of CF is likely to fill the gap in the study of photoluminescence behavior in the process of crystallization conversion of the natural polymer (fiber). More meaningful is that these results can be used as a theoretical reference for real-time monitoring of CF or other natural fiber in the actual mercerizing process.

DATA AVAILABILITY STATEMENT

The original contributions presented in the study are included in the article/**Supplementary Material**, further inquiries can be directed to the corresponding authors.

AUTHOR CONTRIBUTIONS

QZ, ML, and SL did all the experiments. CL, YZ, and YY assisted in data analysis. All authors discussed the results. QZ, BL, and JJ wrote the paper. QZ and YS designed and supervised the research and revised the manuscript.

FUNDING

This work was financially supported by the National Natural Science Foundation of China (52103233), the Key R&D Program of Zhejiang Province, China (2021C03149), Zhejiang Basic Public Welfare Research Project (LQ21E030017), and the Research Start-up Funding of Zhejiang Sci-Tech University (20202215-Y).

SUPPLEMENTARY MATERIAL

The Supplementary Material for this article can be found online at: https://www.frontiersin.org/articles/10.3389/fchem.2022.805252/full#supplementary-material

REFERENCES

Abidi, N., Cabrales, L., and Haigler, C. H. (2014). Changes in the Cell Wall and Cellulose Content of Developing Cotton Fibers Investigated by FTIR Spectroscopy. *Carbohydr. Polym.* 100, 9–16. doi:10.1016/j.carbpol.2013.01.074

Akerholm, M., Hinterstoisser, B., and Salmén, L. (2004). Characterization of the Crystalline Structure of Cellulose Using Static and Dynamic FT-IR Spectroscopy. *Carbohydr. Res.* 339 (3), 569–578. doi:10.1016/j.carres.2003.11.012

Cai, S., Ma, H., Shi, H., Wang, H., Wang, X., Xiao, L., et al. (2019). Enabling Long-Lived Organic Room Temperature Phosphorescence in Polymers by Subunit Interlocking. *Nat. Commun.* 10 (1), 1–8. doi:10.1038/s41467-019-11749-x

Chen, G., Zhou, J., Feng, H., Feng, F., Xu, P., Pan, S., et al. (2019). A Simple and Efficient Phosphorescent Probe for Iodide-specific Detection Based on Crystallization-Induced Phosphorescence of Organic Ionic Crystals. *J. Mat. Chem. C* 7 (1), 43–47. doi:10.1039/c8tc04781b

Chen, X., Luo, W., Ma, H., Peng, Q., Yuan, W. Z., and Zhang, Y. (2018). Prevalent Intrinsic Emission from Nonaromatic Amino Acids and Poly(amino Acids). *Sci. China Chem.* 61 (3), 351–359. doi:10.1007/s11426-017-9114-4

Dong, X., Ye, J., Chen, Y., Tanziela, T., Jiang, H., Wang, X., et al. (2022). Intelligent Peptide-Nanorods against Drug-Resistant Bacterial Infection and Promote Wound Healing by Mild-Temperature Photothermal Therapy. *Chem. Eng. J.* 432, 134061. doi:10.1016/j.cej.2021.134061

Du, L.-L., Jiang, B.-L., Chen, X.-H., Wang, Y.-Z., Zou, L.-M., Liu, Y.-L., et al. (2019). Clustering-triggered Emission of Cellulose and its Derivatives. *Chin. J. Polym. Sci.* 37 (4), 409–415. doi:10.1007/s10118-019-2215-2

Fang, M., Yang, J., Xiang, X., Xie, Y., Dong, Y., Peng, Q., et al. (2018). Unexpected Room-Temperature Phosphorescence from a Non-aromatic, Low Molecular Weight, Pure Organic Molecule through the Intermolecular Hydrogen Bond. *Mat. Chem. Front.* 2 (11), 2124–2129. doi:10.1039/c8qm00396c

Gert, E. V., Morales, A. S., Zubets, O. V., and Kaputskii, F. N. (2000). The Features of Nitric Acid 'mercerization' of Cellulose. *Cellulose* 7, 57–66. doi:10.1023/A:1009206113613

Gong, Y., Tan, Y., Mei, J., Zhang, Y., Yuan, W., Zhang, Y., et al. (2013). Room Temperature Phosphorescence from Natural Products: Crystallization Matters. *Sci. China Chem.* 56 (9), 1178–1182. doi:10.1007/s11426-013-4923-8

Guan, X., Zhang, D., Jia, T., Zhang, Y., Meng, L., Jin, Q., et al. (2017). Unprecedented Strong Photoluminescences Induced from Both Aggregation and Polymerization of Novel Nonconjugated β-Cyclodextrin Dimer. *Ind. Eng. Chem. Res.* 56 (14), 3913–3919. doi:10.1021/acs.iecr.6b04979

Jiang, J., Lu, S., Liu, M., Li, C., Zhang, Y., Yu, T. B., et al. (2021). Tunable Photoluminescence Properties of Microcrystalline Cellulose with Gradually Changing Crystallinity and Crystal Form. *Macromol. Rapid Commun.* 42 (17), 2100321. doi:10.1002/marc.202100321

Klemm, D., Philipp, B., Heinze, T., Heinze, U., and Wagenknecht, W. (1998). *Comprehensive Cellulose Chemistry:Functionalization of Cellulose*, 2. New York: Wiley, 33. doi:10.1002/3527601937

Lee, W. I., Bae, Y., and Bard, A. J. (2004). Strong Blue Photoluminescence and ECL from OH-terminated PAMAM Dendrimers in the Absence of Gold Nanoparticles. *J. Am. Chem. Soc.* 126 (27), 8358–8359. doi:10.1021/ja0475914

Liao, P., Zang, S., Wu, T., Jin, H., Wang, W., Huang, J., et al. (2021b). Generating Circularly Polarized Luminescence from Clusterization-Triggered Emission Using Solid Phase Molecular Self-Assembly. *Nat. Commun.* 12 (1), 5496–5499. doi:10.1038/s41467-021-25789-9

Liao, P., Huang, J., Yan, Y., and Tang, B. Z. (2021a). Clusterization-triggered Emission (CTE): One for All, All for One. *Mat. Chem. Front.* 5 (18), 6693–6717. doi:10.1039/d1qm00808k

Lin, S. Y., Wu, T. H., Jao, Y. C., Liu, C. P., Lin, H. Y., Lo, L. W., et al. (2011). Unraveling the Photoluminescence Puzzle of PAMAM Dendrimers. *Chem. Eur. J.* 17 (26), 7158–7161. doi:10.1002/chem.201100620

Lin, Y., Gao, J.-W., Liu, H.-W., and Li, Y.-S. (2009). Synthesis and Characterization of Hyperbranched Poly(ether Amide)s with Thermoresponsive Property and Unexpected Strong Blue Photoluminescence. *Macromolecules* 42 (9), 3237–3246. doi:10.1021/ma802353f

Liu, P., Fu, W., Verwilst, P., Won, M., Shin, J., Cai, Z., et al. (2020). MDM2-Associated Clusterization-Triggered Emission and Apoptosis Induction Effectuated by a Theranostic Spiropolymer. *Angew. Chem. Int. Ed.* 59 (22), 8435–8439. doi:10.1002/anie.201916524

Lu, H., Feng, L., Li, S., Zhang, J., Lu, H., and Feng, S. (2015). Unexpected Strong Blue Photoluminescence Produced from the Aggregation of Unconventional Chromophores in Novel Siloxane-Poly(amidoamine) Dendrimers. *Macromolecules* 48 (3), 476–482. doi:10.1021/ma502352x

Moon, R. J., Martini, A., Nairn, J., Simonsen, J., and Youngblood, J. (2011). Cellulose Nanomaterials Review: Structure, Properties and Nanocomposites. *Chem. Soc. Rev.* 40 (7), 3941–3994. doi:10.1039/c0cs00108b

Nitti, A., Botta, C., Forni, A., Cariati, E., Lucenti, E., and Pasini, D. (2020). Crystallization-induced Room-Temperature Phosphorescence in Fumaramides. *CrystEngComm* 22 (45), 7782–7785. doi:10.1039/d0ce01253j

Okano, T., and Sarko, A. (1985). Mercerization of Cellulose. II. Alkali-Cellulose Intermediates and a Possible Mercerization Mechanism. *J. Appl. Polym. Sci.* 30 (1), 325–332. doi:10.1002/app.1985.070300128

Pastor-Pérez, L., Chen, Y., Shen, Z., Lahoz, A., and Stiriba, S.-E. (2007). Unprecedented Blue Intrinsic Photoluminescence from Hyperbranched and Linear Polyethylenimines: Polymer Architectures and pH-Effects. *Macromol. Rapid Commun.* 28 (13), 1404–1409. doi:10.1002/marc.200700190

Rajkumar, R., Manikandan, A., and Saravanakumar, S. S. (2016). Physicochemical Properties of Alkali-Treated New Cellulosic Fiber from Cotton Shell. *Int. J. Polym. Analysis Charact.* 21 (4), 359–364. doi:10.1080/1023666x.2016.1160509

Ramamoorthy, S. K., Skrifvars, M., and Rissanen, M. (2015). Effect of Alkali and Silane Surface Treatments on Regenerated Cellulose Fibre Type (Lyocell) Intended for Composites. *Cellulose* 22 (1), 637–654. doi:10.1007/s10570-014-0526-6

Roche, E., Chanzy, H., Boudeulle, M., Marchessault, R. H., and Sundararajan, P. (1978). Three-dimensional Crystalline Structure of Cellulose Triacetate II. *Macromolecules* 11 (1), 86–94. doi:10.1021/ma60061a016

Samsudin, N. A., Low, F. W., Yusoff, Y., Shakeri, M., Tan, X. Y., Lai, C. W., et al. (2020). Effect of Temperature on Synthesis of Cellulose Nanoparticles via Ionic Liquid Hydrolysis Process. *J. Mol. Liq.* 308, 113030. doi:10.1016/j.molliq.2020.113030

Shen, N., Li, J., Wu, Z., Hu, B., Cheng, C., Wang, Z., et al. (2017). A- and β-[Bmim][BiCl4 (2,2′-bpy)]: Two Polymorphic Bismuth-Containing Ionic Liquids with Crystallization-Induced Phosphorescence. *Chem. Eur. J.* 23 (62), 15795–15804. doi:10.1002/chem.201703552

Sudhakar, P., and Radhakrishnan, T. P. (2019). Stimuli Responsive and Reversible Crystalline-Amorphous Transformation in a Molecular Solid: Fluorescence Switching and Enhanced Phosphorescence in the Amorphous State. *J. Mat. Chem. C* 7 (23), 7083–7089. doi:10.1039/c9tc01600g

Tsuboi, M. (1957). Infrared Spectrum and Crystal Structure of Cellulose. *J. Polym. Sci.* 25 (109), 159–171. doi:10.1002/pol.1957.1202510904

Ujhelyiova, A., Bolhova, E., Oravkinova, J., Tiňo, R., and Marcinčin, A. (2007). Kinetics of Dyeing Process of Blend Polypropylene/polyester Fibres with Disperse Dye. *Dyes Pigments* 72 (2), 212–216. doi:10.1016/j.dyepig.2005.08.026

Wang, Q., Dou, X., Chen, X., Zhao, Z., Wang, S., Wang, Y., et al. (2019). Reevaluating Protein Photoluminescence: Remarkable Visible Luminescence upon Concentration and Insight into the Emission Mechanism. *Angew. Chem. Int. Ed.* 58, 12667–12673. doi:10.1002/ange.20190622610.1002/anie.201906226

Wang, S., Wu, D., Yang, S., Lin, Z., and Ling, Q. (2020). Regulation of Clusterization-Triggered Phosphorescence from a Non-conjugated Amorphous Polymer: a Platform for Colorful Afterglow. *Mat. Chem. Front.* 4 (4), 1198–1205. doi:10.1039/d0qm00018c

Wang, Y., Bin, X., Chen, X., Zheng, S., Zhang, Y., and Yuan, W. Z. (2018). Emission and Emissive Mechanism of Nonaromatic Oxygen Clusters. *Macromol. Rapid Commun.* 39 (21), 1800528. doi:10.1002/marc.201800528

Wu, D., Liu, Y., He, C., and Goh, S. H. (2005). Blue Photoluminescence from Hyperbranched Poly(amino Ester)s. *Macromolecules* 38 (24), 9906–9909. doi:10.1021/ma051407x

Xing, Y., Wang, Y., Zhou, L., and Zhu, L. (2021). Highly Tunable Aggregate-Induced Phosphorescence Properties in Persulfurated Arenes. *Dyes Pigments* 186, 109032. doi:10.1016/j.dyepig.2020.109032

Xu, L., Liang, X., Zhong, S., Li, Z., Gao, Y., and Cui, X. (2021a). Natural Silk Fibroin Based on Aggregation-Induced Emission with a Clustering-Triggered Mechanism and its Multiple Applications. *ACS Sustain. Chem. Eng.* 9 (36), 12043–12048. doi:10.1021/acssuschemeng.1c02865

Xu, L., Zhong, S., Meng, Q., Zhang, Z., Gao, Y., and Cui, X. (2021b). Novel Material from Natural Resource, Agarose with Clustering-Triggered Emission and its Diverse Applications. *Dyes Pigments* 194, 109558. doi:10.1016/j.dyepig.2021.109558

Yang, Z., Xu, C., Li, W., Mao, Z., Ge, X., Huang, Q., et al. (2020). Boosting the Quantum Efficiency of Ultralong Organic Phosphorescence up to 52 % via Intramolecular Halogen Bonding. *Angew. Chem. Int. Ed. Engl.* 132 (40), 17604–17608. doi:10.1002/ange.20200734310.1002/anie.202007343

Yazdanshenas, M. E., and Shateri-Khalilabad, M. (2013). *In Situ* synthesis of Silver Nanoparticles on Alkali-Treated Cotton Fabrics. *J. Industrial Text.* 42 (4), 459–474. doi:10.1177/1528083712444297

Yuan, W. Z., Shen, X. Y., Zhao, H., Lam, J. W. Y., Tang, L., Lu, P., et al. (2010). Crystallization-induced Phosphorescence of Pure Organic Luminogens at Room Temperature. *J. Phys. Chem. C* 114 (13), 6090–6099. doi:10.1021/jp909388y

Zhang, H., Zheng, X., Xie, N., He, Z., Liu, J., Leung, N. L. C., et al. (2017). Why Do Simple Molecules with "Isolated" Phenyl Rings Emit Visible Light? *J. Am. Chem. Soc.* 139 (45), 16264–16272. doi:10.1021/jacs.7b08592

Zheng, S., Zhu, T., Wang, Y., Yang, T., and Yuan, W. Z. (2020). Accessing Tunable Afterglows from Highly Twisted Nonaromatic Organic AIEgens via Effective Through-Space Conjugation. *Angew. Chem. Int. Ed.* 59 (25), 10018–10022. doi:10.1002/anie.202000655

Zhou, Q., Yang, T., Zhong, Z., Kausar, F., Wang, Z., Zhang, Y., et al. (2020). A Clustering-Triggered Emission Strategy for Tunable Multicolor Persistent Phosphorescence. *Chem. Sci.* 11 (11), 2926–2933. doi:10.1039/c9sc06518k

Conflict of Interest: Author BL was supported by the company Dali Silk (Zhejiang) Co., Ltd., Dali Science and Technology Park.

The remaining authors declare that the research was conducted in the absence of any commercial or financial relationships that could be construed as a potential conflict of interest.

Advantages of publishing in Frontiers

OPEN ACCESS
Articles are free to read
for greatest visibility
and readership

FAST PUBLICATION
Around 90 days
from submission
to decision

HIGH QUALITY PEER-REVIEW
Rigorous, collaborative,
and constructive
peer-review

TRANSPARENT PEER-REVIEW
Editors and reviewers
acknowledged by name
on published articles

Frontiers
Avenue du Tribunal-Fédéral 34
1005 Lausanne | Switzerland

Visit us: www.frontiersin.org
Contact us: frontiersin.org/about/contact

REPRODUCIBILITY OF RESEARCH
Support open data
and methods to enhance
research reproducibility

DIGITAL PUBLISHING
Articles designed
for optimal readership
across devices

FOLLOW US
@frontiersin

IMPACT METRICS
Advanced article metrics
track visibility across
digital media

EXTENSIVE PROMOTION
Marketing
and promotion
of impactful research

LOOP RESEARCH NETWORK
Our network
increases your
article's readership